From the Red River to the Gulf of Tonkin : dynamics and sediment transport along the estuary-coastal area continnum

Violaine Piton

THÈSE

En vue de l'obtention du

DOCTORAT DE L'UNIVERSITÉ DE TOULOUSE

Délivré par : *l'Université Toulouse 3 Paul Sabatier (UT3 Paul Sabatier)*

Présentée et soutenue le *16/12/2019* **par :**

VIOLAINE PITON

Du Fleuve Rouge au Golfe du Tonkin: dynamique et transport sédimentaire le long du continuum estuaire-zone côtière

JURY

ISABELLE BRENON	LIENSs	Rapportrice
SABINE CHARMASSON	IRSN	Rapportrice
ALDO SOTTOLICHIO	EPOC	Rapporteur
ROBERT LAFITE	M2C	Examinateur
ROMARIC VERNEY	IFREMER	Examinateur
JEAN-MICHEL MARTINEZ	GET	Examinateur
CATHERINE JEANDEL	LEGOS	Présidente du Jury
SYLVAIN OUILLON	LEGOS, IRD	Directeur de thèse
MARINE HERRMANN	LEGOS, IRD	Co-Directrice de thèse

École doctorale et spécialité :
   SDU2E : Océan, Atmosphère, Climat
Unité de Recherche :
   Laboratoire d'études en géophysique et océanographie spatiales (UMR5566)
Directeur(s) de Thèse :
   Marine Herrmann et *Sylvain Ouillon*
Rapporteurs :
   Isabelle Brenon, Sabine Charmasson et *Aldo Sottolichio*

Remerciements

Je tiens tout d'abord à chaleureusement remercier mon directeur de thèse, Sylvain Ouillon, pour avoir partagé avec moi sa passion et son savoir sur les petites particules qui se baladent dans l'eau, pendant 3 ans. Merci de m'avoir fait confiance pour cette thèse au tout début, merci de m'avoir permis de réaliser les campagnes dans la Van Uc, merci d'avoir sorti l'ADCP des herbes folles en pleine nuit, merci pour ton expérience avec les campagnes de mesures, pour ta connaissance sans faille des processus estuariens et enfin merci pour tes précieux conseils, tes orientations et encouragements tout au long de ce travail. Promis, maintenant je vais lire ton livre! Je remercie également très fort ma co-directrice de thèse, Marine Herrmann, qui même à distance a su m'orienter et me conseiller dans ce travail de recherche. Merci pour ton engouement pour la recherche et pour ta motivation communicative, merci aussi pour ton soutien lors de mes séjours à l'USTH, merci d'avoir fait en sorte que les campagnes de terrain se réalisent, et désolée de t'y avoir traîné toute une nuit froide. Merci pour les explorations by night de la charmante bourgade de Qingdao et celles à vélo de Perth et ses petits quokkas. Et merci pour ta sympathie, tes super blagues et ta cape de pluie! Cette thèse, et surtout son aspect modélisation, n'auraient bien sûr pas été possibles sans le soutien de mon co-co-directeur de thèse, Patrick Marsaleix. Merci beaucoup pour ton aide dévouée lors de la mise en place du modèle et les heures passées à la bidouille des rivières. Merci de m'avoir passionné pour la modélisation et m'en avoir montré les possibilités infinies. Merci pour toutes tes idées lumineuses, pour les améliorations qui n'en finissent plus d'améliorer, pour les "cherries on top" et pour avoir été présent et enthousiaste à chaque étape.

Cette thèse est le fruit de nombreuses collaborations intra et inter laboratoires. Tout d'abord, un merci particulier à Florent Lyard qui a tenté de m'initier aux joies de la modélisation spectrale de la marée… et merci à Damien Allain d'avoir mis à jour POCViP quand j'en avais besoin. Many thanks to Vu Duy Vinh (from IMER) for your help organizing and performing the Van Uc surveys. Thank you for you knowledge of the region, for your precious network and for your help with the

Contents

List of Figures

List of Tables

List of abbreviations

ADCP: Acoustic Doppler Current Profiler
DFR: Delta du Fleuve Rouge
DMI: Dipole Mode Index
DN: survey during the Dry season at Neap tide
DS: survey during the Dry season at Spring tide
ECMWF: European Centre for Medium-Range Weather Forecasts
EOF: Empirical Orthogonal Function
ENSO: El Niño Southern Oscillation
GOM: Global Ocean Model
GdT: Golfe du Tonkin
GoT: Gulf of Tonkin
LISST: Laser In situ Scattering and Transmissometry
MCM: Mer de Chine Méridionale
MES: Matière En Suspension
NHMS: National Hydro-Meteorological Service
NP: Northern Pacific
NTU: Nephelometric Turbidity Unit
PDO: Pacific Decadal Oscillation
PSD: Particle Size Distribution
PSU: Practical Salinity Unit
SAM: Marshall Southern Annular Mode
SCS: South China Sea
SLA: Sea Level Anomaly
SOI: Southern Oscillation Index
SPM: Suspended Particulate Matter
SSC: Suspended Sediment Concentration
SSH: Sea Surface Height
SST: Sea Surface Temperature
SSS: Sea Surface Salinity
TT: Trung Trang
WN: survey during the Wet season at Neap tide
WS: survey during the Wet season at Spring tide

Abstract

Deltas and coastal regions deliver the largest inputs of freshwater and sediments to the shelf and open ocean, understanding water and sediment dynamics and variability in those regions is therefore crucial. The spatio-temporal variability of estuarine and ocean dynamics under the influence of natural forcings and their impact on sediment transport and fate was assessed along the Red River estuary - coastal ocean - Gulf of Tonkin continuum. First, in-situ estuarine observations evidenced the seasonal and tidal variabilities of flow and suspended matter, and showed in particular the role of tidal pumping in the estuary siltation. Second, a 3D realistic hydrodynamic model was set up and calibrated with various observations and satellite data. Beforehand, a high-resolution model configuration was implemented and optimized with sensitivity tests of the Gulf of Tonkin's tidal components to bathymetry and various bottom friction parameterizations. Third, the resulting optimized configuration was used to study the large scale Gulf of Tonkin circulation at daily, seasonal and interannual scales, and to identify the drivers of their variabilities. Ekman transport variability due to monsoon winds reversal drives the seasonal circulation, which can be reversed in summer by episodic typhoon events and intensified in winter. ENSO, strong typhoon activity and Arctic Oscillation have been identified as drivers of the interannual circulation variability. Lastly, preliminary tests with a sediment transport module coupled with the hydrodynamics model revealed the importance of the seabed composition and of the parameterization of the erosion coefficients.

Keywords : estuarine to regional circulation, sediment transport, variability, in-situ observations, regional ocean modelling, estuary-coastal ocean continuum, Red River, Gulf of Tonkin

Résumé

Les deltas et les régions côtières constituent les sources les plus importantes d'eau douce et de matière en suspension vers le plateau continental puis le large, la compréhension de leur dynamique et de leur variabilité est donc cruciale. Cette thèse vise à mieux comprendre la variabilité spatio-temporelle de la dynamique estuarienne et océanique sous l'influence de forçages naturels et l'influence de cette variabilité sur le transport et devenir des sédiments le long du continuum estuaire - océan côtier du Fleuve Rouge au Golfe du Tonkin. Des observations in-situ collectées dans l'estuaire ont d'abord mis en évidence l'influence de la variabilité saisonnière et de la variabilité due à la marée sur le débit et sur le devenir des matières en suspension, en particulier le rôle du pompage tidal dans l'envasement de l'estuaire. Deuxièmement, un modèle hydrodynamique 3D réaliste, basé sur une configuration haute-résolution et un paramétrage optimisés et validés à partir de plusieurs jeux d'observations in-situ et de données satellitaires, a été utilisé pour l'étude de la circulation à l'échelle du Golfe du Tonkin. Cette configuration a préalablement été optimisée à l'aide de tests de sensibilité des solutions de marée à la bathymétrie et à la paramétrisation du frottement de fond. Les facteurs de la variabilité de cette circulation aux échelles journalière, saisonnière à interannuelle ont été identifiés. La variabilité du transport d'Ekman due à l'inversion saisonnière des vents de mousson a été identifiée comme le principal moteur de la circulation saisonnière, cette dernière pouvant être inversée (intensifiée) en été (hiver) par le passage de typhons. ENSO, l'Oscillation Arctique ou encore une forte activité cyclonique ont été identifiés comme les facteurs de la variabilité interannuelle. Des tests préliminaires avec un module de transport sédimentaire couplé au modèle hydrodynamique ont révélé l'importance, pour la représentation réaliste du transport de matière en suspension, de la composition du sédiment de fond et du paramétrage des coefficients d'érosion.

Mots clés : circulation estuarienne à régionale, transport sédimentaire, variabilité, observations in-situ, modélisation océanique régionale, continuum estuaire-océan côtier, Fleuve Rouge, Golfe du Tonkin

General introduction

General context: understanding the transport and fate of water and matter in the delta-coastal regions continuum, a socio-economic and scientific key question.

Since the start of civilization, humans have settled along rivers, subsequent deltas formed by them and near coastal regions, as the sediments carried along and deposited by flowing rivers created areas rich in nutrients, ideal for agriculture and fishing. Nowadays, deltaic regions hold more than ever ecological and economic values throughout the world. At the transition between water and land, these regions are strategically positioned for trade with the world market, and are major centers of population with intensive agriculture and industry activities (Pont et al., 2002). While these low elevated coastal regions represent only 2% of the earth's land area (McGranahan et al., 2007), they are home for 10% of the total population (i.e., ~ 600 million people in 2000; ~ 650 million in 2050, CIESIN, 2009). In many nations, deltaic and coastal regions are the engines of the national economies with the highest contributions to national GDPs (Gross Domestic Production). For example, the Bengal Delta represents 1.1% of India's GDP, the Volta Delta, 4.4% of Ghana's GDP and the Ganges-Brahmaputra-Meghna Delta represents up to 28% of the Bangladesh's GDP (DECCMA project, 2019). In Vietnam, aquaculture and fisheries in both delta regions (Mekong Delta and Red River Delta) represent 5% of GDP and most of the rice that is worldwide exported (Vietnam is the world's 2nd rice exporter) is produced in these deltaic regions.

Coastal and delta regions are now considered as "hotspots" in the context of global changes, i.e., as places where high exposure to climate stress and anthropogenic pressure (industrialisation, urbanisation, resources overexploitation ...) coincides with high levels of vulnerability (IPCC, 2001). Combined to the deltaic subsidence enhanced by local groundwater withdrawal and hydrocarbon and sand extraction, and to the global sea level rise inducing flooding, coastal erosion and salinization, many deltas and surroundings have moved from a condition of active growth to a destructive

7

phase (Milliman et al., 1989; Poulos and Collins, 2002; Day et al., 1995). Giosan et al. (2014) further showed that sediment input to most major deltas is insufficient to maintain elevation with rising sea level. Coastal systems and low-lying areas will increasingly experience sea level rise and associated phenomena throughout the 21st century and beyond (IPCC, 2014). Economically, climate change has the potential to impact the deltas by reducing the GBP per capita by 8.5 to 14.5% , through impacts on infrastructures, agriculture and fisheries (DECCMA project, 2019).

Deltas and coastal oceanic regions are not only key interfaces between the land and the ocean, transferring huge quantities of water, organic and inorganic matter of natural and anthropogenic origins between those two compartments of our planet system. They also represent preferential concentration areas for land-derived material (as sediments, dissolved and particulate nutrients), which play a main role in the sequestration of chemical elements (carbon, nitrogen, pollutants) and in the sedimentary budget of the continental margins. The richness of those areas in terms of matter availability explains their high biodiversity. Indeed, coastal zones sustain sensitive ecosystems, provide critical habitat for many endangered species and are often classified as public heritage (Ramesh et al., 2015). Considering the East Asian Seas, the coastal regions are hosts for 35% of the world's mangrove, 33% of the world's seagrass bed and 33% of the world's coral reef (Daily Bulletin EAS Congress, 2018). Globally, coastal ocean represents 15% of the global oceanic primary production, 47% of the global annual export of particulate organic carbon, 90% of the sedimentary mineralization and 75-90% of the oceanic sink of suspended load (Jahnke, 2010; Simpsons and Sharples, 2012).

A better understanding of the functioning, variability and evolution of deltas and coastal regions in terms of water and matter transport and fate is therefore of high socio-economic and scientific importance.

To address these issues, the response of the scientific community is organized on the basis of the LOICZ (Land-Ocean Interaction in the Coastal Zone), which federates global scientific organizations around common objectives of addressing the issue of the actual responses of the coastal ocean to anthropogenic and climatic forcings (Ramesh et al., 2015). One of the fundamental approach of this project was to recognize the coastal zone as a global compartment rather than a geographical boundary of interaction between the land and sea. Indeed, the riverine and oceanic shelf processes were often considered separately, with hydrologists on one side and physical oceanographers on the other. However, understanding the complex connexions of deltaic and

coastal regions is not possible through sector-based approaches and requires strong interdisciplinary studies, which connect hydrology, oceanography, atmospheric and soil sciences, but also geology, chemistry, biology and ecology.

The study of delta and coastal regions is therefore not only a scientific challenge, but also a methodological challenge, requiring the connection and coupling of existing tools and methods from different scientific disciplines, and the development of new ones. For example, since estuarine and coastal processes are very fine processes at the scale of the global ocean, studies based on numerical tools imply to increase regional model resolution and to use grid meshes that can adapt to the fine river/coastal geography and bathymetry. In addition, forcing field data (continental, atmospheric and oceanic) as well as bathymetry data are key ingredients for those numerical studies and constitute a real stake for the scientific community as they require high temporal and spatial resolutions and are often difficult to access, for physical or political reasons. Furthermore, due to the different regions locations and to associated external forcings, the characteristics and processes largely vary from one region to another. Therefore, dedicated in-situ observations campaigns for each case study are needed and are a prerequisite for understanding and studying their specific processes and variabilities. Such observations are however often few and far between, and can constitute a real acquisition challenge for scientists.

Case study: the Red River Delta and Gulf of Tonkin system

The Red River Delta (RRD), located in the western coast of the Gulf of Tonkin (GoT) in the South China Sea (SCS), is an ideal case study for those questions since it gathers most of the issues described above. It has one of the highest demographic densities in the world (>1000 inhab km^{-2}), gathering highly populated rural areas and big urban centers in very low elevated areas (<10 m): Hanoi (7.6 M) and Haiphong (2.4 M) (from the Statistical Yearbook of Vietnam, 2017). The Red River is the principal source of freshwater (3500 m^3 s^{-1}) and sediments (40 Mt y^{-1}) to the GoT. In terms of delta plain surface, the RRD is the fourth largest delta in Southeast Asia after the Mekong, Irrawaddy and Chao Praya deltas. The RRD is fertile, with approximately 47% of its superficy used for agriculture or aquaculture, and it constitutes 56% of the country's rice production (General Statistics Office, 1996-2006). This region is also a key to the economy of Vietnam, with the capital city of Hanoi, with Ha Long Bay (a UNESCO world heritage site) for its particular touristic value and with the Hai Phong ports system which connects the north of Vietnam to the world market. This latter is the second biggest harbour of Vietnam with a particular fast-growing rate in terms

of volume of cargos passing through, of about $4.5x10^6$ to $36.3x10^6$ tons from 1995 to 2016, respectively (Statistical Yearbook of Vietnam, 2017).

The RRD and GoT system constitutes an estuarine, coastal and marine environment that is submitted to a large range of influences of several origins (atmospheric, oceanic, continental and anthropogenic) and scales (from daily to decadal and climate change). The atmospheric variability is associated to typhoons, drought and flooding, seasonal monsoon, interannual ENSO oscillation and long term climate change. The oceanic influence on the RRD and GoT system resembles storm surges, wave and tidal forcing and large scale circulation (Wyrtki, 1961). The RRD-GoT systems is furthermore submitted to continental fluxes of freshwater and associated matter from the Red River watershed and rivers. In addition, anthropogenic pressures impact the system, such as the pollution due to activities associated to a galloping economic, groundwater and surface water pumping, dams and sand dredging (Le et al., 2007). The Red River delta and surroundings regions are therefore threatened by many natural and anthropogenic hazards. For example, sea level has risen by 20 cm over the past 50 years, and a 1 m rise is planned for 2100, potentially resulting in the salinization of 30 to 50% of the RRD (Duc et al, 2012). The illegal release of 300 tons of toxic waste water from the Formosa plan killed marine life along almost 200 km of the GoT coast in April 2016 and more than 100 tons of dead fishes were washed up on the shores, resulting in a $ 5 M loss for local fishermen, a 30% decrease of tourists' visits, not to mention the unevaluated indirect economic and health impacts. This last event moreover revealed the strong lack of marine and coastal pollution monitoring (from *in-situ* measurements to operational modeling and satellite image exploitation), management and mitigation in this region.

In this context, it is fundamental to improve the understanding of the response of Red River - GoT continuum waters and sediment load, from the watershed to coastal and marine environments, to those different forcing factors, and to develop tools and expertise for the applied and operational management and monitoring of this environment. For example, since pollutants (such as dissolved metals and pathogens) can attach to the riverine suspended sediments, understanding sediment spread and fate in the coastal area would be a great asset in monitoring catastrophic events such as the Formosa one. This need has been formally identified by the Vietnamese government and clearly appears in the objectives of « The Strategy for Science and Technology Development for the 2011-2020 period » document published by the Ministry of Science and Technology.

Objectives

The general scientific objective of this Ph.D. is to contribute to improve the understanding of the estuary-coastal-open sea continuum in terms of transport and fate of water and sediments taking the case study of the Red River Delta - GoT system. First, the focus is made on understanding the hydrodynamics and identifying the drivers of its variability, from the Red River to the GoT. The second step consists in understanding how the hydrodynamics and associated variability combined to the sedimentary processes along the continuum influence the fate of suspended matter. For that, specific methodologies were developed, with field campaigns dedicated to the analysis of the seasonal and tidal variability of estuarine parameters (hydrodynamics and sediment fate), and with high-resolution models implemented for the first time over the region.

This manuscript is organized around 5 chapters. The first chapter presents the scientific and regional contexts of this thesis, reviewing the existing knowledge on hydro-sedimentary dynamics in macrotidal systems in general and on characteristics and specificities of the RRD-GoT system. Methodologies developed and results obtained during this Ph.D. are presented in the next three chapters (Chapter II, III and IV). Chapter II explores the variability of estuarine hydro-sedimentary dynamics, based on in-situ observations in the Red River estuary at tidal and seasonal scales. Chapter III focuses on the tidal representation over the Gulf of Tonkin in numerical models using a 2D unstructured grid numerical model. Chapter IV describes the circulation and fluxes variability of the GoT at daily, seasonal and interannual scales, based on 3D numerical simulations presented and evaluated in the same chapter.

Finally, Chapter V gives the conclusions and discusses preliminary results on sediment transport along the RRD, and proposes perspectives for future work.

References

- CIESIN (Center for International Earth System Science Information Network) (2009) Low-elevation coastal zone (LECZ) urban-rural estimates. Global Rural-Urban Mapping Project (GRUMP), Alpha Version, Pallisades, NY; Socioeconomic Data and Applications Center (SEDAC), Columbia Univsersity, http://sedac.ciesin.columbia.edu/data/collection/lecz
- Day J. W., Pont D., Hensel P. F., Ibanez C. (1995) Impacts of sea-level rise on deltas in the Gulf of Mexico and the Mediterranean: the importance of pulsing events to sustainability, Estuaries, 18: 636-647, https://doi.org/10.2307/1352382.
- Daily Bulletin East Asia Seas Congress (2018) Iloilo Convention Center, Philippines; 27-30 November 2018. Available at http://eascongress2018.pemsea.org/wp-content/uploads/2018/11/EASC2018-Daily-Bulletin-Day-2-2.pdf
- Deltas, vulnerability and Climate Change; Migration as an Adaptation (DECCMA): Climate change and the economic future of deltas in Africa and Asia: Policy brief, 2019.
- Duc Nguyen, Umeyama M., Shintani T. (2012) Importance of geometric characteristics for salinity distribution in convergent estuaries, J. Hydrol., 448-449, 1-13, doi: 10.1016/j.jhydrol.2011.10.044.
- General Statistics Office: Statistical Yearbook of Vietnam 2017, Statistical Publishing House: Hanoi, Vietnam, http://www.gso.gov.vn/default_en.aspxtabid=515&idmid=5&ItemID=18941 , 2017.
- Giosan L., Syvitski J. P. M., Constantinescu S., Day J. (2014) Protect the world's deltas, Nature, 516, 31-33, doi: 10.1038/516031a.
- IPCC (2001) Climate change 2001: impacts, adaptation and vulnerability. Tech. rep., Intergovernmental Panel on Climate Change.
- IPCC (2014) Climate change 2014: Synthesis report summary for policymakers, https://www.ipcc.ch/site/assets/uploads/2018/02/AR5_SYR_FINAL_SPM.pdf.
- Jahnke R. A. (2010) Global synthesis. Carbon and Nutrient Fluxes in Continental Margins: A Global Synthesis. Liu K. K., Atkinson L., Quinones R. A., Talaue-McManus L., Berlin Heidelberg, Springer-Verlag, 597-615. Le, T. P. Q.,Garnier J., Billen G., Théry S., Chau V. M. (2007) The changing flow regime and sediment load of the Red River, Viet Nam. J. Hydrol. 334: 199-214, doi:10.1016/j.jhydrol.2006.10.020
- McGranahan G., Balk D., Anderson B. (2007) The rising tide: assessing the risks of climate change and human settlements in low-elevation coastal zones. Environ. Urbanization 19(1), 17-37, doi: 10.1177/0956247807076960.
- Milliman J. D., Broadus J. M., Gable F. (1989) Environmental and economic implications of rising sea-level and subsiding deltas: the Nile and Bengal examples, Ambio, 18(6), 340-345.
- Pont D., Day J. W., Hensel P., Fanquet E., Torre F., Rioual P., Ibanez C., Coulet E. (2002) Response scenarios for the deltaic plain of the Rhone in the face of an accelerated rate of sea-level rise with special attention to Salicornia-type environments, Estuaries, 25, 337-358, https://doi.org/10.1007/BF02695978.
- Poulos S. E., Collins M. B. (2002) Fluviate sediment fluxes to the Mediterranean Sea: a quantitative approach and the influence of dams. In: Jones S. J., Frostick L. E. (ed.), Sediment Flux to Basins: Causes, Controls and Consequences. Special Publications, 191. Geological Society, London, pp. 227-245.
- Ramesh R., Chen Z., Cummins V., Day J., D'Ellia C., Dennison B., Forbes D. L., et al., (2015) Land-Ocean interactions in the Coastal Zone: Past, present & future, Anthropocene 12, 85-98, doi: 10.1016/j.ancene.2016.01.005/
- Simpson J. H., Sharples J. (2012) Introduction to the physical and biological oceanography of shelf seas. Cambridge University Press.
- Wyrtki K. (1961) Physical oceanography of the Southeast Asian waters. Naga Rep. 2, 195 pp.

[Available from: https://escholarship.org/uc/item/49n9x3t4].

Introduction générale

Contexte général : comprendre le transport et le devenir de l'eau et de la matière dans le continuum delta-océan côtier, une question socio-économiquement et scientifiquement clé.

Dès les débuts de la civilisation, attiré par la fertilité des terres et des eaux riches en nutriments apportés par les rivières, l'Homme s'est préférentiellement installé le long des cours d'eau, des deltas et des zones côtières. De nos jours, les régions deltaïques sont, et plus que jamais, particulièrement précieuses pour l'écologie et l'économie mondiale. Stratégiquement positionnées à la transition entre la terre et la mer, ces régions regroupent d'intenses activités agricoles, industrielles et commerciales avec le monde, et abritent de grands centres de population (Pont et al., 2002). En effet et bien que ces régions côtières de faibles altitudes ne représentent que 2% de la superficie terrestre (McGranahan et al., 2007), elles abritent jusqu'à 10% de la population totale (soit 600 millions de personnes en 2000 et jusqu'à 650 millions en 2050, CIESIN, 2009). Dans de nombreux pays, les régions deltaïques et côtières sont les moteurs des économies nationales et contribuent largement au PIB (Production Intérieure Brute). Par exemple, le delta du Bengale représente 1,1% du PIB de l'Inde, le delta de la Volta, 4,4% du PIB du Ghana et le delta du Gange-Brahmapoutre-Meghna représente jusqu'à 28% du PIB du Bangladesh (projet DECCMA, 2019). Au Vietnam, les activités aquacoles et piscicoles des régions deltaïques (delta du Mékong et delta du Fleuve Rouge) représentent au total 5% du PIB. De plus, la majeure partie du riz exporté dans le monde est produite dans ces régions deltaïques, le Vietnam étant le deuxième exportateur mondial de riz. Le Groupe d'experts intergouvernemental sur l'evolution du climat a classifié les régions côtières et deltaïques comme des "points chauds" dans le contexte du changement climatique global, c'est-à-dire comme zones où une forte exposition au stress climatique coïncide avec des niveaux élevés de vulnérabilité (rapport du GIEC, 2001). Au cours des dernières décennies, de nombreux deltas et régions côtières associées sont passés de conditions de croissance active à des conditions de décroissance, causées par l'affaissement deltaïque qui est lui-même accentué par

les actions combinées de prélèvements locaux d'eau souterraine et l'extraction d'hydrocarbures et par l'élévation du niveau de la mer à l'échelle mondiale qui induit inondations, érosions des zones côtières et salinisation des terres (Milliman et al., 1989 ; Poulos et Collins, 2002 ; Day et al., 1995). Giosan et al. (2014) ont en outre montré que l'apport de sédiments dans la plupart des plus gros deltas mondiaux est insuffisant pour maintenir l'élévation de ces deltas face à la montée du niveau de la mer, qui au cours du 21e siècle et au delà, devrait continuer d'augmenter (GIEC, 2014). Sur le plan économique, il a été estimé que les répercussions du changement climatique sur les infrastructures et sur les activités agricoles et piscicoles des zones deltaïques et côtières pourraient réduire le PIB par habitant de 8,5 à 14,5% (projet DECCMA, 2019).

Les deltas et les régions océaniques côtières sont des interfaces clés entre la terre et l'océan, qui transfèrent d'énormes quantités d'eau, de matière organique et inorganique d'origine naturelle et anthropiques entre ces deux compartiments. Elles représentent également des zones préférentielle pour l'accumulation de matériaux d'origine terrestre (sédiments, nutriments dissous et particulaires), qui jouent un rôle essentiel dans la séquestration des éléments chimiques (carbone, azote, polluants) et dans le bilan sédimentaire des marges continentales. La richesse de ces zones en termes de disponibilité de matière, liée à cette situation d'interface clé, explique la grande biodiversité et la richesse des écosystèmes qui y sont rencontrés. En effet, les zones côtières peuvent abriter des écosystèmes sensibles et fournir des habitats essentiels à de nombreuses espèces menacées, et sont souvent classées comme patrimoine public commun (Ramesh et al., 2015). Les régions côtières des mers d'Asie de l'Est abritent 35% des mangroves, 33% des herbiers marins et 33% des récifs coralliens mondiaux (Daily Bulletin EAS Congress, 2018). De plus, il a été estimé que l'océan côtier global représente 15% de la production primaire océanique mondiale, 47% de l'exportation annuelle mondiale de carbone organique particulaire, 90% de la minéralisation sédimentaire et représente 75 à 90% du puits océanique de matière en suspension (Jahnke, 2010 ; Simpsons and Sharples, 2012).

Une meilleure compréhension du fonctionnement, de la variabilité et de l'évolution des deltas et des régions côtières, en termes de devenir de l'eau et de la matière, est donc socio-économiquement et scientifiquement primordiale. Pour répondre à ces questions, la communauté scientifique s'est organisée autour du projet LOICZ (Land-Ocean Interaction in the Coastal Zone), qui fédère des organisations scientifiques mondiales autour d'objectifs communs pour comprendre les réponses de l'océan côtier face aux forçages anthropiques et climatiques (Ramesh et al, 2015). L'une des approches fondamentales de ce projet est de reconnaître la zone côtière comme un compartiment tel

quel plutôt que comme une frontière géographique entre la terre et la mer. Les processus fluviaux et océaniques sont en effet souvent considérés séparément avec les hydrologues d'un côté et les océanographes de l'autre. Il n'est cependant pas possible de comprendre les liens complexes entre les régions deltaïques et côtières avec des approches par secteur; il faut au contraire considérer des études interdisciplinaires qui relient l'hydrologie, l'océanographie, les sciences atmosphériques ainsi que la géologie, la chimie, la biologie et l'écologie. L'étude des deltas et des régions côtières n'est donc pas seulement un défi scientifique, mais aussi un défi méthodologique, qui exige la connexion et le couplage d'outils et méthodes issus de différentes disciplines scientifiques ainsi que le développement de nouveaux outils. Par exemple, les processus estuariens et côtiers sont des processus à très fines échelles comparés aux processus de l'océan global. Il est donc nécessaire d'adapter et d'augmenter la résolution des modèles numériques régionaux et d'utiliser des maillages de grille qui peuvent suivre les détails de la géographie et bathymétrie des rivières et des côtes, ce qui peut entraîner des coûts informatiques élevés. De plus, les champs forçants (continentaux, atmosphériques et océaniques) ainsi que les données bathymétriques constituent un véritable enjeu pour la communauté scientifique car ils nécessitent des résolutions temporelles et spatiales élevées et sont souvent difficiles d'accès, pour des raisons physiques et/ou politiques. De plus, en raison de l'emplacement des différentes régions et des forçages externes associés, les caractéristiques et les processus varient largement d'une région à l'autre. C'est pourquoi des campagnes d'observation in-situ dédiées à chaque site sont nécessaires et constituent une condition nécessaire et préalable à la compréhension et à l'étude de la variabilité des processus. Cependant, ces observations sont souvent peu nombreuses et éloignées les unes des autres et peuvent constituer un véritable défi d'acquisition pour les scientifiques.

Étude de cas : le système Delta du Fleuve Rouge Golfe du Tonkin

Le Delta du Fleuve Rouge (DFR), situé sur la côte ouest du Golfe du Tonkin (GdT) en Mer de Chine Méridionale (MCM), est un cas idéal pour étudier ces questions puisqu'il recense la plupart des problèmes décrits ci-dessus. Cette région possède l'une des densités démographiques les plus élevées du monde (>1000 hab km²), regroupant des zones rurales très peuplées et de grands centres urbains dans des zones de très faibles altitudes (<10 m) : Hanoï (7,6 M) et Haiphong (2,4 M) (Statistical Yearbook of Vietnam, 2017). Le Fleuve Rouge constitue la principale source d'apports d'eau douce ($3\,500$ m^3 s^{-1}) et de sédiments (40 Mt y^{-1}) pour le GdT. En termes de surface, le delta est le quatrième plus grand delta d'Asie du Sud-Est après les deltas du Mékong, de l'Irrawaddy et du Chao Praya. Il est également très fertile, avec environ 47% de sa superficie utilisée pour

l'agriculture et l'aquaculture, et il représente 56% de la production rizicole du pays (General Statistics Office, 1996-2006). Cette région est également clé pour l'économie vietnamienne, grâce à sa capitale Hanoï, à la baie d'Ha Long (patrimoine mondial de l'UNESCO) qui attire de nombreux touristes et grâce au port d'Hai Phong qui permet de relier le nord du Vietnam au commerce mondial. Ce dernier est le deuxième plus grand port du Vietnam avec un taux croissant de volume de cargaisons transitant par le port, particulièrement rapide, avec une augmentation de $4,5\times10^6$ à $36,3\times10^6$ tonnes de 1995 à 2016, respectivement (Statistical Yearbook of Vietnam, 2017).

Le système DFR et GdT est donc composé de milieux estuariens, côtiers et océaniques soumis à un large éventail d'influences qui ont plusieurs origines (atmosphérique, océanique, continentale et anthropique) et plusieurs échelles (du journalier au décennal et au changement climatique). Les typhons, les sécheresses, les inondations, les moussons, l'oscillation ENSO et le changement climatique à long terme composent la variabilité atmosphérique.

L'influence océanique sur le système DFR et GdT correspond aux forçages par la marée, par la circulation grande échelle et celle impactée par les tempêtes (Wyrtki, 1961). Le système DFR-GdT est également soumis aux flux continentaux d'eau douce et de matières associées (sédiments, nutriments, matières organiques, polluants) qui proviennent du bassin versant et des rivières, et à l'influence météorologique naturelle. Les activités anthropiques impactent aussi le système, comme par exemple la pollution due aux économies croissantes, le pompage des eaux souterraines et de surface, les barrages qui perturbent les cours d'eau et les dragages de sable (Le et al., 2007). Le DFR et ses régions environnantes sont donc menacés par de nombreuses pressions naturelles et anthropiques. Par exemple, le niveau de la mer a augmenté de 20 cm au cours des 50 dernières années et une élévation de 1 m est prévue pour 2100, ce qui pourrait entraîner la salinisation de 30 à 50% du DFR (Duc et al, 2012). De plus, le déversement illégal de 300 tonnes d'eaux usées toxiques de l'usine Formosa en Avril 2016 a anéanti la vie marine le long de 200 km de la côte du Golfe, et plus de 100 tonnes de poissons morts ont été rejetés sur les côtes, entraînant une perte de 5 M\$ pour les pêcheurs locaux, une diminution de 30% des visites touristiques, sans parler des impacts économiques et sanitaires indirects qui n'ont pas été évalués. Ce dernier événement a d'ailleurs révélé un manque de surveillance de la zone marine et côtière (absence de mesures in situ, de modélisation opérationnelle et d'exploitation d'images satellites) ainsi qu'un manque de gestion de la catastrophe.

Dans ce contexte, il est fondamental d'améliorer les connaissances du système et de comprendre

les réponses du continuum Fleuve-Rouge - GdT à ces différents forçages, en termes d'eau et de charge sédimentaire, depuis le bassin versant vers les milieux côtiers et océaniques, et de développer des outils et expertises pour la gestion appliquée et opérationnelle, et pour la surveillance de ce milieu. Comme les polluants (tels que les métaux dissous et les agents pathogènes) peuvent, par exemple, se fixer aux sédiments en suspension présents dans les rivières, il est très utile de comprendre la dispersion et le devenir de ces sédiments dans la zone côtière afin de surveiller des catastrophes telles que celle de l'usine Formosa. Ce besoin a été formellement identifié par le gouvernement vietnamien et apparaît clairement dans les objectifs du document " Stratégie de développement scientifique et technologique pour la période 2011-2020 " publié par le Ministère de la Science et de la Technologie.

Les objectifs de la thèse

L'objectif scientifique général de cette thèse est de contribuer à améliorer la compréhension du continuum estuaire-côte-océan en termes de transport et de devenir de l'eau et des sédiments apportés par les fleuves des régions deltaïques, en prenant le cas du système DFR-GdT. Premièrement, l'accent est mis sur la compréhension de l'hydrodynamique et sur l'identification des facteurs de sa variabilité, depuis le Fleuve Rouge vers le GdT. La deuxième étape consiste à comprendre comment l'hydrodynamique et la variabilité associée, combinées aux processus sédimentaires le long du continuum, peuvent influencer le devenir de la matière en suspension. Ces étapes sont réalisées à l'aide de méthodologies spécialement développées pour cette étude, de campagnes de terrain dédiées à l'analyse de la variabilité saisonnière et marémotrice sur des paramètres estuariens (hydrodynamique et devenir des sédiments), et de modèles haute-résolution implémentés pour la première fois dans la région qui sont combinés à des forçages précis.

Ce manuscrit s'articule autour de cinq chapitres. Le premier chapitre présente les contextes scientifiques et régionaux de cette thèse, passant en revue les connaissances existantes sur la dynamique hydro-sédimentaire dans d'autres systèmes macrotidaux et sur les caractéristiques et spécificités du système DFR-GdT. Les méthodologies développées et les résultats obtenus au cours de cette thèse sont présentés dans les trois chapitres suivants (chapitres II, III et IV). Le Chapitre II explore la variabilité de la dynamique hydro-sédimentaire estuarienne, à partir d'observations *in-situ* dans l'estuaire du Fleuve Rouge aux échelles de la marée et des saisons. Le chapitre III porte sur la représentation des principales composantes de la marée du GdT dans des modèles numériques, en utilisant un ensemble de données bathymétriques à haute résolution et une paramétri-

sation ajustée du frottement du fond. Le chapitre IV décrit la variabilité de la circulation et des flux dans le GdT aux échelles journalières, saisonnières et interannuelles, sur la base de simulations numériques 3D présentées et évaluées dans ce même chapitre.

Enfin, le chapitre V présente les conclusions de cette thèse et discute de résultats préliminaires sur le transport sédimentaire le long du delta, et propose des perspectives de travaux futurs.

Chapter I

Introduction

Contents

I.1 Complexity of hydro-sedimentary processes along the estuary - coastal ocean - open ocean continuum

The nature and the intensities of the dynamics that dominates the hydro-sedimentary processes are dependent on such factors as water and sediment discharges from river systems and physical oceanographic regimes of the shelves onto which the sediment is transported (Wright and Nittrouer, 1994). This sections aims at summarizing the roles of continental and oceanic dynamics on hydro-sedimentary processes and transport of suspended sediments.

I.1.1 Continental processes

Worldwide, rivers bring on average $1.3 \ 10^6$ m^3 s^{-1} of freshwater to the sea and constitute the principal input of suspended matter to the sea, of 630 t s^{-1} (i.e. $20 \ 10^9$ t y^{-1}) (Inman and Jenkins, 2003). Asia and Oceania contribute to up to 70% of this global suspended matter supply (Milliman and Syvitski, 1992; Farnsworth and Milliman, 2003). Rivers flows (water and sediments) are mostly influenced by two forcings: the gravitational circulation from high slopes to plains, and the precipitation runoffs. However, recent anthropogenic activities on large rivers have severely altered sediment discharges, especially as a consequence of artificial dam impoundments (Syvitski et al., 2005). Approximately 53% of the global sediment flux is considered trapped in reservoirs (Vörösmarty et al., 2003). For example, the sediment load from Missouri-Mississippi River decreased from 400 to $145 \ 10^6$ t y^{-1} over a 20-year period (Meade and Moody, 2010) and the Yellow River from 1200 to $150 \ 10^6$ t y^{-1} over a 40-year period (Wang et al., 2007; Wang et al., 2008). While suspended loads of large rivers have been described in past decades, a need exists in monitoring both small and medium rivers (i. e. mean annual river discharges <10000 m^3 s^{-1}), as they represent approximately half of the annual suspended sediment load to the sea (Milliman and Meade, 1983; Milliman and Syvitski, 1992).

In terms of transport capacity, typical rivers can transport sediments from mud (1-63 µm) and sand (63 µm to 2 mm) to gravels (2-64 mm), but larger floods can carry cobbles (64-256 mm) and boulders (>256 mm). The biggest material (large boulders and rocks) are "rolling" by traction along the river bed, while smaller pebbles and stones are "bounced" along the river bed by saltation (Fig. I.1 a). Smaller mineral particles of clay (1-4 µm), silt (4-63 µm) and sand are held within the water and transported along in the flow of water, this constitutes the suspended load. Clays are the smallest solid constituents of mud and they are responsible for cohesion properties (cohesive

sediments), whereas silt and sand have no effect on cohesion (non-cohesive sediments) (Maggi, 2005). The suspended solid load is also composed of organic material such as phyto/zooplankton and bacteria. All of this solid suspended load is known as the suspended particulate matter (SPM). Lastly, particles of rock can be dissolved in the water and carried along without being seen, it is the dissolved suspended load (Fig. I.1).
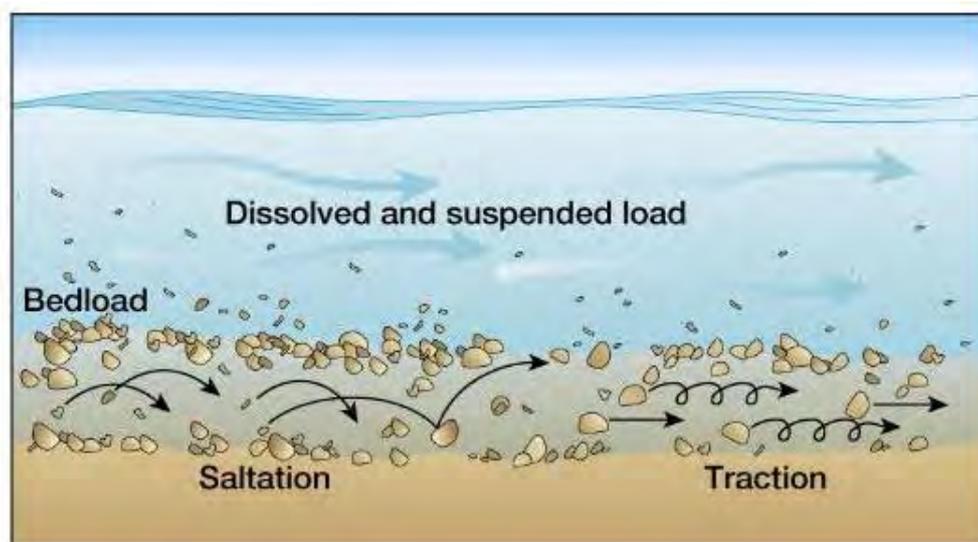
Figure I.1: Schematic representation of sediment transport within a river.

Due to river flows, the SPM load reaches the coastal zones and meet marine waters; the following sections describe the SPM load dynamics when it encounters marine waters.

I.1.2 Coastal processes

I.1.2.1 SPM fate on ocean margins

Riverine SPM is the main sediment load delivered to the shelf. In water (riverine and marine), the turbidity is a proxy of the concentration of SPM, and defines the clarity index of seawater. It quantifies the quantity of light scattered or attenuated by suspended matter when light passes through a water sample. Suspended solids, dissolved colored material, and also biological organisms (plankton) reduce water clarity by creating an opaque, hazy or muddy appearance. Pollutants, such as a dissolved metals and pathogens can attach to SPM and enter the water (this is why an increase in turbidity can often indicate potential water pollution). Figure I.2 presents a classification of the different particles in seawater (Stramski et al., 2004).

The SPM spreads onto the shelf as a plume and thus, the fate of this plume controls the distribution of the sediments and turbidity in the coastal zone. The plume dispersal and subsequent sediment
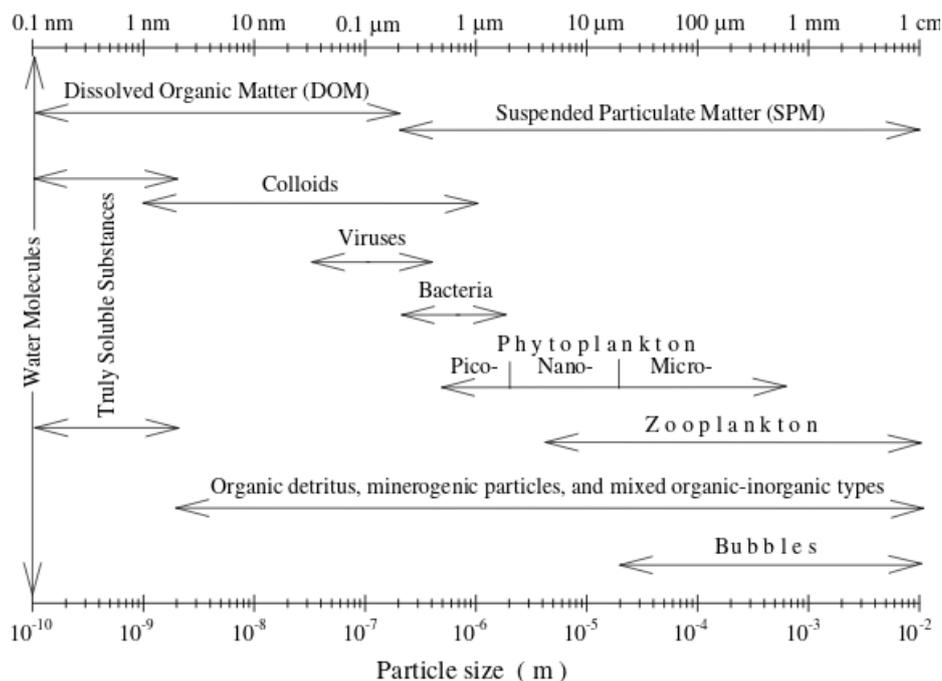
Figure I.2: Schematic diagram of the size spectra of the different components of seawater, with arrow delimiting the size classes of each constituent, from Stramski et al. (2004).

deposition over continental margins are controlled by wave, tide and current actions, as well as by the inertia and buoyancy of the plume, and its frictional interaction with the seafloor (Goodbred, 2001; Nittrouer and Wright,1994).

Firstly and without any meteorological forcing, Coriolis force controls the plume's dynamics by deflecting its orientation to the right (left) in the northern (southern) hemisphere. This deviation induces an along-coast flow. In case of wind forcing, an Ekman transport is generated, which in return, can affect river plume directions (Chao, 1988) (Fig. I.3). Besides impacting the plume direction, wind also impacts sediment dynamics within the plume by generating waves, which tend to keep the sediments close to shore (Fig. I.3). Wave dominated plumes are mostly found in high-latitudes in regions of high wind stress (southern Australia, southern Africa, north and south Pacific). In contrast, tides force a general onshore-offshore movement of sediments mostly along the coast, where the tidal energy is the strongest (Fig. I.3). Tide-dominated plumes are found in shallow basins with wide shelves such as the Yellow Sea or North Sea.

Then, the fate of the SPM transported by the plume depends upon a balance of several processes such as transport, particulate deposition and resuspension (Fig. I.3).

Transport in suspension is primarily related to the turbulence in the water column induced by the waves and currents (tides and wind-driven) (Eisma, 1993). In wave-dominated environments,
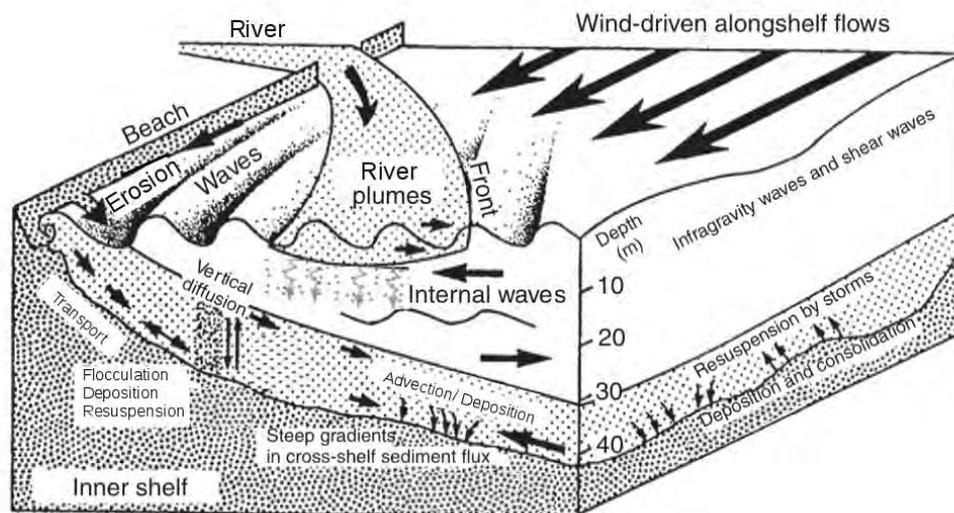
Figure I.3: Conceptual diagram illustrating the major process responsible for sediment transport, from Nittrouer and Wright (1994).

the transport of sand occurs along-shore, where it can feed local beaches, and is generally limited to depths <10 m, where wave action is still strong enough to induce sand motion. On the contrary, the finer suspended load is commonly transported towards the mid-shelf (depths >10 m), by several processes such as wave-generated diffusion (Swift, 1970), advection from bottom currents (McCave, 1982) and transport within density-driven flow (Moore, 1969). Beyond the coastal zone, different mechanisms are responsible for advecting sediments across the outer shelf (Goodbred, 2001). First, storms can be a major agent for cross-shelf transport. Even though they are episodic, storms generate steep and long-period waves that can resuspend sediments at great depths. Second, the suspended sediments can be transported by a near-bottom return flow or by internal waves, which can maintain a layer of high turbidity near the sea-bed (Cacchione and Drake, 1986). Finally, sediments can also be exported off-shelf by gravity-driven flows, downwelling or advection along slumps and slides (Nittrouer and Wright, 1994).

Deposition (or settling) of SPM occurs when the forces responsible for suspended transportation (i.e., turbulence) are too weak to overcome the forces of gravity and friction (Ueberman and O'Neill, 1988; Stephenson, 2013). Deposition causes decrease in SPM concentration in the water and can be enhanced by fine sediment flocculation (see section I.1.3.2) processes which increases the particle size.

Once deposited, particles can be redistributed over the entire shelf by different mechanisms such as erosion (i.e. resuspension by wave-induced turbulence) and transport (by tides and currents). If

the difference between deposition and erosion is positive, there is an accumulation of sediments, otherwise there is a depletion (Nittrouer and Wright, 1994).

I.1.3   Transition zone between continental and marine waters: estuarine processes

The river estuary is the area of interactions between continental fresh and marine salty water masses. Hydro-sedimentary processes are therefore influenced by the combined actions of river discharges and tides, which induce formations of salty structures and sediments processes varying at different time-scales (high-low tide cycle, neap-spring tide cycle, seasonal cycle).

I.1.3.1   Cycle of fine sediments within the estuary

According to Nichols and Biggs (1985), the hydro-sedimentary processes within the estuary are controlled by four processes: erosion, transport, deposition and consolidation. Fig. I.4 summarizes the different phases of the SPM cycle within the estuary, regarding the cohesive sediments. This suspended matter varies during its cycle, from a non-flocculated to a flocculated state. Indeed, cohesive sediments are subjected to aggregation and breakup processes. First of all, the turbulent mixing of the fluid (by currents) causes the suspended particles to come in contact, favoring the coagulation and aggregation of these particles into large aggregates (i.e., flocs). In the meantime, the fluid force can disrupt these aggregates, which cannot withstand the shear stress, and cause breakage. Therefore, the rate at which the suspended particles aggregate and break up highly depends on the turbulence intensity. Then, flocs can fall by settling (when gravity force overcomes turbulence) and can accumulate on the estuary bed. When turbulence picks up, aggregates forming part of the bed are eroded and lifted up, and take part in the flocculation reactions again.

In the end, the SPM assemblage is composed of unique particles (or primary particles, <10 µm), microflocs (10 -125 µm) and macroflocs (>125 µm) (Eisma, 1993) (Fig. I.5). Microflocs are usually dense and resistant to turbulence, whereas macroflocs present lower density and can be easily fragmented into microflocs by shear forces. Both types of flocs are in lower abundance than the primary particles, but can largely contribute to the total volume concentration (Dyer and Manning, 1999; Manning et al., 2004).
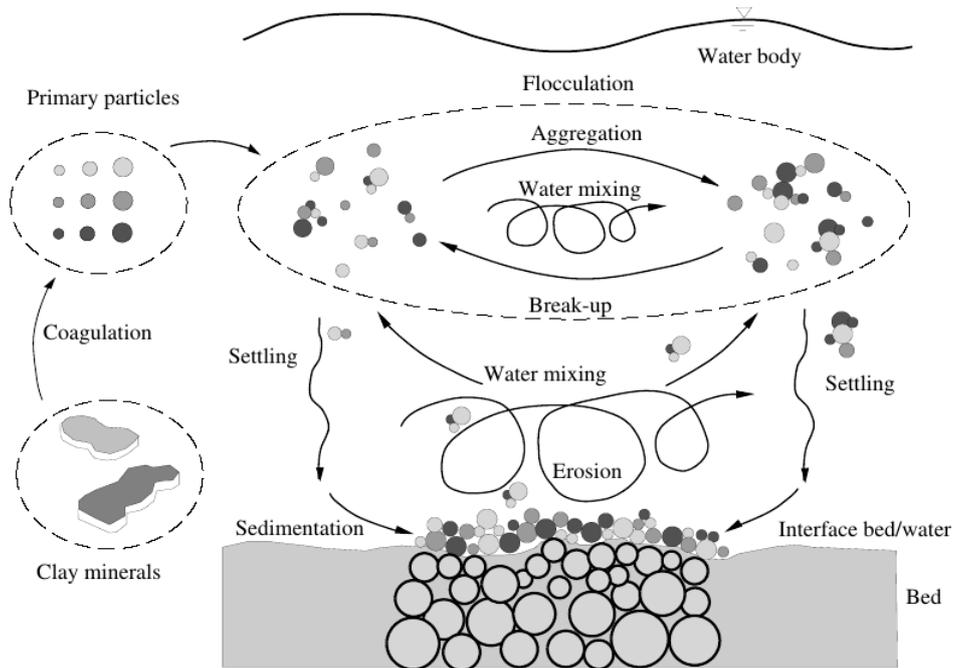
Figure I.4: Conceptual representation of the cohesive fine-sediments cycle within the estuary, from Maggy (2005).
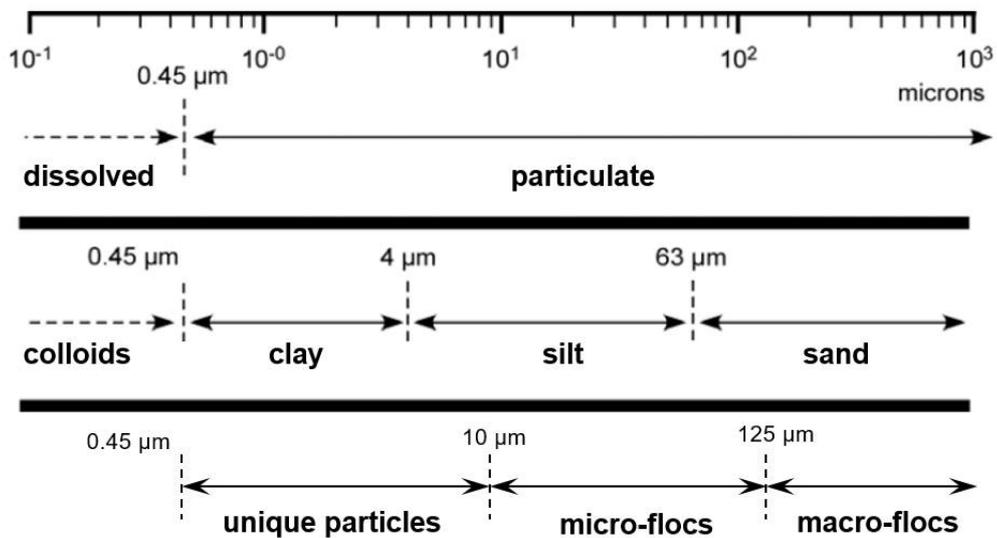
Figure I.5: Representation of the SPM granulometric classification (from Many, 2016).

I.1.3.2 Fine sediment aggregation

Previous section highlighted the importance of aggregation processes in the cycle of fine suspended sediments such as clays. The aggregation capability is an intrinsic characteristic of cohesive sediments, although the medium also plays an important role. Indeed, in the aggregation process, while particle concentration, size and fluid dynamics control collision rate, adhesion depends upon the physico-chemical properties of the particles, such as the van der Waals forces (Jackson, 1990). It is also assumed that the presence of transparent exopolymeric particles (TEP),

which are formed by phytoplankton and other microorganisms, can enhance aggregation in estuaries (Wolanski and Spagnol, 2003; Bhaskar et al., 2005). Furthermore, the formation of aggregates is not constant in space and time. Fine-sediment particles in the initial assemblage can be destabilized by both an increase of the particle concentration and the setup of strong salinity or biological gradients, which favor the formation of microflocs in few seconds (Montgomery 2005; Jarvi 2005; Mari et al. 2012) (Fig. I.6). Then, depending on the SPM concentration and transport, macroflocs can be formed and this can take up to hours. Therefore, the final SPM assemblage is composed of unique particles, micro flocs and macroflocs.
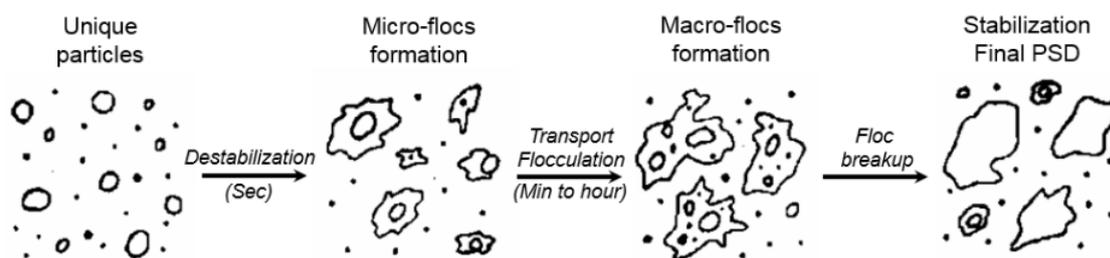
Figure I.6: Conceptual representation of the formation of micro and macro flocs within an SPM assemblage (from Montgomery, 1985; Many, 2016).

I.1.3.3   Estuarine turbidity maximum

One result of the interaction of freshwater and marine water is the appearance of a region of high sediment concentrations compared to the lower and upper estuarine parts (Dyer and Manning, 1999; Uncles et al., 2006). These highly turbid regions are called Estuarine Turbidity Maxima (ETMs). The SPM trapped in ETM encompasses a huge range of concentrations with maximum values from less than 100 mg l^{-1} in the Kennebec Estuary, USA (Kistner and Pettigrew, 2001), to >200 mg l^{-1} as in the Severn Estuary, UK (Kirby and Parker, 1983). ETM show intense particle deposition rates, such as in the Hudson estuary, with rates as high as 30 cm y^{-1} (Olsen et al., 1978).

In macrotidal estuaries, the ETM formations and dynamics depends on two mechanisms. First, sediment accumulation is favored at convergence at the saltfront by the seaward sediment flux from the river flow and by the landward sediment flux from gravitational circulation. The point of convergence of the residual flow is called the nodal point (Fig. I.7).

Second, in shallow estuaries, an asymmetry between ebb and flood tides is observed. Since the celerity of the tidal wave increases with increasing water depth, the tide propagates faster at high water than at low water. This tidal asymmetry favors a landward sediment transport at flood, which generates a sediment accumulation at the tidal nodal point (Allen et al., 1980).
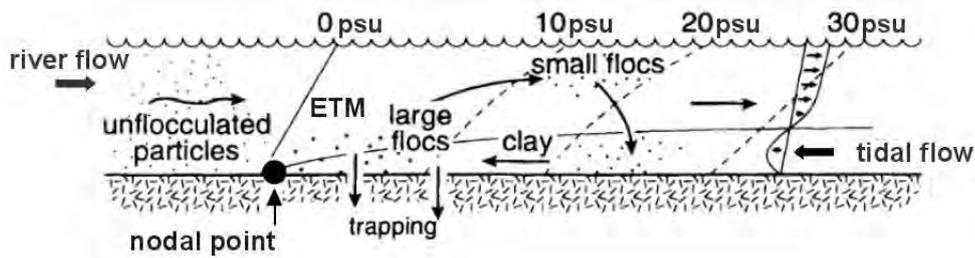
Figure I.7: Sketch of the ETM formation by gravitation circulation, adapted from Wolanski and Gibbs (1995).

These two mechanisms, by promoting upstream transport of SPM, induce sediment trapping down-stream of the point where the river regime is dominant (Fig. I.8). This trapping point moves up-stream when the river flow decreases, and vice versa when the river flow increases. In macrotidal estuaries, this type of transport dominates over density currents.
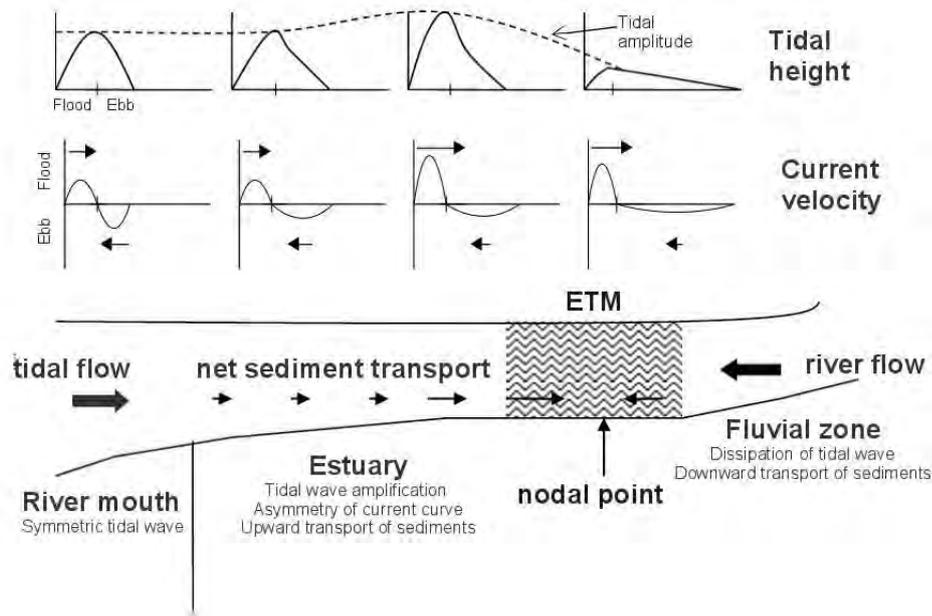
Figure I.8: General scheme of net tidal transport and trapping of suspended sediments in a macrotidal estuary with low density currents (from Allen et al., 1980).

Furthermore, tidal resuspension in ETM has been recognized as a key factor in maintaining high SPM concentration (Brenon and Le Hir, 1999; Schubel, 1968; Sottolichio et al., 2000).

Since ETMs are key zones in sediment accumulation within estuaries, identifying the mechanisms behind their formation is of interest for river management as they can influence water quality and estuarine siltation.

I.1.3.4   Influence of anthropogenic activities

Human activities along the coast (including land reclamation, port development, wind-farms impoundment), within river catchments and watersheds (dam impoundments, river diversion, irrigation) and offshore (dredging, sand mining, oil and gas extraction) in combination with the above mentioned natural forces often exacerbate coastal erosion. Furthermore, since the ongoing climate change may impact the frequency and intensity of extreme events such as typhoons, climate change could also influence the erosion rate and sediment transport through the wave and current actions.

Increases of erosion rates are particularly observed in Asia. The Jiangsu Province in China suffers from erosion rates as high as 85 m y^{-1} (Bilan, 1993). The author attributes these rates to river damming and diversion that lead to decrease in sediment supply to the coast, and to the clearing of mangrove forests which makes coastal areas more susceptible to hazards. Also due to mangrove clearing, 30% of the Malaysian coastlines are estimated to be undergoing fast erosion (Othman 1994). Thampanya et al. (2006) measured a net erosion rate of 1.3 to 1.7 m y^{-1} along the southern coast of Thailand and attributed it to combines effects of dam impoundments, clearing mangrove forests and coastal land subsidence. Since the early 20th century, southern Vietnam has been eroded at a rate of ~ 50 m y^{-1}, mostly due to waves and currents actions on a vanishing mangrove vegetation (Mazda et al., 1997; Cat et al., 2006).

The hydro-sedimentary processes detailed above (SPM transport, erosion, deposition, flocculation, ETM) are key factors triggering the sediment dynamics in the Red River Delta and Gulf of Tonkin system, from estuarine and coastal to regional scales. The following section presents the characteristics and current knowledge regarding hydro-sedimentary dynamics of our study area.

I.2 Regional settings and scientific questions in our study area : the Red River Delta to Gulf of Tonkin system

This section highlights the regional settings of the study area, which extends from the Red River Delta (RRD) to the Gulf of Tonkin, called more globally GoT afterwards. First, a general overview of the characteristics of the GoT is presented. Then, the focus is made on the shelf hydrodynamics, and lastly the hydrodynamics and SPM dynamics in the estuarine and coastal areas are presented. The scientific questions raised by the presentation of the study area and to which this thesis will respond are presented in boxes.

I.2.1 General description of the Gulf of Tonkin

I.2.1.1 Geography

The GoT covers an area of 115000 km² from about 16° 10'-21° 30'N and 105° 30'-111° E (Fig. I.9). This crescent-shape semi-enclosed basin, also referred as Vinh Bac Bo in Vietnamese or as Beibu Gulf in Chinese, is 270 km wide and 500 km long and lies in between China to the North and East, and Vietnam to the West. It is characterized by shallow waters as deep as 90 m and is open to the South China Sea (SCS, or Vietnamese East Sea) through the South of the Gulf and to the East through the narrow Hainan Strait. This latter, also known as Quiongzhou Strait, is on average 30 km wide and 50 m deep and separates the Hainan Island from the Zhanjiang Peninsula (mainland China). The bottom topography in the GoT and around Hainan Island is rather complex, constantly changing, especially along the coastlines, and partly unknown. Furthermore, the Ha Long Bay area counts about 2000 islets, also known as notched, sometimes no bigger than a few hundred square meters. Lastly, the Red River Delta (RRD) coastlines is composed of low-lying plains and tidal flats (Tong Si Son, 2016).

I.2.1.2 RRD geology

Both Red River and RRD are located in a tectonically active region, and the middle and lower parts of the river flows along the NW-SE elongated fault-bound structure of the Cenozoic Song Hong Basin (Wetzel et al., 2017). Geological, geomorphological and archaeological studies suggest that the evolution of the delta itself was closely related to the GoT sea-level changes during the Holocene (12000 years BP to present) (Hoekstra and Weering, 2007). In early Holocene and in response to the inundations attributed to this period, the delta propagated into the drowned val-
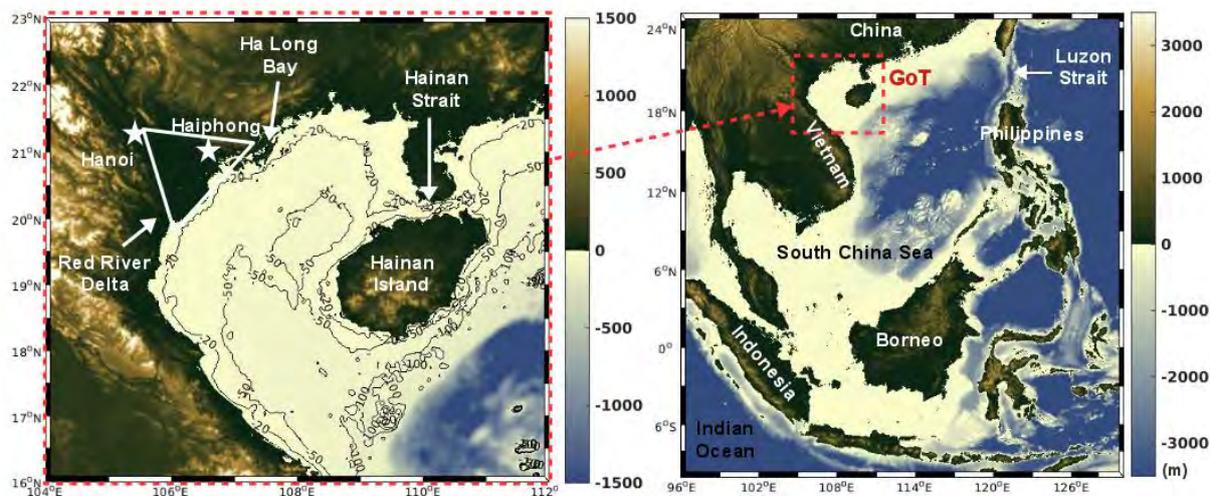
Figure I.9: Geography of the Gulf of Tonkin and interesting features.

ley. In mid-Holocene, the sea-level rising (2 to 3 m above the present sea level), allowed widespread mangrove development on the delta plain, as well as the formation of the famous marine notches in Ha Long Bay and Ninh Binh areas (Hori et al., 2004). In recent Holocene (4000yrs BP), the former delta plain emerged as the results of sea-level lowering, and the delta changed into the present wave and tide-influenced delta (Tanabe et al., 2003). The northern part of the RRD, which is tide-dominated, developed from 2000 to 1000 years BP. About 1000 BP, depositional processes shifted southwards, leading to the construction of the southern delta which appears to be dominated by fluvial and wave-induced morphological features. The actual shape of the RRD is therefore the product of thousands of years of fluvial sediment inputs but also, the product of reworking waves and currents, whose relative importance varies in time and space (van Maren et al., 2007).

At steady state, deltas are naturally slowly sinking due to sediment deposition. Natural subsidence rates in deltas generally range from 1 to 10 mm y^{-1} (Jelgersma, 1996; Stanley and Warne, 1998), even though accurate measurements remain rare. In combination with global rising sea-level, the subsidence phenomena may be enhanced by anthropic activities such as oil and gas extraction, sand mining, urban constructions, groundwater removal, decreasing sediment load by sediment trapping in reservoirs upstream or diversion of freshwater for households and land-uses (Syvtski et al., 2009). Accelerated subsidence has been documented in many deltas and can locally reach up to 300 mm y^{-1} (Haq, 1997). Ericson et al. (2005) classified 40 deltas throughout the world based on an assessment of the effective sea-level rise (ESLR) defined by the combination of eustatic sea-

level rise, the natural rate of fluvial deposition and subsidence, and the accelerated subsidence
due to groundwater and hydrocarbon withdrawal. The RRD appeared to be only subjected to
eustatic sea-level rise, whereas neighboring deltas were subjected to sediment trapping (e.g. due
to reservoirs) or accelerated subsidence (e.g. by groundwater use). These results should be taken
into consideration with a careful attention since the methodology described in this study relies on
a number of assumptions, including a uniform eustatic sea-level rise. However, is it known that
the SCS sea-level rising rate is 3 times faster than the global mean rate (Dieng et al., 2015; Piton
and Delcroix, 2018).

I.2.1.3 Climate

The GoT climate, as well as the South China Sea (SCS) region climate, is mainly governed by two
alternative monsoon cycles, characteristics of subtropical climates. A southwest (SW) monsoon
during boreal summer and a northeast (NE) monsoon during boreal winter (Wyrtki 1961; Wang
and LinHo, 2002). A detailed view of this reversal of wind direction from winter to summer in the
GoT is shown in Fig. I.10 a.
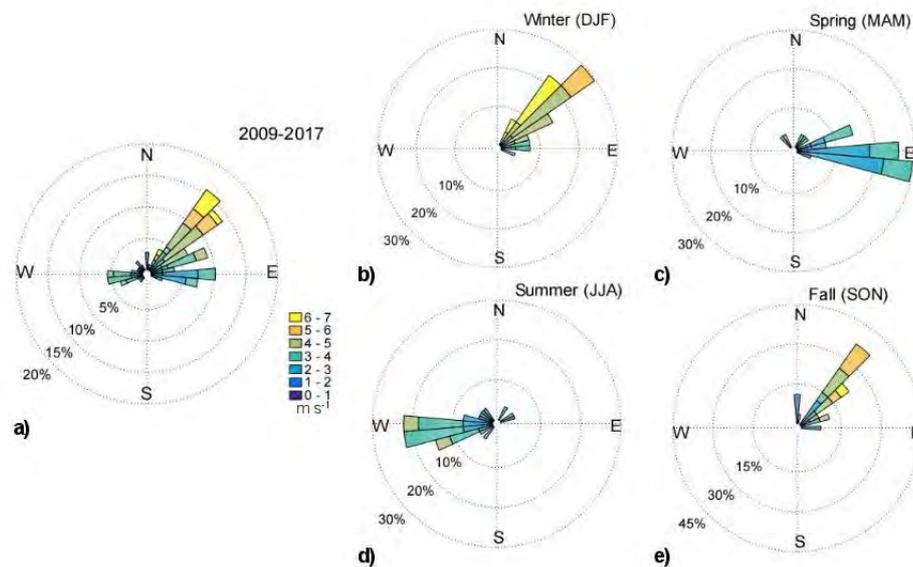
Figure I.10: Annual (a) and seasonal (b, c, d, e) wind distribution over the GoT from ECMWF over the period
2005-2017.

The winter monsoon lasts from fall to winter with almost homogeneous NE wind direction over
the GoT (Fig. I.10 b, e), with mean speed peaks in winter of ~ 7 m s^{-1}. In spring, the winds relax
with mean maximum values ~ 4 m s^{-1} and change direction into becoming easterlies (Fig. I.10
c). The summer monsoon starts from June and lasts through September, and implies W-SW wind
direction with peaks of ~ 5 m s^{-1} (Fig. I.10 d).

The winter monsoon originates from the Siberian High (Wang and He, 2012) and thus brings cold and dry conditions; whereas the summer monsoon originates from the Southern Pacific and Indian Ocean (Lau and Yang, 1997), and thus bring warm and wet conditions over the GoT. Consequently, the GoT shows a strong seasonal rainfall variability: driest from January to April, with net water flux of ~ 3 mm d^{-1}, and wettest in Summer and Fall (~ 6 mm d^{-1}) (Fig. I.11).
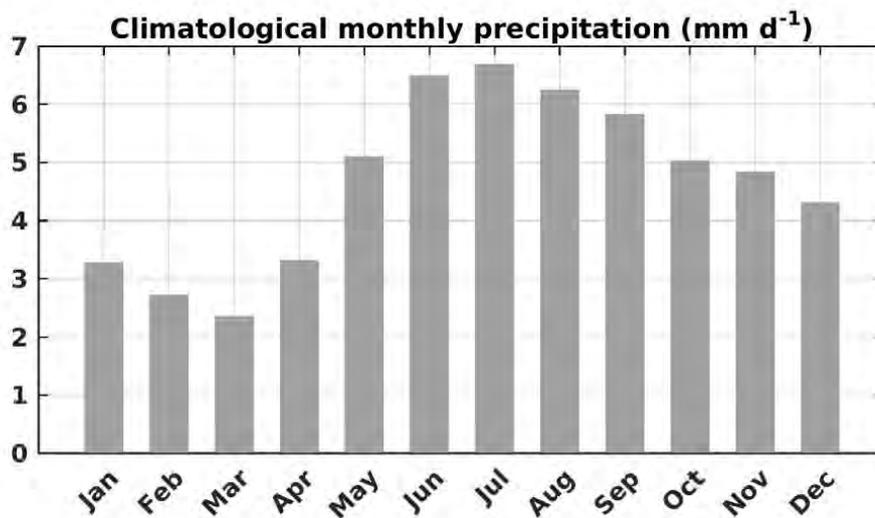
Figure I.11: Climatological monthly precipitation (in mm d^{-1}) over the GoT for the period 2005-2017 from ECMWF.

At shorter time-scales, the GoT atmospheric circulation is under the influence of typhoons (or tropical cyclones), which hit northern Vietnam about 4-5 times every year and predominantly from June to November, when the ITCZ (Intertropical Convection Zone) is positioned in the SCS. The frequency of typhoons affecting the coast of Vietnam has increased during the second half of the 20th century (Thanh et al., 1997). Typhoons are usually generated over the western Pacific and are known to cause great destruction and death as they move over lands. The deadliest one occurred in 1881, killing 300000 persons while swiping away Haiphong harbor. Besides the severe impacts in terms of human loss, typhoons brings along high water levels, large waves, strong winds and heavy rain that can lead to flooding, dikes and sand dunes erosion, as well as saltwater intrusion in land crops (Vinh et al., 1996; Quynh et al., 1998). Furthermore, typhoons are associated with strong impulse of momentum, heat and water exchanges between the ocean and the atmosphere and thus can induce strong intraseasonal variations in the wind-driven circulation and in the thermohaline structure of the SCS upper layer (Chu and Li, 2000; Lin et al., 2003; Tseng et al., 2010). In the SCS, Typhoon Ernie (1996) triggered significant SST cooling and sea surface depression in the wake of the storm (Chu et al., 2000). Typhoon Pabuk (2007) largely intensified the

near-bottom current along its route (from the Luzon Strait to the Hainan Strait) (Liu et al., 2011). Wang et al. (2014) also observed a strong deep SCS circulation induced by typhoon activities, which suggests that effects of typhoons can penetrate into the deep ocean.

Lastly, at interannual time scales, the SCS region is dominantly influenced by the El Niño Southern Oscillation (ENSO) phenomena. Several studies have been conducted on interannual (ENSO) variability of the SCS region in terms of sea surface temperature (Huynh et al., 2016; Liu et al., 2014; Tan et al., 2016; Yang et al., 2015: Wang et al., 2006), sea level (Peng et al., 2013; Rong et al., 2007), surface winds (Huynh et al., 2016), precipitation (Juneng and Tangang 2005; Vinh et al., 2014; Räsänen and Kummu, 2013; Räsänen et al., 2016), cyclone frequency occurrences (Camargo and Sobel, 2005; Wu et al., 2005), river runoff (Räsänen and Kummu, 2013; Xue et al., 2011) and upwelling variability (Da et al., 2019). Furthermore, many studies suggested that the SCS summer monsoon is modulated by ENSO such that El Niño/La Niña phases weaken/strengthen the summer monsoon with a later/earlier onset (Lau and Yang 1997; Chou et al., 2003; Liu et al. 2012; Dippner et al., 2013). While ENSO effects have been largely studied over the SCS, no studies (in english) have focused on ENSO effects over the GoT.

In addition, the Madden Julian Oscillation (MJO) and the Indian Ocean Dipole (IOD) also influence the SCS interannual variability, and thus possibly the GoT interannual variability. MJO contributes to ~ 10% of the intra-seasonal anomalous precipitations over the SCS in summer (Zhang et al., 2009) while the IOD may impact the onset of the summer monsoon during non-ENSO years (Yuan et al., 2008). Again, skewing through literature, no studies have focused on the impacts of MJO and IOD over the GoT.

Rising questions:

Both typhoon-induced variability and ENSO induced variability have been studied on various atmospheric and oceanic parameters over the SCS, but remain undocumented in the GoT. In this low elevated and densely populated region, it is essential to understand and estimate regional impacts of short-term extreme events like typhoons to interannual variability factors like ENSO.

I.2.1.4 River influences

Red River - Taking its name from its brown-reddish colour, the Red River has its source in the mountains of Yunnan (China), where it is known as the Yuan River. It then flows into Vietnam and is renamed the Thao River. Once in Vietnam, it receives two major tributaries: the Da and

the Lo Rivers, and continues flowing through seven Vietnamese provinces (Fig. I.12 a, b). With a total length of 1150 km and a watershed of about 169000 km² (Fig. I.12 a), the Red River system is the second largest river system of Vietnam and still is an important commercial and transportation route. Downstream the confluence of the Da, Thao and Lo Rivers, the main river bifurcates into numerous distributaries feeding the Red River Delta and enters the GoT through nine main mouths (Fig. I.12 b).
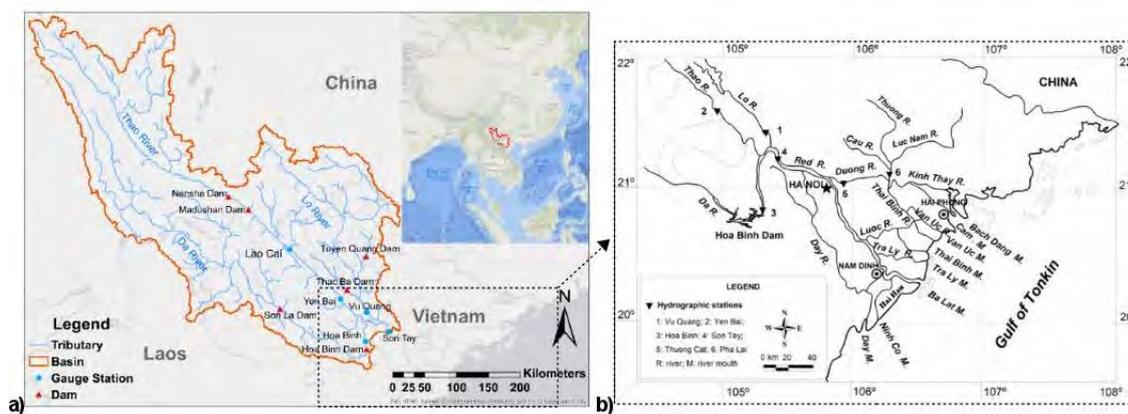
Figure I.12: (a) Red River basin catchments (Wei et al., 2019), (b) scheme of the Red River system (Vinh et al., 2014).

Being dominated by a monsoon climate, the Red River has a large seasonal variation in water discharge and in sediment load. The water discharge during the rainy season (June to October) represents 71-79% of the annual discharge while the dry season (December to April) only represents 9-18% of the annual discharge (Vinh et al., 2014). The remaining 5-10% occurs during the lowest rainfall period from January to March. In terms of values, the annual mean discharge is about 3500 m^3 s^{-1} with maximum peaks in August of $\sim$ 9000 m^3 s^{-1} (Fig. I.13). The suspended sediment concentration is also higher during the rainy season than during the dry season, with peaks of 250 g m^{-3} (Fig. I.13). Vinh et al. (2014) showed that the sediment load during the rainy season corresponded to 87 to 96% of the total annual discharge with an annual mean value of 40 Mt y^{-1}.

In the past decades, several studies indicated that water discharge and sediment load in most large rivers around the world had been drastically regulated by anthropogenic activities, such as irrigation, diversions and dam operations (Nilsson et al. 2004; Syvitski et al. 2005: Vörösmarty et al. 2003). The Red River is no exception to the rule, with serious changes in hydrological regime observed since the impoundment of the first two dams in the region. The Thac Ba dam impoundment (1972) caused a decrease of $\sim$ 5.5% of the sediment load (Lu et al., 2015) while the Hoa Binh impoundment (1989) caused a decrease of 61% of the sediment load (from 119 to 46 10^6 t y^{-1}, Vinh
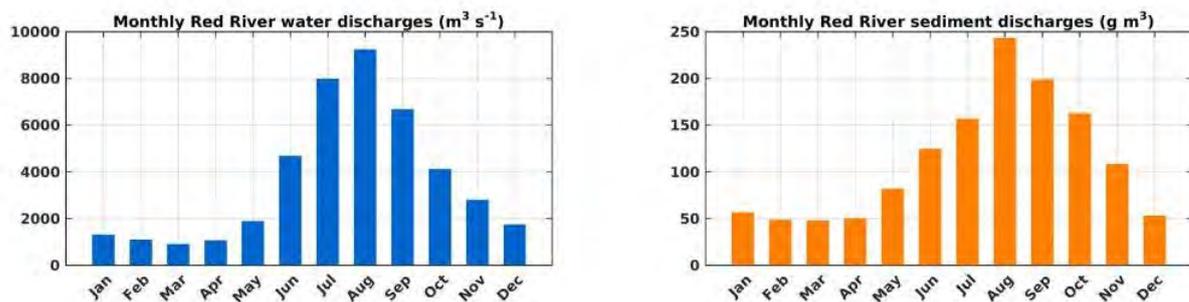
Figure I.13: Climatological monthly Red River water (left) and sediment (right) concentration at Son Tay for
the period 1990-2016 from the National Hydro-Meteorological Service.

et al., 2014). Furthermore, Vinh et al. (2014) showed that seasonal discharges are also impacted,
with a decrease of 14% of water discharge during the wet season (summer) and an increase of 12%
of water discharges during the dry season (winter) corresponding to the regulation role of the dam.

The composition of this sediment load shows a strong seasonal variability, as reported by Vinh
et al. (2018) for the Cam River, which is one of the main distributaries of the RR. During the dry
season, the water column is composed at 27% of fine aggregates (1.48-17.7 μm), at 40% of medium
flocs (17.77-92.6 μm) and at 33% of coarse flocs (92.6-212 μm). During the rainy season, particles
of fine, medium and coarse flocs occupy 35% , 38% and 27% of the total volume concentration of
the Cam River, respectively.

Coastal rivers - Many rivers of much smaller influences feed the GoT, however little is known about
them in terms of water and sediment discharges. From the south of the GoT towards the north,
there are the Lam, Lac Giang and Ma rivers which are Vietnamese rivers, and the Beilun, Qinjiang,
Nanliu and Jiuzhou rivers which are Chinese rivers. Climatological water discharge data suggest
that all of the rivers are subjected to a high seasonal variability, potentially influenced by the mon-
soon climate, similarly to the Red River case (Fig. I.14). Nonetheless, the maximum discharge
peaks reached by the rivers Lam and Ma of ∼ 2000 m^3 s^{-1} in August is ∼ 4 times smaller that the
peaks observed in August for the Red River (Fig. I.13 and Fig. I.14). No information was found con-
cerning the sediment load from these rivers, however is it assumed that it is negligible compared
to the Red River loads.

I.2.1.5   Seabed, tidal flats and river-bed sediments

Niino and Emery (1961) reported that the GoT seabed composition was highly linked to the fluvial
inputs and that fine mud and fine sand were predominant, but that locally coarser sand and gravel
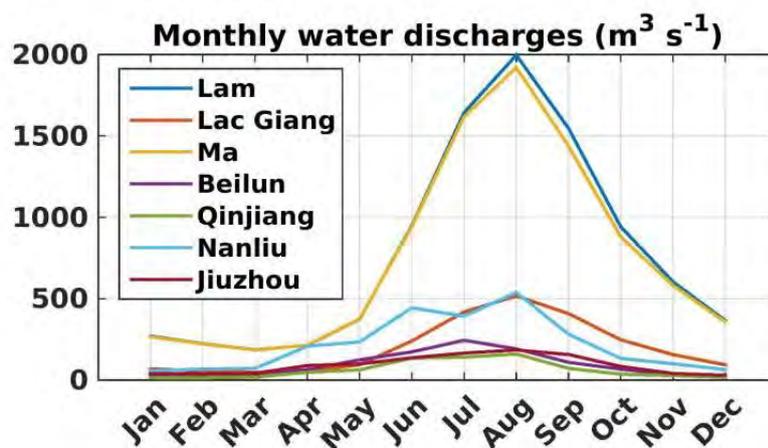
Figure I.14: Climatological monthly freshwater discharges for the Lam, Lac Giang, Ma (Vietnam National Hydro-Meteorological Service) Beilun, Qinjiang, Nanliu and Jiuzhou rivers (from the Global Hydroclimatic Data Network, Dettinger and Diaz, 2000).

could be encountered. In 2007, the Natural Conditions and Environments of Vietnam Sea and Adjacent Area Altas (in Vietnamese) proposed a detailed map of the repartition of different types of muds and sands over the seabed (Fig. I.15). The GoT seems composed of complex alternatives patches of mud, mud mixtures with sand, sand and sand mixture with gravel. The RRD coastlines are mostly composed of mud and of mixtures of mud and sand. Coarser sediments (i.e.: sand, mixtures of sand and gravel) are observed in the central GoT while the southern GoT seems mostly composed of mud and mud mixtures. These results were confirmed, at least in the southern GoT, by Ni et al. (2016) who observed the presence of mud and sand.

Tidal flats are specific environments which are submerged during flood tides and exposed during ebb tide and are found all along the 350 km coastlines of the RRD. These shallow areas are thus directly influenced by the region's tidal regime, the seawater currents and river flows, and are extremely sensitive to changing environments due to natural forces and human activities. Tidal flats are also known as areas of important rates of export and deposition of mud and sand. Therefore, assessing their morphological evolution is difficult but highly necessary in understanding the sediment transport and circulation. Tong (2016) was able to map the RRD tidal flats using remote sensing images (by extraction of waterlines at lowest and highest water level) and classify them into 3 categories. The tidal flats located in the northern part of the RRD are sandy and tide dominated. The central ones are mainly composed by coal sediments (from coal exploitation over the past 100 years). Lastly, the southern RRD hosts tidal flats dominated by sediments brought by the rivers feeding the area.
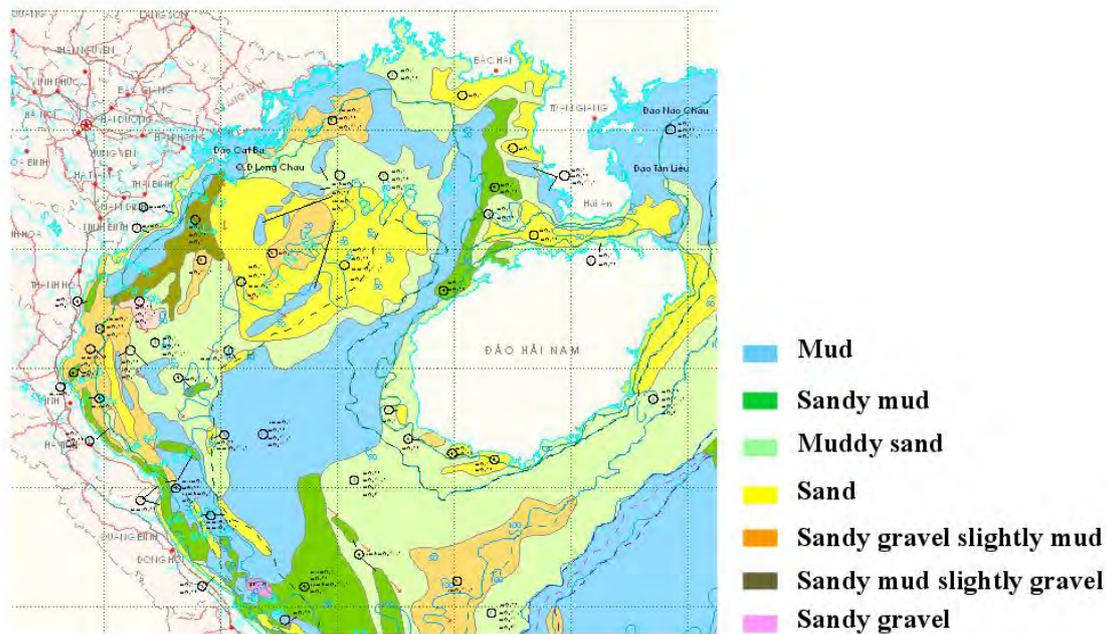
Figure I.15: GoT seafloor composition from the Natural Conditions and Environments of Vietnam Sea and Adjacent Area Altas (2007).

Few studies reported the composition of the river beds. In the Da, Thao and Lo Rivers, the values of the median diameter of superficial sediments are, on average, of 0.35, 0.16 and 0.175 mm respectively (Ministry of Agriculture and Rural Development). Downstream, in the estuaries and coastal zones, the median diameter of the superficial sediments ranges from 5 to 195 μm (Do et al., 2007). In the lower Cam-Bach estuary, which was the most intensively studied estuary until now due to its strategic location (Haiphong harbor), bottom sediments result from a combination of fine silts and fine sand, whose ratio highly varies at a distance of 5-10 km and with season (Lefebvre et al., 2012). Furthermore, sediment samples from the Cam River revealed a high percentage of clay to fine silts and a substrate more enriched in fine sand in the Cam estuary (Vinh et al., 2018).

Rising questions:

Except for the Cam River, observations on the suspended matter composition in the water column and on its variability are non-existent or very limited in other distributaries of the Red River system. Therefore, a need exists in documenting the SPM composition with in-situ observations in other regions of the Red River.

I.2.2 Hydrodynamical conditions of the GoT

I.2.2.1 General circulation

SCS circulation is largely driven by the atmospheric monsoon wind systems (Xu et al., 1982; Chu and Li 2000; Fang et al., 2002) but transport through Luzon Strait plays also a role in the northern SCS surface circulation (Wang et al., 2006b; Gan et al., 2006). In winter, NE winds induce a basin-wide cyclonic circulation with an intense jet along the western coast (Fig. I.16 b). In contrast, the SW summer monsoon induces an anti-cyclonic circulation over the southern SCS with a NE western boundary current which turns eastward/offshore between 11-13° N southern Vietnam (Fig. I.16 a).

From the surface to 150 m, circulation patterns remain similar (even though the current speed decreases with depth), however, the deep layer circulation is shaped by the Luzon strait transport that generates a basin-wide cyclonic circulation (Chao et al., 1996; Lan et al., 2015).
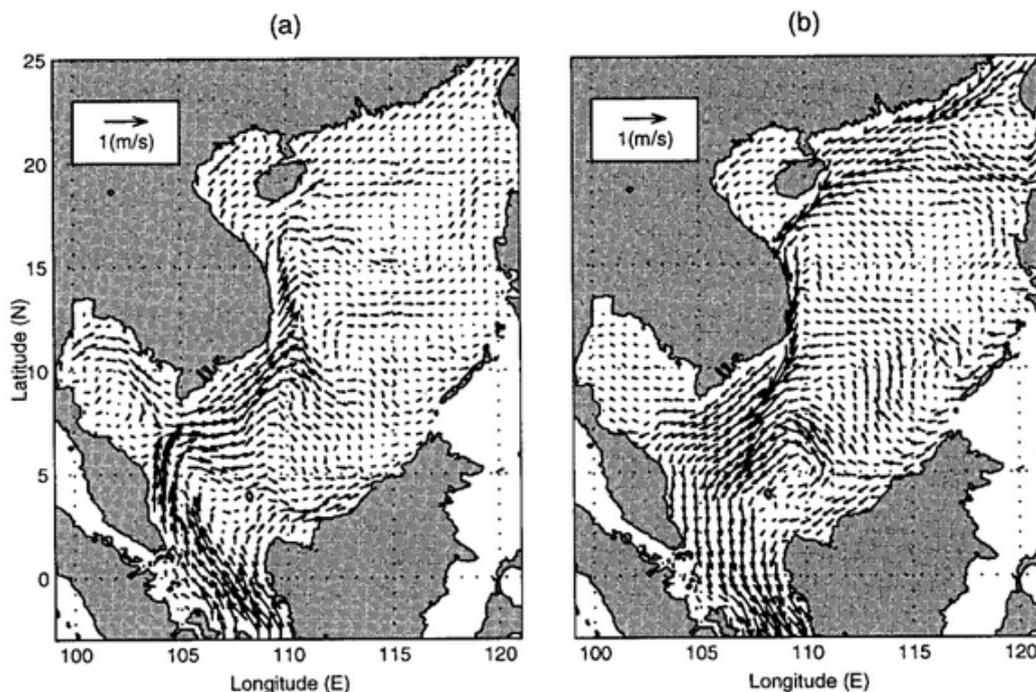
Figure I.16: Mean SCS surface circulation during (a) summer and (b) winter from Chu et al. (1999).

While the SCS oceanic circulation is largely studied and understood, GoT circulation has attracted only limited attention from researchers over recent decades and the GoT circulation remains a topic of debate in the literature.

Winter circulation

Besides a general agreement on a gulf-scale cyclonic circulation in winter, four main structures of

the winter circulation have been proposed (Fig. I.17):

1) The gulf-scale cyclonic circulation consists in two cyclonic gyres: one in the southern GoT
   and one in the middle of the northern GoT (Tan 1987, based on one-year observations).

2) The gulf-scale cyclonic circulation with a small cyclonic gyre enclosed in the northern GoT
   (Yu and Liu, 1993, based on historical in-situ observations).

3) The gulf-scale cyclonic circulation consists in two cyclonic gyres: one in the southern GoT
   and one in the northern GoT, with a southward current following the Vietnamese coast and
   a southwestward currents following the western coasts of Hainan (Manh and Yanagi, 2000;
   Xia et al., 2001; Sun et al., 2001, all based on 3D modeling).

4) The circulation consists in a northern enclosed cyclonic gyre and a southern anticyclonic
   gyre (Liu and Yu, 1980, based on 2D model; Yuan and Deng, 1999; based on 3D model).
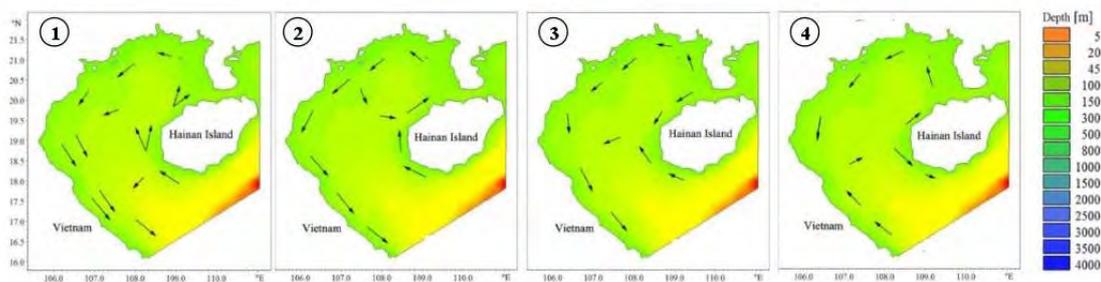
Figure I.17: Schematic patterns of winter circulation in the Gulf of Tonkin from the literature (Gao et al.,
2017). Reference 1 to 4 are given in the text.

Despite these discrepancies in proposed structure circulations, all of the above-mentioned studies
suggested that winter monsoon winds are the primary drivers of the winter surface circulation.
However, Gao et al. (2014b), based on numerical models, found that the density-driven currents
are the most relevant factor that influences the winter circulation.

Summer circulation

Due to the combined effect of wind, heat flux and river plumes, the circulation structure during
summer is complex and generally classified into three patterns (Fig. I.18):

1) A gulf-scale anticyclonic circulation (Wang, 1998; Sun et al., 2001, both based on 3D model-
   ing)

2) A gulf-scale cyclonic circulation (Xia et al., 2001; Zu, 2005, using numerical modeling)

3) A two gyres-structure circulation: one cyclonic gyre enclosed in the northern GoT and one anticyclonic gyre at the southern GoT boundary (Yang et al., 2003, based on field observations; Gao et al., 2013, based on 3D modeling)

In addition, driving mechanisms are still under discussion as some studies suggest that the summer circulation is mainly driven by density-gradients (Xia et al., 2001; Yang et al., 2003; Zu, 2005, based on 3D modeling) while others show that the summer GoT circulation is dominated by the monsoon winds (Manh and Yanahi, 2000; Sun et al., 2001).
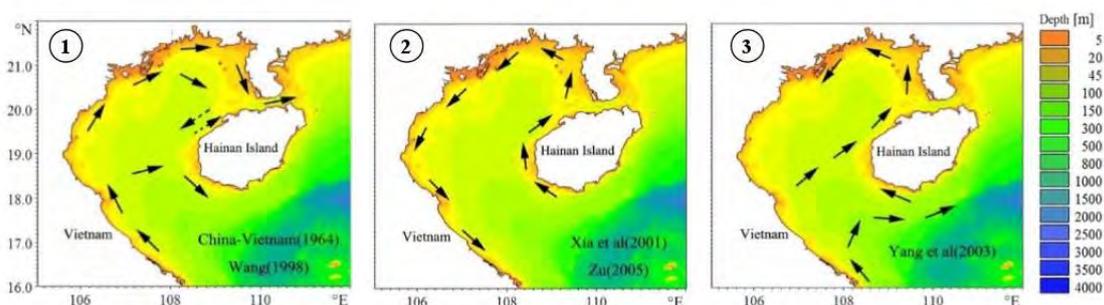
Figure I.18: Schematic patterns of summer circulation in the GoT (from Gao et al., 2017).

Circulation in the Hainan strait

As well as the general seasonal gulf-scale circulation, the circulation in the strait of Hainan remains largely discussed and is generally classified into two patterns:

1) A seasonal alternation in current direction (eastward in summer and westward in winter) (Ke, 1983; Liu et al. 2001; Gao et al., 2013; Rogowski et al., 2019)

2) A year-lasting westward circulation (Shi et al., 2001; Chen et al., 2007; Chen et al., 2009b)

Regarding the first pattern, Liu et al. (2001), based on field SLA observations, associated the circulation reversal directly to the seasonal patterns of the monsoon. Based on a 2D modeling study, Ke (1983) reported that the eastward current occured when the driving wind is southwesterly. Using a 3-D numerical model (ROMS), Rogowski et al. (2019) suggested that the westward buoyant flow observed in fall-winter came from the adjacent Pearl River discharges, which are similar to the mean annual discharges of the Red River, and entered the GoT by wind-induced circulation. However, Gao et al. (2013), with a 3D modeling study, suggested that the sea level difference between the two entrances of the strait had a stronger effect on current direction than local winds.

With respect to the second proposed circulation pattern, numerical and observational studies

showed that tidal rectification over variable bottom topography was the process dominating the westward current that lasts through the year (Shi et al., 2001, based on current observations; Chen et al. (2007, 2009b), both based on 3D modeling). Other scientists suggested that the westward current was driven by the coastal current off the western coasts of China (Bao et al., 2005; Rozowski et al., 2019, both 3D model studies).

Boundary current

Finally, Manh and Yanagi (2000) were the first to observe a current off the Vietnamese coast that moves southward along the shorelines in winter. Ding et al. (2013) furthermore showed that this current was generated by the wind-driven circulation. However, the downcoast current was found to last through the year by Rogowski et al. (2019), and forced by buoyant patterns generated by intense inputs of freshwater from the Red River, in summer.

> Rising questions:
>
> While most studies agree on a predominance of a gulf-scale cyclonic flow during winter, the circulation structure during summer remains a topic of debate. In addition, the scientific community disagrees on the mechanisms dominating the surface current variability, whether it is driven by monsoon wind-induced currents or by density-gradient currents. Therefore, a need exists in the high-resolution description of the GoT seasonal circulation and in the identification of the circulation driving mechanisms.

I.2.2.2 Tides

As previously discussed in sections I.1.2 and I.1.3, tidal currents and breaking tide-induced internal waves play a crucial role in the ocean mixing at all depths and participate to drive the deep circulation (Stewart 2008). Tidal mixing is particularly strong in shallow areas and can strongly influence coastal sediment transport and mixing in the river mouths. In the SCS, their dissipation can affect the vertical distribution of current and temperature, which in turn might play a role in blooms of the biological communities (Nugroho et al., 2018). Wyrtki (1961) was the first to identify the main tidal constituents in the SCS (O1, K1, M2, S2) (Table I.1) and Ye and Robinson (1983), the first to successfully simulate the tides in the area.

Few years later, it has been shown that the SCS and the GoT are one of the few regions in the world where diurnal tides dominate the semidiurnal tides (Fang, 1986). In coastal seas and bays, tides are primarily driven by the open ocean tide at the mouth of the bay. By resonance of a construc-

Tidal wave	Description	Period (h)
O1	Diurnal principal lunar	25.82
K1	Diurnal solar	23.93
M2	Semi-diurnal principal lunar	12.42
S2	Semi-diurnal principal solar	12.00

Table I.1: List of the GoT main tidal constituents.

tive interference between the incoming tide and a component reflected from the coast, large tide amplitude can be generated. In the GoT case, tidal waves enter the basin from the adjacent SCS and due to the basin geometry, O1 and K1 resonate (Fang et al., 1999). Their amplitudes reach 1.00 and 0.90 m respectively (Fig. I.19 a, b). In addition, the major branch of energy flux entering the basin from the southwest is weak for the semi-diurnal tides and strong for the diurnal ones. A second branch of energy (also diurnal tidal waves) enters the GoT through the Hainan Strait (Ding et al., 2013). The tidal form factor (F), or amplitude ratio, defined by the ratio of the amplitude of the two main semi-diurnal and diurnal constituents, provides a quantitative measure of the general characteristics of the tidal oscillations at a specific location. At the entrance of the GoT and at the Hainan strait, the tides are defined as mixed primarily diurnal with F varying from 1.5 and 2.2 depending on the given locations. At the RRD, F is around 15, attesting of a diurnal regime.
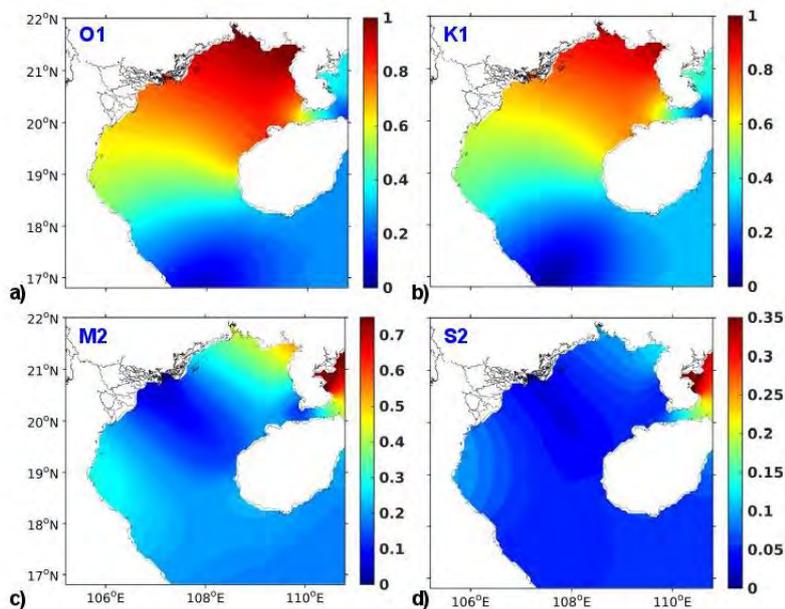
Figure I.19: Tidal amplitude (m) for O1 (a), K1 (b), M2 (c) and S2 (d) from the tidal atlas FES2014b.

In the GoT, the Coriolis force deflects to the right the incoming tidal waves and push them against the northern enclosure of the basin. Once the waves are reflected, they propagate southward until they slowly dissipate by friction. Fang et al. (1999) found that the amplitude of the tide gradually decreases from 4 to 2 m North to South during spring tide. The amplitude of O1 in the GoT is larger

than K1 because of a larger resonance effect, even though its amplitude in the SCS is smaller than K1 (Minh et al., 2014) (Fig. I.19 a, b). The largest semidiurnal waves of the GoT are M2 and S2. They both appear as a degenerated amphidrome with smallest amplitudes near the RRD and with maximum amplitude in the northwestern head of the GoT (0.50 m for M2 and below 0.15 m for S2) (Hu et al., 2001) (Fig. I.19 c, d). Given those values of amplitude, van Maren et al. (2004) defined the tidal regime in the GoT as mesotidal, and locally even macrotidal, even though diurnal tidal regimes are usually mainly microtidal.

Until recently, only few numerical studies have focused on the GoT (Fang et al., 1999; Manh and Yanaghi, 2000; van Maren et al., 2004; Minh et al., 2014) and on the Hainan Strait (Chen et al. 2009). The study of Minh et al. (2014) complemented the existing state of the art in numerically reproducing the tides of the GoT and explored for the first time the GoT resonance spectrum, using a high resolution 3D model (ROMS at 1/25°). In particular, the authors showed that the resonance was not only due to the diurnal waves, but also due to the semi-diurnal waves. In addition, the authors mentioned that the semi-diurnal waves are small in the GoT, because they are small in the SCS. However, this study also showed the limitations of using a 3D model in representing the tidal spectrum. Indeed, large discrepancies between the model and observations (gauge stations and satellite) especially for the M2 harmonics and for the phase of S2 were found. The authors explained those discrepancies by the lack of resolution in the coastal areas due to limitations implied by the use of a regular grid and a poorly resolved bathymetric dataset.

> Rising questions:
>
> A good representation of the GoT tidal spectrum is crucial as tides play a key role in ocean circulation and estuarine dynamics. Despite the large amount of studies on the GoT tides, the numerical representation of the main tidal components is still limited and shows large discrepancies with observations, due to poor bathymetric dataset and poor model resolution in coastal areas. Therefore, a need exists in improving the available bathymetric datasets over the GoT and increasing the resolution of numerical models to improve the tidal representation and understanding in the area.

I.2.2.3 Waves

Rose by the urge of developing non-polluting and renewable energy, the temporal and spatial distribution of wave energy within the Gulf of Tonkin have been lately studied by Zhou et al (2014), using the Simulated Waves Nearshore (SWAN) model. Their results show that the peak wave pe-

riod undergoes no particular variation from summer to winter, with minimum values of 2 s in the northern GoT and near offshore, and maximum values of 3 s in the southwestern GoT (Fig. I.20 a, d). The wave height presents an obvious seasonal variability, with a patch of values >0.5 m confined in the central GoT during summer that extends toward the southern GoT in winter (Fig. I.20 b, e). Lastly, the authors showed that the wave energy is >1 kW m^{-1} in the central part of the GoT, and values up to 1.4 kW m^{-1} in the central and southern GoT in winter.
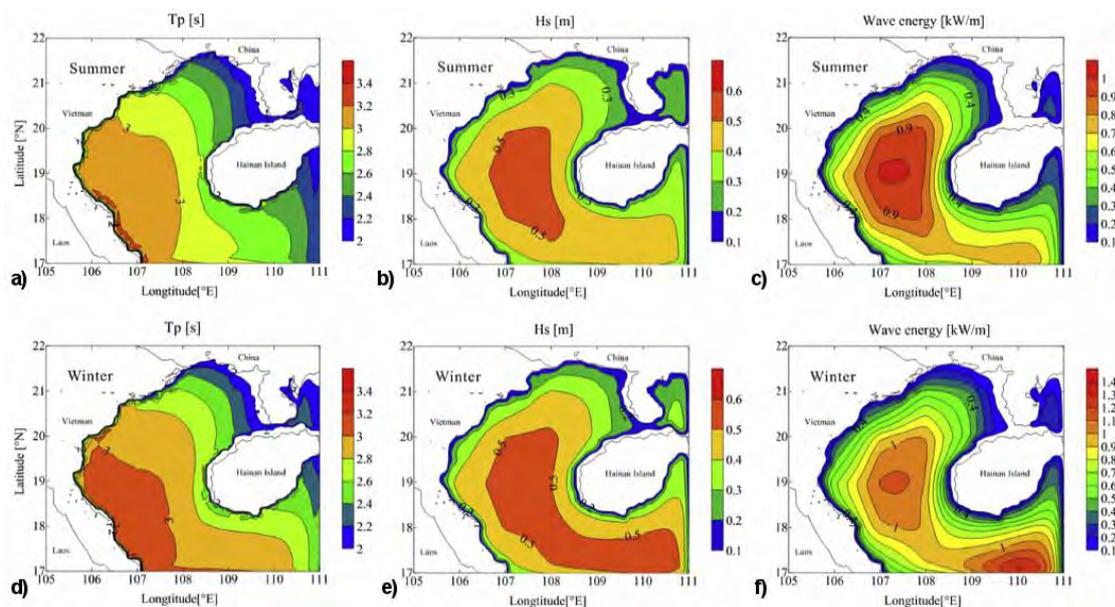
Figure I.20: Spatial distribution of mean seasonal averages (summer, winter) of the wave period (Tp) (a,d), wave height (Hs) (b, e) and wave energy (c, f) from Zhou et al. (2014).

Opposite to the general condition over the GoT, 41 years (1970-2011) of wave observations at the hydrological station of Hon Dau (located in front of the Van Uc river mouth, see Fig. I.12), revealed that waves in the coastal area were dominated by a seasonal variability. Indeed, larger wave heights were observed during the dry season (0.6-0.8 m) than during the wet season (0.5-0.6 m). In addition, small wave heights (<0.5 m) occupied 52% of the total time of observations, while big wave heights (>1.5 m) occupied ~ 15% of the total time of observations (Vinh, 2012).

> Rising questions:
>
> Since waves characteristics vary seasonally in the GoT coastal area and can reach significant heights, it would be crucial to understand and characterize their variability and assess their impacts on the transport of matter is crucial. This question has not been studied during the time frame of this study. However, a need exists in taking them into account in modeling studies of sediment transport, which was done in this Ph.D. for the RRD coastal area.

I.2.3 Hydrological and SPM dynamics in the estuarine and coastal area

I.2.3.1 Estuarine processes

Even though river estuary is a focal point of the interaction between fresh and marine water masses, only few studies focused on the SPM dynamics and processes, in link with Red River estuarine hydrodynamics. Based on field survey in the Ba Lat mouth coastal zone, van Maren and Hoekstra (2004) showed that during the dry season, the flow patterns are determined by the tidal currents which favor the local sediment resuspension. During the wet season, the Ba Lat estuary is flushed at each ebb period and the sediment transport is dominated by advection processes. Several studies focused on the Cam-Bach Dang estuary, rose by the urgence of understanding the mechanisms behind the Haiphong Harbor siltation. Lefebvre et al. (2012) investigated the mechanisms governing cohesive sediment aggregation in the Cam-Bach Dang estuary. Similar to the observation of van Maren and Hoekstra (2004), the authors identified a marked seasonal and tidal contrast in hydrological estuarine conditions. The strong freshwater input characteristics of the wet season tends to generate a high turbulent energy level which in return generates transfers of coarse sediments to fine sediments. During the dry season, the influence of tides on estuarine dynamics dominates and the tidal pumping (flood tides shorter and stronger than ebb tides) produces a net upstream transport of sediments. The effect of tidal pumping is discussed as a potential reason for the silting up of the harbor. Furthermore, bio-aggregation of particles was shown to be enhanced at salinity around 10-15 PSU due to increasing stickiness properties of bio-exopolymeric substances and could also enhance Haiphong harbor siltation (Mari et al., 2012). Finally, the Cam-Bach Dang Estuarine Turbidity Maxima (ETM) was shown to be composed of two parts: an upper well mixed ETM with high SPM concentration up to the surface that starts developing at salinities as low as 0.1 PSU, and a lower ETM confined in the bottom layer, developing at salinity ~ 1 PSU ((Fig. I.21) (Vinh et al., 2018).
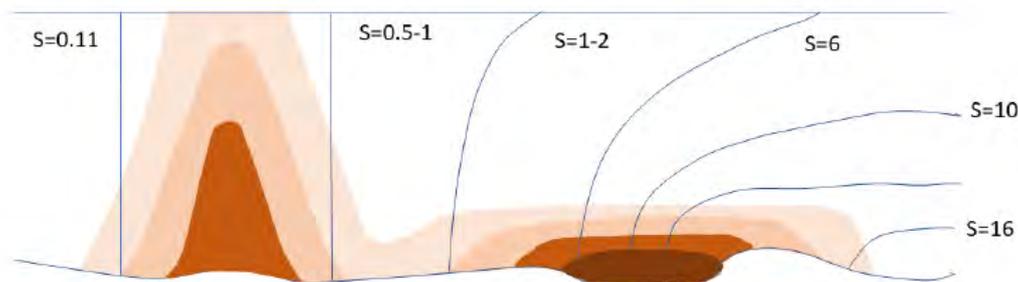
Figure I.21: General pattern of ETM in the Cam-Bach Dang estuary as observed by Vinh et al. (2018). Blue lines represent isolines (in PSU), turbidity patterns are shown in brown with darker color for higher turbidity values.

Rising questions:

Tides and seasonal variations in river discharges are thus decisive factors in both estuarine hydrodynamics and estuarine SPM processes. Also, identification of SPM processes are essential in the understanding of siltation, erosion, accretion along the RR estuaries. For that, a need exists in further documenting Red River estuarine processes along the tidal cycle (low/high tides and neap/spring tides) during high and low seasonal river flow, in order to identify the siltation-favorable conditions.

Furthermore, researchers have mainly focused on two estuaries of the Red River system (the Ba Lat and Cam-Bach Dang), thus nothing is known about the dynamics of other Red River estuaries. Investigating a different estuary will help improve general knowledge on the region.

I.2.3.2   Coastal morphodynamics and sediment transport along the RRD

Coastal morphodynamics

Over the past decades, the RRD coastal zone has been suffering from alternative patterns of erosion and accretion, and some examples are given next. The Ba Lat River mouth has expended seaward with an approximate rate of 6 m in the past 50 years, due to a combined effect of sediment resuspension by wave actions and river floods (van Maren et al., 2004; van Maren et al., 2007). The beach of Hai Hau (south of Ba Lat mouth) has experienced increasing erosion rates over the past 20 years caused by the decrease of sediment supply brought to the beach by the Ba Lat river plume (Duc et al., 2007). Hung et al. (2002) however suggested that the wave action during winter combined with the complex topography of the delta was the prevailing mechanism of Hai Hau beach erosion. Lastly, the touristic area of Do Son (located next to the Van Uc river mouth) have experienced increased turbidity due to dykes impoundments that disturbed the local sediment circulation (Cu and Cham, 2010).

In this context of intense coastal morphological changes, Vinh (2018) used Delft3D to detail the erosion and accumulation areas along the RRD coastal area. The author showed an unstable morphology for depths <10 m with sediment deposition at river mouths (10-50 mm y^{-1}) and erosion areas (2-30 mm y^{-1}) in between river mouths (Fig. I.22). As tidal currents flow in the opposite direction of the river plume, the stability of the river plume leads to sedimentation in front of the river mouths, rather than an offshore dispersal. Further offshore, from 10 to 25 m depth, the author showed a tendency to deposition with a deposition gradually decreasing from 10-30 mm y^{-1} to <10 mm y^{-1} offshore.
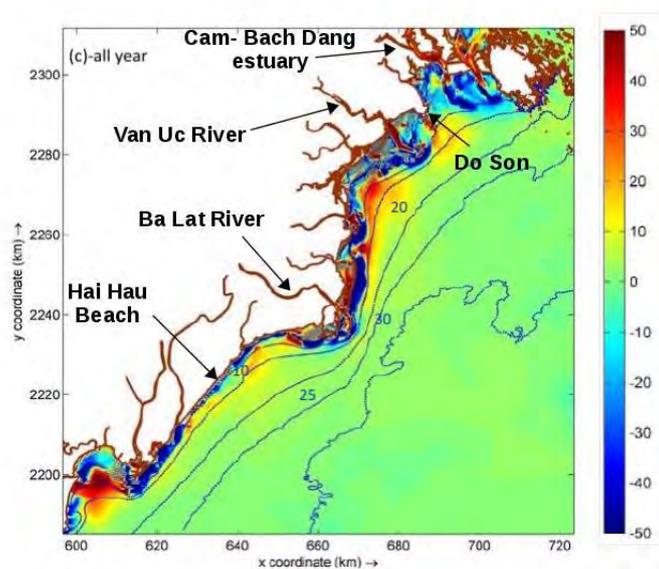
Figure I.22: Morphological changes (mm y^{-1}) in the RRD coastal area from Vinh (2018).

Sediment transport

Few studies addressed the issue of sediment transport in the coastal area along the RRD. First, a numerical study using Delft3D reported that the Ba Lat river plume was the main factor impacting the seaward transport of sediment, while wave asymmetry caused onshore sediment transport (van Maren, 2004, PhD). Second, Duc et al (2007) estimated that directions of sediment transport along the RRD are variable where depths are <5 m, but from 5 to 10 m depth, sediments are mainly transported southwards. Finally, Vinh (2018) quantified the sediment transport along the RRD (Fig. I.23). Although promoted during the rainy season by freshwater from the rivers, sediment fluxes through cross sections along the RRD are smaller than during the dry seasons (Fig. I.23 a), thus the author suggested that erosion processes occurs mainly during the dry season. The small alongshore sediment fluxes observed during the rainy season are potentially caused by sediment gathering in the near river mouth due to flocculation processes, and due to low resuspension pro-

cesses. Annually, the transport is shown to be southward, except in the extreme north of the RRD. Lastly, the author showed that the presence of waves strongly intensifies the resuspension of sediment and intensify their southward transport.
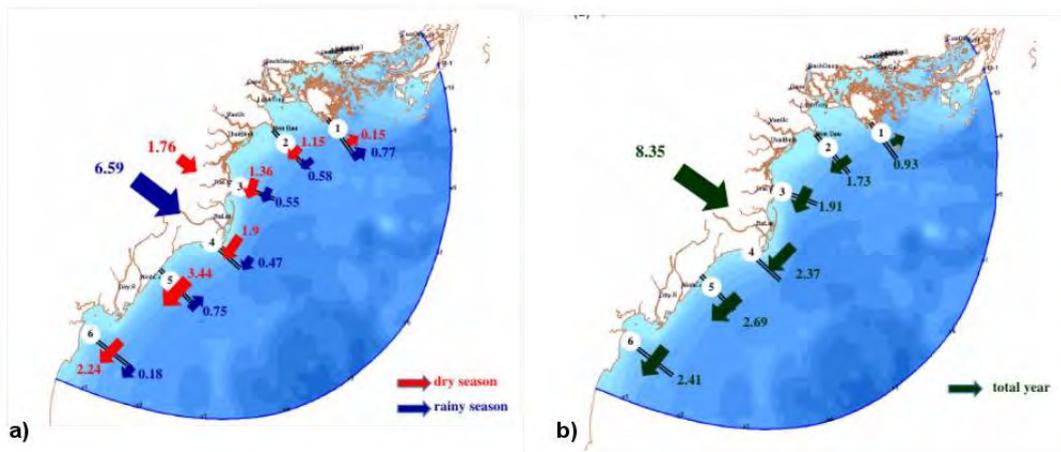
Figure I.23: Alongshore sediment transport for different cross-sections (x10^6 t) in the RRD coastal area during dry and rainy season (a) and annually (b), from Vinh (2018).

Rising questions:

RRD morphodynamics and suspended sediment transport in the RRD have been partly studied and numerical studies remain limited due the lack of observations for model calibration and evaluation. Furthermore, sediment transport and export outside the RRD remains weakly documented. A need exists in detailing the coastal morphodynamics processes in link with the hydrodynamics variability (currents and waves). In addition, questions remain on where and how far the deltaic sediments can be transported alongshore and offshore, and how this transport answers to the different factors of variability.

I.3   Objectives and thesis outlines

The main objectives of this work are to improve our general knowledge on the RRD-GoT system in terms of estuarine and ocean dynamics and their variability at different time and space-scales, and to understand and quantify their impacts on the hydrodynamics and sediment fate and budget, based on both in-situ measurements and fine-resolution modeling. Issues of this work can be resumed as follows:

- What is the variability of the flow and suspended matter dynamics within the Red River estuary, induced in particular by seasonal and tidal changes?

- What is the functioning and variability of the GoT ocean circulation from the tidal to sea-

sonal and interannual scales, and what are their impacts on water and sediment fluxes within and at the boundaries of the studied RRD-GoT system ?

- Can we produce a highly realistic numerical representation of those dynamical processes at all scales and of their impact on sediment transport, and what are the key elements that need to be improved for that ?

The structure of this thesis reflects the issues outlined above and to answer them, an ensemble of observations and numerical models are used.

Chapter II explores the influences of seasonal and tidal changes on flow and suspended matter dynamics in the macrotidal Van Uc river estuary. This chapter is based on the analysis of hydrodynamical and suspended particulate matter measurements, collected along river transects that were organized and performed during 4 field campaigns in the frame of this PhD thesis in 2017.

Chapter III reports the application of the model T-UGO in simulating the GoT tidal spectrum and in optimizing the configuration. The role of bathymetry and model resolution on tidal representation, as well as the importance of fine bottom friction parameterization is presented.

The abilities of the regional ocean model SYMPHONIE in reproducing the observed GoT hydrodynamics and water mass properties are discussed in Chapter IV, then the circulation variability is quantified and studied. In particular, we examine in details the impacts of key factors, namely typhoons and ENSO, on circulation and water budgets.

Chapter V summarizes the key results and findings obtained during this study and raises issues and discusses about the preliminary results obtained with a sediment transport model along the RRD. It further proposes questions to be addressed by future research.

Chapters II and III correspond to two submitted papers in international journals. They were submitted in *Journal of Marine Systems* for Chapter 2 and in *Geoscientific Model Development* for Chapter 3.

I.4 References

- Allen G. P., Salomon J. C., Bassoullet P., du Penhoat Y., de Grandpré C. (1980) Effects of tides on mixing and suspended sediment transport in macrotidal estuaries, Sediment. Geol., 26, 69-90, https://doi.org/10.1016/0037-0738(80)90006-8.
- Bashkar P. V., Grossart H.-P., Bhosle N. B., Simon M. (2005) Production of macro-aggregates from dissolved exopolymeric substances (EPS) of bacterial and diatom origin. FEMS Microbiology Ecology 53(2), 255-264.
- Bilan D. (1993) The preliminary vulnerability assessment of the Chinse coastal zone due to sea level rise, Proceedings of the IPCC eastern hemisphere workshop, Tsukuba, Japan 3-6 August 1993.
- Brenon I., Le Hir P. (1999) Modelling the turbidity maximum in the Seine estuary (France): Identification of formation processes. Estuar. Coast. Shelf Sci. 49, 525-544, https://doi.org/10.1006/ecss.1999.0514.
- Cacchione D. A., Drake D. E. (1986) Nepheloid layers and internal waves over continental shelves and slopes, Geomar. Lett., 6, 147-152, doi: 10.1007
- Camargo S. J., Sobel A. H. (2005) Western North Pacific Tropical Cyclone Intensity and ENSO. Amer. Meteor. Soc., 18: 2996-3006., doi:10.1175/JCLI3457.1.
- Cat N. N., Tien P. H., Sam D. D., Bien N. N. (2006) Status of coastal erosion of Viet Nam and proposed measures for protection, available at http://www.fao.org/forestry/11286-08d0cd86bc02ef85da8f5b6249401b52f.pdf.
- Chao S.-Y., Shaw P.-Y., Wu S. Y. (1996) Deep water ventilation in the South China Sea, Deep Sea Res., Part I, 43(4), 445-466, doi: 10.1016/0967-0637(96)00025-8.
- Chen C., Li P., Shi M., Xuo J., Chen M., Sun H. (2009) Numerical study of the tides and residual currents in the Leizhou Strait, Chin. J. Oceanol. Limnol., 27(4), 931-942, https://doi.org/10.1007/s00343-009-9193-0.
- Chou C., Tu J. Y., Yu J. Y. (2003) Interannual variability of the Western North Pacific summer monsoon: Differences between ENSO and non-ENSO years, J. Clim., 16(13), 2275-2287, doi: 10.1175/2761.1.
- Chu P. C., Edmons N. L., Fan C. (1999) Dynamical mechanisms for the South China Sea seasonal circulation and thermohaline variabilities, J. Phys. Oceanogr., 29(11), 2971-2989, doi: 10.1175/1520-0485(1999)029<2971:DMFTSC>2.0.CO;2
- Chu P.C., Li R. (2000) South China Sea isopycnal-surface circulation, J. Phys. Oceanogr., 30(9), 2419-2438, doi: 10.1175/1520-0485(2000)030<2419:SCSISC>2.0.CO;2.
- Cu N.V., Cham D. D. (2010) Research on Hydrodynamics, Sediment Transport, Deposition in Lach Huyen, South Do Son (Hai Phong) by Influence of the Deep-Port and Propose Solution. Final Report of the KC.08.10/06-10 Project; Institute of Geology: Hanoi City, Vietnam (In Vietnamese with English abstract).
- Da N. D., M. Herrmann, R. Morrow, F. Niño, N. M. Huan, N. Q. Trinh (2019) Contributions of wind, ocean intrinsic variability and ENSO to the interannual variability of the South Vietnam Upwelling: a modeling study. J. Geophys. Res. Oceans doi:10.1029/2018JC014647
- Dettinger M. D., Diaz H. F. (2000) Global characteristics of stream flow seasonality and variability. J. Hydrometeor, 1(4), 289-310, https://doi.org/10.1175/1525-7541(2000)001<0289:GCOSFS>2.0.CO;2
- Ding Y., Chen C., Beardsley R. C., Bao X., Shi M., Zhang Y., Lai Z., Li R., Lin H., Viet N. T (2013): Observational and model studies of the circulation in the Gulf of Tonkin, South China Sea, J. Geophis. Res., 118, 6495-6510, doi:10.1002/2013JC009455.
- Dippner J. W., Bombar D., Loick-Wilde N., Voss M., Subramaniam A. (2013a), Comment on "current separation upwelling over the southeast shelf of Vietnam in the South China Sea" by Chen et al., J. Geophys. Res. Ocean., 118(3), 1618-1623, doi: 10.1002/jgrc.20118.
- Do M. D., Mai T. N., Chu V. N., Tran N., Dao M. T., van Weering Tj. C . E., van den Bergh

G. D. (2007) Sediment distribution and transport at the nearshore zone of the Red River delta, Northern Vietnam, J. Asian Earth Sci., 29, 558-565, https://doi.org/10.1016/j.jseaes.2006.03.007.

- Duc D. M., Nhuan M. T., Ngoi C. V., Nghi T., Tien D. M., van Weering Tj. C. E., van den Bergh G. D. (2007) Sediment distribution and transport at the nearshore zone of the Red River delta, Northern Vietnam, J. of Asian Ear. Sci., 29, 558-565., doi: 10.1016/j.jseaes.2006.03.007.

- Dieng, H. B., Cazenave, A., von Schuckmann, K., Ablain, M., and Meyssignac, B. (2015) Sea level budget over 2005–2013: missing contributions and data errors. Ocean Sci. 11, 789–802, doi: 10.5194/osd-12-701-2015.

- Dyer K. R., Manning A. J. (1999) Observation of the size, settling velocity, and effective density of flocs, and their fractal dimension, J. Sea Res., 41, 87-95, https://doi.org/10.1016/S1385-1101(98)00036-7.

- Eisma D. (1993) Transport of Suspended Matter. In: Suspended Matter in the Aquatic Environment. Springer, Berlin, Heidelberg, https://doi.org/10.1007/978-3-642-77722-6_5.

- Ericson J. P., Vörösmarty C. J., Dingman S. L., Ward L. G., Meybeck M. (2006) Effective sea-level rise and deltas: Causes of change and human dimension implications. Glob. Planet. Change, 50, 63-82. doi: 10.1016/j.gloplacha.2005.07.004.

- Fang G. (1986) Tide and tidal current charts for the marginal seas adjacent to China, Chin. J. Oceanol. Limnol., 4, 1-16, https://doi.org/10.1007/BF02850393.

- Fang G., Kwok Y. K., Yu K., Zhu Y. (1999) Numerical simulation of principal tidal constituents in the South China Sea, Gulf of Tonkin and Gulf of Thailand, Cont. Shelf Res., 19(7), 845-869, https://doi.org/10.1016/S0278-4343(99)00002-3.

- Fang W. (2002) Seasonal structure of upper layer circulation in the southern South China Sea from in situ observations, J. Geophys. Res., 107(C11), 3202, doi: 10.1029/2002JC001343.

- Farnsworth K. L., Milliman J. D. (2003) Effects of climatic and anthropogenic change on small mountainous rivers: Salinas River example, Global Planet. Change, 39, 53-64, https://doi.org/10.1016/S0921-8181(03)00017-1.

- Gan J., Li H., Curchitser E. N., Haidvogel D. B. (2006) Modeling South China Sea circulation: Response to seasonal forcing regimes, J. Geophys. Res. Ocean., 111(6), C06034, doi: 10.1029/2005JC003298.

- Gao J. S., Chen B., He X. Y., et al. (2014b) Responses of the circulation and water mass in the Beibu Gulf to the seasonal forcing regime. Acta Oceanol. Sin., 33(7), 1-11.

- Gao J. S., Wu G., Ya H. (2017) Review of the circulation in the Beibu Gulf, South China Sea. Cont. Shelf Res.. 138: 106-119. https://doi.org/10.1016/j.csr.2017.02.009.

- Gaspar P., Gregoris Y., Lefevre J.M. (1990) A simple eddy kinetic energy model for simulations of the oceanic vertical mixing: tests at station Papa and long-term upper ocean study site. J. Geophys. Res., 95,16179–16193.

- Gao J. S., Xue H. J., Chai F., et al. (2013) Modeling the circulation in the Beibu Gulf, South China Sea. Ocean Dyn.. 63: 979-993.

- Goodbred Jr. S. L. (2001) Ocean Margin Sediments: Encyclopedia of Ocean Sciences, 4, 1965-1973.

- Haq B. U. (1997) Regional and global oceanographic, climatic and geological factors in coastal zone planning. In: Hag B. U., Haq S. M., Kullenber G., Stel J. H. (Eds.), Coastal Zone Management Imperative for Maritime Developing Nations. Kluwer Academic Publishers, pp. 55-74.

- Hart D. E., Mardsen I., Francis M. (2008) Chapter 20: Coastal Systems. In Winterbourn M., Know G. A., Marsden I. D., Burrows C. (eds.), Natural history of Canterbury (3rd ed.). Canterbury University Press, pp. 653-684.

- Hoekstra P., van Weering T. C. E. (2007) Morphodynamics of the Red River Delta, Vietnam, introduction to the special issue, J. Asian Earth Sci., 29, 505-507, doi:10.1016/j.jseaes.2006.05.013.

- Hori K., Tanabe S., Saito Y., Haruyaùa S., Nguyen V., Kitamura A. (2004) Delta initiation and Holocen sea-level change: example from the Song Hong (Red River) delta, Vietnam, Sediment Geol., 237-249, https://doi.org/10.1016/j.sedgeo.2003.10.008.
- Hu J. Y., Kawamura H., Hong H. S., Kobashi F., Xie Q. (2001) Tidal features in the China Seas and their adjacent areas derives from TOPEX/Poseidon altimeter data, Chin. J. Oceanol. Limnol., 19, 293-305, https://doi.org/10.1007/BF02850732 .
- Hung N. M., Larson M., Ninh P. V., Hanson H. (2002) Regional wave transformation and associated shoreline evolution in the Red River Delta, Vietnam, Ocean Wave Measurements and Analysis (2001), doi: 10.1061/49604(273)33.
- Huynh H.-N., Alvera-Azcarate A., Barth A., Beckers J.-M. (2016) Reconstruction and analysis of long-term satellite-derived sea surface temperature for the South China Sea, J. Oceanogr., 1-20, doi: 10.1007/s10872-016-0365-1.
- Inman D. L., Jenkins S. A. (2003) Energy and sediment budgets of the global coastal zone. In: Encyclopedia of coastal Science (M. Schwartz, ed.), The Earth Sciences Encyclopedia Online (www.eseo.com)
- Jackson G. A. (1990) A model of the formation of marine algal flocs by physical coagulation processes. Deep-Sea Res. I, 37, 1197-1211, https://doi.org/10.1016/0198-0149(90)90038-W.
- Jelgersma S. (1996) Land subsidence in coastal lowlands. In: Milliman, J. D., Haq, B.U. (Eds), Sea-Level Rise and Coastal Subsidence. Kluwer Academic Publishers, pp. 47-62.
- Juneng L., Tangang F. T. (2005) Evolution of ENSO-related rainfall anomalies in Southeast Asia region and its relationship with atmosphere-ocean variations in Indo-Pacific sector, Clim. Dynam., 25: 337-350, doi: 10.1007/s00382-005-0031-6.
- Kirby R., Parker W. R (1983) Distribution and behavior of fine sediment in the Severn Estuary and Inner Bristol Channel, UK, Can. J. Fish. Aquat. Sci., 40, 83-95, https://doi.org/10.1139/f83-271.
- Kistner D. A., Pettigrew N. R (2001) A variable turbidity maximum in the Kennebec Estuary, Estuaries, 24, 680-687, https://doi.org/10.2307/1352876.
- Lan J. Y., Wang F. C., Zhang N. (2015) Seasonal variation in the South China Sea deep circulation, J. Geophys. Res. Ocean , 1682-1690, doi: 10.1002/2014JCC010413.
- Lau K. M., Yang S. (1997) Climatology and interannual variability of the southeast asian summer monsoon, Adv. Atmos. Sci., 14(2), 141-162, doi: 10.1007/s00376-997-0016-y.
- Lefebvre, J. P, S. Ouillon, V. D. Vinh, R. Arfi, J. Y. Panché, X. Mari, C. V. Thuoc and J. P. Torréton. (2012) Seasonal variability of cohesive sediment aggregation in the Bach Dang-Cam Estuary, Haiphong (Vietnam), Geo.-Mar. Lett., 32, 103-121, doi: 10.1007/s00367-011-0273-8.
- Lin I. I., Timothy Liu W., Wu C. C., Chiang J. C. H., Sui C. H. (2003) Satellite observations of modulation of surface winds by typhoon-induced upper ocean cooling, Geophys. Res. Lett., 30(3), 1131, doi:10.1029/2002GL015674.
- Liu F. S., Yu T. C. (1980) Preliminary study on the oceanic circulation in Beibu Bay. Trans. Oceanol. Limnol.. 1: 9-15 (in Chinese with English abstract)
- Liu Q., Jiang X., Xie S.-P, Liu W. T. (2014) A gap in the Indo-Pacific warm pool over the South China Sea in boreal winter: Seasonal development and interannual variability, J. Geophys. Res., 109(C07012), doi:10.1029/2003JC002179.
- Liu X., Wang J., Cheng X., Du Y. (2012) Abnormal upwelling and chlorophyll-a concentration off South Vietnam in summer 2007. J. Geophys. Res. Ocean., 117(7), 2-11, doi: 10.1029/2012JC008052.
- Luu. T. M. N., Garnier J., Billen G., Orange D., Némery J., Le T. P. Q, Tran H. T., Le L. A. (2010) Hydrological regime and water budget of the Red River Delta (Northern Vietnam), J. Asian Earth Sci., 37(3), 219-228, https://doi.org/10.1016/j.jseaes.2009.08.004.
- Maede R. H., Moody J. A. (2010) Causes for the decline of suspended-sediment discharge in the Mississippi River systel, 1940-2007, Hydrol. Process., 24, 35-49, doi: 10.1002/hyp.7477.
- Maggi F. (2005) Flocculation dynamics of cohesive sediment. PhD thesis, University of Tech-

nology, Delft, pp 136.
- Manh D. V., Yanagi T. (2000) A study on the residual flow in the Gulf of Tonkin. J. Oceanogr., 56: 59-68. https://doi.org/10.1023/A.1011162524466.
- Manning A.J., Dyer K. R., Lafite R., Mikes D. (2004) Flocculation measured by video based instruments in the Gironde Estuary during the European Commission SWAMIEE project, J. Coast. Res., 41, 58-69.
- Many G. (2016) Impacts of storm and flood events on suspended particulate matter dynamics in the Gulf of Lions. Contributions of gliders to a multi-platform approach. Université de Perpignan, NNT: 2016PERP0033.
- Mari X., Torréton J.-P., Tring C. B.-T., Bouvier T., Thuoc C. V., Lefebvre J.-P., Ouillon S. (2012) Aggregation dynamics along a salinity gradient in the Bach Dang estuary, North Vietnam, Estuar. Coast. Shelf Sci., 96, 151-158, https://doi.org/10.1016/j.ecss.2011.10.028.
- Mazda Y., Wolanski E., King B., Sase A., Ohtsuka D., Magi M. (1997) Drag force due to vegetation in mangrove swamps, Mangrove and Salt Marshes, 1, 1993-1999, doi: 10.1023/A:1009949411068.
- Milliman J. D., Syvitski J. P. M. (1992) Geomorphotectonic control of sediment discharge to the oceans: the importance of small mountain river, J. Geol., 100, 525-544, https://doi.org/10.1086/629606.
- Minh N. N., Marchesiello P., Lyard F., Ouillon S., Cambon G., Allain D., Dinh V. U. (2014) Tidal characteristics of the gulf of Tonkin, Cont. Shelf Res., 91, 37-56, http://dx.doi.org/10.1016/j.csr.2014.08.003.
- Ministry of Agriculture and Rural Development. Research application on the use of MIKE21 model to assess, predict and prevent riverbank erosion (north, central and south Vietnam). Technical report of the project 2006-2008 of the Ministry of Agriculture and Rural Development, 2009, Hanoi, Vietnam.
- Ni Y., Harff J., Xia J., Waniek J. J., Endler M. Schulz-Bull D. E (2016) Post-glacial mud depocentre in the southern Beibu Gulf: acoustic features and sedimentary environment evolution. In: River-Dominated Shelf Sediments of East Asian Seas (Eds P.D. Clift, J. Harff, J. Wu and Q. Yan), Geological Society Special Publication, 429, 87-98.
- Niino H., Emery K. O. (1961) Sediments of shallow portions of East China Sea and South China Sea. Geol. Soc. Am. Bull., 72, 731-762, https://doi.org/10.1130/0016-7606(1961)72[731:SOSPOE]2.0.CO;2. Nittrouer C. A., Wright L. D. (1994) Transport of particles across continental shelves, Rev. Geophys., 32, 85-133, doi: 10.1029/93RG02603.
- Nugroho D., Koch-Larrouy A., Gaspar P., Lyard F., Reffray G., Tranchant B. (2018) Modelling explicit tides in the Indonesian seas: An important process for surface sea water properties, Mar. Poll. Bull., 131, 7-18, http://dx.doir.org/10.1016/j.marpolbul.2017.06.033.
- Olsen C. R., Simpson H. J., Bopp R. F., Williams S. C., Peng T. H., Deck B. L. (1978) A geochemical analysis of the sediments and sedimentation in the Hudson estuary. J. Sediment. Petrol., 48, 401-418, https://doi.org/10.1306/212F7496-2B24-11D7-8648000102C1865D.
- Othman M. A. (1994) Value of mangroves in coastal protection, Hydrobiologie, 285, 277-276, doi: 10.1007/BF00005674.
- Peng D., Palanisamy H., Cazenave A., Meyssignac B. (2013), Interannual Sea Level Variations in the South China Sea over 1950-2009, Mar. Geod., 36: 164-182, doi: http://dx.doi.org/10.1080/01490419.2013.771595.
- Quynh D. N., Ninh P. V., Manh V. M., Lien N. T. V. (1998) The typhoon surges in Vietnam: the regime characteristics and prediction. Center for Marine Environment, Survey, Research, Consultation, 5th Asean Science and Technology Week, Hanoi, Vietnam. 178-194.
- Räsänen T. A., Kummu M. (2013) Spatiotemporal influences of ENSO on precipitation and flood pulse in the Mekong River Basin, J of Hydrol., 476, 154-168, doi: http://dx.doi.org/10.1016/j.hydrol.2012.10.028.
- Räsänen T. A., Lindgren V., Guillaume J. H. A., Buckley B. M., Kummu M. (2016) On the spatial and temporal variability of ENSO precipitation and drought teleconnection in mainland

Southeast Asia, Clim. Past., 12, 1889-1905, doi: 10.5194/cp-12-1889-2016.

- Reeve D., Chadwick S., Fleming C. (2004) Coastal engineering-processes, theory and design practice. New-York: Spon Press.
- Ribbe J., Holloway P. E. (2001) A model of suspended sediment transport by internal tides, Cont. Shelf Res., 21, 395-422, https://doi.org/10.1016/S0278-4343(00)00081-9.
- Rong Z., Liu Y., Zong H., Cheng Y. (2007) Interannual sea level variability in the South China Sea and its response to ENSO, Glob. Planet. Change, 55, 257-272, doi: http://dx.doi.org/10.1016/j.gloplacha.2006.08.001.
- Schubel J. R. (1968) Turbidity maximum of the northern Chesapeake Bay, Science, 161, 1013-1015, doi: 10.1126/science.161.3845.1013.
- Sottolichio A., Le Hir P., Castaing P. (2000) Modeling mechanisms for the stability of the turbidity maximum in the Gironde estuary, France, Proc. Mar. Sci., 3, 373-386, https://doi.org/10.1016/S1568-2692(00)80132-1.
- Stanley J. D., Warne A. G. (1998) Nile Delta in its destructive phase. J. Coast. Res., 14, 794-825.
- Steffen W., Sanderson R. A., Tyson P. D., Jäger J., Matson P. A., Moore III B., Oldfield F., Richardson K., Schellnhuber H. -J., Turner B.L., Wasson R.J. (2004) Global Change and the Earth System: A Planet under Pressure, Global Change - The IGBP Series, Springer.
- Stephenson W. (2013) Coastal erosion. In Bobrowsky, P. T. ed., Encyclopedia of Natural Hazards, Springer Dordrecht, New, 1135 pp.
- Stewart R. H (2008a) Introduction to physical oceanography, Orange Grove.
- Tan C. H. (1987) Preliminary analysis of hydrologic structure and hydrologic feature in the sea region of the Beibu Gulf, Trans. Oceanol. Limnol., 4, 7-15.
- Stramski D., Boss E., Bogucki D., Voss K. J. (2004) The role of seawater constituents in light backscattering in the Ocean, Progr. Oceanogr., 61(1), 27-56, doi: 10.1016/j.ocean.2004.07.001.
- Sun H., Huang W., Zhao J. S. (2001) Three-dimensional numerical simulation for tide and tidal current in the Beibu Gulf. Acta Oceanologica Sinica. 23(2): 1-8.
- Syvitski J. P. M., Vörösmarty C., Kettner A. J., Green P. (2005) Impact of humans on the flux of terrestrial sediment to the global coastal ocean, Science, 308, 376-380, doi: 10.1126/science.1109454.
- Tan W., Wang X., Wang W., Wang C., Zuo J. (2016) Different responses of sea surface temperature in the South China Sea to various El Niño events during boreal autumn, J. Clim., 29(3), 1127-1142, doi: 10.1175/JCLI-D-15-0338.1.
- Tanabe S., Hori K., Saito Y., Haruyama S., Vu V. P., Kitamura A. (2003) Song Hong (Red River) delta evolution related to millenium-scale Holocene sea-level changes, Quatern. Sci. Rev., 2345-2361, https://doi.org/10.1016/S0277-3791(03)00138-0.
- Tanabe S., Saito Y., Vu Q. L., Hanebuth T. J. J., Kitamura A., Ngo Q. T. (2005) Holocene evolution of the Song Hong (Red River) delta system, northern Vietnam, Sediment. Geol., 29-61, https://doi.org/10.1016/j.sedgeo.2005.12.004.
- Thampanya U., Vermaat J. E., Sinsakul S., Panapitukkul N. (2006) Coastal erosion and mangrove progradation of Southern Thailand, Estuar. Coast. Shelf Sci., 68, 75-85, https://doi.org/10.1016/j.ecss.2006.01.011.
- Thanh T.D., Lan T. D., Dinh V. H. (1997) Natural and Human Impact on the Coastal Development of Red River Delta, the LOICZ Open Science Meeting.
- Tseng Y. H., Jan S., Dietrich D. E., Lin I. I., Chang Y. T., Tang T. Y. (2010) Modeled oceanic response and sea surface cooling to typhoon Kai-Tak, Terr. Atmos. Ocean. Sci., 21(1), 85-98, doi: 10.3319/TAO.2009.06.08.02(IWNOP).
- Tong Si Son: Mapping tidal flats in Vietnam using remote sensing techniques, PhD thesis, Univ. de Reims Champagne-Ardenne (in French), 2016.
- Ueberman A. S., O'Neill Jr C. R. (1988) Vegetation use in coastal ecosystems. Cornell Cooperative Extension Information Bulletin 198, Cornell University, Ithica, New York, 32 pp.
- Uncles R. J, Stephens J. A., Harris C. (2006) Runoff and tidal influences on the estuarine tur-

bidity maximum of a highly turbid system: The upper Humber and Ouse Estuary, UK, Mar. Geol., 235, 213-228, https://doi.org/10.1016/j.margeo.2006.10.015.

- van Leussen W. (1994) Estuarine macroflocs and their role in fine-grained sediment transport. PhD thesis, Universiteit van Utrecht, The Netherlands.
- van Maren D. S.(2004) Morphodynamics of a cyclic prograding delta: the Red River, Vietnam, PhD thesis, Utrecht University, Netherlands Geographical Studies 324, Utrecht, 167 pp.
- van Maren D. S. (2007) Water and sediment dynamics in the Red River mouth and adjacent coastal zone, J. Asian Earth Sci., 29: 508-522, https://doi.org/10.1016/j.jseaes.2006.03.012
- van Maren D. S., Hoekstra P. (2004) Seasonal variation of hydrodynamics and sediment dynamics in a shallow subtropical estuary: the Ba Lat River, Vietnam, Estuar. Coastal Shelf Sci., 60(3), 529-540, https://doi.org/10.1016/j.ecss.2004.02.011.
- van Maren D. S., Hoekstra P., Hoitink A. J. F. (2004) Tidal flow asymmetry in the diurnal regime: bed-load transport and morphologic changes around the Red River Delta. Ocean Dynam., 54: 424-434., doi: 10.1007/s10236-003-0085-0.
- Vinh T.T., Kant G., Huan N. N., Pruszak Z. (1996) Sea Dike Erosion and Coastal Retreat at Nam Ha Province, Vietnam. International Coastal Engineering Conference, Am. Soc. Civil Eng., 2820-2828.
- Vinh V. D., Ouillon S., Thanh T. D., Chu L. V. (2014) Impact of the Hoa Binh dam (Vietnam) on water and sediment budgets in the Red River basin and delta, Hydrol. Earth Sci., 18: 3987-4005, doi: 10.5194/hess-18-3987-2014.
- Vinh V. D. (2012) Study characteristics of suspended sediment transport in Hai Phong coastal area by Delft3D model. Master thesis, Hanoi University of Science, Vietnam.
- Vinh V. D. (2018) Suspended sediment dynamics in Red River distributaries and along the Red River delta: Focus on estuarine processes and recent balances, University of Sciences and Technology of Hanoi, Hanoi, Vietnam.
- Vinh V. D., S. Ouillon, D. V. Uu. (2018) Estuarine Turbidity Maxima and Variations of Aggregate Parameters in the Cam-Nam Trieu Estuary, North Vietnam, in Early Wet Season, Water, 68, 1-33. doi: 10.3390/w10010068.
- Vörösmarty C. J., Meybeck M., Fekete B., Sharma K., Green P., Syvitski J. P. M. (2003) Anthropogenic sediment retention: major global impact from registered river impoundments, Glob. Planet. Change, 39, 169-190, https://doi.org/10.1016/S0921-8181(03)00023-7.
- Walstra D. J. R., Hoekstra R., Tonnon P. K., Ruessink B. G. (2013) Input reduction for long-term morphodynamic simulation in wave-dominated coastal settings. Coastal Engineer., 77, 57-70,https://doi.org/10.1016/j.coastaleng.2013.02.001.
- Wang B., LinHo L. H (2002) Rainy season of the Asian-Pacific summer monsoon. J. Climate., 15, 386-398, doi: http://dx.doi.org/10.1175/15200442(2002)015<0383:RSOTAP>2.0.CO;2.
- Wang C., Wang W., Wang D., Wang Q. (2006), Interannual variability of the South China Sea associated with El Niño, J. Geophys. Res., 111: C03023, doi: 10.1029/2005JC003333.
- Wang G., Chen D., Su J. (2006b) Generation and life cycle of the dipole in the South China Sea summer circulation, J. Geophys. Res. Ocean., 111(6), 1-9, doi:10.1029/2005JC003314.
- Wang H. J., He S. P. (2012) Weakening relationship between East Asian winter monsoon and ENSO after mid-1970s, Chinese Sci. Bull., 57(27), 3535-3540, doi: 10.1007/s11434-012-5285-x.
- Wang H. J., Yang Z. S., Saito Y., Liu J. P., Sun X., Wang Y. (2007) Stepwise decreases of the Huanghe (Yellow River) sediment load (1950-2005): impacts of climate changes and human activities, Global Planet. Change, 57, 331-354, doi:10.1016/j.glopacha.2007.01.003.
- Wang H. J., Yang Z. S., Wang Y., Saito Y., Liu J. P. (2008) Reconstruction of sediment flux from the Changjiang (Yangtze River) to the sea since the 1860s, J. Hydrology, 349, 318-332, https://doi.org/10.1016/j.jhydrol.2007.11.005.

- Wei, X., S. Sauvage, T. P. Q. Le, S. Ouillon, D. Orange, V. D. Vinh and J. -M Sanchez-Perez. 2019. A Modeling Approach to Diagnose the Impacts of Global Changes on Discharge and Suspended Sediment Concentration within the Red River Basin. Water 11: 958. doi:10.3390/w11050958

- Wetzel A., Szczygielski A., Unverricht D., Stattegger K. (2017) Sedimentological and ichnological implications of rapid Holocen flooding of a gently sloping mud-dominated incised valley – an example from the Red River (Gulf of Tonkin), Sedimentology, 64, 1173-1202, doi: 10.1111/sed.12357.

- Wolanski E., Gibbs R. J. (1995) Flocculation of suspended sediment in the Fly River Estuary, Papua New Guinea, J. Coast. Res., 11(3), 754-762, https://www.jstor.org/stable/4298378.

- Wolanski E., Spagnol S. (2003) Dynamics of the turbidity maximum in King Sound tropical Western Australia. Estuar. Coastal Shelf Sci., 56, 877-890, https://doi.org/10.1016/S0272-7714(02)00214-7.

- Wu C. R., Chang C. W. K. (2005) Interannual variability of the South China Sea in a data assimilation model, Geophys. Res. Lett., 32(17),1-4, doi: 10.1029/2005GL023798.

- Wyrtki K. (1961) Physical oceanography of the Southeast Asian waters. Naga Rep. 2, 195 pp. [Available from: https://escholarship.org/uc/item/49n9x3t4].

- Xia H. Y., Li S. H., Shi M. C. (2001) Three-D numerical simulation of wind-driven current and density current in the Beibu Gulf. Acta Oceanol. Sin.. 20: 455-472.

- Xu X. (1982) The general descriptions of the horizontal circulation in the South China Sea, in Proceedings of the 1980 Symposium on Hydrometeorology, Chinese Society of Oceanology and Limnology, pp. 137-145, Science Press.

- Xue Z., Liu J. P., Ge Q. (2011) Changes in hydrology and sediment delivery of the Mekong River in the last 50 years: connection to damming, monsoon, and ENSO, Earth Surf. Proc. Land., 36: 296-308, doi: 10.1002/esp.2036.

- Yang S. Y., Bao X. W., Chen C. S. et al. (2003) Analysis on characteristics and mechanism of current system in west coast of Guangdong Province in the summer. Acta Oceanol. Sin., 25(6): 1-8 (in Chinese with English abstract).

- Yang Y., Xie S.-P., Du Y., Tokinaga H. (2015) Interdecadal difference of interannual variability characteristics of South China Sea SSTs associated with ENSO, Amer. Meteor. Soc. 28: 7145-7160, doi:10.1175/JCLI-D-15-0057.1

- Ye A.L., Robinson I. S.(1983) Tidal dynamics in the South China Sea, Geophys. J. Roy. Astronom. Soc., 72, 691-707.

- Yu M.G., Liu J. F (1993) South China Sea circulation system and situation. Mar. Forecasts, 10, 13 -17.

- Yuan S. Y., Deng J. Z. (1999) Numerical research in the circulation in the Beibu Gulf. Nanhai Yanjiu Yu Kaifa, 2, pp. 41-6 (in Chinese with English abstract).

- Yuan Y., Yang H., Zhou W., Li C. (2008) Influences of the Indian Ocean Dipole on the asian summer monsoon in the following year, Int. J. Climatol., 28(14),1849-1859, doi:10.1002/joc.1678.

- Zhang L., Wang B., Zeng Q. (2009) Impact of the Madden-Julian oscillation on summer rainfall in the Southeast China, J. Clim., 22(2), 201-216, doi: 10.1175/2008JCLI1959.1.

- Zhou G., Huang J., Yue T., Luo Q., Zhang G. (2014) Temporal-spatial distribution of wave energy: A case study of Beibu Gulf, China. Renewable Energy, 74, 344-356. doi: http://dx.doi.org/10.1016/j.renene.2014.08.2014.

Chapter II

Study of the seasonal and tidal variability of the hydrology and suspended particulate matter in the Red River estuary with observations

Contents

II.1   Summary of Chapter II

In previous Chapter I, we have seen that the sediment transport and fate in the RRD-GoT system, and the evolution of the Red River delta in terms of siltation, erosion and accretion of its estuaries and coastlines constitute a major concern. As tides and seasonal variations in river discharges are decisive in both estuarine hydrodynamics and estuarine sediment processes, it is crucial to understand and quantify their impacts on hydro-sedimentary processes in the Red River estuary. This chapter aims at documenting the variability of the flow and suspended matter dynamics induced by those variations based on in-situ measurements. Along-estuary hydro-sedimentary processes are studied during a full diurnal tidal cycle (from neap to spring tides) and from the dry season (low river discharges) to the wet season (high water discharges). Results of this chapter are based on in-situ observations collected during 4 field campaigns (including each one tidal cycle) at 3 stations along the Van Uc River estuary, one of the main tributaries of the Red River delta, which has never been sampled before. This particular estuary of the Red River was chosen as it is a typical distributary of the system, with rice crops all along the banks that require water and construction of soil dykes for flood protection, and with constant river bed dredging for both navigable waterways and selling purposes. Above all, the Van Uc estuary is an interesting site to study estuarine dynamics because this meso- to macrotidal estuary (maximum tidal range: 4m) is both influenced by a strong seasonal river signal and a monsoon regime.

These observations reveal that the water and sediment discharges of the Van Uc river undergo a comprehensive regime change between high-seasonal (wet season) and low-seasonal (dry season) discharges, with mixed estuarine conditions during the high-flow season and stratified estuarine conditions during the low-flow season. The study of the flow shows that the seasonal discharges are affected by the neap-spring cycle with different effects between the seasons. For example, only spring tides at high tide can reverse the high downstream river flow of the wet season, while both neap and spring tides affect the flow direction during the dry season. Results of the decomposition of the suspended matter flux reveal that the riverine down-estuary component is the most important during high flow season while gravitational and tidal processes, like local resuspension, are most important during low flow season. Indeed, up-estuary suspended matter flux appears to account for 2/3 of the down-estuary flux in the low-flow season, which indicates that the estuary is silting up and the delta is consolidating mainly during the dry season. The distortion of the tide wave in spring tide is emphasized as the potential dominant process explaining the up-estuary sediment mobility in wet season at spring tide during flood.

Besides complementing knowledge on the Red River estuarine dynamics, these surveys were conceived to provide a new benchmark for future model calibration/validation. Indeed, this chapter constitutes the first step of this Ph.D. work in understanding estuarine dynamics and set the basis of the modeling work for the study of transport and fate of sediments from the Red River to the GoT.

II.2 Article under review in Journal of Marine Systems Seasonal and tidal variability of the hydrology and suspended particulate matter in the Van Uc estuary, Red River, Vietnam

Violaine Piton[1,2], Sylvain Ouillon[1,2], Vu Duy Vinh[2,3], Gaël Many[4], Marine Herrmann[1,2], Patrick Marsaleix[4]

[1] LEGOS, IRD, UMR556 IRD/CNES/ CNRS/Université de Toulouse, 31400 Toulouse, France

[2] LOTUS Laboratory, University of Science and Technology of Hanoi (USTH), Vietnam Academy of Science and Technology (VAST), 18 Hoang Quoc Viet, Cau Giay, Hanoi, Vietnam

[3] Institute of Marine Environment and Resources, VAST, Haiphong city, Vietnam.

[4] LA, CNRS, Université de Toulouse, 31400 Toulouse, France

Corresponding author: violaine.piton@legos.obs-mip.fr

Submitted to Journal of Marine Systems.

Abstract

This study explores the seasonal and tidal changes in flow and suspended matter dynamics in the tropical and macrotidal Van Uc River estuary (North Vietnam) and aims at understanding, among others, the sediment delivery to the ocean and the processes behind the estuary siltation. Four campaigns took place during the contrasting high flow and low flow seasons, for each during neap and spring tides. Water and suspended matter fluxes, salinity, turbidity and suspended sediment concentrations were measured for 24h at three cross sections along the estuary. During the high-flow season, the estuary was mixed, with seaward sediment flux during neap tide and ephemeral up-estuary sediment flux at spring tides due to tidal distortion. During the low-flow

season, the system transitioned from partially mixed to highly stratified with salty waters intrusions, salt wedge presence and up-estuary sediment flux varying with the tidal regime. Estuarine siltation mostly occurred during low-flow at spring tides with a suspended matter inflow, primarily due to local resuspension, which represented 2/3 of the outflow. These findings also provide a new benchmark for hydro-sedimentary model calibration/validation.

Keywords:suspended sediments, estuary, estuarine turbidity maximum, neap/spring tide cycle, Red River, Vietnam

II.2.1   Introduction

Estuaries are links between land and ocean where freshwater coming from the rivers mixes with saline oceanic water (Wolanski et al., 2013). They are typically characterized by strong gradients of salinity, temperature, water surface level and suspended sediment concentrations (Priya et al., 2012; Jay et al. 2014), and contribute to a high amount of sediments, nutrients and contaminants input to the ocean (Milliman, 1991; Meybeck, 1993). These transitional zones are never at a steady state, experiencing a variability at longer time scale from the river basin (interannual to seasonal) than from the ocean. Since the effects of tidal currents on the salt and momentum balances in estuaries were recognized by Pritchard (1954, 1956), tides indeed are known to play a key role in estuarine dynamics. Affecting mixing, influencing a stronger or weaker stratification depending on the sea water intrusion, and determining the characteristics of the water masses that can interact with the shelf circulation, tidal and neap-spring cycles are amongst the main drivers of estuarine dynamics (Geyer and MacCready, 2014). In some cases, estuarine waters may appear being well-mixed during flood and being stratified during ebb (Simpson et al., 1990; Jay and Smith, 1990a). Also, the residual circulation, the turbulent mixing (Simpson et al., 1990; Geyer et al., 2000) and the along-estuary circulation (Lai et al., 2018) appeared to vary in response to the spring-neap cycle.

The evolution of the Red River delta in terms of siltation, erosion and accretion of its estuaries and coastlines constitute a major concern, as the delta is the most populated region of Vietnam, and is the second-most important rice-producing region of the country. The Red River was ranked as the ninth river in the world in terms of sediment discharge but the construction of two dams across the river in the 1980s caused a reduction of sediment discharges from 145-160 Mt y^{-1} in the 1970s (Milliman and Meade, 1983) to 40 Mt y^{-1} nowadays (Le et al., 2007; Vinh et al. 2014; Wei et al., 2019). Changes in water regulation due to the dams, induced an increasing siltation of the harbour of Hai Phong, which is the second biggest harbour of the country and connects north-

ern Vietnam to the world market. Such phenomenon forces an increasing dredging effort each year, with 6.6 million US $ spent on dredging activities in 2013 (Vietnam maritime administration 2017). Recent studies have arisen from this issue, and the tidal pumping has been pointed out as one of the physical processes responsible for the siltation, by creating a net upstream transport of sediments in the dry season, which settled in a near bed layer at low turbulent energy (Lefebvre et al., 2012). In the Cam-Nam Trieu estuary, the Estuarine Turbidity Maxima (ETM, mass of highly concentrated suspended sediments) was shown to start developing at salinities as low as 0.1 PSU (Vinh et al., 2018) and bio-aggregation was shown to be enhanced at salinity around 10-15 PSU due to increasing stickiness properties of bio-exopolymeric substances (Mari et al., 2012). In the coastal zone, the decrease of the suspended sediment loads caused alternative patterns of erosion and accretion to develop. For example, the Ba Lat River mouth (Fig. II.1) has expended seaward due to a combined effect of sediment resuspension by wave actions and river floods (van Maren et al., 2007), and increased turbidity was observed in the touristic region of Do Son, while Hai Hau coasts have experienced a severe erosion of several meters per year. In this context, investigating the fine scale physical processes in estuaries and in their regions of influence is of particular interest for better understanding the Red River system.

The Van Uc River (Fig. II.1) is a typical distributary of the Red River, with rice crops all along the banks that require water and construction of soil dykes for flooding protection, and with constant river bed dredging for both navigable waterways and selling purposes. It is ranked at the third position of the Red River system in terms of both water and sediment discharges. (Vinh et al., 2014). Above all, the Van Uc estuary is an interesting site to study estuarine dynamics because this meso- to macrotidal estuary (maximum tidal range: 4m) is both influenced by a strong seasonal river signal and a monsoon regime. Using the MIKE11 numerical model, Vinh et al. (2014) estimated that 70 % of the annual water discharges were issued in the wet season (June-October) while 16 % were issued in the dry season (December-April), the 14 % remaining being issued in intermediate periods (May and November). For the sediment discharges, 86 % of the total annual discharges were issued in the wet season, against 4 % in the dry season (10% were issued in the intermediate seasons). If seasonal budgets of water and sediments are globally known, forced by the river inputs (Vinh et al., 2014), if seasonal variations of hydrology (water flux, salinity, stratification) and suspended matter was described at one station in the Ba Lat river mouth (Fig. II.1) (van Maren, 2004) and if transects along the estuaries of the Red River tributaries were described at different seasons at spring tides (Vinh et al., 2018), no effort has been initiated so far to document the hydrology

and the suspended matter dynamics of Red River estuaries in terms of tidal variability. This question represents the central objective of the present study, which aims at documenting the lack of knowledge regarding the hydro-sedimentary processes in the Red River.

Based on new *in situ* data, this paper focuses on the analysis of the hydrology and on the characteristics of the suspended particulate matter at different seasons and tidal cycles, along the Van Uc estuary. It is the first step of a more comprehensive modeling study that aims at further analyze the transport and fate of sediments from the Red River to the Gulf of Tonkin, using the hydrodynamical-sediment transport model SYMPHONIE-MUSTANG (Marsaleix et al., 2008; Le Hir et al., 2011) that is configured for the region. Hence, the choice of the parameters studied was made in a modelling perspective.

In Section II.2.2, the estuary of interest is presented and in Section II.2.3, field campaigns and methodologies for data sampling, instruments calibrations and data analyses are described. In Section II.2.4, findings on water and sediment fluxes, water column stratification and particles properties, which are largely impacted by the lunar tidal cycle and related circulation are detailed. The dynamical mechanisms that can explain these results are discussed in Section II.2.5: in particular the distinct effects of gravitational circulation and of the along-estuary tidal distortion on sediment fluxes and deposition.

II.2.2   Regional settings - The Van Uc estuary

The Van Uc estuary is located next to Hai Phong city (the third largest city of Vietnam), northeast of Vietnam (Fig. II.1). The estuary is fed with fresh water and sediments by the Van Uc river, one of the nine tributaries of the Red River, which receives water and sediments from both the Red River, through the Duong River, and from the Thai Binh River through a complex network of connections within the Red River Delta (see Vinh et al., 2014). The total river discharge through the Van Uc estuary was estimated of about $17.7 \; 10^9$ m^3 y^{-1} (for the period 1989-2010), which corresponds to 14.5 % of the total water discharge from the Red-Thai Binh system to the Gulf of Tonkin (Vinh et al. 2014). These authors also evaluated the sediment fluxes and found a drastic drop in the annual fluxes due to the Hoa Binh dam impoundment in the 1980s (from 11.5 to 5.1 Mt y^{-1}). The Van Uc sediment flux represents 14.4 % of the total sediment flux of the Red-Thai Binh River to the Red River coastal area and is therefore the third most important distributary of the Red River Delta in terms of river and sediment discharges (after the Day and the Ba Lat rivers).

The Van Uc estuary is subjected to the South-East Asian sub-tropical monsoon climate (Wyrtki 1961), that is characterized by an alternation of a southwest summer monsoon and a northeast winter monsoon. The wet summer season (June to September) accounts for 85-95% of the total annual rainfall in the region (~ 1161 mm) and is dominated at 72% by winds blowing from the South-West. In the dry winter season, the winds blow at 92% from the North-East and bring cold and dry conditions over the region (Vinh et al., 2018). The seasonal variation of the Red River hydrological regime is therefore strong and largely influences the Van Uc estuary. Vinh et al. (2014) showed that 71-79% of the annual total water discharge of the Van Uc River was brought to the coastal zone during the wet season and only 9-18% in the dry season (December to March).

The South China Sea and the Gulf of Tonkin are one of the few regions in the world where diurnal tides dominate the semidiurnal tides (Fang, 1986). Wyrtki (1961) was the first to identify the main tidal constituents in the South China Sea: O1, K1, M2, S2 (classified by their importance in amplitudes). The diurnal tide dominates due to a double resonance: in the South China Sea because of Helmholtz resonance (Zu et al., 2008), then in the Gulf of Tonkin, higher for O1 than K1 due to a resonant peak period of 29h (Nguyen et al., 2014). The tide gauge measurements next to the Van Uc River mouth (at Hon Dau, Fig. II.1) show a tidal amplitude of about 0.5-1.0 m in neap tides and of about 2.6-3.6 m in spring tides.

II.2.3 Material & Methods

II.2.3.1 Field data and sampling procedure

Four field surveys were performed in the Van Uc estuary during neap and spring tides in the wet and dry seasons. Surveys are noted WN for wet season at neap tide, WS for wet season at spring tide, DN and DS for surveys in the dry season at neap tide and spring tide, respectively. The dates of each survey with corresponding tidal cycles and seasons are listed in Table II.1

Three stations (ST1, ST2 and ST3) spaced by 10 km were selected for sampling (Fig. II.1). ST1 is located next to the river mouth while ST3 is the further upstream. Each station was sampled during 24 hours with cross-river transects measurements every two hours to cover a full diurnal cycle, starting at ST1 and finishing at ST3. Each series of measurements consisted of four different steps. Firstly, cross river velocity profiles were measured with a hull-mounted, downward-looking, 1200 kHz Acoustic Doppler Current Profiler (ADCP RDI Workhorse in bottom tracking mode). Current magnitude and direction were measured in depth cells of 0.25 m with a range of 15 m using a fre-

quency of 0.2 Hz. Secondly, vertical profiles of conductivity and temperature were measured for each transect, in the deep channel at the middle of the river, using a profiling CTD Compact-CTD (ASTD687, Alec Electronics Co., Nishinomiya, Japan, now released by JFE Advantech Co., Nishinomiya, Japan, as Rinko-Profiler). Thirdly and parallel to CTD measurements, depth profiles of floc size distribution and concentration were measured using an *in situ* laser scattering and transmissometry instrument with a 90% path reduction module (LISST-100X, type B, Sequoia Scientific Inc., Bellevue, WA, USA). The LISST-100X determines the volumetric particulate concentration in 32 logarithmically spaced size classes from 1.25 to 250 µm and uses a red laser (660 nm) through a path of 5 cm with a sampling rate of 1 Hz. In order to study the relationship between turbidity and suspended particulate matter concentration, water samples (of ~ 1 l) near subsurface (at ~ 1.5 m depth) were also collected every four hours (i.e. every two CTD deployments) with a Niskin bottle. Turbidity of these samples were measured onboard using a Hach 2100Q Turbidimeter.

Data at the hydrographic station Trung Trang (Fig. II.1), provided by the National Hydro-Meteorological Service (NHMS), were also used in this study. They include hourly water discharges and water elevations.
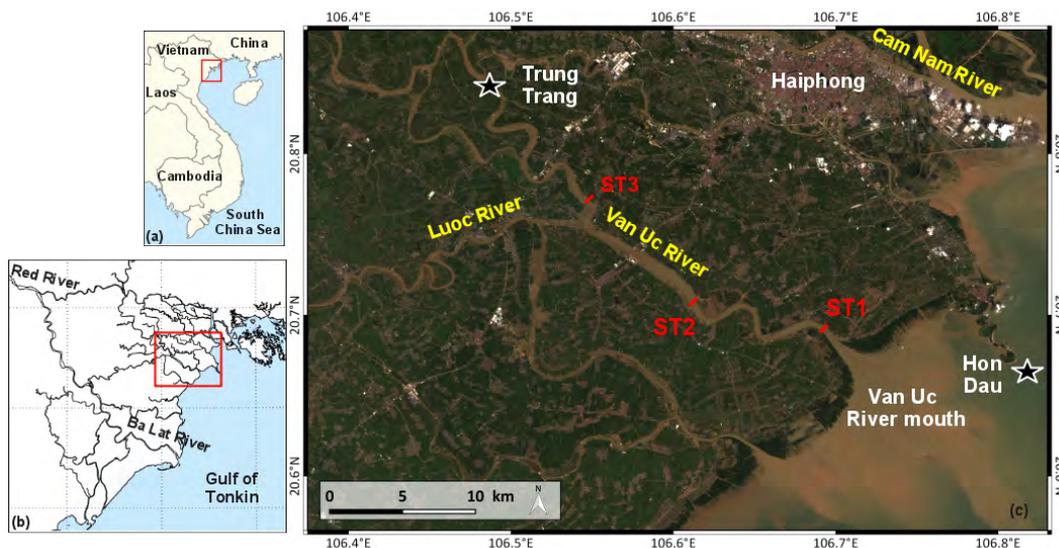
Figure II.1: Location of stations ST1, ST2 and ST3 (in red) in the Van Uc River and of Trung Trang and Hon Dau hydrological stations (black star) (Landsat 8 image from September 29, 2017).

II.2.3.2   Hydrological parameters

Salinity and density were derived from CTD data (temperature and conductivity) following general UNESCO polynomial relationship (UNESCO, 1983).

Survey name	WN			WS			DS			DN		
station	ST1	ST2	ST3	ST1	ST2	ST3	ST1	ST2	ST3	ST1	ST2	ST3
Dates (of 2017)	26/08	27/08	28/08	03/09	04/09	05/09	06/12	07/12	08/12	12/12	13/12	14/12
season	wet			wet			dry			dry		
regime	neap			spring			spring			neap		

Table II.1: Van Uc surveys characteristics and dates of sampling. Each sampling started at 8 am and finished at 6 am the following day.

The Brunt-Vaisala frequency N^2 (in s^{-2}), also known as the buoyancy frequency, was computed from the density depth-profiles and used as an indicator of the water column stratification:

$$N^2 = \frac{-g}{\rho}\frac{\delta\rho}{\delta z} \qquad\qquad (II.1)$$

where g is the acceleration of gravity ($m^2\,s^{-1}$) and ρ the potential water density ($kg\,m^{-3}$). A stable stratification is considered when $N^2 > 0$, while a stratification is considered unstable when $N^2 \sim 0$ (Turner, 1973).

The dimensionless Richardson number (R_i), which is used as a criterion for assessing the stability of stratified shear flow through energy consideration, is computed by comparing N^2 to the vertical gradient of the horizontal current velocities ($\frac{\delta V}{\delta z}$) from ADCP data (Pacanowski and Philander, 1981), as:

$$R_i = \frac{N^2}{\left(\frac{\delta V}{\delta z}\right)^2} \qquad\qquad (II.2)$$

When $R_i \geq 0.25$, the flow is considered stable and if $R_i < 0.25$, the turbulence overcomes the density stratification and generates vertical mixing (Miranda et al., 2002; Kirinus et al., 2002).

Furthermore, the Simpson parameter gives the potential energy ϕ (in $J\,m^{-3}$) that represents the mechanical energy required to completely mix the water column. This parameter was used to quantitatively analyze the physical mechanisms contributing to mixing and stratification in an estuary (Simpson et al. 1978) and was computed as follows:

$$\phi = \frac{1}{H} \int_{-H}^{0} gz\left(\overline{\rho} - \rho\right) \delta z \qquad \text{(II.3)}$$

with H, the water column depth.

II.2.3.3   Water currents and derived water discharges

The ADCP transmits high frequency acoustic signals (pings), that are backscattered from water constituents of different origins: suspended sediment, phyto/zooplankton and bubbles. These constituents are assumed to travel with the speed of water and therefore, the current velocity (horizontal and vertical) and the current direction as a function of depth are estimated through the Doppler effect. Following the recommendations of Mueller et al. (2013), water discharges (noted $Q_{Measured}$) were computed using the measured water velocities (noted V_w) and the boat velocities (noted V_b):

$$Q_{Bin} = (V_{wu}V_{bv} - V_{wv}V_{bu})\, dt\, dz \qquad \text{(II.4a)}$$

$$Q_{Measured} = \sum_{j=1}^{Ensembles} \sum_{i=1}^{Bins} Q_{Bin} \qquad \text{(II.4b)}$$

where V_{wu} and V_{wv} correspond to the meridional and zonal water velocities, respectively, and V_{bu} and V_{bv} correspond to the meridional and zonal boat velocities, respectively. Q_{Bin} (in $m^3\ s^{-1}$) was computed for each ensemble (i.e. time between two measurements) dt (5 s) and for each vertical bin dz (0.25 m). As recommended by Mueller et al. (2013), the total water discharge Q_{ADCP} of the river is the sum of $Q_{Measured}$ and the water discharges estimated in the unmeasured zones by the ADCP (i.e. the top and bottom layers and the right and left edges of the river) as:

$$Q_{ADCP} = Q_{LeftEdge} + Q_{Top} + Q_{Measured} + Q_{Bottom} + Q_{RightEdge} \qquad \text{(II.5)}$$

Detailed descriptions and formulations of $Q_{LeftEdge}$, $Q_{RightEdge}$, Q_{Top} and Q_{Bottom} are available in Mueller et al. (2013) and were computed accordingly.

Furthermore, the flux throughout the water column can flow in opposite directions (downstream

or upstream), whether it is dominated by the river flow or by flood tides. Therefore, we chose to compute Q_{ADCP+} as the component of the flux flowing downstream and Q_{ADCP-} as the component of the flux flowing upstream. Note that the sum of Q_{ADCP+} and Q_{ADCP-} is equal to Q_{ADCP}.

II.2.3.4 Suspended particulate matter parameters

II.2.3.4.1 SPM concentration from water samples

Following the process proposed by Aminot and Kérouel (2004), the suspended particulate matter (SPM) concentrations were determined by filtering onboard a known volume of water (about 100-150 ml) per sample through two kinds of pre-weighed filters: polycarbonate Nuclepore filters (porosity 0.45 μm) and Whatman GF/F glass microfiber filters (porosity 0.7 μm). After filtration, filters were rinsed three times with 5.0 mL of milli-Q water to remove salt. Then, they were dried for 24 hours at 70° C in an oven and weighed on a high-precision electrobalance. The sediment concentration obtained after drying the filters is the total SPM concentration, called $SPM_{Filters}$ hereafter, including organic and inorganic matter.

The particulate inorganic matter concentration was measured after burning the GF/F filter at 450 °C during 4 hours: this process removes all the organic matter from the filter. The difference between the total $SPM_{Filters}$ and particulate inorganic matter provided the particulate organic matter concentration and thus the ratio of organic to inorganic matter (particulate organic matter/particulate inorganic matter) within the $SPM_{Filters}$.

II.2.3.4.2 Optical backscattering sensors (OBS)

Turbidity is an optical proxy of SPM concentration which is measured by nephelometers or optical backscattering sensors (OBS). The CTD was equipped with an OBS measuring in the infrared. The sensor outputs (in Formazin Turbidity Unit - FTU) were calibrated against gravimetric SPM concentrations measurements. The SPM concentrations measured by the CTD are called hereafter SPM_{OBS}.

II.2.3.4.3 ADCP's backscatter index

For the past twenty years, acoustic instruments such as ADCP, originally designed to measure velocity profiles, have been used to quantify SPM concentrations in ocean and coastal environments (Thorne and Hanes, 2002; Tessier et al., 2008; Le Coz et al., 2009). The measurement principle is based on the fact that the acoustic signal is emitted with an initial intensity, that progressively decreases as it travels through the water column, and which is backscattered by suspended particles.

Therefore, the intensity of the backscattered acoustic signal is a function of the quantity of the particles present in suspension in the environment. The acoustic method has the advantage of being non-intrusive.

In order to infer the particle load from the signal recorded by the ADCP, the sonar equation (in dB) was used. The sonar equation represents an energy balance that expresses a signal-to-noise ratio, taking into account the technical characteristics of the instrument. The received acoustic level (RL), can be expressed as follows (Deines, 1999; Lurton, 2002):

$$BI = RL + 2TL - SL \tag{II.6}$$

with SL, the source level emitted by the ADCP (in dB), TL the transmission loss due to attenuation of the acoustic wave within the ambient environment (in dB), and BI the backscatter index, which depends on the SPM concentration.

In our case and following the recommendation of Mullison (2017), the RL was computed as follows:

$$RL = 10log\left(10^{Kc\frac{(E-Er)}{10}} - 1\right) + Br \tag{II.7}$$

where Kc (in dB/counts) is the factor used to convert the amplitude reported by the ADCP, in counts, to decibels. E the backscattered intensity of the acoustic wave, which was measured by the instrument (in counts), Er the backscattered intensity signal, which is seen by the instrument in the absence of any signal (the noise) and Br, the associated pressure level furnished by the manufacturer (dB). In our case, since we will be looking at relative SPM concentrations, neglecting Br will not affect our results.

Two types of transmission losses can be estimated. One is associated to the spherical spreading, which corresponds to the decrease of the signal intensity as the signal travels away from the emission source. The other type of loss corresponds to the acoustic signal attenuation due to the ambient environment, i.e. the attenuation due to the water (α_w) and the attenuation due to the suspended particles characteristics (α_s). In the presence of particles, the total transmission loss, with a distance R from the emission source and ϕ the beam angle (20°), is expressed as follows:

$$TL = 20 log_{10} R + \int_0^R (\alpha_w(r) + \alpha_s(r)) \, dr \qquad (II.8)$$

with the along beam distance $R = \frac{d}{\cos\theta}$, where d is the bin vertical distance and θ is the beam angle (20◦). The attenuation coefficient α_w (dB m^{-1}) was estimated from the model of François and Garrison (1982a, 1982b). According to Tessier (2006), the particle attenuation α_s becomes significant when the SPM concentration is of the order of 200 mg l^{-1} for a 1200 kHz acoustic signal and fine particles. The concentrations of SPM measured during the surveys (estimated from CTD OBS profiling) were rather low in the dry season, and never exceeded 170 mg l^{-1} in the wet season. Therefore, the choice was made to neglect α_s in the calculation of the backscatter index (BI).

An accurate estimate of the acoustic source level (SL) emitted by the ADCP is difficult. It can either be obtained by laboratory calibrations of the instrument, or by using the average reference values provided by the manufacturer. Laboratory experiments showed that for a 1200 kHz ADCP, the values range from 216 to 218 dB (Tessier, 2006). Furthermore, the SL can vary with the battery voltage. This effect could infer a bias in the measurement, when using the manufacturer reference. In our case, the ADCP was not calibrated prior to the survey, and therefore SL is neglected. Again, since we only look at relative SPM concentrations, neglecting SL does not alter our results.

Lastly, the best regression relationship between SPM concentrations measured by optical backscattering (SPM$_{OBS}$) and BI is found to be linear between $10 log_{10}$(SPM) and BI. It is used to estimate SPM concentrations (in mg l^{-1}) from acoustic measurements (in dB), called SPM$_{AC}$ hereafter, following:

$$10 log_{10} (\text{SPM}_{AC}) = a\text{BI} + b \qquad (II.9)$$

with a and b the slope and the intercept of the linear regression.

However, the uncertainties associated with the different terms of the sonar equation remain important, and the calibration of the acoustic signal is done in practice by adjusting the slope.

II.2.3.4.4   Sediment discharges from ADCP

For each ensemble dt (5 s) and vertical bin dz (0.25 m), the sediment discharge (noted Q$_{BinSED}$)

was computed as the product of instantaneous Q_{ADCP} and SPM_{AC} as:

$$Q_{BinSED} = Q_{ADCP} \times SPM_{AC} \tag{II.10a}$$

and the total sediment discharge is then:

$$Q_{SED} = \sum_{j=1}^{Ensembles} \sum_{i=1}^{Bins} Q_{BinSED} \tag{II.10b}$$

Furthermore, $Q_{SED}+$ was computed as the component of the sediment flux flowing downstream and $Q_{SED}-$ as the component of the sediment flux flowing upstream. Note that the sum of $Q_{SED}+$ and $Q_{SED}-$ is equal to Q_{SED}.

II.2.3.4.5 Particles properties measurements from LISST

The laser diffraction spectrum, discretized over 32 classes, was first converted into a particulate volume concentration (in μl^{-1}) using the factory volume calibration constant. The sum of the contributions provided the SPM volume concentration (SPMVC). However, following the recommendation of Mikkelsen et al. (2005), the extreme size classes # 1, # 2, # 31 and # 32 were removed before calculating the SPMVC, the particle size distribution (PSD) and the mean apparent diameter (D_{50}). Indeed, in stratified waters, water masses have different densities and therefore different refractive indexes which can cause significant light scattering. This phenomenon is known and called the schlieren effect. The LISST probe detects the schlieren effect as an accumulation of large or small particles (i.e., the extreme classes of the spectrum) in the pycnocline (Styles 2006; Mikkelsen et al. 2008). In addition, the measurements for which peaks of particles in extreme classes occurred have been removed, as we found that schlieren effect happened to also contaminate classes as high as # 4 and as low as # 26. Based on data between classes # 3 (1.74 μm) and # 30 (179.53 μm), the particulate volume concentration was normalized by the width of each logarithmically-spaced class and gave the PSD (in $\mu\ l^{-1}$ μm). Then, D_{50} (in μm) was calculated as the diameter corresponding to 50% of the cumulative volume concentration of particles.

II.2.4 Results

The effects of seasonal, tidal and spatial forcings on various water column parameters were investigated. Water and sediment fluxes are presented in the first part. The second part is dedicated

to the hydrology and turbidity of the water column. Lastly, the suspended particulate matter variability is discussed.

II.2.4.1 Fluxes

II.2.4.1.1 Calibrations of the optical and acoustical SPM, SPMOBS and SPMAC

Calibrations of optical instruments must be carried out in environments where flocculation of fine grains/particles occurs and where hydrodynamics and grain types/particles properties are highly variable (Bunt et al., 1999). A linear regression was used between the OBS signal (i.e. the turbidity, in FTU) and the filtered $SPM_{Filters}$ concentration (in mg l^{-1}), for the wet season surveys and for the dry season surveys. The slope (a) and the intercept (b) of the fitted regression lines were a=0.90 and b=-9.84 for the wet season (R^2=0.96), and a=1.08 and b=-3.86 for the dry season (R^2=0.88). Based on these relationships, SPM_{OBS} concentrations were determined from the turbidity profiles, for each season.

The best-fit regression relationship between SPM_{OBS} and BI was used at each survey to derive SPM concentrations SPM_{AC} from the acoustic signal (Fig. II.2). The determination coefficient R^2 reflects the different sensitivity of optical and acoustic sensors to changes in SPM size and characteristics/properties. Indeed, backscattering is influenced by sediment type, size, color and composition, with optical and acoustical backscattering showing different sensitivities and responses to these parameters (Thorne et al., 1991; Fugate and Friedrichs, 2002; Voulgaris and Meyers, 2004; Downing 2006). Gartner and Cheng (2001) and Gartner (2002) showed that optical sensors are more sensitive to small particles while acoustic sensors are more sensitive to large particles. Furthermore, Kim and Voulgaris (2003) found a slight bias in the SPM_{AC} estimates when the sediment is silt or finer. Rouhnia et al. (2014) showed that the intensity of the backscattered acoustic signal from flocs is mainly affected by the flocculi (i.e the microflocs). However, flocs can have a smaller influence on the backscatter signal than sand grains of the same size, due to their lower density (Ha et al., 2011). Therefore, the SPM_{AC} should be considered with caution and as estimates only, rather than exact SPM measurements.

Good correlations between SPM_{OBS} and BI were found for surveys WN, WS and DS with R^2 of 0.83, 0.84 and 0.70, respectively (Fig. II.2 a, b, c). Only survey DN showed a poor correlation (0.04) between the datasets (Fig. II.2 d). Following the circulation and thermohaline conditions of the water column in survey DN (Fig. II.3 and see section II.2.4.2), the water column was, at some

specific tidal stages, divided in two water masses flowing in opposite direction. The choice was made to compute different calibrations for the top and bottom layers, and the boundary between the two layers was defined by the reversal in current direction. A good correlation was found for the bottom layer (0.85) (Fig 2 f), but a poor correlation remained in the top layer (0.13) (Fig. II.2 e). Therefore, for this particular case (top layer of the water column, survey DN), SPM_{AC} could not be estimated. As a first guess and instead of using Eq. II.10 b., the contribution of this layer to the sediment discharge Q_{SED} was computed as the product of the mean SPM_{OBS} with the mean Q_{ADCP} of the top layer of the water column. Results of these estimates are presented in the following section.
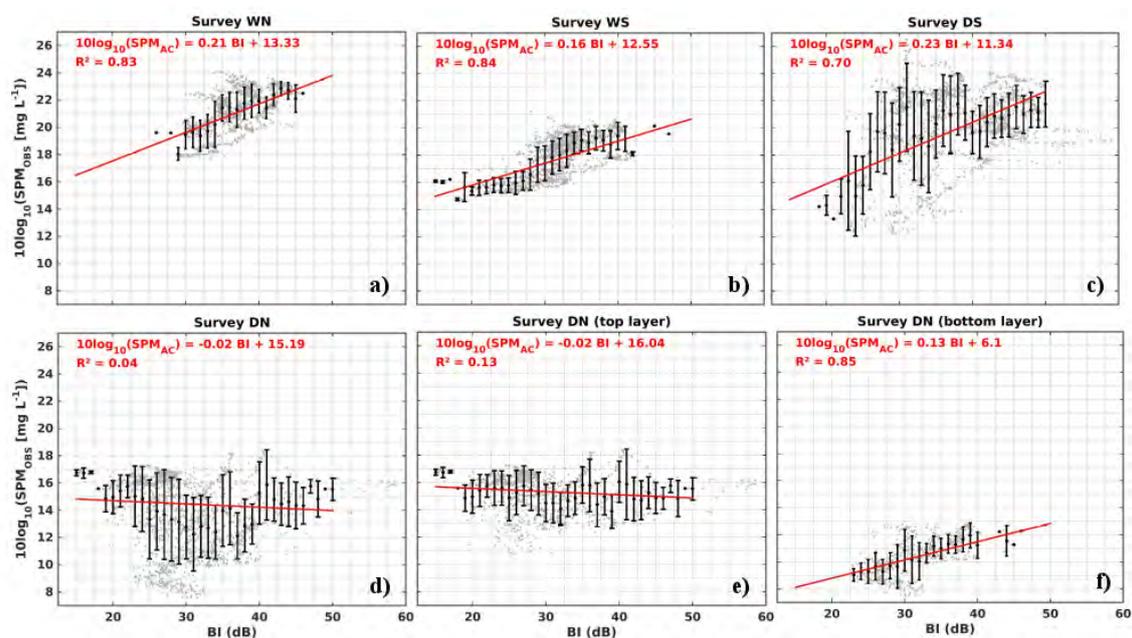
Figure II.2: $10\log_{10}$ of suspended matter concentration estimated from CTD OBS (SPM_{OBS} in mg l^{-1}) against the ADCP backscattering index (BI in dB) for each survey WN, WS, DS and DN (panels a, b, c, d respectively). Raw data are shown in grey and the binned data in black, the data trend line is shown in red. Panels e and f correspond to the top and bottom water layers respectively in survey DN. On the y-axis, 10 corresponds to 10 mg l^{-1}, 16 to 40 mg l^{-1}, 20 to 100 mg l^{-1}, 26 to 400 mg l^{-1}.

II.2.4.1.2 Water and sediment budgets

a) Time variations

Seasonal variations in Q_{ADCP} were high, with wet season water discharges (2425 m^3 s^{-1} in average over the survey WN and 1757 m^3 s^{-1} for survey WS, Table II.2) 4 to 11 times larger than the discharges in dry season (478 and 222 m^3 s^{-1} for survey DS and DN, respectively). Suspended sediment discharges Q_{SED} varied accordingly, with 3 to 170 times larger values in wet season than in the dry season (0.34 t s^{-1} in WN and 0.11 t s^{-1} in WS, as compared to 0.04 and 0.002 t s^{-1} in surveys
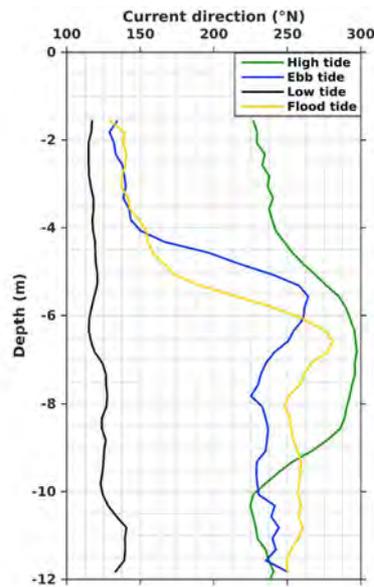
Figure II.3: Mean currents directions (in ° N) measured at ST2 during survey DN at high tide (8 am), ebb tide (12 am), low tide (4 pm) and flood tide (2 am).

DS and DN, respectively).

During the wet season, the total water and sediment discharges Q_{ADCP} and Q_{SED} were dominantly directed down-estuary ($Q_{ADCP}+$ and $Q_{SED}+$) and only very limited fluxes directed up-estuary ($Q_{ADCP}-$ and $Q_{SED}-$) were observed (Fig. II.4 a,b; Table II.2). In neap tide, a mean $Q_{ADCP}+$ of 2432 m^3 s^{-1} was measured against a mean $Q_{ADCP}-$ of 7 m^3 s^{-1}, the associated mean $Q_{SED}+$ being of 0.34 t s^{-1} against a mean $Q_{SED}-$ of 10^{-4} t s^{-1}. In spring tide, up-estuary fluxes were slightly higher but less than 4% of the total water and sediment discharges (Table II.2).

As expected, the up-estuary component of the water discharge ($Q_{ADCP}-$) was much higher in the dry season than in the wet season (Table II.2). During the dry season, both down-estuary and up-estuary flows contributed to the total water and sediment fluxes. Globally, the down-estuary water and suspended sediment discharges were respectively 61 and 66% higher than the up-estuary water and suspended sediment flows in the dry season (Table II.2). The range of Q_{ADCP} was around 3 times higher in spring tide (from -3976 to 3178 m^3 s^{-1}) than in neap tide (from -1252 to 1826 m^3 s^{-1}, Fig 4. c,d). The difference was highly enhanced in the range of Q_{SED} (from -0.55 to 0.45 t s^{-1} in spring tide, while they ranged from -0.015 to 0.022 t s^{-1} in neap tide, Fig 4. c,d).

Fluxes were very sensitive to tidal variations in dry season, and in wet season during spring tide (Fig. II.4).

In the dry season and in the wet season at spring tide, Q_{ADCP} was influenced by the tidal diurnal

cycle with high discharges at low tides, decreasing discharges at rising tides, low discharges at high tides and increasing discharges at falling tides (Fig. II.4 b,c,d). Q_{SED} followed the same patterns.

In the wet season, only spring tides have induced large enough amplitudes (of ~ 2 m) to balance the riverine discharge and induce up-estuary flow (Q_{ADCP}-) at stations ST1 and ST2 (Fig. II.4 b) ; tidal currents at neap tides (maximum amplitudes of 0.5 m) were not strong enough to impact the riverine discharges (Fig. II.4 a). The rest of the diurnal cycle (i.e. low, ebb and flood tides) at each station was dominated by a down-estuary flow (Q_{ADCP}+), which increased with ebb tides and was the highest around low tides.

A noticeable difference can be seen on the flow regime between spring and neap tides in dry season. During spring tides, the flow was alternatively strictly down-estuary and strictly up-estuary with positive Q_{ADCP} values and no Q_{ADCP}- component during 12 hours then the reverse during the next 12 hours from the end of flood until halfway through ebb (Fig. II.4 d). At neap tides (survey DN, Fig 4 c), the reversion of the total flow also occurred, but was more nuanced with both Q_{ADCP}- and Q_{ADCP}+ components contributing at the same time to the flow at ST1 and ST2. This particular case resulted from the strong stratification at neap tide and dry season, with two distinct water masses as explained above in 4.1.1: the upper flowing down-estuary, and the lower flowing up-estuary.

Q_{SED} followed Q_{ADCP} patterns with mean net down-estuary sediment fluxes Q_{SED} 20 times larger in spring tide (0.04 t s^{-1}, Table II.2) than in neap tide (0.002 t s^{-1}) in dry season, and with negligible up-estuary sediment fluxes (Q_{SED}-) in wet season lower than 4% of the down-estuary fluxes (Q_{SED}+), both for spring and neap tides. However, the sediment sources are different: while Q_{SED}+ refers to the fluxes of fluvial suspended sediment, Q_{SED}- refers to the upward transport of sediment from the coastal zone or resuspended in the estuary. A main information of the measurements is to quantify this very high up-estuary flow of coastal sediment Q_{SED}- in dry season and spring tide (0.08 t s^{-1}, Table II.2) which is $\frac{2}{3}$ of the down-estuary discharge of suspended matter Q_{SED}+ from the river basin (0.12 t s^{-1}). In other words, the estuary is silting up and the delta is consolidating mainly in spring tide during the dry season.

At last, the time variations of tidal amplitude and discharge at Trung Trang during spring tides (both in dry and wet seasons) clearly show that flood tides are shorter than ebb tides in the Van Uc estuary. Such a non linear tidal distortion may be explained either by a high tidal energy dissipation by friction (reflected as a/h= tidal amplitude/water depth) or by a low intertidal storage (mea-

sured by V_s/V_c=volume of intertidal storage/volume of channels at mean sea level) (Friedrichs and Aubrey, 1998; Kang and Jun, 2003).

Survey	Q_{TT} (m^3 s^{-1})	Q_{ADCP} (m^3 s^{-1})		R^2 (Q_{ADCP}/ Q_{TT})	Q_{ADCP} +	Q_{ADCP} -	Q_{SED} (t s^{-1})		R^2 (Q_{ADCP}/ Q_{SED})	Q_{SED} +	Q_{SED} -
WN	2406	2425	ST1: 2352 ST2: 2970 ST3: 1955	0.46	2432	-7	0.34	ST1: 0.33 ST2: 0.35 ST3: 0.35	0.77	0.34	-0.0001
WS	1672	1757	ST1: 2043 ST2: 1841 ST3: 1388	0.81	1832	-74	0.11	ST1: 0.15 ST2: 0.10 ST3: 0.08	0.96	0.11	-0.004
DS	374	478	ST1: 418 ST2: 595 ST3: 420	0.81	1236	-758	0.04	ST1: 0.04 ST2: 0.05 ST3: 0.03	0.94	0.12	-0.08
DN	375	222	ST1: 310 ST2: 148 ST3: 208	0.80	575	-353	0.002	ST1: 0.0031 ST2: 0.0017 ST3: 0.0019	0.84	0.006	-0.004

Table II.2: Mean water discharges at Trung Trang (Q_{TT}), mean water (Q_{ADCP}) and mean sediment (Q_{SED}) discharges derived from ADCP measurements and determination coefficients (R^2), for the four surveys (for our 36 values time series, the 99% significance threshold is reached for a correlation of 0.42). The means are computed over the 3-days period of each survey (36 values), and computed over 24h when showed for each station (12 values).

b) Spatial variations

Q_{ADCP} measured in the estuary exhibited very small differences compared to the mean discharges from the hydrological station Trung Trang (noted TT from hereafter) in the wet season (below 1% for WN and around 7% for WS, see Table II.2). However, in the dry season, Q_{ADCP} is 27% higher than the mean discharge at TT (Q_{TT}) in spring tide, and is 41% lower than Q_{TT} in neap tide. Due to its location roughly 15 km upstream of ST3 (Fig. II.1), TT station is less affected than our transect stations by the variation of discharges due to the tides, especially during the dry season, and therefore, discrepancies in measured discharges at our stations and discharges at TT may appear. Overall, time series of Q_{ADCP} and Q_{TT} were highly correlated in surveys WS, DS and DN (R^2=0.80, 0.81 and 0.81 respectively) and only survey WN showed a weaker (but still significant at 99%) average correlation (R^2=0.46) that may be explained by the small amplitudes of variations in Q_{ADCP} in this season and tidal range. Better correlations were obtained with a lag between Q_{TT} and Q_{ADCP} in surveys WS, DN and DN. The best R^2 values (R^2=0.97, 0.98 and 0.97 for survey WS, DS and DN, respectively) were found at each station and for each survey with a lag of two hours, which indicated that Q_{TT} are leading Q_{ADCP} by two hours all along the estuary, in average, as can be seen in Fig 4. b,c,d.

Increases in Q_{ADCP} of about 52% , 33% and 42 % were observed between ST3 and ST2 during surveys WN, WS and DS, respectively (Table II.2). These increases are likely due to water inputs from the Luoc River which flows into the Van Uc River, approximately 2 km downstream of ST3 (see Figure 1). The 40% drop in water discharge that was observed during the survey DN between ST3 and ST2 coincided with decreasing water discharges measured at Trung Trang station (Q_{TT}) during the 3-day period of measurements (Table II.2; Fig. II.4 c), and can thus be explained by a decrease of discharge from the day of ST3 measurements to the day of ST2 measurements. Decreases in water and sediment discharges amplitudes were observed from the river mouth upwards (from ST1 to ST3) during surveys WS, DS and DN (Fig. II.4 b,c,d). These decreases could be explained by the variations in the tidal elevation range along the estuary that impact the capability of currents to transport water and sediments. The tidal range increases towards the mouth before decreasing in the river section, when the convergence effects of the estuary sides exceed the frictional effect of the bed (Dyer, 1995).

Given the scarcity of water discharge data and of their tidal and seasonal variability in the Van Uc river, those values will provide a precious basis for assessing the role of the neap-spring cycle on estuarine dynamics, but will also provide a new benchmark for the calibration/validation of an estuarine hydrodynamic and sediment model.

II.2.4.2   Hydrology and turbidity

Salinity as well as Simpson parameter values (Φ), which correspond to the amount of energy needed to homogenize the water column, exhibited large differences between the two seasons. During the wet season, salinity ranged from 0.8 to 1 PSU (not shown) and Φ from 0.07 to 1.3 J m^{-3} (Fig. II.5), indicating strictly unstratified fresh waters conditions. During the dry season, salinity ranged from 0.8 to 27 PSU (Fig. II.6 a,b) and Φ from 0.1 to 10^5 J m^{-3} (Fig. II.5), which illustrated an oscillation between fresh and unstratified to salty and stratified conditions.

During the wet season, tidal and spatial variations of salinity, of the average Richardson gradient number (Ri) and of the Brunt-Vaisala frequency (N^2) were indeed very limited. Values of R_i >0.25 (not shown) indicate that the turbulent mixing across the stratification is suppressed, therefore the water column is stratified, and conversely R_i < 0.25 indicates a strong vertical mixing. In addition of salinities <1 PSU for WN and WS at all stations, almost all R_i values remained below 0.25 and N^2 < 0.001 s^{-2} (not shown). R_i < 0.25 and homogeneous relatively small values of N^2 are indicative of homogeneous conditions with a strong vertical mixing. However, at 2 pm and 4 pm in survey WS
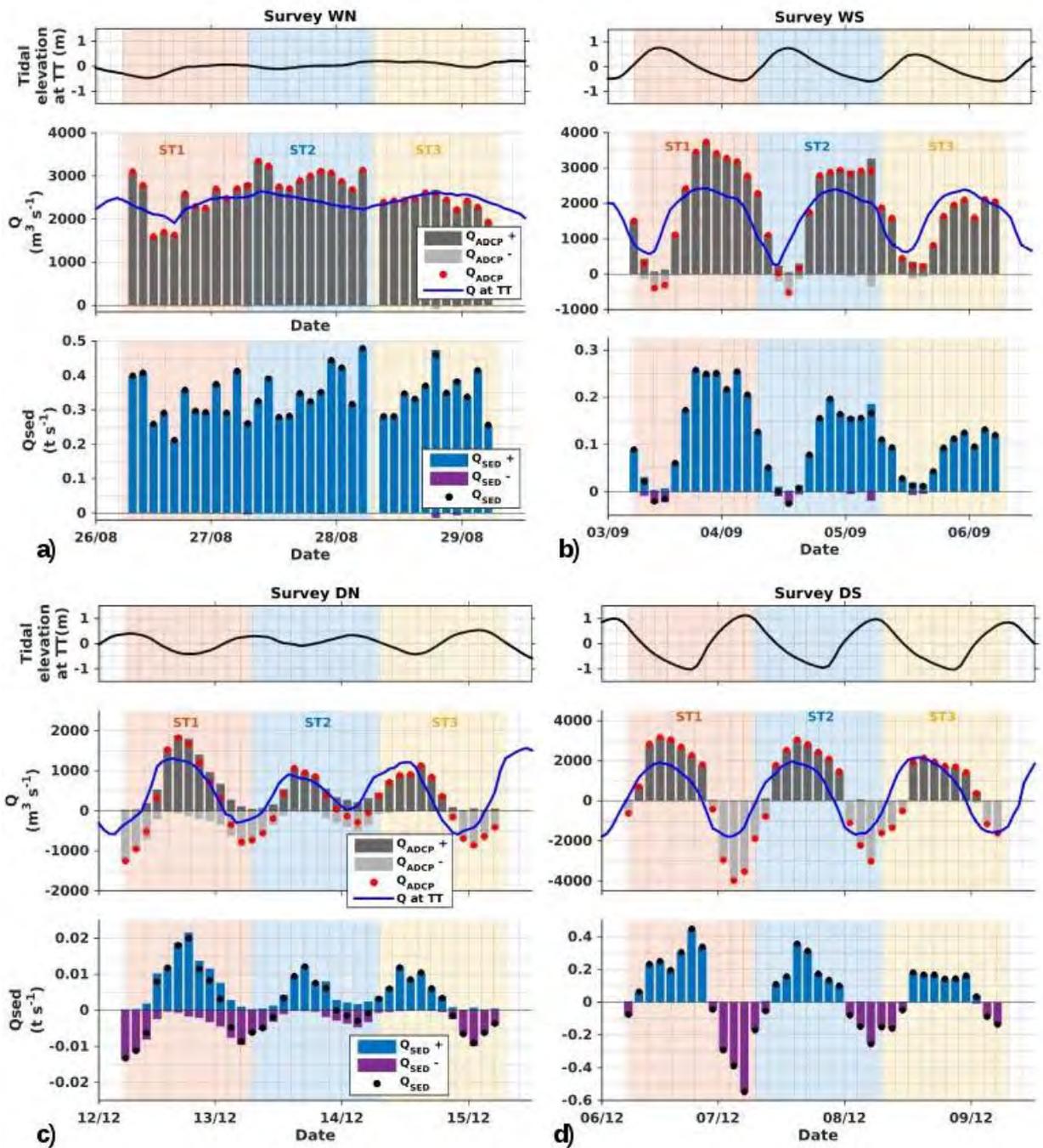
Figure II.4: Tidal elevation (in m, black line) and Q_{TT} ($m^3 s^{-1}$, blue line), measured Q_{ADCP} ($m^3 s^{-1}$, red dots) with associated $Q_{ADCP}+$ and $Q_{ADCP}-$ (dark grey and light grey bars, respectively), and computed Q_{SED} (in t s^{-1}, black dots) with associated $Q_{SED}+$ and $Q_{SED}-$ (blue and purple bars, respectively), at all three stations for all four surveys.

at ST1, $R_i = 0.52$ and 0.64, respectively, and coincided with $\Phi > 1$ (Fig. II.5). This light stratification corresponded to a slight increase of the surface water temperatures (of about 1.5 ° C, not shown), triggered by an intense solar heating during this particular afternoon.

During the dry season, spatial and tidal variations of salinity, turbidity, R_i and N^2 were high. In
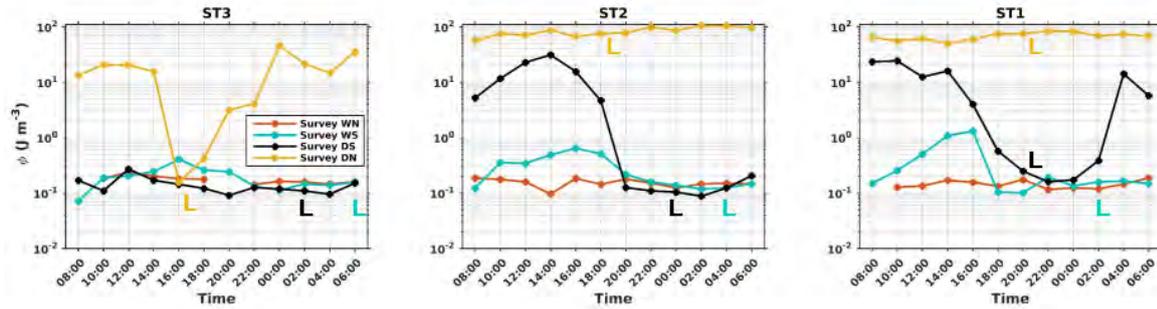
Figure II.5: Simpson parameter values (J m^{-3}) at ST3 (left), ST2 (center) and ST1 (right) for survey WN (orange line), survey WS (cyan line), survey DS (black line) and survey DN (yellow line) during 24h tide cycles. The letters "L" indicates the time of low tide. The missing value at 8pm at ST3 (survey WN) corresponds to a failure in CTD measurement.

spring tides (survey DS), salinity ranges decreased along the estuary from 0.1 to 27 PSU at ST1, from 0.1 to 20 PSU at ST2 and from 0.1 to 0.3 PSU at ST3 (Fig. II.6a). At ST3, the water column remained homogeneous throughout the day, with $R_i < 0.25$ and small homogeneous N^2 values (<0.001 s^{-2}). At ST2 and ST1, the water column alternated between stratified and homogeneous conditions. During low and flood tides, the water column was composed of fresh, turbid (100-250 FTU) and homogeneous waters with $Ri <0.25$ and $N^2 \sim 0 \, s^{-2}$. On the opposite, during high tides and ebb tides, the water column was partly stratified and composed of salty waters with lower turbidity (below 100 FTU). In particular at ST1, Brunt-Vaisälä profiles indicated a stratification near the surface in the top 3 m of the water column with $N^2 \sim 0.05 \, s^{-2}$, which coincided with $R_i > 0.25$. At ST2, the intensity of the stratification decreased with $R_i < 0.25$ and scattered N^2 maxima were observed. Following the results of Fig. II.4 d, both spring and diurnal tides played a key role in influencing the water column conditions of the dry season. The water column was either strictly dominated by fresh turbid riverine waters flowing down-estuary when the tidal amplitude was the lowest, or by salty marine waters flowing up-estuary when the tidal amplitude was high. The tidal intrusion and efficiency to bring salty waters decreased with the distance from the river mouth with a very limited influence at ST3 (20 km upstream of ST1) where the salinity does not exceed 0.3.

Neap tides water column characteristics in the dry season were very different than spring tides characteristics. At ST1 and ST2, the water column was very stratified and divided into two layers: one bottom layer composed of dense salty waters (up to 25 PSU) and one top layer composed of fresh (~ 0 PSU) riverine waters (Fig. II.6b). Overall, the turbidity values of survey DN were lower than in any other surveys, but the top layer showed higher turbidity values (40-60 FTU) than the bottom layer (< 20 FTU). Similar to survey DS case, the salinity (of the bottom layer) decreased

(a)

(b)
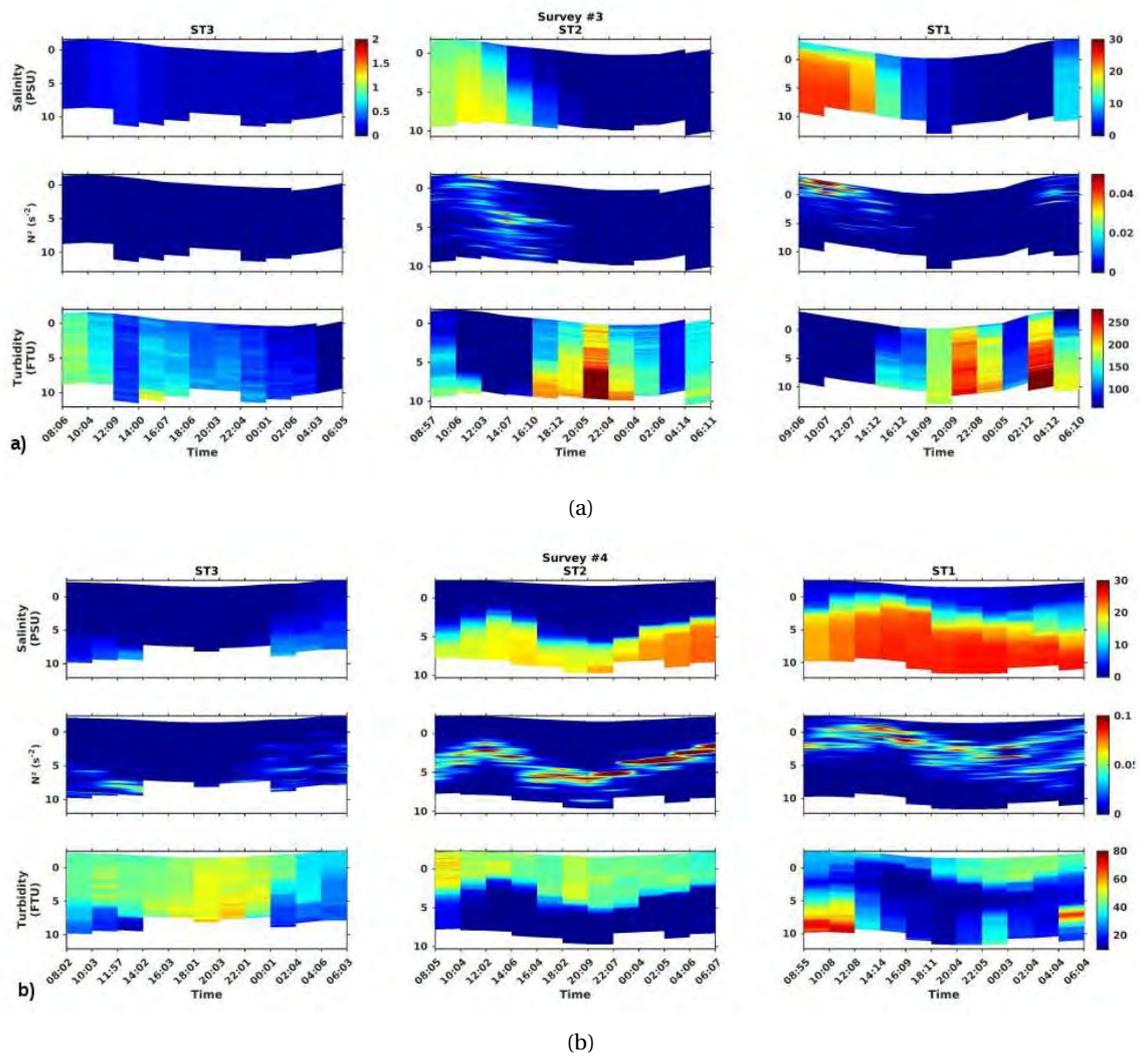
Figure II.6: Salinity (in PSU), N^2 (in s^{-2}), and turbidity (in FTU) temporal series at ST3, ST2 and ST1 measured in survey DS (a, dry season, spring tides) and in survey DN (b, dry season, neap tides). Note the different colorbars for salinity at ST3 for DS, due to very low values, and between DS and DN for N^2 and turbidity.

along the estuary with the distance from the mouth (from 0.8 to 27 PSU at ST1, from 0.8 to 23 PSU at ST2 and from 0.8 to 10 PSU at ST3). At ST1 and ST2, N^2 values were maximum in the halocline ($\sim$ 0.1 s^{-2}) and were twice bigger than in survey DS. In addition, $R_i > 0.25$ at ST2 and $R_i > 0.5$ at ST1 indicated a strong stratification, that lasted throughout the 24 hours of measurements. In accordance with the salinity patterns, the stratification intensity decreased along the estuary, with stronger stratification at the stations close to the mouth. As seen in section II.2.4.1.2 and in Fig. II.4 c, neap tides in the dry season triggered a two layers circulation in the water column. On top, the fresh and turbid river waters flowed downstream (corresponding to $Q_{ADCP}+$ in Fig. II.4 c) whereas, at the bottom the clear salty marine waters flowed upstream (corresponding to $Q_{ADCP}-$ in Fig. II.4 c). Lastly, near bed high turbidity values observed at ST1 were due to particles' resuspension induced by the maximal strength of the upstream flow of high tides (Fig. II.6b).

II.2.4.3   Suspended particulate matter

II.2.4.3.1   Time variations

The PSDs alternated between bimodal and trimodal distributions from a survey to another, with varying contributions of each particle class to the total particle volume (Fig. II.7 a). As mentioned in the literature, PSDs of observed suspensions are more often bimodal or multi-modal rather than unimodal (Ludwig and Hane 1990; Green and Boon, 1993).

In wet season, trimodal PSDs were measured with a first peak for particle diameters < 4 µm, a second peak for particles of diameter 5-10 µm, and a third peak for aggregates of larger diameters (of 30-70 µm for survey WN and of ~ 30 µm for survey WS). From hereafter, we consider the particles < 4 µm as primary particles (PP), the particles of 4-20 µm as flocculi, and the particles > 20 µm as microflocs. In the wet season, spring tides likely induced stronger turbulent stresses than neap tides (see Fig. II.4 b as compared to 2. 4 a) that may cause a breakage of the largest flocs, hence a decrease in populations of microflocs >30 µm in spring tides. This is consistent with the results from Mikkelsen et al. (2006), who demonstrated that when the water column stress increases, the volume occupied by large particles (in their case: macroflocs) decreases, while the volume occupied by finer particles (in their case: microflocs) increases.

In dry season, bimodal PSDs were measured with peaks moving in the spring-neap tide cycle. Peaks of PP and flocculi were observed in spring tides (survey DS, Fig. II.7 a), while peaks of flocculi and microflocs appeared in neap tides (survey DN). However, the tidal average PSDs in spring tides masked a diurnal alternation of PSDs. At low tide (Fig. II.7 b), the instant PSD was similar to the average PSD of survey DS (Fig. II.7 a) but at high tide, the instant PSD (Fig. II.7 b) appeared to be similar to the PSDs of survey DN (Fig. II.7 a). These observations highlight the fact that riverine waters, which dominated the water column around low tides in spring tide (see section II.4.1.2, Fig. II.4 d and section II.2.4.2, Fig. II.6a), carried PP and flocculi. On the other side, marine salty waters, which dominated the water column around high tide in spring tides and all along neap tides, carried flocculi and microflocs. We suggest that the microflocs were formed by salinity-induced flocculation of PP or covarying aggregation by bio-processes, either within the estuary, or in the coastal area and they were brought back into the estuary by the tidal advection. As seen in section II.2.4.2 and Fig. II.6,b, salinity maxima oscillated between 0.8 and 27 PSU during the dry season, and Vinh et al. (2018) showed that flocculation happened for salinity as low as 0.1 PSU in the Cam Nam estuary (Fig. II.1). Besides, Eisma (1993) indicated that salinity flocculation

is complete at 8 PSU or less, and Mari et al. (2012) demonstrated that the stickiness properties of organic exopolymeric substances increase between 10 and 15 PSU, enhancing the bio-induced flocculation in the Cam Nam estuary.

It is important to note that the high concentrations of PP observed in almost all surveys and which sometimes corresponded to 5-15 % of the SPMVC, are to be considered with caution. Rather than providing an exact number, these concentrations should be interpreted as an indication of the presence of very fine particles (Fettweis and Baeye, 2015). Indeed, the LISST-100X (type B) detectors show some limitations and uncertainties related to the characteristics of the particles. Significant concentrations of particles smaller than the lowest LISST detection limit (<1.25 µm) can influence the entire PSD with increase of concentrations of the two smallest size classes, a decrease of the next classes and an increase on the largest size classes (Andrew et al., 2010; Graham at al., 2012).

II.2.4.3.2 Spatial variations

We further investigated the transfer of particles from a class to another, and the relative contribution of each class to the total SPMVC (Fig. II.7 c). During spring tides (surveys WS and DS), the proportion of each class remained quite unchanged along the estuary, while longitudinal variations were observed in neap tides (surveys WN and DN), with decreasing proportion of primary particles and increasing proportion of microflocs from upstream (ST3) to the river mouth (ST1). In survey WN, for example, microflocs made up 23% of the total volume at ST3, 35% at ST2 and 39% at ST1, while PP contribution to SPMVC decreased from ST3 (34%) to ST2 (22%) and ST1 (18%). Similar longitudinal transfers from PP to microflocs were observed in survey DN, even though the PP contributions to SPMVC were about twice larger in survey WN. These discrepancies in PP concentrations between dry and wet seasons could be due to differences in sediments discharges (Q_{SED}) between the seasons (section II.2.4.1.2), with mean Q_{SED} approximately 170 times bigger in survey WN than in DN (Table II.2). In survey DN, salinity-induced flocculation may explain the transfers of PP to microflocs (see previous section), intensifying closer to the river mouth (ST2 and ST1). For spring tide surveys (DS and WS), the proportion of each class remained spatially almost unchanged because the along-estuary salinity gradient was non-existent, limiting the flocculation and therefore the transfer of PP to microflocs.

Lastly, the SPMVC progressively decreased along the estuary with higher volume concentrations recorded at ST3 than at ST2 and ST1, in each case (see the values on Fig. II.7 a). The volume con-

centration ratio between ST3 and ST1 decreased from 12 for survey WN, to ~ 3 for surveys WS, DS and DN. Although SPMVCs should not be considered as exact values but only as indicators, such a volume loss may be explained by particles deposition, with zones of accumulation spanning from ST3 to ST1. Here, hydrodynamical-sediment transport modelling would be a useful tool to detail the transport and deposition of SPM, and could highlight zones of accumulation / accretion in the estuary and along the shorelines.
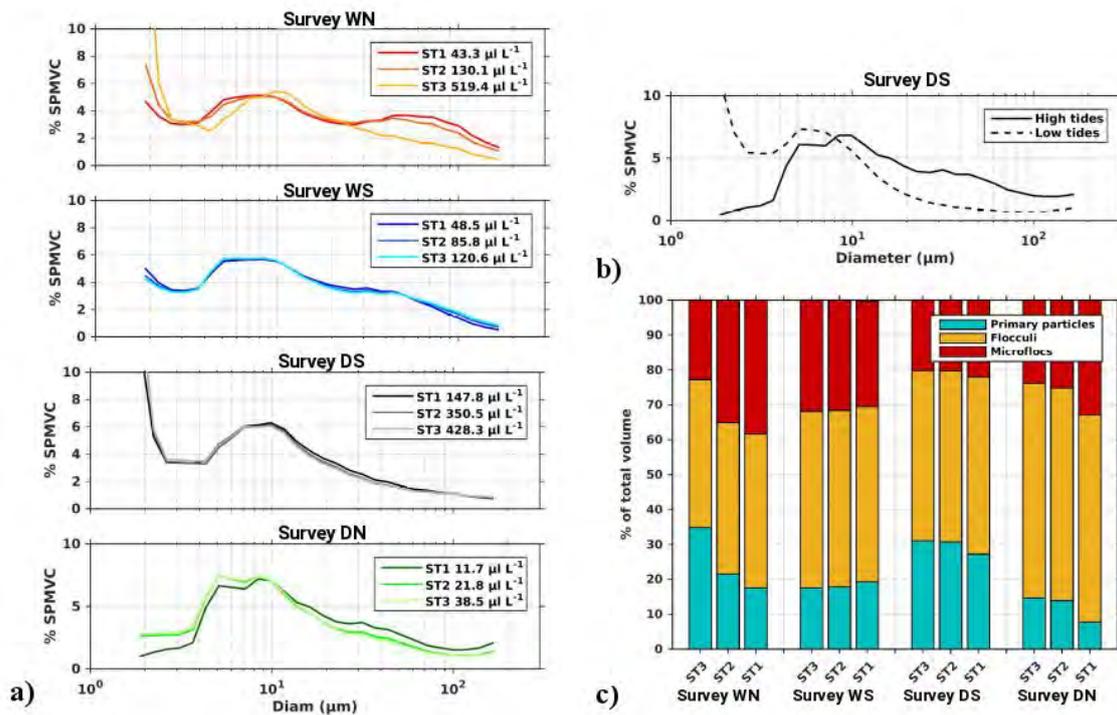
Figure II.7: a) PSD at each station for all surveys and their associated SPMVC. b) PSD at ST2 in survey DS at high tide (measured at 8 am) and low tide (measured at 8 pm). c) Proportions of primary particles, flocculi and microflocs in terms of % of volume occupied, by station and for all four surveys.

II.2.5   Discussion and Conclusion

Water column and sediment time-series observations made along the lowermost 20 km of the Van Uc river, which included acoustic and optical determination of SPM concentration, measurements of flow velocity, salinity, and PSD, at different seasons and neap-spring cycle, showed that:

1 - The water and sediment discharges of the Van Uc river undergo a comprehensive regime change between high-seasonal (wet season) and low-seasonal (dry season) discharges. The sampled portion of the estuary varied from mixed to stratified, depending on tidal state and freshwater inflow. Strictly mixed conditions occurred during high-flow season with low salinity (<0.09 PSU), characterizing the upper estuary. During high-flow season, the middle and lower estuaries (likely located in the bay) was not sampled. In the sampled estuary during low-flow season, water column con-

ditions transited from mixed, partly-stratified to very stratified, with salinity of a few PSU, characterizing the middle or lower estuary, due to the combined effects of neap-spring cycle, diurnal tides and low discharges: in spring tides, the water column was either partly-stratified near the surface with high tides or mixed with low tides, while neap tides triggered a constant and strong stratification.

2 - The seasonal discharges are affected by the neap-spring cycle with different effects between the seasons. The high seasonal flow is not disrupted by neap tides but spring tides can reverse the downstream river flow at high tides. In low-flow season, the spring tides reverse the flow for half the day, while neap tides trigger a gravitational circulation (two-layer circulation) with a flow in both directions (up-estuary for the bottom layer and down-estuary for the top layer) and a very stratified water column. The occurrence of gravitational circulation thus depends both on freshwater flow and on the tidal state.

3- Decomposition of the suspended matter flux revealed that the riverine down-estuary component was the most important during high flow season while gravitational and tidal processes, like local resuspension, were most important during low flow season. Up-estuary suspended matter flux appeared to account for $\frac{2}{3}$ of the down-estuary flux in the low-flow season, which indicates that the estuary is silting up and the delta is consolidating mainly during the dry season. This fine marine sediment importation in the estuary, likely due to a gravitational circulation, is driven by the longitudinal density gradient caused by freshwater inflow, developing an estuarine turbidity maximum near the upstream boundary of the gravitational circulation (Dronkers 1986). This is particularly observable in neap tides when a sediment flux is oriented seaward in a surface layer at the same time than a landward sediment flux in the underlying salted layer. The ETM (estuarine turbidity maximum) was described by Vinh et al. (2018) in another distributary of the Red River, close to the Van Uc River, and our measurements indicates that an ETM is likely located between stations ST1 and ST2 during the dry season. During the wet season, salinity remained very low in the riverine part of the estuary (with maximum value of 0.09 PSU at the river mouth), indicating that mixing between riverine and marine waters develops in the bay and in coastal waters, like in the Cam-Nam Trieu estuary (Vinh et al., 2018). Since stratification remains low during the tidal cycle, another process than gravitational circulation should explain the landward flux of suspended sediment in the wet season, which was observed at spring tides. Important asymmetry (or distortion) can occur in the tidal curve and velocities, in estuaries characterized by larger tidal ranges than water depths and by cross-river sections rapidly decreasing going up-estuary (Dyer, 1986).

In these cases, flood tides become shorter and stronger than ebb tides. The distortion of the tide wave in spring tide may be the dominant process to explain the up-estuary sediment mobility in wet season at spring tide during flood. A combination of the two main estuarine processes could thus explain the estuarine behaviour between two extreme conditions, at neap tides in dry season when gravitational circulation dominates, and at spring tides in wet season, when tidal distortion dominates. The effects of both processes may be further quantified and compared from numerical simulations.

4- Seasonal and tidal flow dynamics are also reflected in grain-size characteristics. All types of particles (PP, flocculi and microflocs) are transported during the high-flow season at any tidal stages, while mainly flocculi and microflocs are transported in the low-flow season, at high tides in spring tides and all along neap tides. The presence of the finest fraction (PP and flocculi) corresponds to the so-called wash load transport, which keeps particles in motion by turbulence at all current speeds and can therefore occur at any season and any tidal stages. The coarser fraction (microflocs) is likely in motion and transported by suspension, re-suspension and bedload (Dyer, 1995). While suspension can occur at any season, bedload occurs mostly during the high-flow season with highest current velocities (high water discharges).

This study took place in the framework of a more comprehensive modeling project which aims at representing the transport and fate of sediment from the Red River to the Gulf of Tonkin and analyzing the relevant processes. As tides have a major effect on the sediment dynamics within the estuaries and in the plume area (Pritchard 1954, 1956; Allen et al., 1980; Fontes et al., 2008; Vinh et al., 2018), and as monsoonal estuaries are highly affected by seasonal water discharges (Wolanski et al., 2013; Vinh et al., 2014; Nowacki et al., 2015), it is necessary to document and understand the estuarine hydrology and suspended matter dynamics, before setting up a set of numerical models and investigating the fine scale sediment physics. Considering model calibration, the primary objective of the field campaigns was to assess the up and down-estuary fluxes of both water and suspended matter, and fixed sampling stations were chosen accordingly. Note that the above-mentioned differences between the wet and dry seasons could be due to spatial aliasing with respect of the salinity intrusion. During the dry season, sampling stations were likely located in the saline estuary, while during the wet season stations seemed located in the tidal river as salinity intrusion was pushed seaward. Such configuration of a delta-front estuary (following the physiographic type defined by Fairbridge, 1980), with a narrow river opening to a large bay, makes very difficult to measure the tidal prism when the estuary develops off the river mouth. Numeri-

cal simulations will offer the possibility to compute the tidal prism and thus to estimate common estuarine dimensionless parameters such as the stratification number, the estuarine number and the circulation number. Nevertheless, this study complemented the understanding of the Van Uc estuary, which, to our knowledge, has never been sampled before. Further field studies are also encouraged to focus on the mixing processes and estuary configuration in wet season along the Red River delta.

Acknowledgments

Authors Contribution

VP, SO and MH conceived the study. VP, VDV, SO and MH organized the field trip, and VP and VDV performed the measurements. VP, SO and GM analyzed the data. VP and SO prepared the manuscript with contributions of GM, MH and PM.

Conflicts of Interest

The authors declare no conflict of interest.

II.2.6   References

- Aminot, A., and R. Kérouel. 2004. Hydrologie des écosystèmes marins: paramètres et analyses. Editions Quae.
- Andrew, S., D. Nover, S. Schladow. 2010. Using laser diffraction data to obtain accurate particle size distributions: The role of particle composition, Limnol. Oceanogr. Methods 8: 507-526, doi:10.4319/lom.2010.8.507.
- Carmeron, W. M., and D. Pritchard. 1963. Estuaries, The sea, 2: 306-324, Wiley, New York.
- Chapalain, M., R. Verney, M. Fettweis, M. Jacquet, D. Le Berre, P. Le Hir. 2018. Investigating suspended particulate matter in coastal waters using the fractal theory. Ocean Dynamics 69 (1): 59-81. http://doi.org/10.1007/s10236-018-1229-6,
- Deines, K.L. 1999. Backscatter estimation using broadband ADCP. R.D. Instruments. Application Note FSA-008.
- Ding, Y., C. Chen, R. C. Beardsley, X. Bao, M. Shi, Y. Zhang, Z. Lai, R. Li, H. Lin and N. T. Viet. 2013. Observational and model studies of the circulation in the Gulf of Tonkin, South China Sea. J. Geophys. Res. Oceans 118: 6495-6510. doi: 10.1002/2013/JC009455.
- Downing, J. 2006. Twenty-five years with OBS sensors: The good, the bad, and the ugly. Cont. Shelf Res. 26: 2299-2318. doi:10.1016/j.csr.2006.07.018.
- Dronkers, J. 1986. Tide-induced residual transport of fine-sediment. In Physics of shallow estuaries and bays, Lecture notes on coastal and estuarine studies. Vol. 16: 228-244.
- Dyer, K. 1986. Coastal and Estuarine Sediment Dynamics. John Wiley and Sons, Chichester.
- Dyer, K. 1995. Chapter 14 Sediment transport processes in estuaries. In: G.M.E, Perillo (Ed.) Developments in Sedimentology, Geomorphology and Sedimentology of Estuaries. Elsevier, pp: 423-449, https://doi.org/10.1016/S0070-4571(05)80034-2
- Eisma, D. 1993. Suspended Matter in the Aquatic Environment. Springer: Berlin, Germany.
- Fairbridge, R. W. 1980. The estuary: its definition and geodynamic cycle. In: Chemistry and Biogeochemistry of Estuaries. E. Olausson and I. Cato edit., Wiley, New-York, 1-39.
- Fang, G., Y. K. Kwok, K. Yu and Y. Zhu. 1999. Numerical simulation of principal tidal constituents in the South China Sea, Gulf of Tonkin and Gulf of Thailand. Cont. Shelf Res. 19(7): 845-869. https://doi.org/10.1016/S0278-4343(99)00002-3.
- Fettweiss, M. and M. Baeye. 2015. Seasonal variation in concentration, size, and settling velocity of muddy marine flocs in the benthic boundary layer, J. Geophys. Res. Oceans 120: 5648-5667. doi:10.1002/2014JC010644.
- Fontes, R. F. C., B. M. Castro and R. C. Beardsley. 2008. Numerical study of circulation on the inner Amazon Shelf, Ocean Dyn. 58:187-198. https://doi.org/10.1007/s10236-008-0139-4.
- François, R.E. and G. R. Garrison. 1982a. Sound absorption based on ocean measurements: Part I: Pure water and magnesium sulfate contributions. J. of the Acoust. Soc. of Amer. 72: 896-907. doi: 10.1121/1.388170.
- François, R.E. and G.R. Garrison. 1982b. Sound absorption based on ocean measurements: Part II: Boric acid contribution and equation of total absorption. J. of the Acoust. Soc. of Amer. 72: 1879-1890. doi: 10.1121/1.388673.
- Friedrichs, C.T., D. G. Aubrey. 1988. Non-linear tidal distorsion in shallow well-mixed estuaries: a synthesis. Est. Coast. Shelf Sci. 27: 521-545. doi:10.1016/0272-7714(88)90082-0
- Fugate, D. C., C. T. Friedrichs. 2002. Determining concentration and fall velocity of estuarine particle populations using ADV, OBS and LISST, Cont. Shelf Res. 22: 1867-1886, https://doi.org/10.1016/S0278-4343(02)00043-2.
- Gartner, J. W. 2002. Estimation of suspended solids concentrations based on acoustic backscatter intensity: theoretical background, Turbidity and other sediment surrogates workshop, Reno, Nevada.
- Gartner, J. W. and Cheng R. T. 2001. The promises and pitfalls of estimating total suspended

solids based on backscatter intensity from acoustic Doppler current profilers. Proceedings 7th Federal Interagency Sedimentation Conference, III-119-III-126, Reno, Nevada.

- Geyer, W. R. and P. MacCready. 2014 The Estuarine Circulation, Annu. Rev. Fluid Mech. 46: 175-97. doi: 10.1146/annurev-fluid-010313-141302.

- Geyer, W. R., J. H. Trowbridge and M. M. Bowen. 2000. The dynamics of a partially mixed estuary, J. Phys. Oceanogr., 30: 2035-2048, https://doi.org/10.1175/1520-0485(2000)030<2035:TDOAPM>2.0.CO;2

- Graham, G. W., E. J. Davies, W. A. M. Nimmo-Smith, D. G. Bowers and K. M. Braithwaite. 2012 Interpreting LISST-100X measurements of particles with complex shape using digital in-line holography, J. Geophys. Res. 117: C05034. doi: 10.1029/2011JC007613.

- Green, M. O. and J. D. Boon III. 1993. The measurement of constituent concentrations in non-homogeneous sediment suspensions using optical backscatter sensors. Mar. Geol.: 110: 73-81, https://doi.org/10.1016/0025-3227(93)90106-6.

- Ha, H. K., J. -P. Y. Maa, K. Park and Y. H. Kim. 2011. Estimation of high-resolution sediment concentration profiles in bottom boundary layer using pulse-coherent acoustic doppler current profilers, Mar. Geol. 279: 199-209. doi:10.1016/j.margeo.2010.11.002.

- Jay, D. A., K. Leffler, H. L. Diefenderfer and A. B. Borde. 2014 Tidal-fluvial and estuarine processes in the lower Columbia River: I, a long-channel water level variations, Pacific ocean to Bonneville Dam, Estuar. Coasts 38: 415-433. doi: 10.1007/s12237-014-9819-0.

- Jay, D. A. and J. D. Smith. 1990. Residual circulation in shallow estuaries: 1. Highly stratified, narrow estuaries, J. Geophys. Res. 95: 711, https://doi.org/10.1029/JC095iC01p00711.

- Kang, J.W. and K. S. Jun. 2003. Flood and ebb dominance in estuaries in Korea. Est. Coastal Shelf Sci. 56: 187-196. doi:10.1016/S0272-7714(02)00156-7.

- Kim, Y. H., G. Voulgaris. 2003 Estimation of suspended sediment concentration in estuarine environments using acoustic backscatter from ADCP (source: http://www.rdinstruments.com/pdfs/Kim_Yong.pdf). Accessed 17 January 2019.

- Kirinus, E. W., J. C. da Costa and E. H. Leao Fernandes. 2012 The contribution of waves in mixing processes of the Patos Lagoon plume. Int. J. Geosci. 3: 1019-1026. doi:10.4236/ijg.2012.35102

- Lai, W., J. Pan and A. T. Devlin. 2018 Impact of tides and winds on estuarine circulation in the Pearl River Estuary, Cont. Shelf. Res. 168: 68-82. https://doi.org/10.1016/j.csr.2018.09.004.

- Le, T. P. Q., J. Garnier, G. Billen, S. Théry and V. M. Chau. 2007. The changing flow regime and sediment load of the Red River, Viet Nam. J. Hydrol. 334: 199-214, doi:10.1016/j.jhydrol.2006.10.020

- Le Hir, P., F. Cayocca and B. Waeles. 2011. Dynamics of sand and mud mixtures: A multiprocess-based modelling strategy. Cont. Shelf Res. 31: 135-149, https://doi.org/10.1016/j.csr.2010.12.009.

- Lefebvre, J. P., S. Ouillon, V. D. Vinh, R. Arfi, J. Y. Panché, X. Mari, C. V. Thuoc and J. P. Torréton. 2012. Seasonal variability of cohesive sediment aggregation in the Bach Dang-Cam Estuary, Haiphong (Vietnam). Geo.-Mar. Lett. 32: 103-121. doi: 10.1007/s00367-011-0273-8.

- Ludwig, K. A. and D. M. Hanes. 1990. A laboratory evaluation of optical basckscatterance suspended solids sensors exposed to sand-mud mixtures. Mar. Geol. 94: 173-179, https://doi.org/10.1016/0025-3227(90)90111-V

- Lurton, X. 2002. Utilisation des ADCP pour la mesure de particules en suspension: synthèse des aspects acoustiques. IFREMER (France). Laboratory report, pp 29.

- Mari, X., J. P. Torréton, V. T. Chu, J. P. Lefebvre and S. Ouillon. 2012. Seasonal aggregation dynamics along a salinity gradient in the Bach-Dang estuary, North Vietnam. Estuar. Coast. Shelf Sci. 96: 151-158, https://doi.org/10.1016/j.ecss.2011.10.028

- Marsaleix, P., F. Auclair, J. W. Floor, M. J. Herrmann, C. Estournel, I. Pairaud and Ulses C. 2008 Energy conservation issues in sigma-coordinate free-surface ocean models. Ocean Modell.

20(1): 61-89, http://dx.doi.org/10.1016/j.ocemod.2007.07.005.

- Meybeck, M. 1993. Riverine transport of atmospheric carbon: sources, global typology and budget. Water Air Soil Pollut. 70(1-4): 443-463. https://doi.org/10.1007/BF01105015.

- Miranda, L. B., B. M. de Castro and B. Kjerfve. 2002. Principios de oceanografia fisica de estuarios. Sao Paulo: EDUSP 414.

- Mikkelsen, O. A., T. G. Milligan, P. S. Hill., R. J. Chant, C.F. Jago, S. E. Jones, V. Krivtsov and G. Mitchelson-Jacob. 2008. The influence of schlieren on in situ optical measurements used for particle characterization. Limnol. Oceanogr. Methods 6: 133-143, https://doi.org/10.4319/lom.2008.6.133.

- Mikkelsen, O. A., P. S. Hill and T. G. Milligan. 2006. Single-grain, microfloc and macrofloc volume variations observed with a LISST-100 and a digital floc camera. J. Sea Res. 55: 87-102. doi: 10.1016/j.seares.2005.09.003.

- Mikkelsen, O. A., P. S. Hill, T. G. Milligan and R. J. Chant. 2005. In situ particle size distributions and volume concentrations from a LISST-100 laser particle sizer and a digital floc camera. Cont. Shelf Res., 25 (16), 1959-78. doi: 10.1016/j.csr.2005.07.001.

- Milliman, J. D. 1991. Flux and fate of fluvial sediment and water in coastal seas. In: Mantoura R.F.C., Martin J.-M., Wollast R. (eds) Ocean Margin Processes in Global Change, John Willey and Sons Ltd., Chichester, 69-89.

- Milliman, J.D. and R. H. Meade. 1983. World-wide delivery of river sediment to the oceans. J. Geol. 91: 1-21, https://doi.org/10.1086/628741.

- Mueller, D. S., C. R. Wagner, M. S. Rehmel, K. A. Oberg and F. Rainville. 2013. Measuring discharge with the Acoustic Doppler Current Profilers from a moving boat (ver 2.0, December 2013): U.S. Geological Survey Techniques and Methods, 3, (A22): 95. http://dx.doi.org/10.3133/tm3A22/

- Mullison J. (2017) Backscatter estimation using broadband Acoustic Doppler Current Profilers - Updated. Presented at the ASCE Hydraulic Measurements & Experimental Methods Conference, Durham, NH.

- Pacanowski, R. C., and S. G. H. Philander (1981) Parameterization of vertical mixing in numerical models of tropical oceans. Journal of Physical Oceanography 11 (11): 1443-51, https://doi.org/10.1175/1520-0485(1981)011<1443:POVMIN>2.0.CO;2

- Pritchard, D. W. 1954. A study of the salt balance in a coastal plain estuary. J. Mar. Res. 13(1): 133-144.

- Pritchard, D. W. 1956. The dynamic structure of a coastal plain estuary. J. Mar. Res. 15: 33-42.

- Priya, K. L., P. Jegathambal and E. J. James. 2012. Hydrodynamic modelling of estuaries a-state-of-art. Int. J. Environ. Sci. 3: 223-240. doi:10.6088/ijes.2012030131024.

- Rouhnia, M., A. Keyvani and K. Storm. 2014. Do changes in the size mud flocs affect the acoustic backscatter values recorded by a Vector ADV? Cont. Shelf. Res. 84: 84-92. doi:10.1016/j.csr.2014.05.015.

- Simpson, J. H., C. M. Allen and N. C. G. Morris. 1978. Fronts on the continental shelf. J. Geophys. Res. 83: 4607-14.

- Simpson, J. H., J. Brown, J. Matthews and G. Allen. 1990. Tidal straining, density currents, and stirring in the control of estuarine stratification. Estuaries 13: 125-132, https://doi.org/10.2307/1351581

- Styles, R. 2006. Laboratory evaluation of the LISST in a stratified fluid. Mar. Geol. 227: 151-162, https://doi.org/10.1016/j.margeo.2005.11.011.

- Tessier, C. 2006. Caractérisation et dynamique des turbidités en zone côtière: l'exemple de la région marine Bretagne Sud. PhD thesis. Université de Bordeaux 1.

- Thorne, P. D., C. E. Vincent, P. J. Hardcastle, S. Rehman and N. D. Pearson. 1991. Measuring suspended sediment concentrations using acoustic backscatter devices. Mar. Geol. 98: 7-16, https://doi.org/10.1016/0025-3227(91)90031-X

- Turner, J. S. 1973. Buoyancy effects in fluids. Cambridge University.

- Uncles, R. J. and J. A. Stephens. 1996. Salt intrusion in the Tweed Estuary. Est. Coast. Shelf Sci. 43: 271-273, https://doi.org/10.1006/ecss.1996.0070.
- Unesco. 1983. Algorithms for computation of fundamental properties of seawater. Unesco.
- Van Maren, D. S. 2007. Water and sediment dynamics in the Red River mouth and adjacent coastal zone. J. Asian Earth Sci. 29: 508-522, https://doi.org/10.1016/j.jseaes.2006.03.012.
- Vietnam maritime administration (Vinamarine). Approved planning for dredging in Hai Phong port. Available online: http://vinamarine.gov.vn (accessed on 10 January 2019).
- Vinh, V. D., S. Ouillon, T. D. Tanh, V. L and Chu. 2014. Impact of the Hoa Binh dam (Vietnam) on water and sediment budgets in the Red River basin and delta. Hydrology and Earth System Sciences 18: 3987–4005. doi:10.5194/hess-18-3987-2014
- Vinh, V. D., S. Ouillon and D. V. Uu. 2018. Estuarine Turbidity Maxima and Variations of Aggregate Parameters in the Cam-Nam Trieu Estuary, North Vietnam, in Early Wet Season. Water 68: 1-33. doi: 10.3390/w10010068.
- Voulgaris, G. and S. Meyers. 2004. Temporal variability of hydrodynamics, sediment concentration and sediment settling velocity in a tidal creek. Cont. Shelf Res. 24: 1659-1683. doi:10.1016/j.csr.2004.05.006.
- Wei, X., S. Sauvage, T. P. Q. Le, S. Ouillon, D. Orange, V. D. Vinh and J. -M Sanchez-Perez. 2019. A Modeling Approach to Diagnose the Impacts of Global Changes on Discharge and Suspended Sediment Concentration within the Red River Basin. Water 11: 958. doi:10.3390/w11050958
- Wolanski, E., F. Andutta and E. Delhez. 2013. Estuarine Hydrology. In Bengtsson L., Herschy R. W., Fairbridge R. W. (eds) Encyclopedia of Lakes and Reservoirs, Encyclopedia of Earth Sciences. 238-249. doi: 10.1007/978-1-4020-4410-6_77.
- Wyrtki, K. 1961. Physical oceanography of the Southeast Asian waters. Naga Rep. 2, 195 pp. [Available from: https://escholarship.org/uc/item/49n9x3t4].
- Zu, T., J. Gan, S. Y. Erofeeva. 2008. Numerical study of the tide and tidal dynamics in the South China Sea. Deep-Sea Res. I 55: 137–154. doi:10.1016/j.dsr.2007.10.007

Chapter III

Bathymetry and bottom friction contributions to the tide representation in the Gulf of Tonkin

Contents

III.1   Summary of Chapter III

The major role played by tides on sediment dynamics within the estuaries and in the plume area and, at a larger scale, on circulation and sediment transport in coastal and open seas have been detailed in Chapter I. In addition, the results of Chapter II confirmed and described the role of tides in hydro-sedimentary dynamics in the Red River estuary. This also shed light on the need of accurate tidal solutions for modelling estuarine and coastal processes in macrotidal regions. In particular, bathymetry and bottom shear stress are crucial parameters to consider in shallow-water regional and coastal modeling since they both influence the propagation and distortion of the tides. In this context, the first objective of this chapter is to propose a robust and simple approach that allows to solve the tidal representation of the main constituents of the GoT. The second objective is to provide an optimized model configuration, in terms of bathymetry and bottom friction parameterization, based on tide representation in the GoT, which will be used in the rest of this thesis for modeling the hydro-sedimentary dynamics along the estuarine-coastal ocean-open sea continuum. For that, an improved bathymetry and coastline database over the GoT is constructed and sensitivity experiments performed with the hydrodynamical model T-UGOm, which allows the user to perform fast and low-cost tests on various parameterizations and bathymetry configurations. These experiments are compared with satellite altimetry data and with previous results from the literature. This strategy allows to assess and quantify the importance of each element considered and to determine the best configuration and parameterization that will be applied in the forthcoming sediment transport modeling study. Results from these experiments allow to quantify the importance of the bathymetry and shoreline dataset and of the choice of bottom friction parameters for the representation of tidal simulations over a shallow area like the GoT. First, they show that the new bathymetry dataset constructed for this study allows to reduce the errors (taking along-track altimetry data as a reference) of the representation of M2 and S2 in T-UGOm simulations by 40% and 25% respectively and O1 and K1 by 32% and 6% respectively, compared to simulations that use the regular GEBCO dataset. Second, tests on the bottom friction parameterization reveal that the regionalisation of the roughness length into three regions, for addressing the issue of representing the complexity of seabed composition and morphology, improves the accuracy of our simulation in terms of tidal solutions. However, finer local adjustments of the roughness length or the choice of a linear velocity profile in the area of fine mud, do not improve the accuracy of our simulations.

III.2 Article under review in Geoscientific Model Development: Sensitivity study on the main tidal constituents of the Gulf of Tonkin by using the frequency-domain tidal solver in T-UGOm.

Violaine Piton[1,2], Marine Herrmann[1,2], Florent Lyard[1], Patrick Marsaleix[3] , Thomas Duhaut[3], Damien Allain[1], Sylvain Ouillon[1,2]

[1] LEGOS, IRD, UMR556 IRD/CNES/CNRS/University of Toulouse, 31400 Toulouse, France

[2] LOTUS Laboratory, University of Science and Technology of Hanoi (USTH), Vietnam Academy of Science and Technology (VAST), 18 Hoang Quoc Viet, Cau Giay, Hanoi, Vietnam

[3] LA, CNRS, University of Toulouse, 31400 Toulouse, France

Correspondence to: Violaine Piton violaine.piton@legos.obs-mip.fr

Abstract

Tidal dynamics consequences on hydro-sedimentary processes are a recurrent issue in estuarine and coastal processes studies and accurate tidal solutions are a prerequisite for modelling sediment transport, especially in macro-tidal regions. The motivation for the study presented in this publication is to implement and optimize the model configuration that will satisfy this prerequisite in the frame of a larger objective to study the sediment dynamics and fate in the Red River delta to the Gulf of Tonkin from a numerical hydrodynamical-sediment coupled model. Therefore, we focus on the main tidal constituents to conduct sensitivity experiments on the bathymetry and bottom friction parameterization. The frequency-domain solver available in the hydrodynamic unstructured grid model T-UGOm has been used to reduce the computational cost and allow for wider parameter explorations. Tidal solutions obtained from the optimal configuration were evaluated from tide measurements derived from satellite altimetry and tide gauges: the use of an improved bathymetry dataset and fine friction parameters adjustment significantly improved our tidal solutions. However, our experiments seem to indicate that the solution error budget is still dominated by bathymetry errors, which is the most common limitation for accurate tidal modelling.

III.2.1 Introduction

The tide impacts on open seas and coastal seas are nowadays largely studied as they influence the oceanic circulation as well as the sediment transport and the ecosystems biogeochemical activity. For instance, Guarnieri et al. (2013) found that tides can influence the circulation by modification of the horizontal advection and can impact on the mixing. According to Gonzalez-Pola et al. (2012) and Wang et al. (2013), tides can also generate strong tidal residual flows by non-linear interactions with the topography. In the South China Sea (SCS), their dissipation can affect the vertical distribution of current and temperature, which in turn might play a role in blooms of the biological communities (Nugroho et al., 2018). The inclusion of tides and tidal forcings in circulation models is therefore not only critical for the representation and study of tides, but also for simulating the circulation and the mixing through different processes: bottom friction modulation by tidal currents, mixing enhanced by vertical tidal currents shear and mixing induced by internal tides, and non-linear interactions between tidal currents and the general circulation (Carter and Merrifield, 2007; Herzfeld, 2009; Guarnieri et al., 2013). Including these mechanisms in circulation models has improved the representation of the seasonal variability of stratifications cycles compared to models without tides (Holt et al., 2017, Maraldi et al, 2013).

At a smaller scale, the effects of tidal currents on the salt and momentum balances in estuaries were first recognized by Pritchard (1954, 1956). Since then, tides are known to play a key role in estuarine dynamics. Affecting mixing, influencing a stronger or weaker stratification depending on the sea water intrusion, and determining the characteristic of the water masses that can interact with the shelf circulation, tides influence is often the main driver of the estuarine dynamics. Amongst others, tidal asymmetry and density gradients are responsible for the presence of estuarine turbidity maximum (mass of highly concentrated suspended sediments, Allen et al., 1980). Slack waters are found to favor sedimentation and deposition, while flood and ebb tend to enhance erosion and resuspension within the estuary, and the tidal asymmetry induce a tidal pumping (i.e. spring tides are more energetic than neap tides). Understanding the dynamics of these turbidity maxima is crucial for harbours and coastal maritime traffic managements as they are often related to high siltation rates, necessitating regular dredging by local authorities (Owens et al., 2005; Vinh et al., 2018). These zones of accumulation of suspended sediments are also important for the ecology of coastal areas as sediments can carry pollutants that endanger water quality (Eyre and McConchie, 1993). The ability to understand and predict the formation of these zones related to tide cycles is therefore crucial for coastal and local activities.

The Gulf of Tonkin (from hereafter GoT) covers an area of 115 000 km^2 from about 16° 10′ - 21° 30′N and 105° 30′ - 111° E. This crescent-shape semi-enclosed basin, also referred as Vinh Bac Bo in Vietnam or as Beibu Gulf in China, is 270 km wide and 500 km long and lies in between China to the North and East, and Vietnam to the West. It is characterized by shallow waters as deep as 90m and is open to the South China Sea (SCS) through the South of the Gulf and to the East through the narrow Hainan Strait (Fig. III.1a). This latter, also known as Quiongzhou Strait, is on average 30km wide and 50m deep and separates the Hainan Island from the Zhanjiang Peninsula (mainland China). The bottom topography in the GoT and around Hainan Island is rather complex, constantly changing, especially along the coastlines, and partly unknown. Furthermore, the Ha Long Bay area counts about 2000 islets, also known as notches, sometimes no bigger than a few hundreds square meters.

The GoT is subjected to the South-East Asian sub-tropical monsoon climate (Wyrtki 1961), therefore largely influenced by seasonal water discharges from the Red River (Vietnam) and by many smaller rivers such as the Qinjiang, Nanliu and the Yingzai Rivers (China). The Red River, which brings in average 3500m^3 s^{-1} (Dang et al., 2010) of water along 150km of coastlines, was ranked as the ninth river in the world in terms of sediment discharge in the 1970s with 145-160 Mt/year (Milliman and Meade, 1983). Its sediment supply was drastically reduced since then to around 40 Mt/year of sediments (Le et al., 2007; Vinh et al., 2014). The Red River area accounts for the most populated region of the GoT, with an estimated population of 21.13 millions in 2016, corresponding to an average population density of 994 inhabitants/km^2 (from the Statistical Yearbook of Vietnam, 2017). This region is also a key to the economy of Vietnam, with Ha Long Bay (a UNESCO world heritage site) for its particular touristic value, and with the Hai Phong ports system, connecting the North of the country to the world market. This latter is the second biggest harbour of Vietnam with a particular fast-growing rate in terms of volume of cargos passing through the port, of about 4.5 10^6 to 36.3 10^6 tons from 1995 to 2016, respectively (Statistical Yearbook of Vietnam, 2017). However, the harbour of Hai Phong is currently affected by an increasing siltation due to tidal pumping, related to changes in water regulation by dams since the late 80's. Such phenomenon forces a dredging effort more and more important each year, with 6.6 million US $ spent on dredging activity in 2013 (Lefebvre et al. 2012, Vietnam maritime administration, 2017). In this particular case, fine scale tidal modeling is of great interest for harbour management and risks prevision.

The tides in the SCS and in the GoT have been extensively studied since the 1940s (Nguyen, 1969;
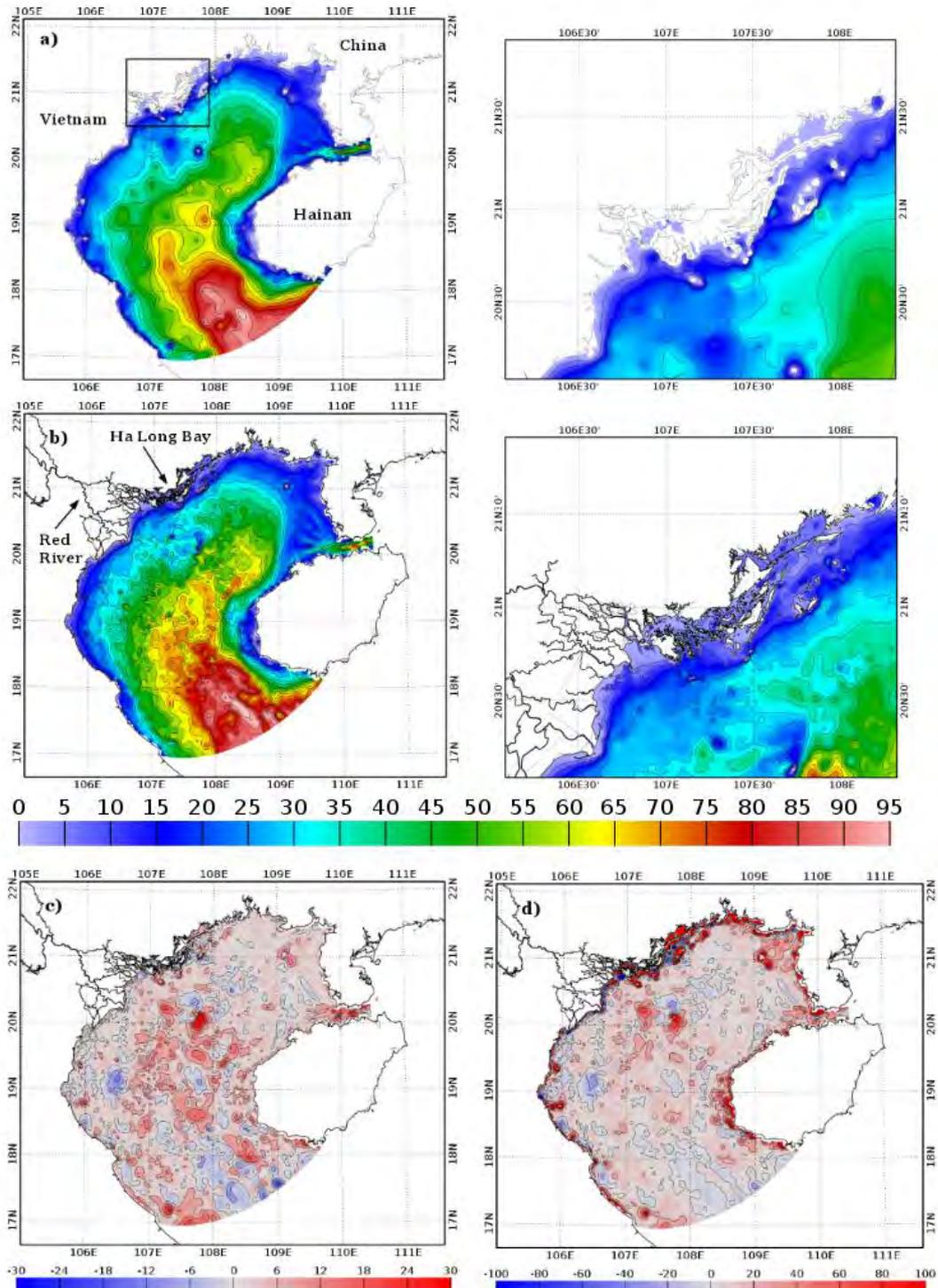
Figure III.1: (a, left) Gebco bathymetry (in m) and (a, right) details of the Ha Long Bay area (black rectangle in a,left). (b, left) TONKIN_bathymetry data set merged with TONKIN_shorelines over GoT and (b,right) zoom in the Ha Long Bay area. (c) Absolute (m) and (d) relative (%) differences between TONKIN_bathymetry and Gebco bathymetry (in m).

Ye and Robinson, 1983; Yu, 1984; Fang, 1986). Skewing through the literature, a lot of discrepancies exist in the cotidal charts before the 1980s, especially over the shelf areas. With the development of numerical models, the discrepancies have been significantly reduced by improving the accuracy of tides and tidal currents prediction. Wyrtki (1961) was the first to identify the main tidal constituents in the SCS (O1, K1, M2, S2) and Ye and Robinson (1983), the first to successfully simulate the tides in the area. Until recently, only few numerical studies have focused on the GoT (Fang et al., 1999; Manh and Yanaki, 2000; van Maren et al., 2004) and on the Hainan Strait (Chen et al. 2009). By using, for the first time, a high resolution model (ROMS at $1/25°$) and a combination of all available data, Minh et al. (2014) gave an overview of the dominant physical processes that characterize the tidal dynamics of the GoT, by exploring its resonance spectrum. This study improved the existing state of the art in numerically reproducing the tides of the GoT, however it also showed the limitations of using a 3D model in representing the tidal spectrum. Indeed, large discrepancies between the model and observations especially for the M2 harmonics and for the phase of S2 were found. The authors explained those discrepancies by the lack of resolution in the coastal areas due to limitations implied by the use of a regular grid and a poorly resolved bathymetric dataset.

The SCS and the GoT are one of the few regions in the world where diurnal tides dominate the semidiurnal tides (Fang, 1986). The tidal form factor (F), or amplitude ratio, defined by the ratio of the amplitude of the two main diurnal over the semi-diurnal constituents (as F=(O1+K1)/(M2+S2)), provides a quantitative measure of the general characteristics of the tidal oscillations at a specific location. If 0< F<0.25, then the regime is semi-diurnal, if 0.25<F<1.5, the regime is mixed primarily semi-diurnal, if 1.5<F<3, the regime is mixed primarily diurnal and if F>3, the regime is diurnal. Values of F shown on Fig. III.2 are calculated using tidal amplitudes from FES2014b-with-assimilation (product described in section 2.2.3). At the entrance of the GoT and at the Hainan strait, the tides are defined as mixed primarily diurnal with F varying from 1.5 and 2.2 depending on the given locations . At the Red River Delta, F is around 15, attesting of a diurnal regime. Indeed, the major branch of energy flux entering the basin from the southwest is weak for the semi-diurnal tides and strong for the diurnal ones. A second branch of energy (also diurnal tidal waves) enters the GoT through the Hainan Strait (Ding et al., 2013).

In coastal seas and bays, tides are primarily driven by the open ocean tide at the mouth of the bay. By resonance of a constructive interference between the incoming tide and a component reflected from the coast, large tide amplitude can be generated. In the GoT case, tidal waves enter
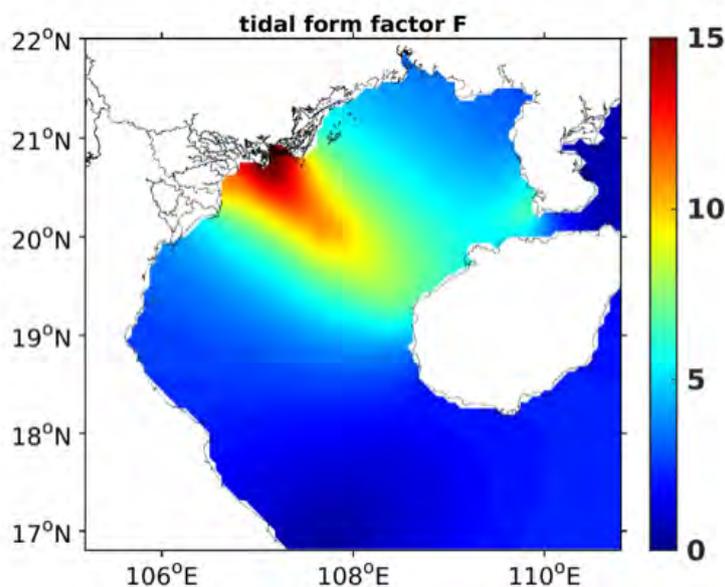
Figure III.2: Map of tidal form factor F computed with the amplitudes of tidal waves O1, K1, M2 and S2 obtained from FES2014b-with-assimilation.

the basin from the adjacent SCS and due to the basin geometry, O1 and K1 resonate (Fang et al., 1999). Their amplitudes reach 90 and 80 cm respectively. The Coriolis force deflects to the right the incoming waves and push them against the northern enclosure of the basin. Once the waves are reflected, they propagate southward until they slowly dissipate by friction. Fang (1999) found that the amplitude of the tide gradually decreases from 4 to 2 m North to South during spring tide. The amplitude of O1 in the GoT is larger than K1 because of a larger resonance effect, even though its amplitude in the SCS is smaller than K1 (Minh et al., 2014). The largest semidiurnal waves of the GoT are M2 and S2. They both appear as a degenerated amphidrome with smallest amplitudes near the Red River delta in the northwestern head of the Gulf (between 5 to 15 cm for M2 and below 5 cm for S2) (Hu et al., 2001). Given those values of amplitude, Van Maren et al. (2004) defined the tidal regime in the GoT as mesotidal, and locally even macrotidal, even though diurnal tidal regimes are usually mainly microtidal.

Our first objective in this paper is to propose a robust and simple approach that allows to quantify the sensitivity of the tidal solutions to bottom friction parameterization and to bathymetric changes in the Gulf of Tonkin. This article furthermore represents the first step in a more comprehensive modeling study aiming at representing the transport and the fate of sediments from the Red River to the Gulf using the tridimensional structured coupled SYMPHONIE-MUSTANG model (Marsaleix et al., 2008; Le Hir et al., 2011). In this framework, our final objective is to optimize the configuration (bathymetry) and parameterization (bottom stress) that will be used in this

forthcoming study. These objectives are based on the quantification of the response of the tidal solutions to the calibration of the bottom friction and to the improvements of the bathymetry.

As evidenced by Fontes et al. (2008) and Le Bars et al. (2010), local tidal simulations are mainly affected by the bathymetry and the bottom stress parametrization. These latter often lack of details in remote coastal regions and/or in poorly sampled regions (in terms of bathymetry and tide gauges). It is particularly the case for the GoT. By its location at the boundary between China and Vietnam and by its intense maritime transport activity, the region is extremely difficult to sample, in particular in the highly protected region of Ha Long Bay, in the strait of Hainan and in the nearshore/ coastal areas. In situ data and soundings are consequently rare and yet extremely valuable. The precise goal of the present study is therefore to build an improved bathymetry and coastline database over the GoT and to define the best configuration for bottom stress parameterization in this region, evaluating the impact of those parameters on the tidal representation in the GoT. The resulting optimized configuration will then be used for future numerical studies of ocean dynamics and sediment transport in the region. For that, we first worked on the improvement of the general and global bathymetric datasets available, i.e.: GEBCO (Monahan, 2008), the Smith and Sandwell bathymetry (Smith and Sandwell 1997) and the ETOPO1 Global Relief Model (Amante and Eakins, 2009) by incorporating new sources of data. We then worked on the optimization of the bottom stress parameterization. Our approach to address the issue of the parametrization and to evaluate the impact of our configuration setup is based on the use of the hydrodynamical model T-UGOm model of Lyard et al. (2006). Thanks to its frequency-domain solver, shortly described in the next sections, T-UGOm can indeed perform tidal simulations at an extremely limited computational cost (compared to time-stepping solver), in our case roughly 80 times faster than usual time-stepping hydrodynamical models (i.e. from few minutes for T-UGOm against hours/days). Furthermore, different formulations for the bottom friction can be prescribed as well as a varying spatial distribution of its related parameters (roughness or friction factor). These particular assets allow to perform a large number of sensitivity tests at a reasonable computational cost on bathymetric and bottom stress parametrization, hence to fasten up the processes of precise tuning and calibration/validation of our configuration.

In section III.2.2, we describe the bathymetry, shorelines and waterways construction as well as the numerical model and the modeling strategy in terms of sensitivity experiments. The data used for model evaluation and the metrics used for this evaluation are also presented in this section. In section III.2.3 we present the results regarding the sensitivity of simulations to bottom stress

parametrization and to bathymetry. Conclusions and outlook are given in section III.2.4.

III.2.2   Methods and tools

III.2.2.1   Shorelines and bathymetry construction

The first step of our work is to improve the shoreline and bathymetry precision. Two global digital shorelines are commonly used for representing the general characteristics of the GoT shorelines: the Global Self-consistent, Hierarchical, High-resolution Geography Database (GSHHG, Wessel and Smith, 1996) and the free downloadable maps from OpenStreetMap (OpenStreetMap contributors, 2015; retrieved from http://www.planet.openstreetmap.org). The GSHHG and OpenStreetMap shoreline products are both superimposed on satellite and aerial images of the GoT downloaded from Bing (https://www.bing.com/maps) and used now as our reference. Bing is chosen here for the accessibility to its opendata, which makes our shoreline construction method do-able by everyone. Fig.III.3 shows the shorelines products superimposed on a downloaded image of a small region of the GoT. When closely comparing the shorelines products to the images, it appears that the OpenStreetMap product looks fairly reasonable all along the coastlines of the GoT, except in the Halong Bay area (not shown) where the complex topography and the islets are clearly too numerous. However, the OpenStreetMap shoreline is most of the time shifted by a few meters westwards compared to the land (Fig. III.3). The GSHHG dataset suffers from the same problem but shifted by up to 500m eastwards. The observed shifts in both OpenSteetMap and GSHHG products are not documented but could be due, among others, to the use of nautical charts and/or local topography maps for product construction, which could have been collected before accurate GPS measurements in the area. Our objective in this study is to propose a grid matching the reality (i.e. Bing maps, our reference) as close as possible, therefore, none of these databases looked precise enough to meet our expectations. Consequently, we have built our own shorelines data set, named TONKIN_shorelines, by using the POC Viewer and Processing (POCViP) software (available on the CNRS sharing website , https://mycore.core-cloud.net/index.php/s/ysqfIlcX5njfAYD/download), developed at LEGOS. The satellite and aerial images of the region, previously downloaded from Bing, are georeferenced with POCViP. The software allows the user to draw nodes and segments with a resolution as fine as needed. The resulting TONKIN_shorelines database has a resolution down to 10m and its accuracy is observable on Fig.III.3. We followed the same procedure for building a waterways database of the Red River system. This latter is also included in TONKIN_shorelines. For the Ha Long Bay area, another

strategy has been considered since drawing by hand each islet would have been unaffordably time consuming. In this case, images from the Shuttle Radar Topography Mission (SRTM) (https://earthexplorer.usgs.gov/) were downloaded and coastlines got extracted and merged to TONKIN_shorelines.
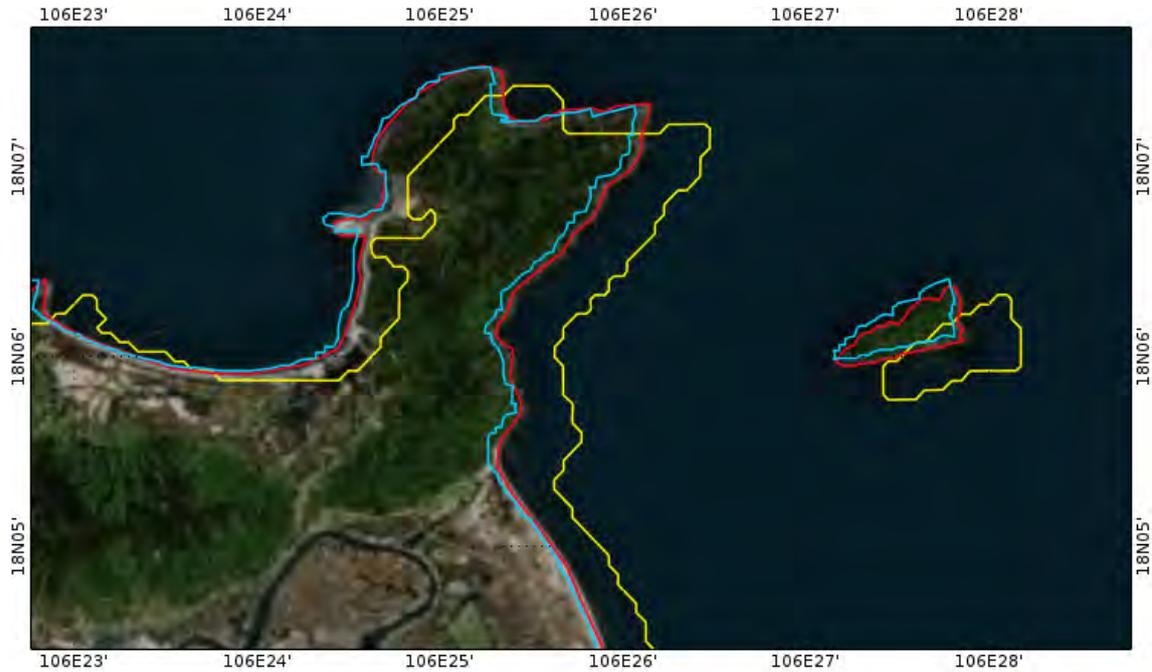
Figure III.3: Shorelines products from OpenStreetSap (blue line), GSHHS (yellow line) and TONKIN_shorelines (red line) superimposed on a satellite image downloaded from Bing over a small region of the GoT.

Because of the shallowness of the area, the bathymetry of the GoT is a critical point and could have a strong impact on tidal simulations as it is often the main constraint in tidal propagation (Fontes et al., 2008). The GEBCO 2014 (30 arc-second interval grid) dataset is largely based on a database of ship-track soundings, whose resolution can be locally much finer than 1 km resolution, but gridded data are provided with a 1 km resolution (as explained on the GEBCO website: https://www.gebco.net/data_and_products/historical_data_sets/. GEBCO dataset can hence be used to represent the slope and the shape of the basin at a relatively large scale (Fig.III.1 a,b). However, its resolution of approximately 1 km is too low to accurately represent detailed geomorphological features, in particular in coastal regions, near the delta and in the Ha Long Bay area. In the purpose of providing an improved tidal solution, we have developed a bathymetry with a better precision, named TONKIN_bathymetry (Fig. III.1 c,d). For that, we have merged the GEBCO bathymetry with digitalized nautical charts of type CM-93 via OpenCPM (https://opencpn.org/). Note that bathymetric data from nautical charts in coastal shallow areas are often chosen shallower than the "real" bathymetry for navigation security purposes. We also incorporated the tidal flats digital el-

evation model from Tong (2016). This author used waterlines from Landsat images of 2014 to construct a surface model from elevation contours. As tidal flats are suffering tidal regime with submersion during flood tide and exposure during ebb tide, their representation is crucial in tidal modelling. TONKIN_bathymetry is merged to TONKIN_shorelines dataset.

This scattered bathymetric dataset shows realistic small-scale structures and depths over the shelf and in the Ha Long Bay area. The details and the islets of the bay are now represented (Fig.III.1 c,d), as well as the Red River waterways. In the deeper part of the basin, near the boundary, two deeper branches (in light red) are distinguishable. These latter could correspond to the location of the ancient river bed of the Red River during the last glacial time, which split in two around 18° N-108° E (Wetzel et al., 2017). The biggest differences compared to GEBCO are observed in the central part of the region and in the Hainan Strait (Fig.III.1 e,f). In the strait, the GEBCO bathymetry underestimates depths by roughly 20m (approx. 50% in terms of relative difference) compared to TONKIN_bathymetry. In the center, differences can be up to 30m between the two datasets (not shown on the colorbar), corresponding to relative differences up to 100%. Such high observed discrepancies are due to the interpolation of the scattered measuring points from the nautical charts. High relative differences are also observed all along the coastlines, corresponding for most of them to the integration of the intertidal DEM in the Red River delta area, as well as to a better resolution in shallow areas obtained from the nautical charts. Discrepancies in most other parts of the basin remain roughly inferior to 30%. Patches of differences of about 40% between the datasets are also observed at the open ocean boundary of the domain, with GEBCO also underestimating depths in the southernmost part.

We draw attention to the fact that the TONKIN_bathymetry dataset provides an improvement to the available bathymetric dataset, but that some flaws and uncertainties still exist, partly due to sampling methods and shallower waters induced by nautical charts data.

III.2.2.2   Model, configuration and forcings

III.2.2.2.1   T-UGOm hydrodynamic model

The tidal simulations are based on the unstructured grid model T-UGOm (Toulouse Unstructured Grid Ocean Model) developed at LEGOS, and is the follow-up of MOG2D (Carrère and Lyard, 2003). In its standard applications, T-UGOm uses unstructured triangle meshes allowing for an optimal grid resolution flexibility, in particular to discretize complex coastal geometry regions, to follow various local dynamical constraints, such as rapid topography changes or to simply adapt

resolution in regions of special interest. The flexibility of unstructured triangle meshes is fully adequate for fine scale modelling, especially in delta or estuarine systems, whereas usual structured meshes may struggle to represent fine geography of certain areas. The T-UGOm model is widely used in global to coastal modelling, mostly for tidal and storm surges simulations: in the representation of semi and quarter-diurnal barotropic tides in the Bay of Biscay (Pairaud et al., 2008), in studying the tidal dynamics of the macro-tidal Amazon estuary (Le Bars et al. 2010),), in the representation of tidal currents over the Australian shelves (Cancet et al., 2017) and in assessing the role of the tidal boundary conditions in a 3D model in the Bay of Biscay (Toublanc et al., 2018). Furthermore, T-UGOm has proven its accuracy in global barotropic tidal modelling in the Corsica Channel (Vignudelli et al., 2005) and in a global assessment of different ocean tide models (Stammer et al., 2014).

In addition to its traditional time-stepping solver, it has the remarkable particularity to include a frequency-domain solver kernel, that solves for the 2D/3D quasi-linearized tidal equations. This spectral mode solves the quasi-linearized Navier-Stokes equations in the spectral domain, in a wave by wave, iterative process (to take into account non-linear effects such as bottom friction). It has demonstrated its efficiency (accuracy, computational cost) as well for the astronomical tide simulation as for the non-linear tides. The frequency-domain solver can be used either on triangle or quadrangle unstructured mesh, and therefore can be used on any C-grid configuration. Compared to a traditional time-stepping mode that simulates the temporal evolution of the tidal constituents over a given period, the numerical cost of the frequency-domain mode (2D) is roughly 1000 times smaller.

For our purpose of assessing the sensitivity to various parameters of the tide representation by the model, T-UGO is set up in a 2D barotropic, quadrangle grid, shallow-water and frequency-domain mode (version of the code: 4.1 2616). This configuration (including TONKIN_bathymetry and the specific version of T-UGOm code) is from hereafter named TKN. The main advantage of this fast and reduced-cost-solver is the possibility to perform in an affordable time a wide range of experiments at the regional or global scale, in order to parameterize the model: optimize bottom stress parametrization, test bathymetry improvements and others numerical developments. In our case, the run duration of a spectral simulation with T-UGOm lasts on average 6 mn (CPU time), which is roughly 40 times quicker than a simulation with a regional circulation model such as SYMPHONIE (Marsaleix et al., 2008, CPU time is approximately 4h for a 9-month simulation, corresponding to the required time with SYMPHONIE to separate the tidal waves).

Another useful functionality from T-UGOm for our study is the possibility to locally prescribe the bottom friction, including the roughness length but also the choice of parametrization type. In some shallow coastal regions like the GoT, the presence of fluid mud flow and fine sediments can induce dramatic changes on bottom friction. The quadratic parameterization may be obsolete and a linear parameterization more adequate (Le Bars et al., 2010) and will be tested hereafter. This functionality is essential in those particular regions like shallow estuaries, where the influence of bottom friction on the tides propagation is crucial.

III.2.2.2.2   Numerical domain over the GoT

The numerical domain over the GoT, built from the TONKIN_bathymetry, is discretized on an unstructured grid made of quadrangle elements (Fig III.3). The most commonly used elements in T-UGO are triangles, however here the final goal of our work is to use the resulting grid for coupled hydrodynamical-sediment transport models like SYMPHONIE-MUSTANG (Marsaleix et al., 2008; Le Hir et al., 2011) using quadrangle structured C-grids. We therefore run the T-UGO tidal solver on a quadrangle grid. As in Madec and Imbard (1996), this grid is semi-analytical. A first guess is provided by the analytical reversible coordinate transformation of Bentsen et al (1999) which produces a bipolar grid. The singularities associated with the two poles are located in the continental mask, slightly to the north of the numerical domain, where the horizontal resolution is the strongest (Fig.III.4). This first guess is then slightly modified to control the extension of the grid offshore, in practice to prevent extension beyond the continental shelf. As in Madec and Imbard (1996) this second stage is partly numerical (and preserves the orthogonality of the axes of the grid). The largest edges of the quadrangles are about 5 km at the boundaries of the domain and the smallest of about 150 m long, with a maximum refinement located in the river channels (Fig.III.4). This grid allows to represent the complexity of the islets of Ha Long Bay as well as the details of the coastlines of the Red River Delta. A regular C-grid would hardly take into account such complex topography and details.

III.2.2.2.3   Tidal open-boundary conditions

For modelling barotropic tidal waves, nine tidal constituents have been imposed as open boundary conditions (OBC) in elevation (amplitude and phase) for our domain: O1, K1, M2, S2, N2, K2, P1, Q1 and M4. Since the astronomical spectrum of tide is dominant in the GoT, 8 out of the 9 constituents simulated are astronomical constituents, and M4 is chosen here as a representative of all linear interactions. These constituents, ordered by their amplitudes (in the GoT),
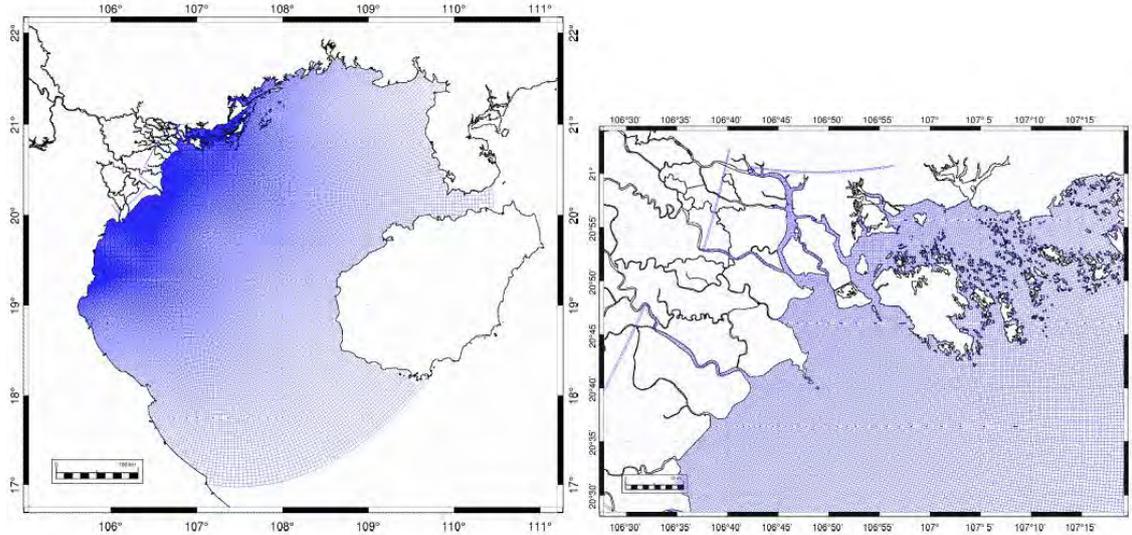
Figure III.4: Model mesh over the GoT (left) with a zoom in Halong Bay region (right). The maximum refinement (150 m) is reached in the river channels.

are the main tidal waves in the GoT, and come from the FES2014b global tidal model resolved on unstructured meshes but distributed on a resolution coherent $1/16° \times 1/16°$ grid. FES2014b (Carrère et al., 2016) is the most recent available version of the FES (Finite Element Solution) global tide model that follows the FES2012 version (Carrère et al., 2012). The FES2014b global tidal atlas includes 34 tidal constituents and is based on the resolution of the tidal barotropic equations with T-UGOm (frequency-domain solver for the astronomical tides and time-stepping solver for the non-linear tides, described in the above section). The FES2014b bathymetry has been constructed from the best available (compared to previous FES versions) global and regional DTMs (Dynamical Topography Models), and corrected from available depths soundings (nautical charts, ship soundings, multi-beam data) to get the best possible accuracy, typically 1.3 cm RMS (Root Mean Square error) for the M2 constituent in the deep ocean before data assimilation. The tidal simulation performed using this configuration and without assimilation is called FES2014b-without-assimilation. Moreover, in addition to the hydrodynamic solutions, altimetry data-derived and tide gauges harmonic constants have been assimilated, using a hybrid ensemble/representer approach, to improve the atlas accuracy for 15 major constituents and fulfill the accuracy requirements in satellite ocean topography correction. This version of FES will from hereafter be named FES2014b-with-assimilation in the following, in comparison to FES2014b-without-assimilation. Thanks to the accuracy of the prior FES2014b-without-assimilation solutions and the subsequent higher efficiency of data assimilation, this latest FES2014b-with-assimilation version of

the FES2014 atlas has reached an unprecedented level of precision and has shown a superior accuracy than any others previous versions (see http://www.aviso.altimetry.fr/en/data/products/auxiliary-products/global-tide-fes.html and F. Lyard personal comments).

The tidal distribution of the O1, K1, M2 and S2 tidal waves and their first harmonics from FES2014b-with-assimilation and FES2014b-without-assimilation is shown in Figs. III.5 ab, III.6ab, III.7 ab, III.8ab, as well as their error along the satellite altimetry track dataset of CTOH-LEGOS (described below in section III.2.2.3.1). FES2014b-with-assimilation shows negligible errors compared to FES2014b-without-assimilation thanks to the assimilation. The main interest of using FES2014b-without-assimilation in our study is to assess the real capacity of the FES model in reproducing the tidal harmonics without using data assimilation, whereas FES2014b-with-assimilation can be used together with satellite altimetry as a reference to evaluate tidal solutions errors.

III.2.2.3   Simulations and evaluation

We use the model configuration described above to assess the impact of the improvement of our bathymetry database and to optimize the representation of bottom friction in the model. For that we perform sensitivity simulations that we compare with available data using specific metrics. Those tools and methods are presented in this section.

III.2.2.3.1   Modelling strategy and sensitivity experiments

The T-UGO 2D model (in its frequency-domain, iterative mode) is run on the high-resolution grid described in section III.2.2.2. The following sections describe the tests performed for the bottom friction parametrization.

a) Bottom stress parametrization

In shallow areas where current intensities are strong due to a macro-tidal environment combined to strong rivers flows and winds forcing, the sensitivity of the model to the bottom stress is significant. The bottom stress is thus a crucial component for modelling nearshore circulation and sediment transport dynamics (Gabioux et al. 2005; Fontes et al., 2008). The bottom stress formulation depends upon a non-dimensional bottom drag coefficient (or friction coefficient) C_D and can be obtained as follows, in barotropic mode:

$$\tau_b = \rho C_D |\overline{u}| \overline{u} \tag{III.1}$$

with $\overline{u}$ the depth averaged velocity and the fluid density.

In this study, we test two commonly used parameterizations: a constant drag coefficient C_D assuming a constant speed profile and a drag coefficient C_D depending upon the roughness height z_0.

In the first parameterization, a constant profile of the speed is assumed over the whole water height, leading to quadratic bottom stress and a constant C_D that depends on the Chézy coefficient C and on the acceleration due to gravity g (Dronkers 1964):

$$C_D = \frac{g}{C^2} \tag{III.2}$$

In the second parameterization, a logarithmic profile of the speed is assumed over the whole water column (Soulsby et al. 1993), leading to a C_D depending upon the roughness length z_0, the total water height H and the von Karman's constant $\kappa = 0.4$:

$$C_D = \left(\frac{\kappa (H - z_0)}{H \ln \frac{H}{z_0} + z_0 - H} \right)^2 \tag{III.3}$$

The roughness length z_0 (also called roughness height) depends not only on the morphology of the bed (i.e. the presence of wavelets or not) but also on the nature of the bottom sediment. In presence of fluid mud, the friction is considered as purely viscous (Gabioux, 2005). However, the repartition of sediments and the structure of the sea bed are not uniform over the GoT shelf as the Red River discharge causes patches of sediments of different natures (Natural Conditions and Environment of Vietnam Sea and Adjacent Area Atlas, 2007). Consequently, we can expect z_0 to vary spatially. This issue can be addressed with T-UGOm since it contains a domain partition algorithm allowing to take into account the spatial variability of the sea bed roughness. Furthermore, this C_D parameterization which includes a logarithmic profile of the speed, allows to adapt the C_D to the model vertical resolution by considering the water column depths, as a way to correspond to the friction coefficient resolution in 3D models.

In the case of fluid mud when the bottom friction is purely viscous and the velocity profiles are linear, Gabioux et al. (2005) described the τ_b as follows:

$$\tau_b = \rho r \overline{u} \tag{III.4}$$

with r corresponding here to the friction coefficient.

A third parameterization of the coefficient of friction is tested in this study: a linear profile of the speed is assumed over the whole water column which characterizes viscous conditions. In this case, a linear bottom stress is assumed and r depends on the frequency of the forcing wave ω (here O1) and the fluid kinematic viscosity ν:

$$r = \sqrt{\omega \nu} \tag{III.5}$$

In this study, these three formulations of the coefficient of friction (Eqs. III.2, III.3 and III.5) are tested for model parameterization, varying respectively the value of C_D, the value of z_0 and the value of r.

b) Sensitivity to uniform friction parameters

Sensitivity numerical experiments were first conducted in order to assess the sensitivity of the model to uniform parameters of friction for two of the parameterizations described above: a quadratic bottom stress with a uniform drag coefficient C_D (Eqs. III.1 and III.2) and a logarithmic variation of C_D depending on a uniform bottom roughness height z_0 (Eq. III.3). For that, we performed a first set (SET1) of 45 tests running the model with a constant C_D with C_D values spanning from 0.5 10^{-3} to 5.0 10^{-3} m (see Fig.III.9 where we plotted C_D values spanning from 0.5 to 2.5 10^{-3} m). We then performed a second set (SET2) of 6 tests running the model with a logarithmic C_D by testing values from 1.0 10^{-1} to 1.0 10^{-6} m for z_0 (see Fig.III.10).

c) Sensitivity to the regionalization of the roughness coefficient

As mentioned in the previous section, a uniform roughness coefficient does not usually allow for reaching a satisfying level of accuracy over the whole domain, since the variability of the seafloor morphology is not fully taken into consideration. To take this variability into account, the spatial

SET 3	A	B	C	D	E	F	SET 4	1	2	3	4	5	6	7
Mud region (r)	1.18×10^{-4}	1.18×10^{-4}	1.18×10^{-4}	1.18×10^{-4}	1.18×10^{-4}	1.18×10^{-4}	Region 1 (z_0)	1.0×10^{-2}	1.0×10^{-3}	1.0×10^{-4}	1.0×10^{-4}	1.0×10^{-4}	1.0×10^{-5}	1.0×10^{-5}
z_0 in the rest of the domain	1.0×10^{-6}	1.0×10^{-5}	1.0×10^{-5}	1.0×10^{-4}	1.0×10^{-3}	1.0×10^{-2}	Region 2 (z_0)	1.5×10^{-5}	1.5×10^{-5}	1.5×10^{-5}	1.5×10^{-5}	1.0×10^{-4}	1.5×10^{-5}	1.5×10^{-5}
							Region 3 (z_0)	1.0×10^{-4}	1.0×10^{-4}	1.0×10^{-4}	1.5×10^{-5}	1.5×10^{-5}	1.0×10^{-4}	1.0×10^{-3}

Table III.1: Description of SET 3 and SET 4 (in m).

variability of the seabed roughness must be prescribed to the model. For that, our study area is divided into several zones based on seabed sediment types repartition obtained from the Natural Conditions and Environment of Vietnam Sea and Adjacent Area Atlas (2007). The third set of sensitivity experiments (SET3, tests A to E in Table III.1) consisted in prescribing a linear velocity profile only in the area of fine mud, following Eqs. III.4 and III.5, with a fixed r = 1.18×10^{-4} m (see Fig.III.10 a), and to test different values of uniform z_0 (from 1.0×10^{-2} to 1.0×10^{-6} m) over the rest of the region, prescribing a logarithmic velocity profile. This value of r is taken from the value empirically tuned on the region of the Amazon estuary and shelf with the configuration described in Le Bars et al. (2010).

The fourth set of sensitivity experiments (SET4, tests 1 to 7 in Table III.1) consisted in dividing the region into three zones, according to a supposed spatial distribution of the seabed sediments, inspired from the above-mentioned Vietnamese atlas (Fig.III.12 b): zone 1 is mostly composed of muddy sand, zone 2 of mud and zone 3 of sand and coarser aggregates. In each zone, a value of z_0 (from 1.0×10^{-2} to 1.0×10^{-5} m) is prescribed following a logarithmic speed flow (Eq. III.3). Note that for this set of experiments every combination of z_0 were tested, yet for the sake of clarity we show and describe in section III.2.4 only the ones with errors (see section III.2.2.3.3) for S2 solutions below 2.5 cm. The fifth and last set of experiments (SET5) consisted in dividing the domain into twelve zones, in order to refine the representation of the spatial distribution of the seafloor's sediments following the Vietnamese atlas (Fig. III.12c). Zones 1 and 11 correspond to muddy sand; zones 2, 6, 10 and 12 to sand slightly gravel; zones 3 and 5 to sandy mud; zone 4 to fine mud; zone 7 to sandy gravel; zone 8 to mud slightly gravel; and zone 9 to sand. Different z_0 values

(varying from 1.0×10^{-2} to 1.0×10^{-5} m), using a logarithmic velocity profile, were prescribed to each of the 12 twelve zones and corresponding run were performed, each time imposing a random and different value to each zone.

III.2.2.3.2 Satellite data and tide gauges data for model assessment

The evaluation of the performance of the simulations is made with along-track tidal harmonics obtained from a 19-year (1993 - 2011) long time series of satellite altimetry data available every ten days from TOPEX/Poseidon (T/P), Jason-1, and Jason-2 missions (doi: 10.6096/CTOH_X-TRACK_-Tidal_2018_01). These data are provided by the CTOH-LEGOS (Birol et al., 2016). The tracks of the altimeters passing over the GoT are shown in Fig. III.5 to III.8, and are spaced by approximately 280 km. To complement those data in the intertrack domain, we also compare our simulations with the FES2014b-with-assimilation tidal atlas, as explained in section III.2.2.3.

Harmonic tidal constituents at 11 tide gauge stations are also used for evaluation of the simulations. The data are distributed by the International Hydrographic Organization (`https://www.iho.int/`) and are available upon request at `https://www.admiralty.co.uk/ukho/tidal-harmonics`. The name and position of these stations are shown on III.5a. Amplitudes and phases of O1, K1, M2 and S2 at the 11 gauge stations are available in Chen et al. (2009).

III.2.2.3.3 Metrics

For comparison of the simulations with the tidal harmonics from satellite altimetry, two statistical parameters (metrics) are used. These are the root mean square error (RMS*) and the mean absolute error (MAE). The RMS* computation is based on a vectorial difference which combines both amplitude error and phase error into a single error measure. The errors computations are detailed in Appendix.

III.2.3 Results

In this section we present the results concerning the sensitivity of the modeled tidal solutions to the choice of bathymetry dataset and to the choice of bottom friction parameterization. Spatially varying uniform friction parameters only slightly improve the tidal solutions compared to uniform parameters. Furthermore, prescribing a linear parameterization in supposed fluid mud areas does not allow to significantly improve the solutions, unlike in Le Bars (2010). Lastly, the reconstructed bathymetry dataset allows to strongly improve the semi-diurnal tidal solutions. The improvements consist mainly in a correction near the coasts and in reducing the errors in phase
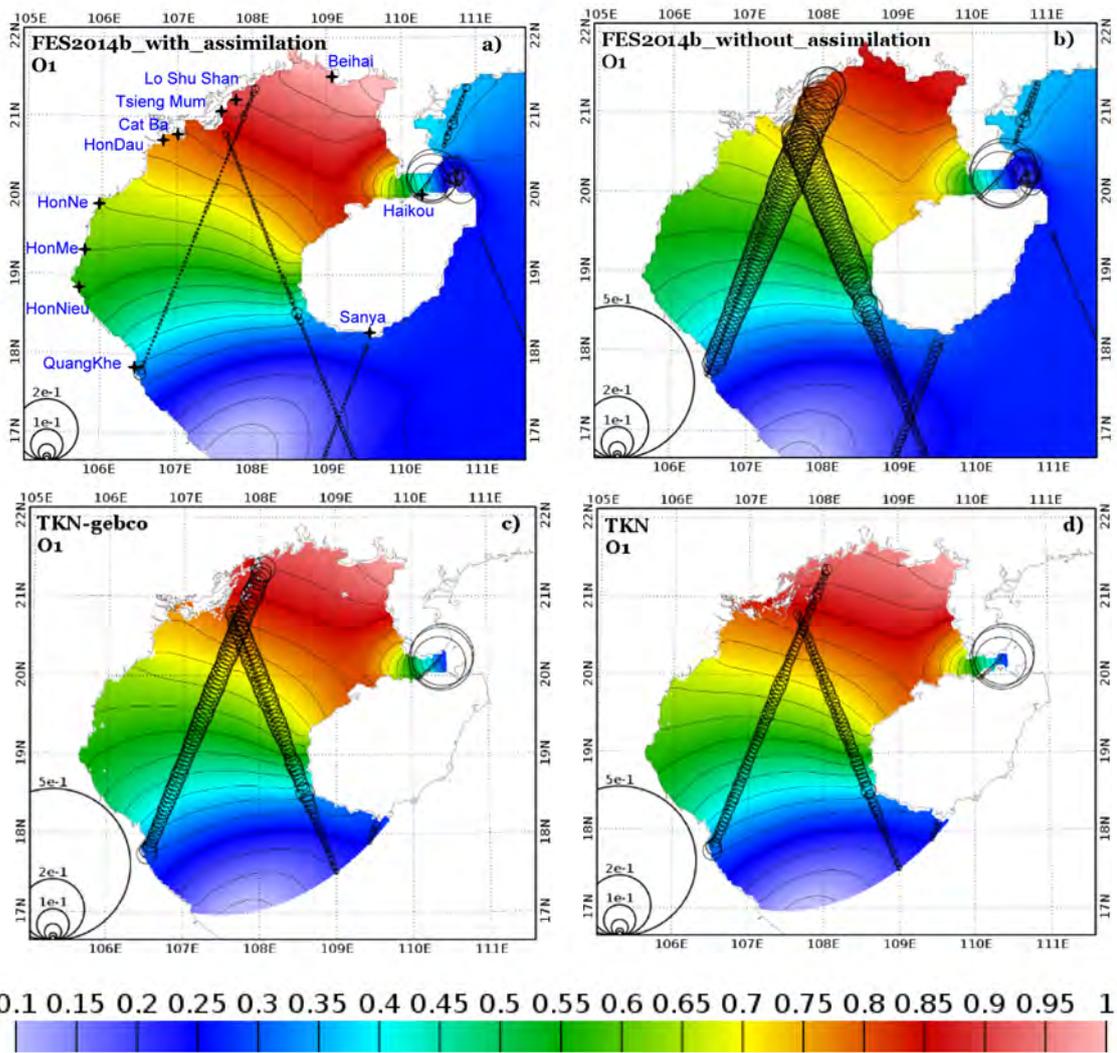
Figure III.5: O1 tidal amplitude (in m) from different products: (a) FES2014b-with-assimilation, (b) FES2014b-without-assimilation, (c) TKN-gebco and (d) TKN. The circle diameter is proportional to the complex error (Appendix ; Eq. III.6) between the solutions and satellite altimetry (in m).

0.05 0.1 0.15 0.2 0.25 0.3 0.35 0.4 0.45 0.5 0.55 0.6 0.65 0.7 0.75 0.8 0.85 0.9 0.95
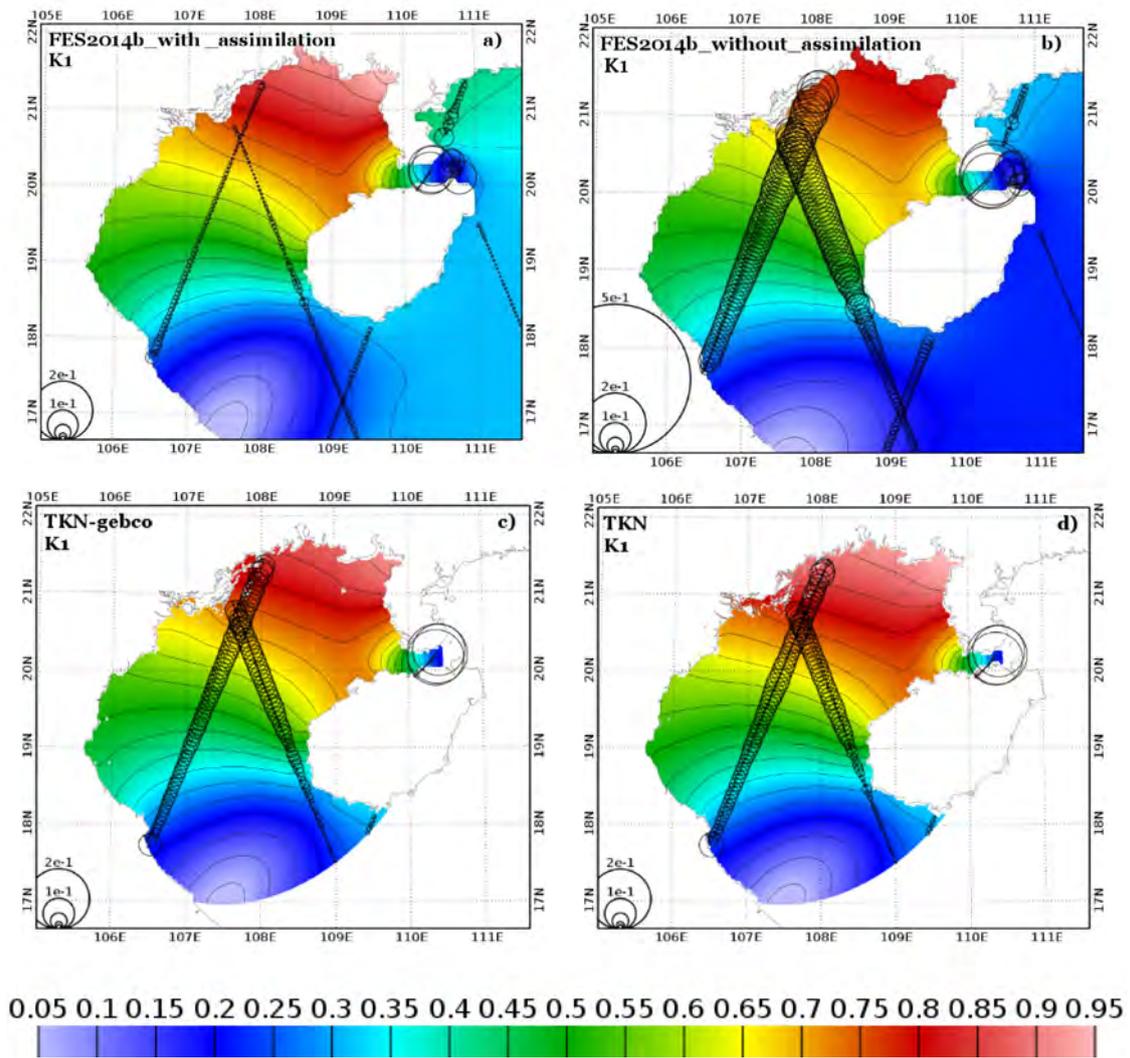
Figure III.6: Same as Fig. III.5 for K1.
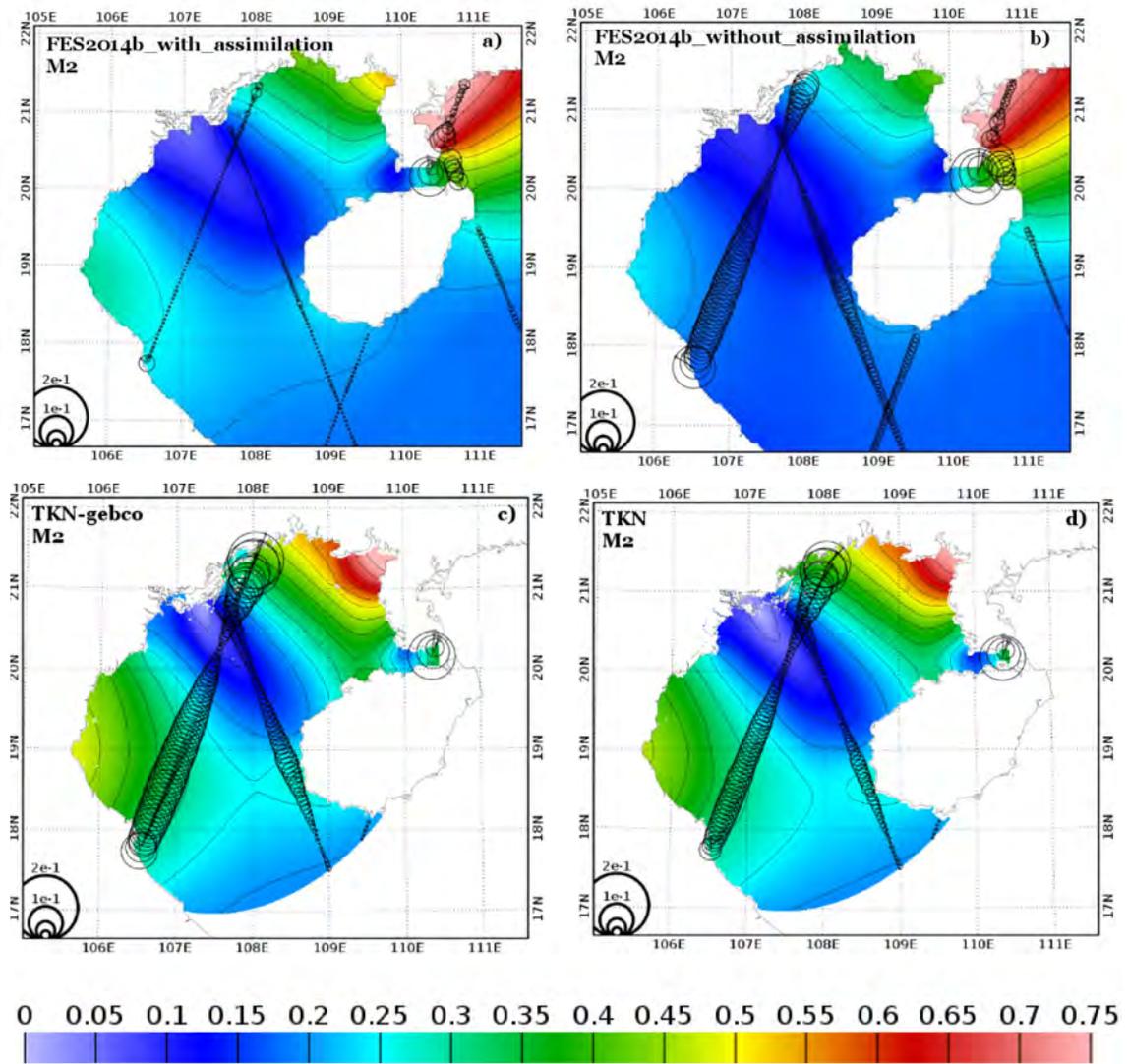
Figure III.7: Same as Fig. III.5 for M2.
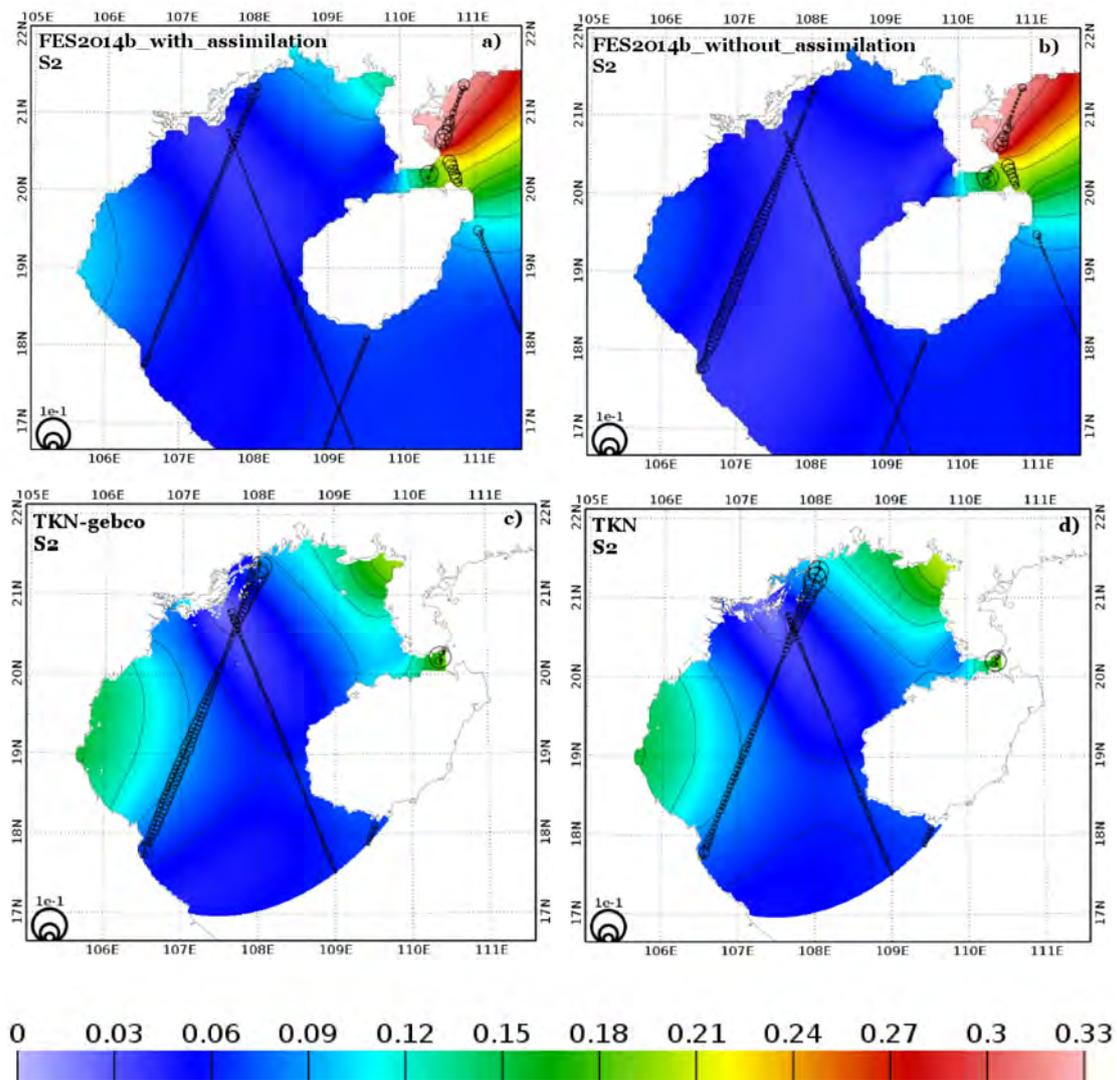
Figure III.8: Same as Fig. III.5 for S2.

(as it can be expected from a bathymetry upgrade). We present the results of the conducted sensitivity experiments in details in the following sub-sections.

III.2.3.1 Model sensitivity to bottom stress parameterization

III.2.3.1.1 Sensitivity to a constant or varying C_D (SET1 and SET2)

We first analyse in this section and in the next one the sensitivity to the parameterization of bottom friction. Firstly, to show the sensitivity to the choice of uniform friction parameters, the model errors (Appendix; Eq. III.6) compared to satellite altimetry are shown in Fig.III.9 (SET1) and III.9 (SET2), for the main tidal constituents (O1, K1, M2, S2) for each values of uniform C_D and z_0 tested in SET1 and SET2 described in section III.2.2.3. On both Figs. III.8 and III.9, the space in between two solid lines corresponds to the errors for the considered wave (see legend) and the yellow line represents the cumulative errors for the four waves. The dashed red line represents the smallest cumulative error (i.e. the minimum value reached for the yellow line).
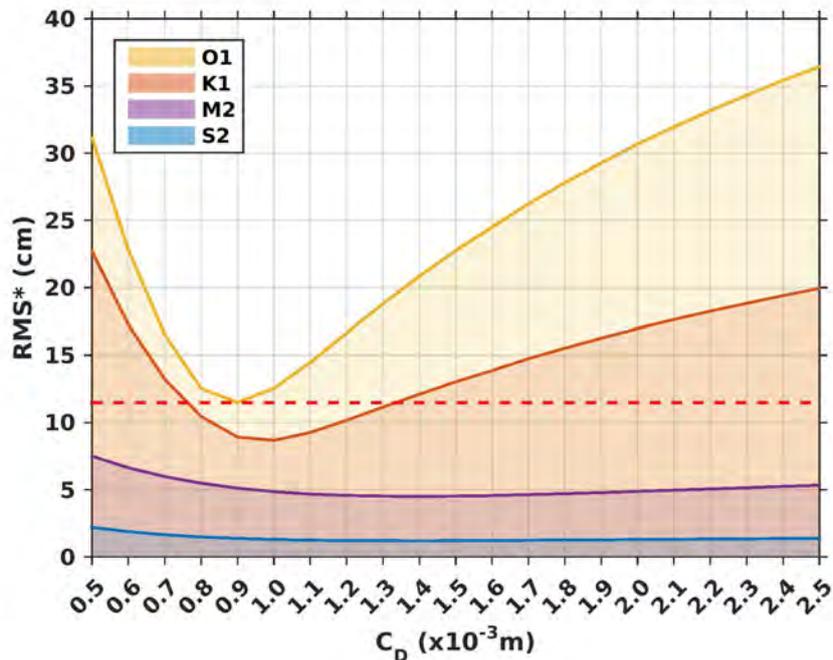
Figure III.9: Model complex errors (Appendix ; Eq. III.6) relative to altimetry alongtrack data for tests performed with varying the values of the uniform drag coefficient C_D over the domain (SET1). The space in between two lines corresponds to the error for each wave. The yellow line therefore corresponds to the cumulative error for all four waves. The red dashed line corresponds to the smallest cumulative error, here equals to 11.50 cm, and obtained for $C_D = 0.9 \times 10^{-3}$ m.

First of all, the diurnal waves O1 and K1 are more affected by the changes in the values of C_D and z_0 than the semi-diurnal waves M2 and S2 (Figs. III.8 and III.9). This can be explained by the fact that diurnal tides are of greater amplitude than semi-diurnal in the Gulf of Tonkin, thus the tidal friction is truly non-linear for O1 and K1 and marginally only for M2 and S2. For C_D values below
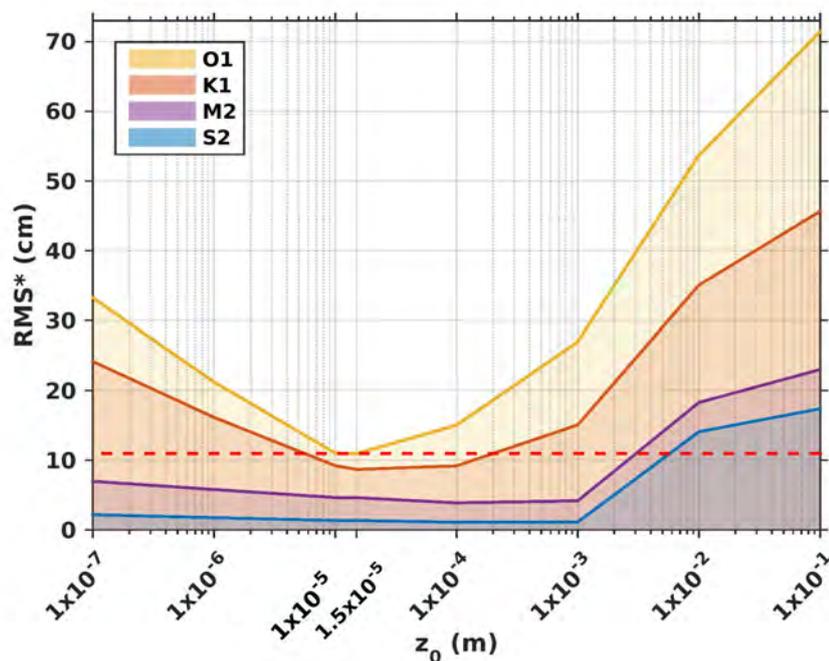
Figure III.10: Model complex errors (Appendix ; Eq. III.6) relative to altimetry data for tests performed with varying the values of the uniform z_0 over the domain (SET2). The space in between two lines corresponds to the error for each wave. The yellow line corresponds to the cumulative errors for all four waves. The red dashed line corresponds to the smallest cumulative error, here equals to 10.96 cm, and obtained for z_0=1.5 $\times 10^{-5}$ m.

0.6 and above 1.0×10^{-3} m, O1 and K1 errors are larger than errors for M2 and S2. For example, for C_D=2.5$\times 10^{-3}$ m the errors for O1 are roughly 4 to 11 times larger than errors for M2 and S2 and errors for K1 are roughly 3 to 10 times larger than errors for M2 and S2, respectively). Small values of C_D also induce large errors of O1 and K1 (for C_D=0.5 $\times 10^{-3}$ m, errors for O1 are roughly 1.5 to 3.8 times larger than errors for M2 and S2, and errors for K1 are roughly 2.8 to 6.9 times larger than errors for M2 and S2, respectively). High and small values of z_0 also trigger larger errors on the diurnal waves (Fig.III.10). Secondly, the tests of sensitivity to a spatially constant friction coefficient C_D show that the lowest error is reached for C_D=0.9$\times 10^{-3}$ m (the cumulative error is equal to 11.50 cm) (Fig.III.9). This value of C_D is roughly half lower than those used for the whole South China Sea (2.0$\times 10^{-3}$ m: Fang et al. 1999; Cai et al., 2005) and similar to the one used in the GoT by Nguyen et al. (2014) of 1.0$\times 10^{-3}$ m. The tests of sensitivity to the roughness length z_0 show that the value z_0=1.5$\times 10^{-5}$ m yields the least errors (the cumulative error is equal to 10.96cm) (Fig.III.10). This is a relatively small roughness length value, indicating a sea bed composed of very fine particles. Finally, the use of a constant C_D parametrization with a C_D of 0.9 $\times 10^{-3}$ m or a constant roughness length with a z_0 of 1.5 $\times 10^{-5}$ m leads to almost identical errors (0.54 cm of differences). The similarity of the results between the two simulations are due to the values of C_D obtained for z_0=1.5$\times 10^{-5}$ m: those values vary spatially from 0.8 to 1.1$\times 10^{-3}$ m, and are thus very

close to the optimized value of C_D=0.9× 10^{-3} m for a constant C_D (figure not shown). This small spatial variability of the varying C_D explains why the results of the two optimized simulations from SET1 and SET2 are finally similar. The rather low values of friction (0.9 × 10^{-3} m) and roughness coefficients (1.5× 10^{-5} m) suggest the presence of a majority of fine sediments in the GoT. This is consistent with the results from Ma et al. (2010), who found the western and central parts of the GoT to be mainly composed of fine to coarse silts, with a few patches of sand next to Hainan island.

Thirdly, the lowest error for each wave is reached for different values of C_D and z_0. In SET1, the lowest error value for O1 is reached when C_D= 0.9× 10^{-3} m, while the lowest error value for K1 is reached for C_D= 1.0× 10^{-3} m. The lowest errors values of the semi-diurnal waves are reached for C_D= 1.4× 10^{-3} m (Fig.III.8). In SET2, the lowest errors values of the diurnal waves are reached for z_0 =1.5× 10^{-5} m and are reached for z_0 =1× 10^{-3} m for the semi diurnal waves (Fig.III.9). This finding is of course unphysical, and the reader must keep in mind that optimal parameter setting also often deals with model errors numerical compensation. In our study, it is quite obvious that the model bathymetry is far from perfect despite the large efforts carried out to improve the topographic dataset, and remaining errors due to bathymetry imperfections can be partly canceled by the use of an adequate (i.e. numerical, not physical) friction parameter. As bathymetry-induced errors will strongly be affected by the tidal frequency group (species), and since bathymetry directly and distinctly impacts the waves' phase propagation, we can expect that optimal friction parameterization alteration (and corresponding alterations of the bottom shear stress) will slightly vary in a given frequency group but strongly from one to another. The examination of sensitivity studies tends to promote the idea that these differences are mostly due to remaining errors in the bathymetric dataset and the final decision for an optimal friction parameterization will be based on the best compromise for the overall solution errors. As the K1 and O1 sensitivity to friction alteration is prevailing, the compromise is of course mostly driven by these two tidal waves.

To assess the significance of the differences between two parameterizations, Fig. III.11 presents spatially the relative differences between the two simulations (SET1 and SET2), in terms of performance in amplitude and phase, taking FES2014b-with-assimilation as a reference. Negative values (in blue) indicate that the simulation from SET2 with a z_0 of 1.5× 10^{-5} m produces the smallest differences to the reference, while positive values (in red) indicate that the simulation from SET1 with a constant C_D of 0.9× 10^{-3} m produces the smallest differences to the reference. For K1, values are positive almost all over the GoT basin, indicating that the tidal solution from simulation with a

constant C_D (SET1) performs better. However the differences of performance between the two simulations are very small: 0.5%. For O1, M2 and S2 cases, values are mostly negative over the GoT, suggesting that simulation with a z_0 of 1.5×10^{-5} m (SET2) better represents the tidal solutions for these three waves than simulation with a constant C_D (SET1). Once again however, these improvements are really small (lower than 5%). These results finally show that the tidal solutions are not very sensitive to changes of bottom friction parameterization, from a constant C_D to a C_D varying with z_0.
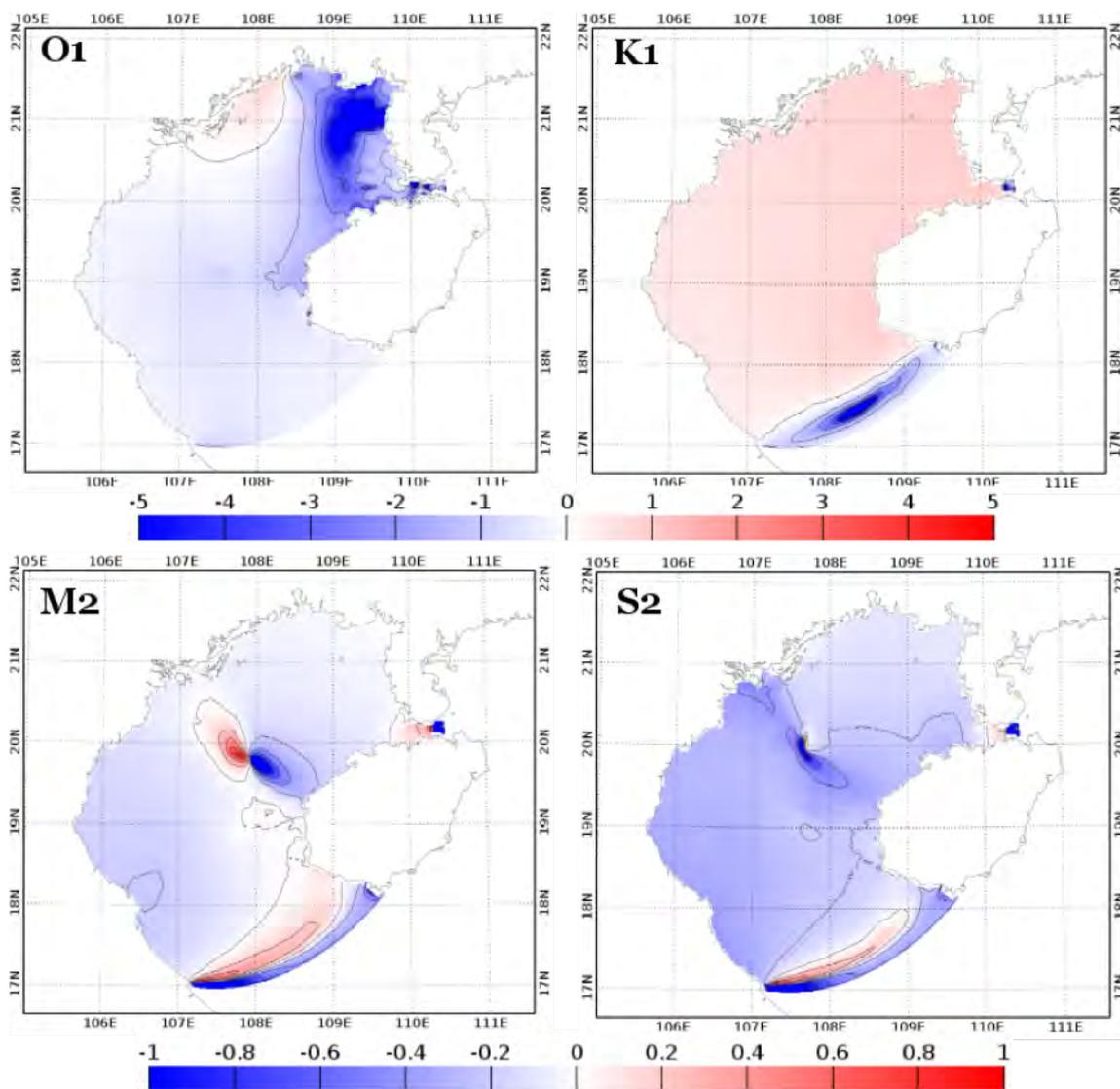
Figure III.11: Relative differences (in %) between simulation with C_D=f(z_0=1.5×10^{-5},H) and simulation with C_D=0.9×10^{-3} m compared to FES2014b-with-assimilation (as a reference) for the tidal harmonics of O1, K1, M2 and S2.

III.2.3.1.2 Sensitivity to the value of spatially varying roughness length (SET3, SET4, SET5)

This section presents the results of the tests performed to assess the model sensitivity to a regionalized roughness coefficient (see Table III.1 and Fig.III.12).
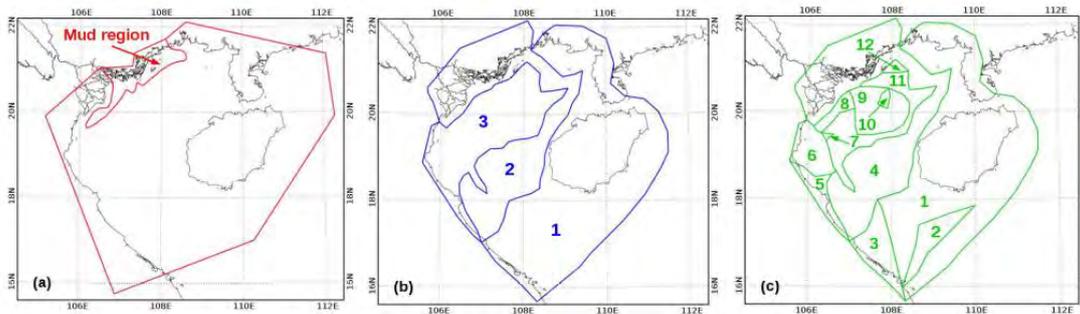
Figure III.12: Spatial partitioning of the domain for the set of experiment SET3, (a), for SET4 (b) and for SET5 (c).

a) Sensitivity to a quadratic or linear stress (SET3 vs. SET2)

No significant improvement of the tidal solutions is obtained from SET3, i.e. by imposing a linear flow in the mud region (where the resolution is the highest), compared to the tests performed with spatially uniform parameters (drag coefficient, SET1 and bottom roughness length, SET2, Figs. III.8 and III.9)(Fig. III.13). The cumulative error of all four waves (yellow line) is always above the 10.96 cm value of the smallest error found for SET2 (the smallest cumulative error of 11.33 cm is obtained for test C). Results from SET3 (Tests A to F) show that the solutions still greatly depends upon the roughness length values imposed to the rest of the region, with errors increasing with low and high values of z_0 : from tests D to F, cumulative errors increase by a factor 3.5 with z_0 values increase from 1×10^{-4} to 1×10^{-1} m; from test A to B, errors decrease by a factor 2 with values decreasing from 1×10^{-6} to 1×10^{-5} m (Fig. III.13). As previously observed, the diurnal waves O1 and K1 (in tests A to F) are more sensitive to changes in z_0 than the semi-diurnal M2 and S2 waves: for $z_0 = 1 \times 10^{-2}$ m, errors of O1 are 3 and 7 times larger than errors of M2 and S2 respectively, and errors of K1 are 4.5 to 11 times larger than errors of M2 and S2, respectively.

Tests from SET3 suggest that the model sensitivity to bottom friction parameterization in the area
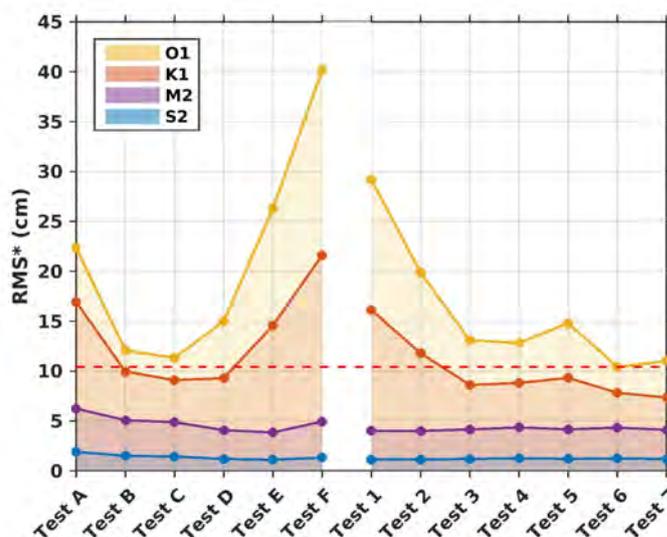
Figure III.13: Model complex errors (Appendix; Eq. 6) relative to altimetry data for tests listed in Table 1 performed with non-uniform values of z_0 (SET3 and SET4). The space in between two lines corresponds to the errors for each wave. The yellow line corresponds to the cumulative errors for all four waves. The red dashed line corresponds to the smallest cumulative error, found for Test 6 (SET 4), equals to 10.43 cm.

of fine mud is limited and therefore poorly influences the cumulative errors over the GoT. This is due to the fact that tidal energy fluxes and bottom dissipation rates are extremely small in this area of fine mud near the Red River delta, as can be seen on Fig. III.14. : most of the tidal dissipation occurs along the western coast of Hainan Island and in the Hainan Strait (values up to -0.2 W m^{-2} in these areas for O1, K1 and M2). Note that the value of r (which is here set to 1.18x10^{-4} m following the optimization of Le Bars et al. 2010 over the Amazon shelf) could be tested and could lead to an optimized value for the GoT. However, this would have presumably not significantly affected the final tidal solutions since the choice of a linear parameterization in the area of fine mud did not significantly modify the tidal solutions.

b) Sensitivity to a spatially varying roughness length (SET4 and SET5 vs. SET2)

Improvement of the tidal solutions is obtained from SET4, i.e. by varying spatially the values of the bottom roughness length (imposing a logarithmic speed profile). The cumulative error of all four waves (yellow line) reach a minimum value of 10.43 cm for Test 6 (red dashed line), which reduced the error found in SET2 by 0.53 cm. This value is reached by imposing values of z_0=1.5$\times$ 10^{-5} m in regions 1 and 2 (Fig.III.12) and z_0=1$\times$ 10^{-4} m in region 3. Moreover, results from Test 1 and Test 2 show that the solutions largely depend upon the roughness length imposed in region 1 (z_0 values of 1$\times$ 10^{-2} to 1$\times$ 10^{-3} m). Again, as already mentioned in the previous section, the remaining bathymetry-induced errors in our solutions have probably damaged the precise identification of
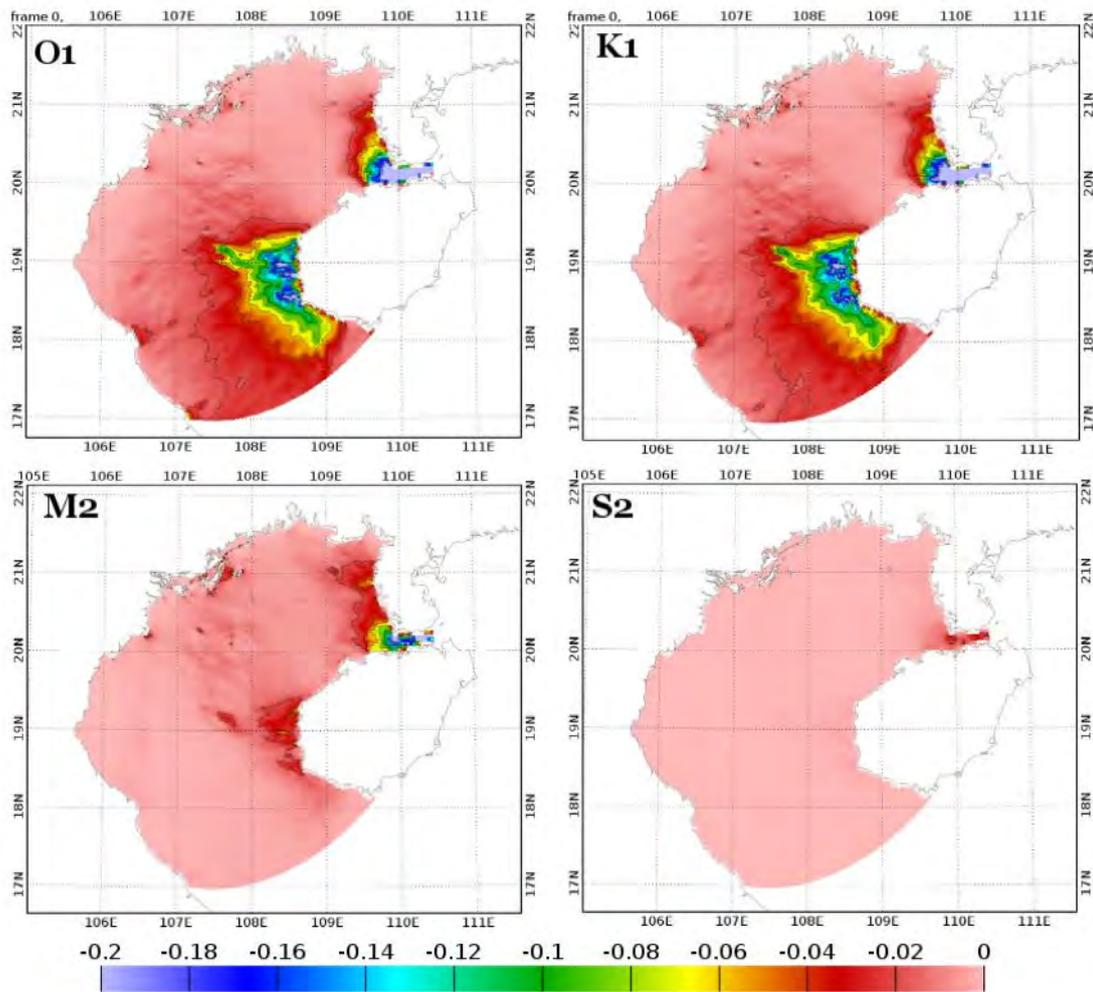
Figure III.14: Bottom dissipation flux (W m^{-2}) for O1, K1, M2 and S2 computed from model outputs of simulation "TEST 6".

truly physical friction parameterization in this spatially varying roughness length experiment.

The significance of these results is assessed on Fig. III.15. Simulation from Test 6 (SET4) better represents K1 harmonics while simulation with varying $C_D = f(z_0 = 1.5 \times 10^{-5}$ m) (SET2) better represents O1 harmonics, taking FES2014b-with-assimilation as a reference. However the relative improvements from a simulation to another are again very small (<3%). Considering the semidiurnal waves, the differences are heterogeneous over the basin, with overall a slightly better representation (difference of 2%) of the waves by the simulation with $C_D = f(z_0 = 1.5 \times 10^{-5}$ m) (SET2). These results finally suggest that differences between simulations from SET2 and SET3 are locally and globally insignificant, and that the tidal solutions in the GoT are therefre not very sensitive to changes of bottom friction parameterization, from a constant z_0 to a spatially varying z_0.
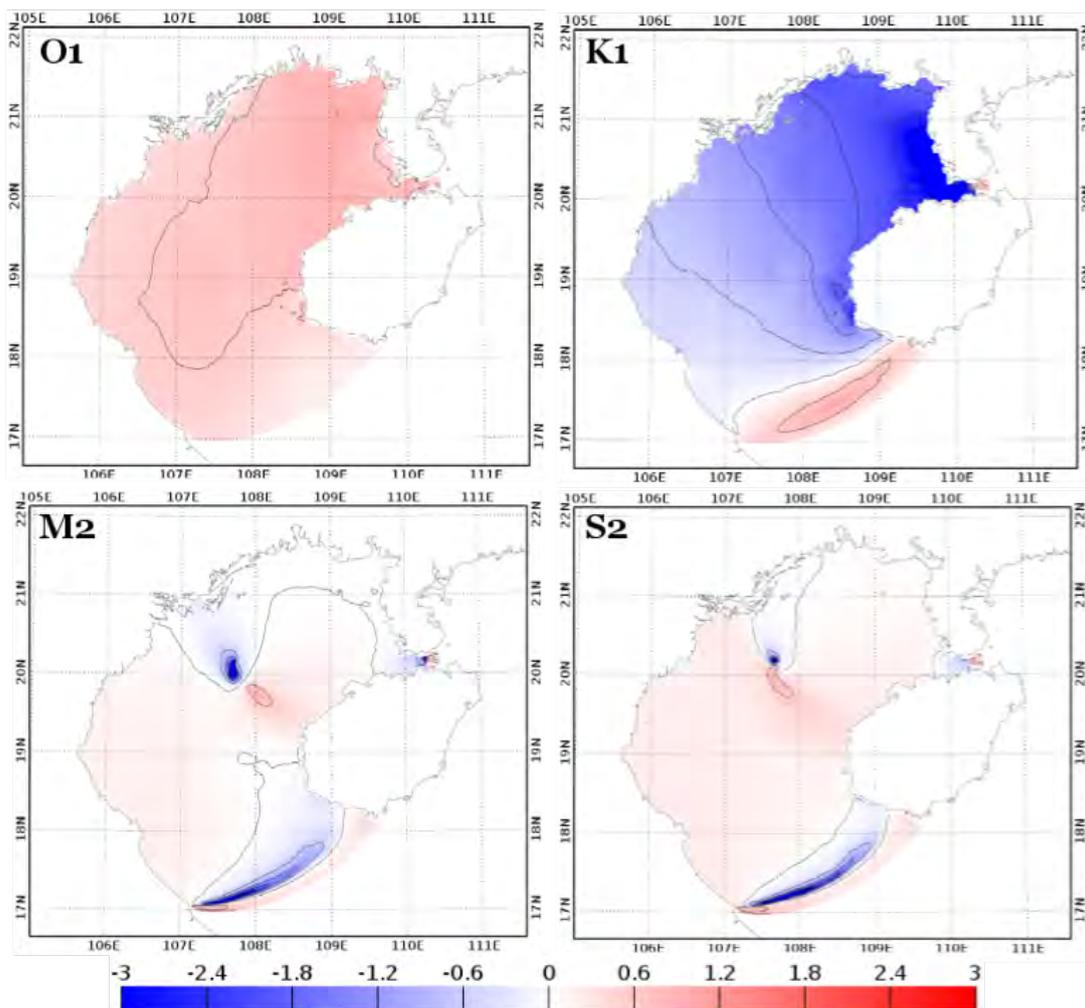
Figure III.15: Relative differences (in %) between simulation TEST6 and simulation with $C_D = f(z_0 = 1.5e-5,H)$ compared to FES2014b-with-assimilation (as a reference) for the tidal harmonics of O1, K1, M2 and S2.

b) Sensitivity to a spatially varying roughness length (SET4 and SET5 vs. SET2)

Lastly, the results of the tests from SET5 did not show any improvement on the tidal solutions, compared to SET3 and SET4. The minimum cumulative error found in SET5 is reached by imposing z_0 values that correspond exactly to the configuration of Test 6 in SET4 and is consequently also equal to 10.43 cm (i.e. the same as in SET4). This result again suggests that the model seems to be insensitive to high spatial refinement of the bottom sediment composition and associated roughness for the representation of tidal solutions.

III.2.3.2 Sensitivity to the bathymetry

Model bathymetry is a key parameter for tidal simulations. In order to evaluate the sensitivity of the model to the bathymetry, an additional sensitivity simulation is performed. First, the solutions obtained with the grid configuration with improved bathymetry and shoreline datasets described in section III.2.2.1 (Fig.III.4) and a spatially varying roughness length (described in Test 6, Table III.1) with a logarithmic velocity profile are chosen as this choice of bottom roughness parameterization has shown the best tidal solutions (the least errors to satellite altimetry) in section III.2.3.1.2. This simulation is named TKN hereafter. Second, we run a twin simulation with exactly the same configuration, parameterizations and choice of parameters, except that the bathymetry and shoreline are not built from our improved dataset but from the default GEBCO bathymetry dataset and default-shoreline dataset. This simulation is hereafter named TKN-gebco. The results from these tests are presented in this section, where we evaluate the quality of the tidal solution obtained in our different simulations.

III.2.3.2.1 Average assessment over the domain

We first evaluate the tidal solution in average over the domain. Integrated alongtrack RMS* errors (Appendix; Eq. III.6) between modelled and altimetry derived ocean tide harmonic constants (noted hereafter AH for Altimetric Harmonic) are shown in Fig. III.16. FES2014b-with-assimilation errors are globally always lower than errors given by the three other simulations, thanks to the assimilation of the satellite altimetry: 3 to 4.7 times lower for O1, 2.6 to 3.2 times for K1, 2.3 to 3.7 times smaller M2 and 1.3 to 2.7 times for S2. As explained in section III.2.2.2.3, FES2014b-with-assimilation, which minimizes the error, is used in the following as a reference for the evaluation of our simulations to spatially complement altimetry data which are only available along the altimetry tracks.

Alongtrack RMS* errors for M2 are reduced by 12% in TKN-gebco relative to FES2014b-without-
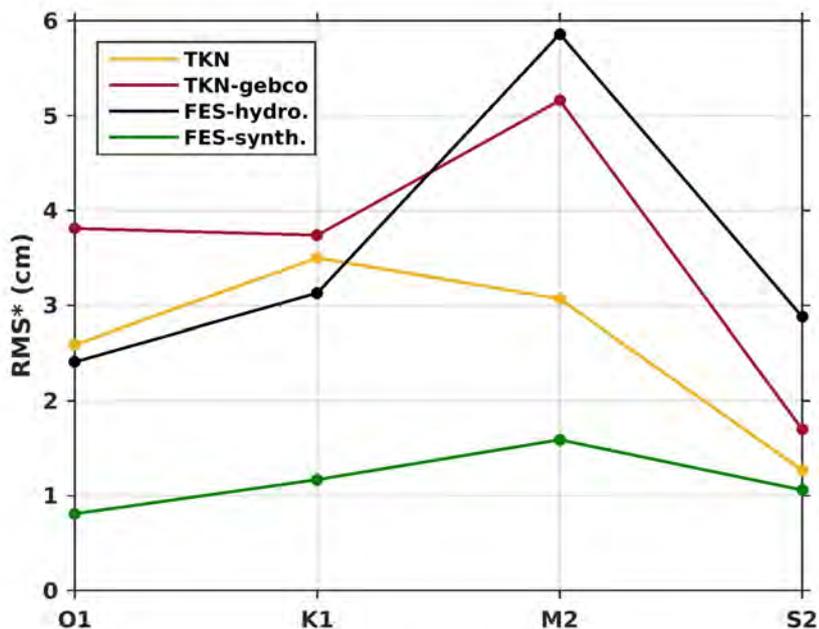
Figure III.16: RMS* errors (Appendix ; Eq. 6) between numerical simulations (TKN, TKN-gebco, FES2014b-without-assimilation and FES2014b-with-assimilation) and altimetry data for O1, K1, S2 and M2.

assimilation and by 47% in TKN. The errors are also lower for S2, with a reduction of the errors by 41% between FES2014b-without-assimilation and TKN-gebco, and by 56% between FES2014b-without-assimilation and TKN. On the other hand, both TKN and TKN-gebco simulations show bigger errors than FES2014b-without-assimilation for O1 and K1. However, TKN simulation increases the errors for O1 by 7% relative to FES2014b-without-assimilation whereas TKN-gebco increases the errors by 58%. The complex errors for K1 obtained from both TKN and TKN-gebco simulations increase by roughly 12 and 20% compared to FES2014b-without-assimilation, respectively. Such results illustrate the fact that K1 wavelengths are longer than the other waves' wavelengths considered here, e.g.: at 60 m depth, K1 wavelength is 2000 km and M2 wavelength is 1000 km (Kowalik and Luick, 2013), therefore K1 is less sensitive to bathymetric variations. These results further illustrate FES model efficiency in tidal simulation in coastal areas, which is related in particular to the use of an unstructured triangle grid mesh specifically dedicated to finely adapt to complex coastal topography and coastline.

The mean absolute differences MAE (Appendix; Eq. III.7) of amplitude and phase of the four tidal constituents between our simulation TKN and AH, and between the two FES2014b products and AH are given in Table III.2. The errors to AH in both amplitude and phase are always reduced in TKN compared to FES2014b-without-assimilation (except for the phase of S2): from 1.2 times for the phase of K1 to 2.7 times for the amplitude of S2. However, errors to AH are increased in both

amplitude and phase in TKN compared to FES2014b-with-assimilation (except for the amplitude
of S2). In addition, integrated RMS* errors between simulated and observed tidal harmonics from
tide gauges are presented in Fig. III.17. Again, FES2014b-with-assimilation errors are globally
always lower (for O1, K1 and M2) than errors given by the three other simulations, thanks to the
assimilation of including those tide gauges data.
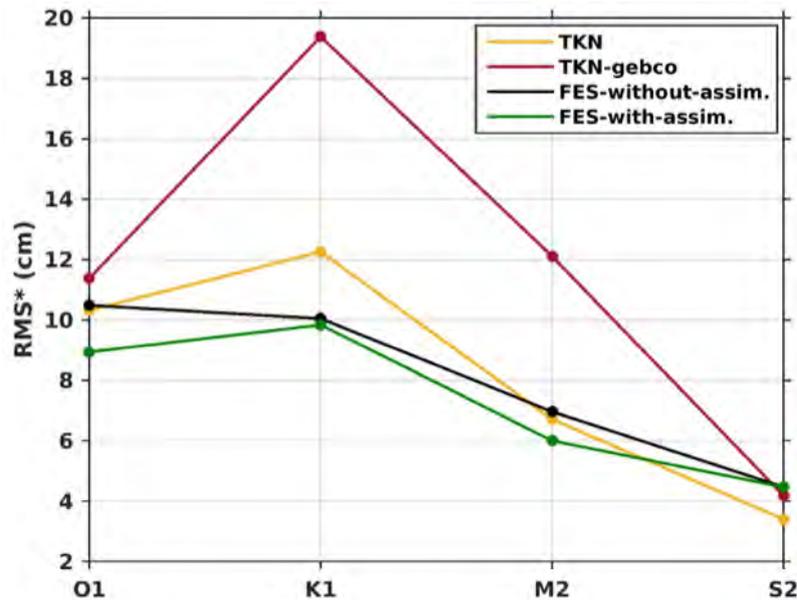
Figure III.17: RMS* errors (Appendix ; Eq. 6) between numerical simulations (TKN, TKN-gebco, FES2014b-
without-assimilation and FES2014b-with-assimilation) and tide gauges for O1, K1, S2 and M2.

TKN-gebco increases the errors for O1 by 27% relative to FES2014b-with-assimilation while TKN
increases it by 16%. TKN also slightly reduces (by 0.2 cm) the integrated tidal gauge RMS* errors for
O1 compared to FES2014b-without-assimilation. The complex errors for K1 obtained from both
TKN and TKN-gebco simulations increase by roughly 25% and 90% compared to FES2014b-with-
assimilation, respectively. The errors for M2 are increased by 11% with TKN and by 101% with
TKN-gebco compared to FES2014b-with-assimilation. Similar to O1 case, TKN slightly reduces
(by 0.3 cm) the RMS* errors for M2 compared to FES2014b-without-assimilation. Finally, both
TKN and TKN-gebco simulations reduces the errors for S2 by 44% and 9% compared to FES2014b-
with-assimilation, respectively. So for the 4 main tidal constituents, errors between simulated and
observed tidal harmonics from tide gauges are significantly reduced in TKN compared to TKN-
gebco.

These results show first that TKN configuration brings a clear improvement in tidal solutions
compared to TKN-gebco configuration, and second that it only slightly improves tidal solutions
for some of the tidal components compared to FES2014b-without-assimilation. This last result

related to the use of an unstructured grid in FES2014b (with and without-assimilation), better adapted for the representation of the complex coastal topography that the structured grid that is used to optimize our TKN configuration since it will be used in our tridimensional structured grid model.

III.2.3.2.2   Spatial assessment of tidal solutions

The modelled O1, K1, M2 and S2 fields for TKN, TKN-gebco, FES2014b-without-assimilation and FES2014b-with-assimilation are shown in Figs. III.5 to III.8. For each tidal component and simulation, the complex errors RMS* between these simulations results and AH are represented for each point of the altimetry track by the circles superimposed on the maps.

Both model simulations (TKN-gebco and TKN) reproduce well the distribution patterns of O1 harmonics compared to FES2014b-with-assimilation, improving the results compared to FES2014b-without-assimilation. Moreover, TKN solutions look more accurate than TKN_gebco. Errors to AH for O1 (circles on the maps) are smaller than 10 cm in TKN_gebco and are reduced by 35% compared to FES2014b-without-assimilation. They are further reduced in TKN: most of the errors are smaller than 5 cm and are reduced by 50% compared to FES2014b-without-assimilation (Fig.III.5). Note that higher errors of AH (of about 20cm) are observed in TKN and TKN-gebco in the Hainan Strait and also near the coasts. These errors also appear in FES2014b-without-assimilation and, to a lesser extent (with values of about 15 cm in the Hainan Strait) in FES2014b-with-assimilation. The increase of complex errors in these particular areas could be explained by either model errors associated with errors in coastal bathymetry and shorelines, whose accuracy is decisive to shallow water tidal wave and/or to erroneous altimetric data (land contamination in the altimeter footprint). For K1, even though both model simulations reproduce well the distribution pattern of the harmonics compared to FES2014b-with-assimilation, the errors to AH compared to FES2014b-without-assimilation are not reduced in TKN-gebco nor in TKN (Fig.III.6). Errors to AH for K1 are equals or smaller than 10 cm in FES2014b-without-assimilation, TKN-gebco and TKN along the altimetry tracks, and are extremely similar between those simulations. As observed for O1, larger and similar errors of about 20 cm are also observed in the Hainan Strait in TKN-gebco and TKN and in the two FES2014b products (though with smaller values of about 15 cm in FES2014b-with-assimilation that includes assimilations). Furthermore, the angle of the circles' radius indicates which of the error in amplitude or the error in phase dominates the complex error. The smaller the angle is to the ordinate axis, the more the error in phase dominates the complex error. On the

contrary, the bigger the angle is to the ordinate axis, the more the error in amplitude dominates the complex error. When the angle to the ordinate axis approaches 45°, the error in phase and the error in amplitude account equally for the complex error. For both O1 and K1, errors in phase are dominating the northern and central parts of the region, while the phase and amplitude account equally for the complex errors in the southernmost part of the region and in the Hainan Strait (Fig.III.5 c,d; III.6 c,d).

Fig.III.7 shows that M2 amplitude is globally overestimated by TKN and TKN-gebco compared to FES2014b-with-assimilation and FES2014b-without-assimilation, especially in the areas where the wave resonates (i.e. in the north eastern bay and in the south-western part). Differences to FES2014b-without-assimilation are up to 30 to 35 cm in TKN and in TKN-gebco (in the north-eastern bay), with amplitudes increasing by almost 45% in model simulations. Both model simulations increase the resonance of M2 in the bays. These amplitude overestimations could be partially explained by the bathymetry dataset (TONKIN_bathymetry) which integrates nautical charts that underestimate depths, especially in shallow areas, for navigation purposes. However, the amplitudes are underestimated near the amphidromic point (20.7° N, 107.3° E) by both simulations compared to FES2014b-without-assimilation (by up to 10 cm, roughly 80%). Globally, errors to AH are reduced in TKN by 30% compared to TKN-gebco: most of the errors in TKN are smaller than 10 cm while most of the errors in TKN-gebco are equals or larger than 10 cm. Both simulations show also smaller errors to AH south of Hainan Island compared to FES2014b-without-assimilation by up to 50%, with errors of about 1 cm in FES2014b-without-assimilation and of about 0.5 cm in model simulations). Again, large errors are observed in the Hainan Strait in simulations and both FES2014b products, however the errors are reduced by 25% in TKN and TKN-gebco compared to FES2014b-without-assimilation. Furthermore, these errors are dominated by errors in phase rather than in amplitude.

Lastly, both TKN and TKN-gebco model simulations overestimate the amplitude of S2 compared to FES2014b-with-assimilation and FE2014b-hydrodynamics by up to 10 cm (approximately 50%) in the south-western and north-eastern bays, where S2 resonates (Fig.III.8). The resonance of S2 in the bays is therefore amplified in both model simulations. These amplitude amplifications observed in both models could be again partly explained by the bathymetric soundings of TONKIN_bathymetry that underestimate depths in shallow water areas. Similar to M2 case, both simulations also underestimate by roughly 5 cm the amplitude of S2 near the amphidromic point (20.7° N, 107.3° E) compared to the two FES2014b products. However, the complex errors to AH

are globally 50% smaller in TKN (between 2 to 3 cm) than in TKN-gebco (between 4 to 5 cm). Furthermore, errors to AH remain large in the Hainan Strait (up to 6 cm) in both FES products and both model simulations. In the very near coastal areas, errors to AH in TKN and TKN-gebco are larger than in the rest of the basin (up to 6 cm). However, the errors to AH in TKN are reduced by 30% in the south-western most part of the region. Like M2 case, the complex errors of S2 are dominated all over the basin the by errors in phase rather than errors in amplitudes.

III.2.3.3   Assessment of tidal solutions with previous studies

The mean absolute differences MAE (Appendix; Eq. 7) of amplitude and phase of the four tidal constituents between our simulation TKN and the satellite altimetry are given in III.2.

Our results are compared with the errors given in Minh et al. (2014) and in Chen et al. (2009). Minh et al. (2014) authors used a ROMS_AGRIF simulation at a resolution of 1/25° × 1/25° over the GoT, and compared their solutions to the same altimetric dataset as the one used in our study. Chen et al. (2009) compared their simulations, performed with ECOM (Extended Control Model) at a 1.8 × 1.8 km resolution (covering the area 16° N-23° N, 105.7° E-114° E), to gauge stations located along the GoT coast. Our simulation TKN shows large improvements in both amplitude and phase for the four constituents (except for the phase of M2) compared to the results of Minh et al. (2014). The errors are reduced by approximately 60% for the amplitudes of M2 and S2 approximately, and by roughly 40% for the amplitudes of K1 and O1, respectively. The errors in phase for O1 and K1 are also reduced by approximately 50% in our simulation. Our results show also improvements compared with the errors proposed by Chen et al. (2009), for both amplitude and phase of S2 (by 65% in amplitude and by 35% in phase), O1 (by 50% in amplitude and almost 60% in phase) and K1 (by 68% in amplitude and by 41% in phase). Only the solutions of M2 are not improved by our simulation compared to Chen et al. (2009): they remain the same in amplitude and increase by 14% in phase.

The improvement of our tidal solution from TKN compared to these two previous studies could be due first to the use of T-UGO that is specifically developed for tidal modelling purpose, compared to models used by Minh et al. (2014) and Chen et al. (2009), which are hydrodynamical model not specifically conceived for tidal representation. Second, to our model configuration which has been specifically optimized for tidal modelling purpose, in terms of grid resolution, bathymetry accuracy and resolution and bottom friction parameterization.

Tides	O1		K1		M2		S2	
	Amplitude (cm)	Phase (°)	Amplitude (cm)	Phase (°)	Amplitude (cm)	Phase (°)	Amplitude (cm)	Phase (°)
TKN - this study *Compared to Satellite altimetry*	1.5	3.7	1.9	5.4	2.3	7.6	0.9	14.7
Minh et al. (2014) *Compared to Satellite altimetry*	2.4	8.4	2.8	10.4	8.0	7.8	2.4	17.7
Chen et al. (2009) *Compared to Satellite altimetry*	3.0	9.0	5.4	8.9	2.3	6.7	2.8	22.0

Table III.2: Mean absolute differences (Appendix ; Eq. III.7) of amplitudes (in cm) and phase (in deg) of M2, S2, O1, K1 constituents between our reference TKN and satellite altimetry. For comparison, the work of Minh et al. (2014) compared with satellite altimetry and the work Chen et al., (2009) compared to gauge stations are presented.

III.2.4 Conclusions

This study takes place in the framework of a more comprehensive modeling project which aims at representing the transport and fate of the sediments from the Red River to the GoT. In this future study, the ocean dynamics and the sediments transport will be represented using the regional circulation model SYMPHONIE coupled with the sediment model MUSTANG. As tides have a major effect on the sediment dynamics within the estuaries and in the plume area (Pritchard 1954, 1956; Allen et al., 1980; Fontes et al., 2008; Vinh et al., 2018), it is necessary to accurately represent the tidal processes before investigating the fine scale sediment physics.This coupled-model will allow for example to study the impact on tides of freshwater discharges and its strong seasonal variability, since this effect could be relatively important in the very nearshore coastal area. The optimization of the configuration and parameterizations of this coupled tridimensional structured grid model is the final objective of this study. Optimizing the bathymetry and the parameterization of the bottom shear stress is crucial in shallow-water regional and coastal modeling since they both are critical parameters influencing the propagation and distortion of the tides (Fontes et al., 2008; Le Bars et al., 2010). The T-UGO hydrodynamical model is used in this study in its spectral mode, which allows the user to perform fast and low-cost tests (compared to simulations with sequential models like SYMPHONIE) on various parameterizations and bathymetry configurations.

This strategy allows to assess and quantify the importance of each element considered and to determine the best configuration and parameterization that will be applied in the above-mentioned forthcoming modeling study with SYMPHONIE-MUSTANG model.

In this study, we have first constructed an improved bathymetric dataset for the region of the GoT from digitalized nautical charts, soundings, intertidal DEM and GEBCO bathymetry dataset. We also integrated to this bathymetry a new coastline dataset created with POCViP and satellite images, since the existing descriptions of the GoT coastlines, the Ha Long Bay islets and the Red River delta were very poor. We then performed tests with the fast-solver 2D T-UGOm model on an unstructured grid refined in the Red River delta and Ha Long Bay area to test the added value of this improved bathymetric dataset. With this new bathymetry, we have been able to reduce the errors (taking along-track altimetry data and tide gauges data as a reference) of the representation of M2 and S2 in T-UGOm simulations by 40% and 25% respectively and O1 and K1 by 32% and 6% respectively, compared to simulations that use the regular GEBCO dataset. Our improved bathymetry showed also better solutions for the semi-diurnal waves than the tidal atlas FES2014b_hydrodynamics (errors reduced by 47% or M2 and by 25% for S2), even though our model seems to amplify their resonance. Moreover, our simulations also improved accuracy over the existing state of the art, by reducing the errors in amplitude of the semi-diurnal waves by 60%, the errors in amplitude of the diurnal waves by 40%, and the errors in phase of the diurnal waves by 50% compared to the results found by Minh et al. (2014). We believe the remaining errors in our best tidal solutions are due to potential lacks of details and resolution in the bathymetric dataset. Since bathymetry directly impacts the waves' speeds, bathymetric uncertainties may lead to alterations of the bottom shear stress.

The other key parameter influencing shallow-water tidal modelling is the bottom friction. In this study, the use of a constant C_D parametrization or the use of a C_D depending on the roughness length led to fairly similar results, in line with the results found by Le Bars et al. (2010) in the Amazon estuary. Furthermore, our study shows that the model is very sensitive to the values imposed to C_D and z_0, especially for the diurnal waves with errors increasing for extreme C_D and z_0 values. The lowest cumulative errors of all four waves (of 11.50 and 10.96cm) were found for a uniform C_D of 0.9×10^{-3} m (prescribing a constant velocity profile) and for a uniform z_0 of 1.5×10^{-5} m (prescribing a logarithmic velocity profile), respectively. More importantly, the regionalisation of the roughness length into three regions, for addressing the issue of representing the complexity of seabed composition and morphology, only slightly improved the accuracy of our simulation, with

a lowest cumulative error for all four waves of 10.43 cm. Finer local adjustments of the roughness length or the choice of a linear velocity profile in the area of fine mud, did not significantly improve the accuracy of our simulations. In particular, the model in this configuration showed a very limited sensitivity to the presence of fine mud and a greater sensitivity to the roughness length values prescribed in the rest of the region, which was unexpected following the results of Le Bars et al., 2010 and explained by the low energy dissipation occurring in this area of fine mud.

Our results therefore quantitatively showed that the key parameter for the representation of tidal solutions over a shallow area like the GoT is the choice of bathymetry and shoreline dataset. Second, they revealed that the choice of the bottom stress parameterization does not significantly affect the performance of the model, but that, for a given parameterization, the choice of the value of the friction coefficient is important. Furthermore, the use of T-UGOm in a 2D barotropic mode showed its efficiency in tidal spectral modelling with reduced simulation durations in both CPU and running times compared to structured grid numerical models. This allowed us to optimize our configuration in terms of grid, bathymetry and bottom friction parameterization regarding the representation of the tidal solutions. Our resulting configuration brought a clear improvement in the tidal solutions compared to previous 3D simulations from the literature and to the tidal atlas FES2014b (without data assimilation) for the semi-diurnal waves. The modeling strategy proposed here showed its efficiency in quickly optimizing the configuration that will be used in future works to address the issue of sediment transport and fate in the GoT, which was our primary objective. Finally, our configuration did not produce a clear improvement compared to FES2014b-without-assimilation, and perform worse than FES2014b-with-assimilation, due to the use in both FES2014b simulations of an unstructured grid better representing the coastal topography complexity, and the use of assimilation in FES2014b-with-assimilation. This underlines the importance of data assimilation for the production of tidal atlases, and the need to go on developing satellite mission and in-situ campaigns, despite the great improvements of numerical models in the last decades.

The evaluation of T-UGO performances should be completed with the study of tidal currents, which is for now limited in the area due to in-situ data unavailability, but will be possible in the future thanks to the on-going development of observed current datasets from high-frequency radars (Rogowski et al., 2019). Note also that the use of nautical charts for bathymetry construction could have led to overestimation of the tidal amplitudes in coastal areas, due to underestimation of real depths for navigation safety purposes. Furthermore, using bathymetry data available from digi-

talized navigation charts was a relatively simple way (compared to performing additional in-situ measurements) to significantly improve the representation of topography in the coastal and estuarine areas of the GoT, and could be applied successfully in other regions. However, updates and improvements in shorelines and bathymetry databases, particularly in the river channels, coastal areas and in the Hainan strait would still improve the present results and especially reduce the tendency to increasing errors at the coasts. Continuous efforts should be made in bathymetric data acquisition and sharing them with the community should be a crucial concern.

Code and/or data availability:

The model grid, which integrates the bathymetry and the coastline datasets developed in this study, is available for download via `https://zenodo.org/record/2640763#.XLSBcJzgreM`. The T-UGO model code installation instructions are updated at `ftp://ftp.legos.obs-mip.fr/pub/ecola/README.html`, and the code, as well as the updated tools and the poc-solvers are available on `https://hg.legos.obs-mip.fr/tools/`. An archive of the exact version of T-UGOm used in this study (version 2616:78a276dd7882) is also available on `https://zenodo.org/record/2669397#.XNBDLJzgreM`. The configuration files (initial conditions and modified drag coefficients) are available on `https://zenodo.org/record/2640793#.XLSGYZzgreM`. Model boundary conditions (i.e. FES2014 products) are available through: `https://www.aviso.altimetry.fr/en/data/products/auxiliary-products/global-tide-fes.html`. The satellite altimetry track dataset of CTOH-LEGOS for model outputs comparison are available through:`http://ctoh.legos.obs-mip.fr/products/coastal-products/coastal-products-1/sla-1hz` (doi: 10.6096/CTOH_X-TRACK_Tidal_2018_01).

Authors contribution:

VP, MH, SO and FL designed the experiments and VP carried them out. FL developed the model code and VP performed the simulations. VP, TH and DA constructed the bathymetry dataset. VP prepared the manuscript with contributions of MH, FL, SO and PM.

Acknowledgments:

III.2.5 Appendix

For comparison of the simulations with the tidal harmonics from satellite altimetry, we first introduce the vectorial difference z, or complex difference, as:

$$z = z_m - z_0 \tag{III.6}$$

with $z_m = A_m e^{ig_m}$ the vector representing a given modelled tidal constituents (of amplitude Am and phase G_m) and z_0 the vector representing the observed tidal constituent. For assessing the errors between the simulations (modelled constituents) and altimetry (observed constituents), we compute the root mean square error (RMS*), like in Stammer et al. (2014) and in Minh et al. (2014). RMS* depends upon the vectorial difference z and is computed for each given constituent of each simulation, as follows:

$$\text{RMS} * = \sqrt{\left(\frac{1}{N} \sum_{i=1}^{N} 0.5 |z|^2\right)}$$

$$\text{RMS} * = \sqrt{\left(\frac{1}{N} \sum_{i=1}^{N} 0.5 [(A_m \cos(G_m) - A_o \cos(G_o))^2 + (A_m \sin(G_m) - A_o \sin(G_o))^2]\right)} \tag{III.7}$$

with Am and Gm being respectively the amplitude and phase of the modelled constituent, Ao and Go , the amplitude and phase of the constituent from satellite altimetry and N the number of points of comparison (i.e. the number of equivalent gauge stations along the altimetry tracks). The model performance is also estimated using the mean absolute error (MAE). MAE measures the mean of the difference between the simulated and the observed values and is computed for each constituent according to:

$$\text{MAE} = \frac{\sum_{i=1}^{N} |E_i|}{N} \tag{III.8}$$

with E_i representing for each point i of the track the difference between the modeled constituent and the observed constituent. The MAE is separately calculated for amplitudes and for phases.

III.2.6 References

- Allen G. P., Salomon J. C., Bassoullet P., Penhoat Y. D., Grandpré C.: Effects of tides on mixing and suspended sediment transport in macrotidal estuaries Sediment. Geol., 26(1-3), 69-90, 1980.
- Amante C., Eakins B. W.: ETOPO1 1 Arc-Minute Global Relief Model: Procedures, Data Sources and Analysis. NOAA Technical Memorandum NESDIS NGDC-24, National Geophysical Data Center, NOAA, doi: 10.7289/V5C8276M, 2009.
- Bentsen M., Evensen G., Drange H., Jenkins A. D.: Coordinate Transformation on a Sphere Using Conformal Mapping, Month. Weath. Rev., 2733-2740, 1999
- Birol F., Fuller N., Cancet M., Nino F., Delebecque C., Fleury S., Toublanc F., Melet A., Saraceno M., Léger F.: Coastal applications from nadir altimetry: example of the X-TRACK regional products, Adv. Space Res., 59, 936-953, doi: http://dx.doi.org/10.1016/j.asr.2016.11.005, 2016.
- Cai S., Long X., Liu H., Wang S.: Tide model evaluation under different conditions. Cont. Shelf. Res., 26, 104-112, 2005.
- Carrère L., Lyard F.: Modeling the barotropic response of the global ocean to atmospheric wind and pressure forcing - comparison with observations, Geophys. Res. Lett., 30(6), 1- 4, doi:10.1029/2002GL016473, 2003.
- Carrère L., Lyard F., Cancert M., Guillot A., Picot N.: FES2014, a new tidal model – Validation results and perspectives for improvements, presentation to ESA Living Planet Conference, Prague 2016.
- Carrère L., Lyard F., Cancert M., Guillot A., Roblou L.: FES2012: a new global tidal model taking advantage of nearly 20 years of altimetry, Proceedings of 20 years of Altimetry, Venice, 2012.
- Chen C., Li P., Shi M., Xuo J., Chen M., Sun H.: Numerical study of the tides and residual currents in the Leizhou Strait, Chin. J. Oceanol. Limnol., 27(4), 931-942, 2009.
- Dang T. H., Coynel A., Orange D., Blanc G., Etcheber H., Le L. A.: Long-term monitoring (1960-2008) of the river-sediment transport in the Red River Watershed (Vietnam): Temporal variability and dam-reservoir impact, Sci. Total Environ., 408, 4654-4664, doi: 10.1016/j.scitotenv.2010.07.007, 2010.
- Debreu L., Marchesiello P., Penven P., Cambon G.: Two-way nesting in split-explicit ocean models: algorithms, implementation and validation, Ocean Model. 49-51, 1-21, doi: http://dx.doi.org/10.1016/j.ocemod.2012.03.003, 2012.
- Ding Y., Chen C., Beardsley R. C., Bao X., Shi M., Zhang Y., Lai Z., Li R., Lin H., Viet N. T.: Observational and model studies of the circulation in the Gulf of Tonkin, South China Sea, J. Geophis. Res., 118, 6495-6510, doi:10.1002/2013JC009455, 2013.
- Dronkers J.J.: Tidal Computations in Rivers and Coastal Waters, North-Holland, Amsterdam. 1964.
- Eyre B., McConchie D.: Implications of sedimentological studies for environmental pollution assessment and management: examples from fluvial systems in North Queensland and Western Australia, Sediment Geol., 85, 235-252, 1993.
- Fang G.: Tide and tidal current charts for the marginal seas adjacent to china, Chin. J. Oceanol. Limnol., 4, 1-16, 1986.
- Fang G., Kwok Y. K., Yu K., Zhu Y.: Numerical simulation of principal tidal constituents in the South China Sea, Gulf of Tonkin and Gulf of Thailand, Cont. Shelf Res., 19(7), 845-869, 1999.
- Fontes R. F. C. Castro B. M., Beardsley R. C.: Numerical study of circulation on the inner Amazon Shelf, Ocean Dyn., 58,187-198, 2008.
- Gabioux M., Vinzon S. B., Paiva A. M.: Tidal propagation over fluid mud layers on the Amazon shelf, Cont. Shelf Res., 25, 113-125, 2005.
- Gonzalez-Pola C., Diaz del Rio G., Ruiz-Villareal M., Sanchez R.F., Mohn C.: Circulation pat-

terns at Le Danois bank, an elongated shelf-adjacent seamount in the Bay of Biscay, Deep-Sea Res., Part I, 60, 7-21, doi: http://dx.doi.org/10.1016.j.dsr.2011.10.001 , 2012.

- Guarnieri A., Pinardi N., Oddo P., Bortoluzzi G., Ravaioli M.: Impact of tides in a baroclinic circulation model of the Adriatic Sea, J. Geophys. Res., 118(1), 166-183, doi: http://dx.doi.org/10.1029/2012JC007921, 2013.

- Herzfeld M.: Improving stability of regional numerical ocean models, Ocean Dyn., 59(1), 21-46, doi: http://dx.doi.org/10.1007/s10236-008-0158-1, 2009.

- Holt J., Hyder P., Ashworth M., Harle J., Hewitt H.T., Liu H., New A.L., Pickles S., Porter A., Popova E., Allen J.I., Siddorn J., Wood R.: Prospects for improving the representation of coastal and shelf seas in global ocean models, Geosci. Model Dev. 10, 499-523, doi: http://dx.doi.org/10.5194/gmd-2016-145, 2017.

- Hu J. Y., Kawamura H., Hong H. S., Kobashi F., Xie Q.: Tidal features in the China Seas and their adjacent areas derives from TOPEX/Poseidon altimeter data, Chin. J. Oceanol. Limnol., 19, 293-305, 2001.

- Kovalik Z., Luick J.: The Oceanography of Tides, Fairbanks, USA. https://www.uaf.edu/files/sfos/Kowalik/tide_book.pdf , 2013.

- Le T. P. Q., Garnier J., Billen G., Théry S., Chau V. M.: The changing flow regime and sediment load of the Red River, Viet Nam, J. Hydrol., 334, 199-214, 2007.

- Le Bars Y., Lyard F., Jeandel C., Dardengo L.: The AMANDES tidal model for the Amazon estuary and shelf, Ocean modell., 31, 132-149, doi : 10.1016/j.ocemod.2009.11.001, 2010.

- Le Hir P., Cayocca F., Waeles B.: Dynamics of sand and mud mixtures : A multiprocess-based modelling strategy, Cont. Shelf Res., 31, 135-149, doi :https://doi.org/10.1016/j.csr.2010.12.009, 2011.

- Lefebvre J. P., Ouillon S., Vinh V. D., Arfi R., Panché J. Y., Mari X., Thuoc C. V., Torréton J. P.: Seasonal variability of cohesive sediment aggregation in the Bach Dang-Cam Estuary, Haiphong (Vietnam), Geo.-Mar. Lett., 32, 103-121, doi: 10.1007/s00367-011-0273-8, 2012.

- Lyard F., Lefevre F., Letellier T., Francis O.: Modelling the global ocean tides: modern insights from FES2004, Ocean Dyn., 56(5-6), 394-415, doi: http://dx.doi.org/10.1007/s10236-006-0086-x, 2006.

- Ma F., Wang Y., Li Y., Ye C., Xu Z., Zhang F.: The application of geostatistics in grain size trend analysis: a case study of eastern Beibu Gulf, J. Geogr. Sci., 20(1), 77-90, 2010.

- Madec G. Imbard M.: A global ocean mesh to overcome the North Pole singularity, Climate Dynamics, 1, 381–388, 1996.

- Manh D. V., Yanagi T.: A study on residual flow in the Gulf of Tonkin, J. Oceanogr., 56, 59-68, 2000.

- Maraldi C., Chanut J., Levier B., Ayoub N., De Mey P., Reffray G., Lyard F., Cailleau S., Drevillon M., Fanjul E. A., Sotillo M. G., Marsaleix P. and the Mercator Research and Development Team: NEMO on the shelf: assessment of the Iberia–Biscay–Ireland configuration, Ocean Sci., 9, 745–771, http://dx.doi.org/10.5194/os-9-745-2013 , 2013.

- Marsaleix P., Auclair F., Floor J. W., Herrmann M. J., Estournel C., Pairaud I., Ulses C.: Energy conservation issues in sigma-coordinate free-surface ocean models, Ocean Modell., 20(1), 61-89, http://dx.doi.org/10.1016/j.ocemod.2007.07.005, 2008.

- Milliman J.D., Meade R.H.: World-wide delivery of river sediment to the oceans, J. Geol., 91, 1-21, 1983.

- Monahan D.: Mapping the floor of the entire world ocean: the general bathymetric chart of the ocean, J. of Oc. Technol., 3(1), 108, 2008. Natural Conditions and Environment of Vietnam Sea and Adjacent Area Atlas, Hanoi, 2007.

- Nguyen N. T.: Some pecularities of the formation of tidal phenomena in the South China Sea. Okeanoloiia, 9, 235-249, 1969.

- Nguyen N. M., Marchesiello P., Lyard F., Ouillon S., Cambon G., Allain D., Dinh V. U.: Tidal characteristics of the gulf of Tonkin, Cont. Shelf Res., 91, 37-56, http://dx.doi.org/10.1016/j.csr.2014.08.003, 2014.

- Nugroho D., Koch-Larrouy A., Gaspar P., Lyard F., Reffray G., Tranchant B.: Modelling explicit tides in the Indonesian seas: An important process for surface sea water properties, Mar. Poll. Bull., 131, 7-18, http://dx.doir.org/10.1016/j.marpolbul.2017.06.033, 2018.

- Owens P. N., Batalla R. J., Collins A. J., Gomez B., Hicks D. M., Horowitz A. J., Kondolf G. M., Marden M, Page M. J., Peacock D. H., Petticrew E. L., Salomons W., Trustrum N. A.: Fine-grained sediment in river systems: environmental significance and management issues, River Res. Appl. 21(7), 693-717, 2005.

- Pairaud I. L., Lyard F., Auclair F., Letellier T., Marsaleix P.: Dynamics of the semi-diurnal and quarter-diurnal internal tides in the Bay of Biscay. Part 1 : barotropic tides, Cont. Shelf. Res., 28 (10-11), 1294-1315, http://dx.doi.org/10.1016/j.csr.2008.03.004, 2008.

- Penven P., Debreu L., Marchesiello P., McWilliams J. C.: Evaluation and application of the ROMS 1-way embedding procedure to the central california upwelling system, Ocean Model., 12, 157-187, doi: 10.1016/j.ocemod.2005.05.002, 2006.

- Pritchard D .W.: A study of the salt balance in a coastal plain estuary, J. Mar. Res., 13(1), 133-144, 1954.

- Pritchard D .W.: The dynamic structure of a coastal plain estuary. J. Mar. Res., 15, 33- 42, 1956.

- Tong Si Son: Mapping tidal flats in Vietnam using remote sensing techniques, PhD thesis, Univ. de Reims Champagne-Ardenne (in French), 2016.

- Smith W. H. F., Sandwell D. T.: Global seafloor topography from satellite altimetry and ship depth soundings, Science, 277, 1957-1962, 1997.

- Soulsby R.L., Hamm L., Klopman G., Myrhaug D., Simons R.R., Thomas G.P.: Wave-current interaction within and outside the bottom boundary layer, Coastal Engin., 21, 41-69, 1993.

- Stammer D. Ray R., Andersen O., Arbic B., Bosch W., Carrère L., Cheng Y., Chinn D., Dushaw B., Egbert G., Erofeeva S., Fok H., Green J., Griffiths S., King M., Lapin V., Lemoine F., Luthcke S., Lyard F., Morison J., Müller M., Padman L. Richman J., Shriver J., Shum C., Taguchi E., Yi Y.: Accuracy assessment of global barotropic ocean tide models, Rev. Geophys., 52, 243-282.http://de.doi.org/10.1002/2014RG000450, 2014.

- General Statistics Office: Statistical Yearbook of Vietnam 2017, Statistical Publishing House: Hanoi, Vietnam. http://www.gso.gov.vn/default_en.aspxtabid=515&idmid=5&ItemID=18941 , 2017.

- Toublanc F., Ayoub N. K., Lyard F., Marsaleix P., Allain D. J.: Tidal downscalling from the open ocean to the coast : a new approach applied to the Bay of Biscay, Ocean modell., 124, 16-32, https://doi.org/10.1016/j.ocemod.2018.02.001, 2018.

- van Maren D. S., Hoekstra P.: Seasonal variation of hydrodynamics and sediment dynamics in a shallow subtropical estuary: the Ba Lat River, Vietnam, Estuar. Coastal Shelf Sci., 60(3), 529-540, 2004.

- Vietnam maritime administration (Vinamarine). Approved planning for dredging in Hai Phong port. Available online: http://vinamarine.gov.vn (accessed on 15 July 2018).

- Vignudelli S., Cipollini P., Roblou L., Lyard F., Gasparini G. P., Manzella G., Astraldi M.: Improved altimetry in coastal systems : Case study of the Corsica Channel (Mediterranean Sea), Geophys. Res. Lett., 32, 1-5, https://doi.org.insu.bib.cnrs.fr/10.1029/2005GL022602, 2005.

- Vinh V.D., Ouillon S., Tanh T.D., Chu L.V.: Impact of the Hoa Binh dam (Vietnam) on water and sediment budgets in the Red River basin and delta, Hydrol. Earth Syst. Sci., 18, 3987–4005, doi:10.5194/hess-18-3987-2014, 2014.

- Vinh V.D., Ouillon S., Dinh V.U.: Estuarine Turbidity Maxima and Variations of Aggregate Parameters in the Cam-Nam Trieu Estuary, North Vietnam, in Early Wet Season, Waters, 68, 1-33, doi: 10.3390/w10010068, 2018.

- Wang X., Chao Y., Zhang H., Farrara J., Li Z., Jin X., Park K., Colas F., McWilliams J.C., Paternostro C., Shum C.K., Yi Y., Schoch C., Olsson P.: Modeling tides and their influence on the circulation in Prince Williams Sound, Alaska, Cont. Shelf Res., 63, S126-S137,

http://dx.doi.org/10.1016/j.csr.2012.08.016, 2013.

- Wessel P., Smith W. H. F.: A global, self-consistent, hierarchical, high-resolution shoreline database, J. Geophys. Res., 101(B4), 8741–8743, doi:10.1029/96JB00104, 1996.
- Wetzel A., Szczygielski A., Unverricht D., Stattegger K.: Sedimentological and ichnological implications of rapid Holocen flooding of a gently sloping mud-dominated incised valley – an example from the Red River (Gulf of Tonkin), Sedimentology, 64, 1173-1202, doi: 10.1111/sed.12357, 2017.
- Wyrtki, K. : Physical oceanography of the Southeast Asian waters,195 pp, Available from: https://escholarship.org/uc/item/49n9x3t4, 1961.
- Ye A.L., Robinson I. S.: Tidal dynamics in the South China Sea, Geophys. J. Roy. Astronom. Soc., 72, 691-707, 1983.
- Yu M.: A preliminary study of tidal characteristics in the South China Sea, Acta. Oceanol.

Chapter IV

Hydrodynamics of the estuary - coastal zone - open sea continuum in the Gulf of Tonkin

Contents

IV.1 Introduction

Previous 2D study on the principal tidal components of the GoT (Chapter III) provides valuable tools (improved bathymetry dataset and bottom friction parameterization) for a hydrodynamical 3D study. In addition, in-situ data collected in 2017 in the Van Uc estuary (Chapter II) constitute a benchmark for hydrodynamical model calibration and evaluation. These elements are helpful to implement the regional ocean model SYMPHONIE in the GoT, which is presented here. After presenting the model and the forcing parameters, the construction and calibration of the configuration is detailed. The model performances are then evaluated against in-situ data, model reanalysis and satellite observations. Based on validated model results, the patterns of surface circulation are presented and the processes behind the circulation variability are discussed. Lastly, the impacts of extreme events on water budgets over the GoT are assessed.

IV.2 Material & Methods

IV.2.1 The regional circulation model SYMPHONIE

IV.2.1.1 Governing equations

SYMPHONIE is a 3D hydrodynamical model developed by the SIROCCO group at the Laboratoire d'Aérologie (Marsaleix et al., 2008, 2009, 2012). The model equations are based on mass conservation, momentum conservation, Boussinesq approximations and hydrostatic equilibrium. In a Cartesian coordinate system, where the origin O corresponds to the rest level of the sea surface, where Ox and Oy are the horizontal axes and Oz is the vertical ascending axis, the velocity components u, v and w (for Ox, Oy and Oz axes respectively) are given as follows:

$$\frac{\delta u}{\delta x} + \frac{\delta v}{\delta y} + \frac{\delta w}{\delta z} = 0 \tag{IV.1}$$

$$\frac{\delta u}{\delta t} + \frac{\delta u u}{\delta x} + \frac{\delta v u}{\delta y} + \frac{\delta w u}{\delta z} - f v = -\frac{1}{\rho_0}\frac{\delta p}{\delta x} + \upsilon \Delta^2 u + \frac{\delta}{\delta z}\left(\mathrm{K}_m \frac{\delta u}{\delta z}\right) \tag{IV.2}$$

$$\frac{\delta v}{\delta t} + \frac{\delta u v}{\delta x} + \frac{\delta v v}{\delta y} + \frac{\delta w v}{\delta z} + f u = -\frac{1}{\rho_0}\frac{\delta p}{\delta y} + \upsilon \Delta^2 v + \frac{\delta}{\delta z}\left(\mathrm{K}_m \frac{\delta v}{\delta z}\right) \tag{IV.3}$$

where f is the Coriolis parameter, ρ_0 is the reference water density, p is the pressure, υ is the kinematic viscosity, Δ^2 is a horizontal squared Laplacian operator and K_m is the vertical coefficient of eddy diffusivity.

The hydrostatic hypothesis gives the vertical pressure gradient as:

$$p\,(z) = \int_z^{\eta} g\rho\,dz \tag{IV.4}$$

where g is the acceleration due to gravity, ρ the density, and η is the free surface elevation anomaly, which is derived from the depth-averaged component of the current $\left(\overline{u,v}\right) = \frac{1}{H}\int_{-h}^{\eta}(u,v)\,dz$ by:

$$\frac{\delta\eta}{\delta t} + \frac{\delta}{\delta x}\left(H\overline{u}\right) + \frac{\delta}{\delta y}\left(H\overline{v}\right) = 0 \tag{IV.5}$$

where $H = h + \eta$ is the sum of the water column thickness at rest and the free surface elevation anomaly.

Temperature (T) and salinity (S) variations are linearly deduced from a simple advection diffusion tracer equation, since pressure effects on water density, in a coastal context, remain limited as long as the shallow water approximation is considered:

$$\frac{\delta T}{\delta t} + \frac{\delta u T}{\delta x} + \frac{\delta v T}{\delta y} + \frac{\delta w T}{\delta z} = \frac{\delta}{\delta z}\left(K_h\frac{\delta T}{\delta z}\right) + \frac{1}{\rho_0 C_p}\frac{\delta I_s}{\delta z} + \frac{\delta F_x^T}{\delta x} + \frac{\delta F_y^T}{\delta y} \tag{IV.6}$$

$$\frac{\delta S}{\delta t} + \frac{\delta u S}{\delta x} + \frac{\delta v S}{\delta y} + \frac{\delta w S}{\delta z} = \frac{\delta}{\delta z}\left(K_h\frac{\delta S}{\delta z}\right) + \frac{\delta F_x^S}{\delta x} + \frac{\delta F_y^S}{\delta y} \tag{IV.7}$$

where I_s is the radiative solar forcing, Cp the water heat capacity and $F_{(x,y)}^{(T,S)}$ are the diffusion fluxes, for temperature and salinity. T, S, and p variables are involved in the non-linear state equation that computes the density (Jackett et al., 2006). The eddy diffusivity coefficient K_h is determined by the turbulence closure scheme.

IV.2.1.2 Turbulence closure scheme

Turbulence closure schemes are used to compute the two coefficients of eddy diffusivity (K_h and K_m). In the present study, the k-ξ turbulence closure scheme is chosen, which includes the wave-current effect, and has been implemented according to Michaud et al. (2012). Following Gaspar et al. (1990), the horizontal eddy viscosity coefficient K_h is written as:

$$K_h = \sqrt{2E_k}\, l_k S_h \tag{IV.8}$$

while the vertical eddy diffusivity coefficient K_m is defined as:

$$K_m = \sqrt{2E_k}\, l_k S_m \tag{IV.9}$$

In Eqs. IV.8 and IV.9, l_k is a mixing length which depends on the turbulent kinetic energy E_k. The l_k parameter is computed as :

$$l_k = c_0^3 E_k^{\frac{3}{2}} \xi^{-1} \tag{IV.10}$$

where c_0 is a constant and ξ is the dissipation rate of the turbulent kinetic energy E_k. S_h and S_m in Eqs. IV.8 and IV.9 respectively, refer to stability factors described in Canuto et al. (2001). These factors depend on the Brunt-Vaisala frequency (N), on E_k and ξ for which, Burchard and Bolding (2001) established the following equations:

$$\frac{dE_k}{dt} = \frac{\delta}{\delta z}\left(K_m \frac{\delta E_k}{\delta z}\right) + P + B \tag{IV.11}$$

$$\frac{d\xi}{dt} = \frac{\delta}{\delta z}\left(\frac{K_m}{\sigma_k} \frac{\delta E_k}{\delta z}\right) + \frac{\xi}{E_k}(c_1 P + c_3 B - c_2 \xi) \tag{IV.12}$$

where c_1, c_2, and c_3 correspond to constants of calibration determined following the recommendations of Canuto et al. (2001). Furthermore, σ_k is the Schmidt number for dissipation, P is the production of turbulent kinetic energy and B is the buoyancy flux as:

$$P = K_m \left[\left(\frac{\delta u}{\delta z} \right)^2 + \left(\frac{\delta v}{\delta z} \right)^2 \right] \tag{IV.13}$$

$$B = \frac{g}{\rho} K_h \frac{\delta \rho}{\delta z} \tag{IV.14}$$

Boundary conditions approximations for E_k:

- At the surface, fluxes (F) follow the formulation of Craig and Banner (1994): $\left(F = 100 \left(\frac{\tau}{\rho} \right)^{1.5} \right)$ where τ is the wind stress computed by the bulk formulas.

- At the bottom, E_k corresponds to the equilibrium between energy production and dissipation:

$$E_{k_{z=-h}} = \frac{||\tau||}{\rho_0 \sqrt{2^{0.5} c_0^3 S_m}} \tag{IV.15}$$

Boundary conditions approximations for ξ:

Bottom and surface boundary conditions for the dissipation term ξ are derived from the mixing length l and E_k as:

$$\xi = c_0^3 E_k^{\frac{3}{2}} l^{-1} \tag{IV.16}$$

This condition is computed at the first level below the surface, or at the first above the bottom. The mixing length corresponds to the equilibrium between kinetic energy and the Brunt-Vaisala frequency N:

$$l = \frac{(2E_k)^{\frac{1}{2}}}{N} \tag{IV.17}$$

IV.2.1.3   Grid discretization, terrain-following coordinate system and discretization schemes

To solve the model equations, the GoT domain is spatially discretized over a Arakawa staggered C-grid (Fig. IV.1 a) (see section III.2.2.2 of Chapter III for grid construction details). This mesh has
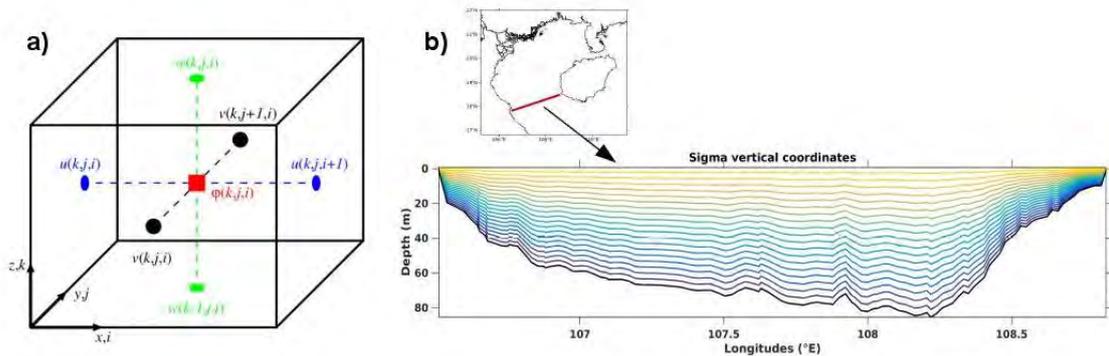
Figure IV.1: (a) Arakawa C-grid representation: indices, *i, j, k* refer to grid points in *x, y* and *z* directions, respectively, and scalar quantities are represented by φ. (b) σ (sigma) vertical layers coordinates along the red transect.

the particularity to define the scalar quantities (such as temperature and salinity) at the center of each grid volume, whereas velocity components are shifted by half a grid width in their respective direction so that they are defined at the edges of the grid volumes. Besides its bipolarity and curvilinearity, which offers a horizontal resolution as high as 150 m in the river channels and as low as 5 km at the open boundaries (see Chapter III, section III.2.2.2), the grid over our GoT domain is composed of Nx x Ny = 431 x 602 horizontal points, and of 20 vertical σ coordinates (Fig. IV.1 b). Sigma coordinates provide a strong advantage over regular z-coordinates in regions with complicated bathymetry where a high resolution of the vertical grid is required, not only near the surface but also near the bottom. In our case, sigma coordinates allow a high resolution in the coastal area where most of the sediment transport and transformation usually occurs.

Two different schemes are used for solving the equations in space. The scalar quantities are computed by an advection-diffusion scheme of type upwind of order 3, whereas the vectorial quantities (velocities) are computed by a centered scheme of order 4. In time, the forward-backward scheme is used and is further described in Marsaleix et al. (2019).

IV.2.1.4 Boundary conditions and associated forcings

In order to carry out realistic simulations of the ocean dynamics of the Gulf of Tonkin, good quality boundary conditions are crucial.

IV.2.1.4.1 Free surface boundary

The free surface represents the interface between the ocean and the atmosphere. In SYMPHONIE, the wind stress τ_s represents the source of kinetic energy and affects the surface conditions as fol-

lows:

$$\rho_0 K_m \left(\frac{\delta u}{\delta z}, \frac{\delta v}{\delta z} \right) = \left(\tau_{s,x}, \tau_{s,y} \right) \tag{IV.18}$$

where τ_{sx} and τ_{sy} are the wind stresses.

The atmospheric heat forcings gather different types of fluxes: the sensible heat Q_s, the latent heat Q_l, the short waves radiative flux Q_c and the long waves radiative flux Q_e. The sum of these fluxes corresponds to the total heat fluxes such as:

$$K_m \frac{\delta T}{\delta z} = Q_l + Q_c + Q_s + Q_e \tag{IV.19}$$

The salinity flux is zero at the surface and depends on the fresh water budget at the surface. This latter is estimated from the surface boundary condition applied to the vertical velocity W_{surf}:

$$W_{surf} = -\left(\frac{Q_l}{\rho L_v} + Pr \right) \tag{IV.20}$$

where L_v is the latent heat of condensation ($L_v = 2.5 \times 10^6$ J kg^{-1}) and *Pr* represents the precipitation rate. The turbulent fluxes at the ocean-atmosphere interface provide Q_s, Q_l and τ_s and are computed following formulations of Large and Yeager (2004). In this study, the atmospheric conditions (i.e. wind intensity, potential temperature, atmospheric pressure, relative humidity, precipitation rate, short and long waves radiative flux) come from the European Centre for Medium-Range Weather Forecasts (ECMWF), the product used is a forecast CF-1.0 with analyses every 3 hours.

IV.2.1.4.2   Lateral boundaries (ocean and river)

The lateral boundary conditions are described in Marsaleix et al. (2006). Lateral boundaries can be closed along the continent or islands, in this case the variables equal zero. However, lateral boundaries can be open when connected with other bodies of water, including oceans or rivers.

With open ocean boundaries, the values for u, v, w, T, S and the surface elevation η associated with the large scale circulation should be provided at every time step by a larger scale model. Vari-

ables u, v and η moreover also include the tidal circulation. In this study, lateral ocean boundary conditions are provided by Mercator Ocean (http://www.mercator-ocean.fr). The product used is the daily mean fields from Global Ocean 1/12° Physics Analysis and Forecast, (downloaded from: http://marine.copernicus.eu/services-portfolio/access-to-products/). Concerning the tides and despite the effort made on improving the tidal solutions by using an improved bathymetry dataset and an appropriate parameterization (Chapter III), solutions obtained for the main tidal constituents of the GoT (O1 and K1) with TKN simulation showed greater errors compared to altimetry than solutions (for O1 and K1) from FES2014b (which performs better thanks to the assimilation procedure). Therefore, the choice is made to use FES2014b for tidal solutions at the lateral boundaries.

Scalar variables

The scalar variables (T, S) are advected at the open boundaries by a hybrid scheme composed of an upstream scheme and a centered scheme.

Barotropic currents

A Flather type condition is applied to the surface elevation η when considering barotropic currents:

$$\eta - \eta_f = -\sqrt{\frac{H}{g}} \left(\overline{u} - \overline{u_f} \right) \ \text{ at } \ x = 0 \tag{IV.21}$$

$$\eta - \eta_f = \sqrt{\frac{H}{g}} \left(\overline{u} - \overline{u_f} \right) \ \text{ at } \ x = x_m \tag{IV.22}$$

where f corresponds to the sum of forcings (i.e., large scale circulation and tidal circulation).

Moreover, a Neumann condition is applied to the tangential transport at the boundaries:

$$\frac{\delta H \left(\overline{v} - \overline{v}_f \right)}{\delta x} = 0 \ \text{ at } \ x = 0 \ \text{ and } \ x = x_m \tag{IV.23}$$

Tide

In this section, details of the formulations for u, v and η derived from the tidal forcing are given.

In coastal open seas, tidal forcing consists mainly of tidal surface elevations and currents intro-
duced as forcing terms in the lateral boundary. Tidal forcings are also composed, to a smaller ex-
tent, of astronomical and loading potentials (Π_A and Π_L , respectively), which provide a barotropic
force added to the momentum equation, through the horizontal components of their gradients.
Tidal sea surface elevations and associated currents can be written as follows:

$$\eta\left(\lambda,\varphi,t\right)=\sum_k f_k \eta_{0,k}\left(\lambda,\varphi\right)\cos\left(\omega_k\left(t-t_0\right)+V_{0,k}+u_k-G_{\eta,k}\left(\lambda,\varphi\right)\right) \tag{IV.24a}$$

$$u\left(\lambda,\varphi,t\right)=\sum_k f_k u_{0,k}\left(\lambda,\varphi\right)\cos\left(\omega_k\left(t-t_0\right)+V_{0,k}+u_k-G_{u,k}\left(\lambda,\varphi\right)\right) \tag{IV.24b}$$

$$v\left(\lambda,\varphi,t\right)=\sum_k f_k v_{0,k}\left(\lambda,\varphi\right)\cos\left(\omega_k\left(t-t_0\right)+V_{0,k}+u_k-G_{v,k}\left(\lambda,\varphi\right)\right) \tag{IV.24c}$$

where $\left(\eta_0,u_0,v_0\right)$ and $\left(G_\eta,G_u,G_v\right)$ are the amplitudes and phase lags for sea surface elevations
and currents which depend on the latitude φ and the longitude λ . The subscript k represents the
partial tides taken into account in this configuration: O_1, K_1, M_2, S_2, N_2, K_2, P_1, Q_1 and M_4. The
terms f_k and u_k are the nodal factors and are considered as constants (Doodson, 1927), ω is the
tidal frequency and V_0 is a constant related to the reference time t_0 . The tidal potential due to
astronomical effects Π_A (Hendershott, 1972) is then taken into account as follows:

$$\Pi_A = (1+k_2+h_2)\,fa\times\left(v_0\frac{1-3sin^2\left(\varphi\right)}{2}+v_1 sin\left(2\varphi\right)+v_2 cos^2\left(\varphi\right)\right)\times cos(\omega\left(t-t_0\right)+\upsilon\lambda+V_0+u) \tag{IV.25}$$

with a the equilibrium amplitude of the tide considered and k_2 and h_2 the Love numbers. The
values of the terms (v_0,v_1,v_2) and υ vary with the type of tide considered. In the case of long
period tide, $v_0=1$ and $\upsilon=0$, for the diurnal tide $v_1=1$ and $\upsilon=1$ and for the semi-diurnal tide
$v_2=1$ and $\upsilon=2$.

Then, the loading potential Π_L , also called LSA potential, which is considered as the retroactive
effect of tides on themselves, is provided by FES2014b atlas and given as :

$$\Pi_L = f\Pi_0\left(\lambda, \varphi\right) cos(\omega\left(t - t_0\right) + G_\Pi\left(\lambda, \varphi\right) + V_0 + u) \tag{IV.26}$$

Lastly, the horizontal momentum equation for the hydrostatic pressure force is defined as:

$$-\frac{\nabla p}{\rho_0} = -\frac{g}{\rho_0}\nabla\int_z^\eta\left(\rho - \rho_0\right)dz' - g\nabla\left(\eta - \Pi_A - \Pi_L\right) \tag{IV.27}$$

Baroclinic currents

When considering baroclinic currents, a radiative condition of Sommerfeld type is applied on the difference between the SYMPHONIE model variables (Φ) and the forcing model variables (Φ_f):

$$\frac{\delta\left(\Phi - \Phi_f\right)}{\delta t} + C_c\frac{\delta\left(\Phi - \Phi_f\right)}{\delta x} = 0 \text{ at } x = 0 \tag{IV.28a}$$

$$\frac{\delta\left(\Phi - \Phi_f\right)}{\delta t} - C_c\frac{\delta\left(\Phi - \Phi_f\right)}{\delta x} = 0 \text{ at } x = x_m \tag{IV.28b}$$

with C_c the phase velocity of baroclinic waves.

Sponge layer

Correction terms (or recall terms) are combined with Eqs. IV.21, IV.22, IV.28 and if the boundary is as x=0, the terms are written as follows:

$$e^{-\frac{x}{d}}\frac{\Phi_f - \Phi}{\tau_r} \tag{IV.29}$$

where Φ is the velocity, or T or S depending on the equation considered. The term d corresponds to a distance of exponential decrease that depends on the size of the domain, which is chosen by the user according to the buffer zone considered. The term τ_r corresponds to the recall time and is also addressed by the user.

Rivers

This study includes 14 rivers inputs, listed in Fig. IV.2 a. Each of the rivers mouths are located at the closest grid points compared to their real locations. The green dots represent rivers for which, their associated discharges were prescribed as climatological monthly means. Each of these rivers is represented as one simple grid point, on which forcing is applied. The red dots represent the 7 distributaries of the Red River system for which, daily mean discharges for the study period (2009-2017) were prescribed as forcings. Unlike the previous rivers (green dots), and due to their geographical configuration over the delta, the choice has been made to represent the 7 rivers of the Red River system as simple channels. Each channel is constructed as a straight row of meshes, with one mesh in width. The construction of these particular channels is further described in section IV.3.1.

Water discharges data were collected by the National Hydro-Meteorological Service (NHMS) of Vietnam at the hydrographic station of Son Tay (Fig. IV.2 b). Following the work of Vinh et al. (2014), who estimated the contribution of each distributary to the total Red River discharges using the MIKE11 model, a percentage of the total Son Tay's daily discharges was attributed accordingly to each distributary: 7% of the total discharge was attributed to the Bach Dang channel, 13.2% to the Cam channel, 14.5% to the Van Uc channel, 6.4% to the Thai Binh channel, 30.3% to the Ba Lat channel, 5.6% to the Ninh Co channel and 23% to the Day channel. The forcing variables Q (discharge), T and S are imposed at the river grid point (in case of river represented by green dots), or at the most upstream channel grid point (in case of river represented by red dots), where S=0 and T varies from 17°C in winter to 29°C in summer.

IV.2.1.4.3 Bottom

Losses of turbulent kinetic energy, generated by the friction of currents on the sea bed, depend on the bottom stress (τ_c) as:

$$\tau_{\vec{c}} = \rho_0 C_D ||\vec{V}_b|| \vec{V}_b = \rho_0 u_*^2 \qquad \text{(IV.30)}$$

where $(\vec{V}_b)$ are the bottom velocities and u_* the friction velocity. In SYMPHONIE, the parametrization of the non-dimensional bottom drag coefficient (C_D) is based on the assumption of a logarithmic speed profile over the whole water column and is written as:
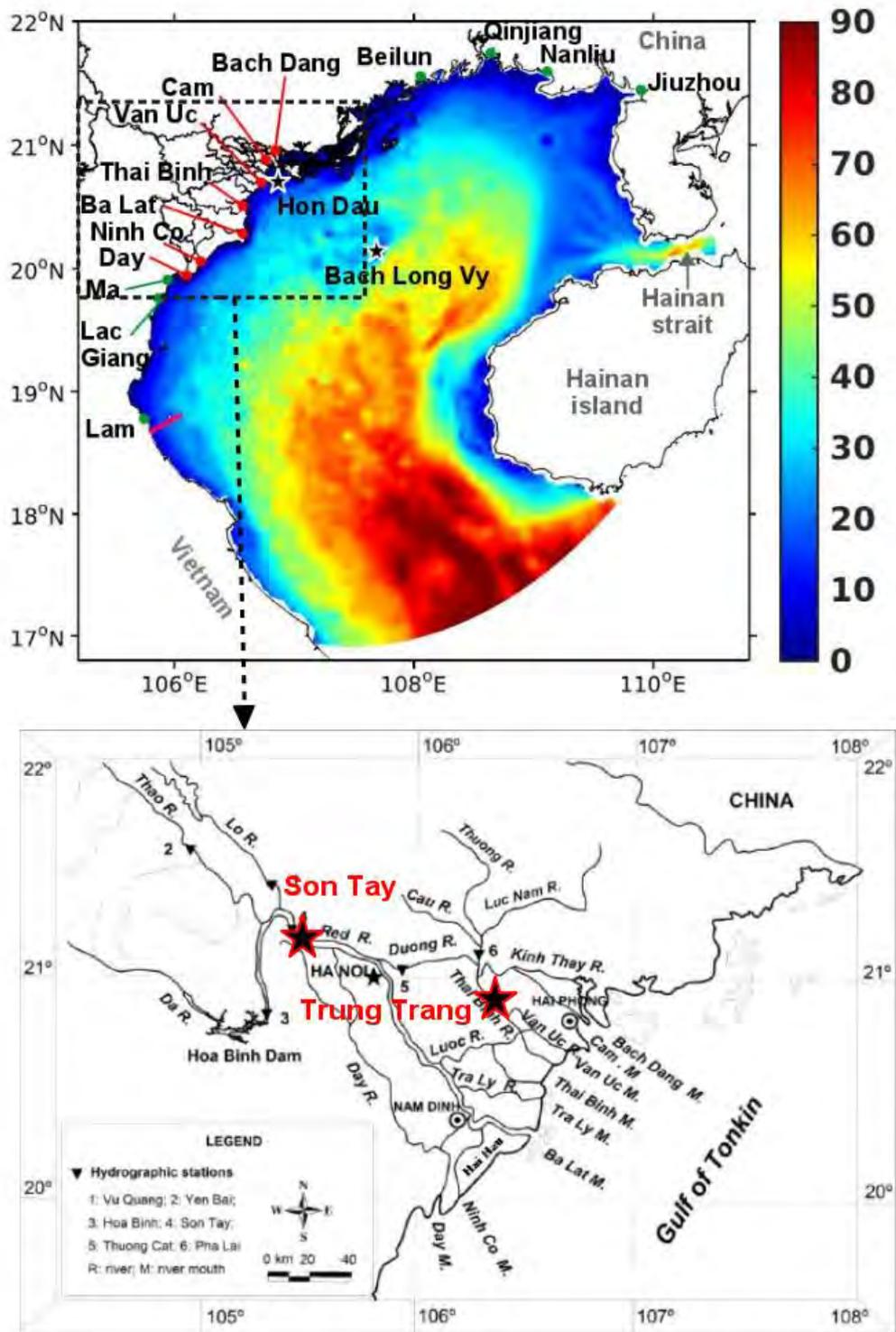
Figure IV.2: GoT bathymetry (in m) (a) and details of the Red River system (b). Green dots correspond to rivers represented as a simple grid point in the model, red dots correspond to rivers of the Red River system represented as channels in the model, the pink line represents the position of the CTD transects and the black stars represent Hon Dau, Bach Long Vy, Son Tay and Trung Trang hydrological stations.

$$C_D = \left(\frac{\kappa}{ln\left(\frac{z_1}{z_0}\right)} \right)^2 \qquad (IV.31)$$

with z_0 the roughness length at the bottom, z_1 the height of the first layer of the model and κ the von Karman's constant ($\kappa = 0.41$). In this bottom layer, the turbulent heat and salt fluxes are considered as zero.

IV.2.2 In-situ and satellite observation datasets

In this study, various in-situ data and products were used to evaluate the performance of the SYM-PHONIE hydrodynamical model.

In situ datasets

In the Gulf of Tonkin, two hydrographic stations provide temporal coverage of sea surface salinity (SSS), sea surface temperature (SST) and sea level over the period 1991-2017: Hon Dau and Bach Long Vi (Fig. IV.2 a). The data are provided by the NHMS at hourly time scale. Since the model's SSS, SST and sea level anomaly (SLA) are analysed on monthly averages, the high-frequency signals from the in-situ stations are removed by performing a monthly average of the data. Furthermore, the hydrological station of Trung Trang (TT) located on the Van Uc river (Fig. IV.2 b), 30 km upstream of the mouth, provides hourly water discharges and water elevation. In this case, the high-frequency data are of particular interest for assessing the model's ability to reproduce the tidal influence on water discharges within the river.

For validation of the model's vertical structure of temperature and salinity, a set of CTD transects are used (see Fig. IV.2 a). These 25 km long CTD transects were collected from September 2015 to August 2016 and are distributed by the Vietnamese Administration of Seas and Islands, Center for Oceanography.

To evaluate the modeled surface currents, maps of ocean surface currents derived from high frequency radio waves obtained by three High Frequency (HF) radars are used. These HF radars are located along the coastline of Vietnam at three CODAR stations (Hon Dau, Nghi Xuan and Dong Hoi) and are part of the Global High Frequency Radar Network (Roarty et al., 2019). Hourly data are available from 2012 to present, with a resolution of 5.85 km. The locations of the radars and their spatial coverages, which vary with the seasonal monsoon patterns, are presented in Fig. IV.3.

Products and satellite-observations datasets

For the evaluation of the modeled SST over the GoT, the 1/18° daily Operational Sea Surface Temperature and Sea Ice Analysis (OSTIA) distributed by the UK Met Office (Stark et al., 2007) is cho-
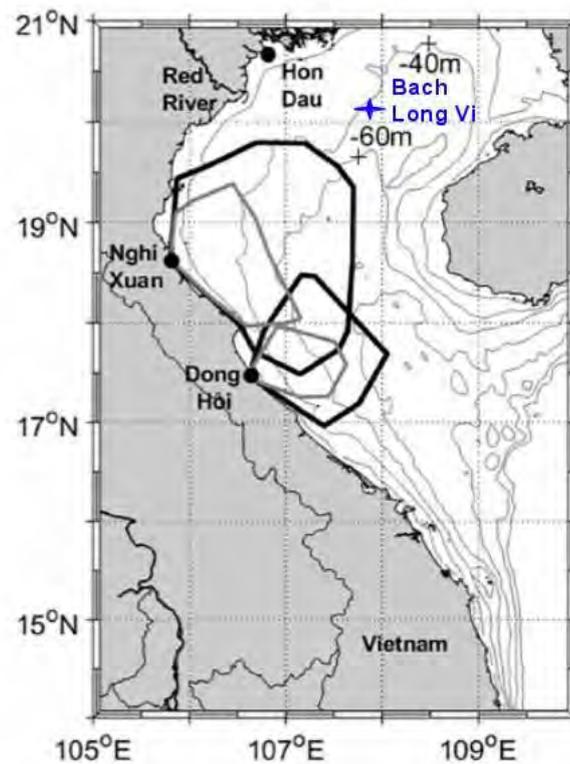
Figure IV.3: Positions of the HF Radars stations (black dots) overlaid with 20 m depth contours. The gray and black polygons indicate the coverage boundaries during the summer and winter seasons, respectively (from Roarty et al., 2019).

sen. The data are available for the period 2006 to present from https://podaac.jpl.nasa.gov/dataset/UKMO-L4HRfnd-GLOB-OSTIA.

The 1/4° L3_DEBIAS_LOCEAN_v3 product from the Soil Moisture and Ocean Salinity (SMOS) satellite mission of the European Space Agency (ESA) launched in 2009 is used for the validation of the model's SSS (Boutin et al., 2018). SMOS is the first satellite mission using L-band interferometric radiometer to measure SSS and soil moisture from space. The L3_DEBIAS_LOCEAN_v3 Sea Surface Salinity maps have been produced by LOCEAN/IPSL (UMR CNRS/UPMC/IRD/MNHN) laboratory and ACRI-ST company. This product is distributed by the Ocean Salinity Expertise Center (CECOS) of the CNES-IFREMER Centre Aval de Traitement des Données SMOS (CATDS), at IFREMER, Plouzane (France) and is available at https://www.catds.fr/Products/Available-products-from-CEC-OS/CEC-Locean-L3-Debiased-v3.

Lastly, to evaluate the modeled sea level anomaly (SLA), the delayed-time Global Ocean Gridded SSALTO/DUACS Sea Surface Height L4 product and derived variables available, from: http://marine.copernicus.eu/services-portfolio/access-to-products/?option=com_csw&view=details&product_id=SEALEVEL_GLO_PHY_L4_REP_OBSERVATIONS_008_047,

is used. This is a global product with 1/4° resolution at daily timescale, from 1993 to present in which, the SLA is computed with respect to a twenty-year mean. For comparison with the model outputs, the mean SLA over the model period (2009-2017) is then subtracted to the SLA at each grid point, both for the model and the data.

Climate indices

The interannual variability of different modeled parameters is compared to well-known climate indices, to search for possible relationships, such as the atmospheric El Niño Southern Oscillation (ENSO) Index (SOI) (Allan et al., 1996; https://www.esrl.noaa.gov/psd/gcos_wgsp/Timeseries/SOI/) and the oceanic ENSO index SST Niño4 (in the box 5° S-5° N, 160° E-150° E) (Rayner et al., 2003; https://www.esrl.noaa.gov/psd/data/correlation/nina4.data). The SST Niño4 index is preferentially used to characterize all types of El Niño events.

The Dipole Mode Index (DMI) (Saji et al., 1999; https://www.esrl.noaa.gov/psd/gcos_wgsp/Timeseries/DMI/), used to characterize the intensity of the Indian Ocean Dipole, as well as the Pacific Decadal Oscillation (PDO) (Mantua and Hare, 2002; http://research.jisao.washington.edu/pdo/PDO.latest.txt), are also considered as they may influence the climate changes of the studied region. Lastly, the Marshall Southern Annular Model (SAM) which characterizes westerlies variability over the southern Pacific (Marshall, 2003; https://legacy.bas.ac.uk/met/gjma/sam.html) and the Northern Pacific (NP) index which characterize changes in sea level pressure over the northern Pacific (Trenberth and Hurrell,1994; https://climatedataguide.ucar.edu/sites/default/files/npindex_monthly.txt) are also used as they may impact atmospheric circulation over the GoT.

IV.2.3   Metrics and statistical methods

For comparison of the simulations with observations, three statistical parameters are used. These are the correlation coefficient R, the Nash-Sutcliffe efficiency coefficient NSE (Nash and Sutcliffe, 1970) and the bias. R calculates the strength of the relationship between the relative movement of two variables. If x_t represents the observed temporal series, y_t the simulated temporal series, and $\overline{x}$ and $\overline{y}$ the mean of each series, R is computed as follows:

$$R = \frac{\sum_{t=1}^{N} \left(x_t - \overline{x}\right)\left(y_t - \overline{y}\right)}{\sqrt{\sum_{t=1}^{N} \left(x_t - \overline{x}\right)^2 \sum_{t=1}^{N} \left(y_t - \overline{y}\right)^2}} \tag{IV.32}$$

The values range between -1.0 and 1.0; a correlation of -1.0 shows a perfect negative correlation, while a correlation of 1.0 shows a perfect positive correlation.

In NSE, the sum of the absolute squared differences between the simulated and observed values of Q is normalised by the variance of the observed temporal series as:

$$\text{NSE} = \frac{\sum \left(x_t - y_t\right)^2}{\sum \left(x_t - \overline{x_t}\right)} \tag{IV.33}$$

NSE varies from 1.0 (perfect fit) to $-\infty$; a negative value indicating that the mean value of the observed temporal series would have been a better predictor than the model (Krause et al., 2005). Lastly, the bias represents the difference between the means of the two temporal series as:

$$bias = \overline{y} - \overline{x} \tag{IV.34}$$

The interannual variability of the simulation outputs can be studied by removing the seasonal variability of the signals by using the method TY-H13 developed in Piton and Delcroix (2018). This method consists in subtracting the typical year from the original time series and filtering the remaining signal with a 13-months low pass Hanning filter. The filter passes almost no signals at periods less than or equal to six months, filtering out the intraseasonal variability (and shortening each time series by 6 months at the two extremities).

Empirical Orthogonal Functions (EOFs) are often used in climate studies to indicate the possible spatial modes of variability of a dataset and how it changes with time, by isolating the dominant signals of variations (North et al., 1982). Each EOF mode separates the spatial function and the temporal functions from the signal. This way, the amplitude of the signal is the direct product of the spatial and temporal functions. Here, EOFs are applied on the modeled surface currents signals to get the principal modes of variability of the seasonal cycles, and on surface currents series filtered with the TY-H13 method to get the principal modes of interannual variability.

IV.3   Configuration Optimization

One of the main objectives of this chapter is to validate SYMPHONIE model's outputs with observations, especially in estuaries and coastal areas, where hydro-sedimentary processes are develop-

ing. Therefore, efforts have been made to configure the river channels, in terms of river discharges, tidal intrusion, salinity and stratification to best fit the in-situ observations (see Chapter II). In this section, steps in river channels construction, water discharges set up along with model evaluation with observations are described.

IV.3.1   Step 1: Rivers constructions and evaluation

As previously mentioned in section IV.2.1.4, the seven Red River distributaries are represented in the model grid as channels, which are constructed as a straight row of meshes with one mesh in width (Fig. IV.4 a).
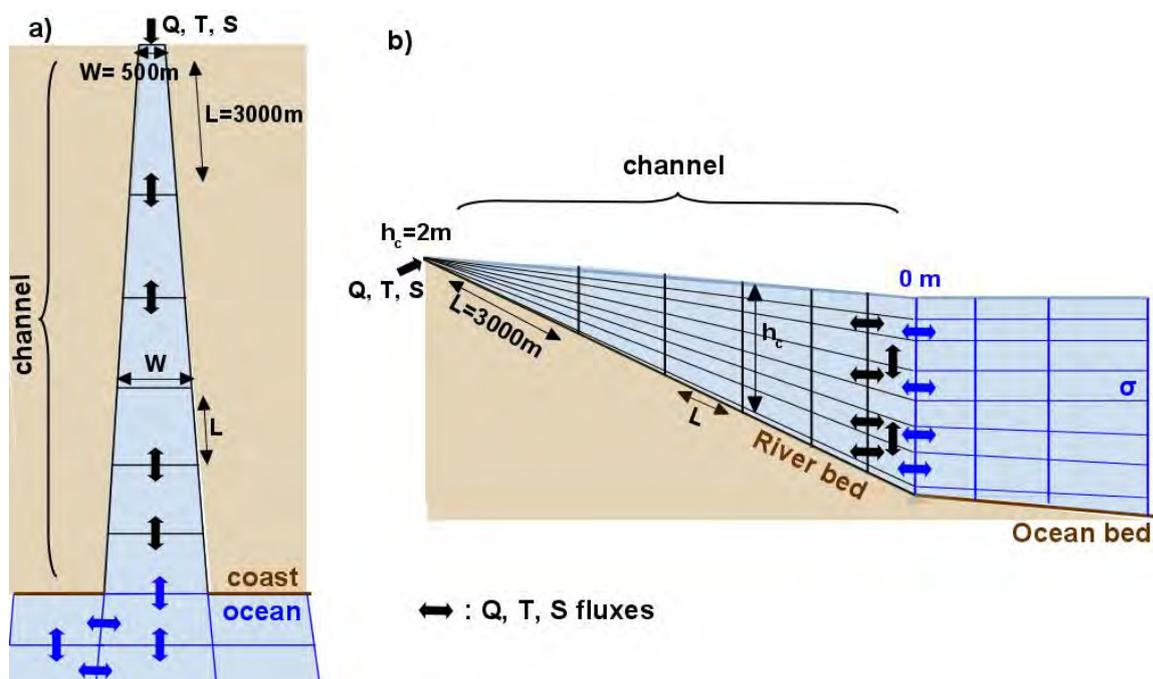
Figure IV.4: Schematic representation of the initial river channels from a top view (a) and from a lateral view (b).

Each mesh has associated "real" longitude and latitude coordinates. However, the width W , the length L and the depth h_c of each mesh can be manually adjusted by the user (Fig. IV.4 b). This tool is of particular interest when modelling tidal intrusion/dissipation or water discharges, since changes in the mesh size directly impact velocities. Indeed the velocity u can be computed as follows:

$$u = \frac{Q}{W h_c} \tag{IV.35}$$

where Q is the water discharge.

Rivers	Bach Dang	Cam	Van Uc	Thai Binh	Ba Lat	Ninh Co	Day
River length (km)	60	81	134	80	123	74	74
D (km)	109	103	59	122	80	144	143
t (h)	32.7	31.0	17.7	36.6	24.0	43.2	43.0

Table IV.1: River lengths as represented in the model of each river of the Red River systems, D the distance between Son Tay station and the first river grid point and t the time lag imposed to each river discharge.

As for most of the rivers, bathymetric and elevation data are not available, channels were constructed the same way: at the first river point, W , L and h_c values match the characteristics of the closest ocean mesh. Going upstream, W and h_c values linearly decrease until reaching 100 m and +2 m, respectively while L linearly increase until reaching 3000 m. Such increase in mesh length allows to artificially extend the channel length, without adding more meshes. The value of $h_c = 2m$ at the last channel points was determined after testing the attenuation of the tidal amplitude through the channels for different values of h_c . Three two-year long simulations were performed with $h_c = 0m$, $h_c = 1m$ and $h_c = 2m$. Regarding the Thai Binh river case, O1 amplitude was ~ 5 cm at the last channel point with an elevation $h_c = 0m$, ~ 2.5 cm with $h_c = 1m$ and < 1 cm with $h_c = 2m$ (Fig. IV.5 a). For M2 case, both simulations with $h_c = 1m$ and $h_c = 2m$ showed the lowest amplitudes at the last channel grid point (Fig. IV.5 b). Similar tests were performed for the Bach Dang, Cam, Van Uc, Ba Lat, Ninh Co and Day channels, and each time, smallest tidal amplitudes were found for $h_c = 2m$. Therefore, for each channel, the elevation was set to 2 m.
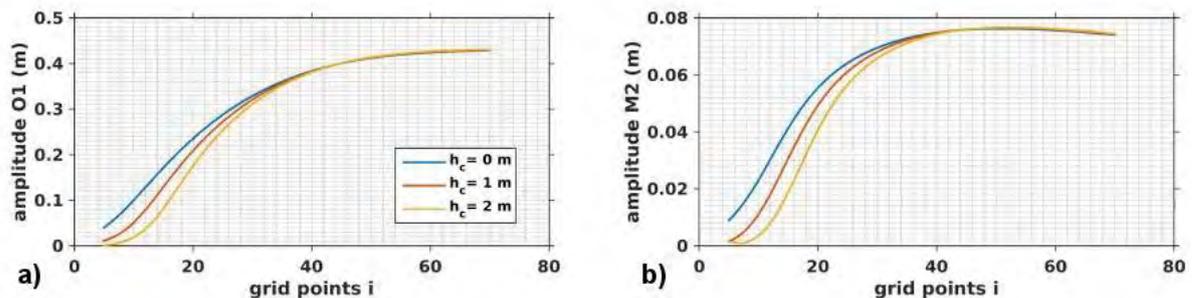
Figure IV.5: Tidal amplitude of waves O1 (a) and M2 (b) along the Thai Binh channel grid points for different values of h_c.

Since each rivers are composed of a different number of grid points, their lengths vary. The total length of each river is given in Table IV.1.

IV.3.2   Step 2: Water discharges set up

Son Tay hydrological station, which provides water discharge data (Q) (section IV.2.1.4), is located upstream of the 7 Red River distributaries. The distances D from Son Tay to the first grid point

of each river channel are listed in Table IV.1. This suggests that a lag should be applied to the discharge Q at the first river mesh, corresponding to the time required for the water to travel the distance D. To determine the lags, a three-year simulation (2009-2011) is performed with initial and boundary conditions mentioned in section IV.2.1.4 and with hourly model outputs. Two Q time series from two points, spaced by 10 km on the Van Uc channel, are extracted. The time series are filtered over 24 h to remove the diurnal tidal signal. The best lagged correlation (R and NSE) between the two Q time series were found for a lag of 3 h. It leads to assume that the current speed is $u = d/lag$ = 10/3 =3.33 km h^{-1} ($\sim$ 93 cm s^{-1}). From this assumption, the time t needed for the water from Son Tay to travel the distance D to the first grid point of each channel is computed as t = D / u (Table IV.1). The value of u is used for each channel. These delays t are therefore applied to each Q time series of each channel.

IV.3.3   Step 3: Van Uc river construction and evaluation

Regarding the Van Uc river case and as described in Chapter 2, various data were collected along the estuary throughout the year 2017 (salinity, temperature, turbidity, SPM, current velocities). In this study, Van Uc survey data are used for the model calibration in the estuary and for evaluating the model performances in representing water discharges and fluxes, tidal intrusion and water mass properties within the estuary. Therefore, Van Uc river channel construction differed from the rather simple method used for the construction of the six other channels (section IV.3.1). Here, a particular attention was given to represent real river bathymetry and river width, based on the collected data.

To do so, W , L and h_c values were manually adjusted, mesh by mesh, based on the depths and widths of the river bed. A schematic representation of the adjustments are presented in Fig. IV.6.

O1 and M2 amplitudes along the Van Uc channel are compared between a simulation with a channel constructed with linearly decreasing W , L and h_c (noted "Channel initial") and a simulation with a channel constructed with realistic W , L and h_c values (noted "Channel real bathy") (Fig. IV.7). Both simulations showed O1 amplitudes $\sim$ 2.5 cm, which are higher compared to amplitudes obtained for Thai Binh (Fig. IV.5 a). To improve tidal attenuation within the Van Uc channel, three grid points are added at the end of the channel, each of L = 15000m (simulation is noted "Channel extended"). Simulation with "Channel extended" showed amplitudes <1 cm upstream for both O1 and M2, suggesting that this simulation allowed a good tidal dissipation (Fig. IV.7 a).
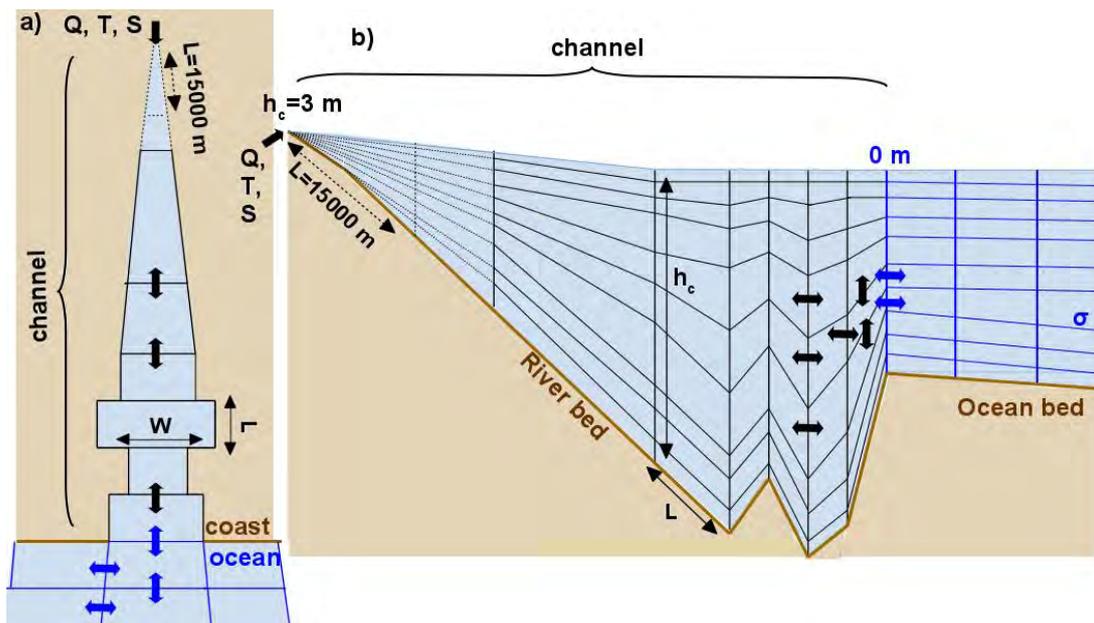
Figure IV.6: Schematic representation of the meshes adjustments made for the Van Uc channel, from a top view (a) and from a lateral view (b).
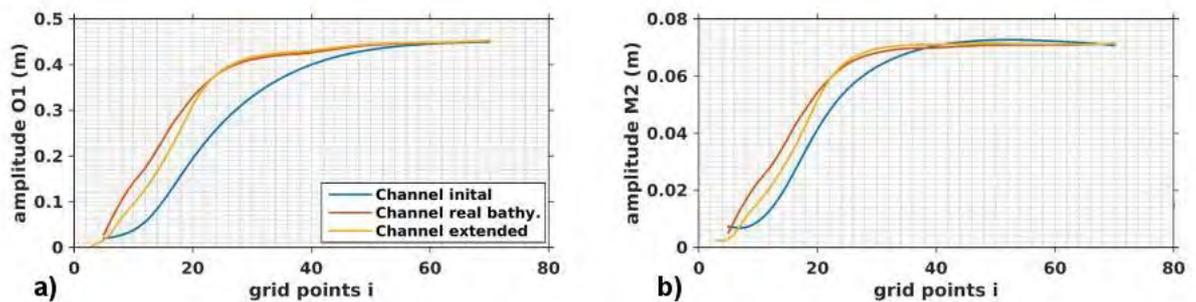
Figure IV.7: Tidal amplitude of waves O1 and M2 along the initial Van Uc channel (blue line, "Channel initial"), the channel with a real bathymetry (red line, "Channel real bathy") and the extended channel (yellow line, "Channel extended").

After constructing a realistic river in terms of depth and width, model performance evaluations led to further modifications of the configuration. Especially, model efficiency to reproduce daily water discharges Q at the hydrological station of Trung Trang was evaluated. Focus was made on the month of December 2017, when data corresponding to the dry season were collected. In Chapter II, it has been shown that neap/spring tide cycle plays a crucial role in water and SPM discharges during this period. Spring tides could reverse the flow for half the day, while neap tides could trigger a gravitational circulation (two-layer circulation) with a flow in both directions (up-estuary for the bottom layer and down-estuary for the top layer) and a very stratified water column. Furthermore, up-estuary suspended matter flux appeared to account for $\frac{2}{3}$ of the down-estuary flux in the low-flow season, which indicated that the estuary was silting up and the delta was consolidating during the dry season. Therefore, a good representation of water discharges

by the model is crucial for the representation of the above-mentioned processes. For the month of December 2017, modeled discharges (with simulation "Channel extended") represented well (NSE=0.89) the discharges at Trung Trang hydrological station. Modeled mean Q value ($370\,\mathrm{m^3\,s^{-1}}$) was however lower than the mean value from Trung Trang ($433\,\mathrm{m^3\,s^{-1}}$). Such results suggest a too strong tidal intrusion that could block the discharges. Tidal propagation within the estuary may be influenced by the bottom roughness length, therefore several simulations were performed with various z_0 values in the channels. Note that in the case of the simulation "Channel extended" , z_0 was set to 0.001 m. While changes in mean Q value were very little (from $367\,\mathrm{m^3\,s^{-1}}$ with $z_0 = 0.01$ m to $371\,\mathrm{m^3\,s^{-1}}$ with $z_0 = 0.0001$ m), simulation with $z_0 = 0.01$ m showed the best representation of observed discharges with NSE=0.92, against 0.89 and 0.85 for $z_0 = 0.001$ m and $z_0 = 0.0001$ m, respectively) with Trung Trang discharges data (Fig. IV.8).
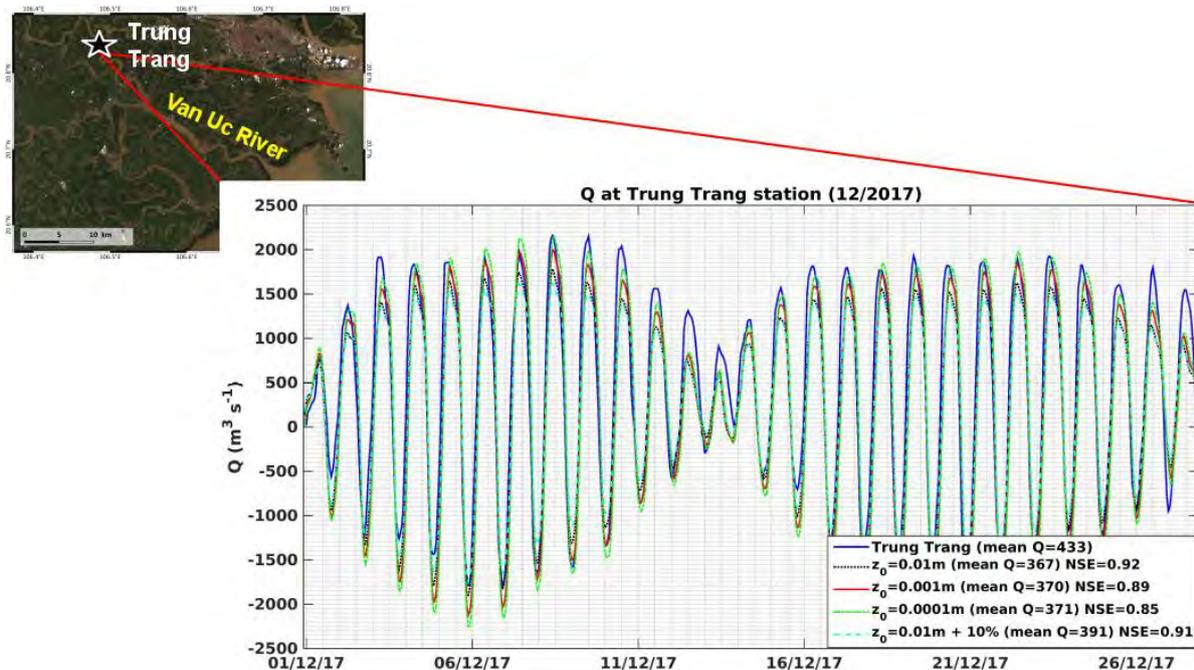
Figure IV.8: Comparisons between measurements of water discharges Q at Trung Trang in the observations (blue) and in the simulations (other colors) during December 2017.

Following these results, a simulation with a $z_0 = 0.01$ m and increased river discharges by 10% was performed (noted $z_0 = 0.01$ m + 10%). Again, correlation with Trung Trang discharges data was good (NSE=0.91) and the mean modeled Q ($391\,\mathrm{m^3\,s^{-1}}$) showed closer values to Trung Trang mean value than the previous simulations. However, concluding on the best parameterization option was difficult as results were very close to one another.

To help with the parameterization choice, modeled salinity profiles along the Van Uc estuary were compared to the observations (detailed in Chapter 2) during neap and spring tides of December

2017. Results from simulations with $z_0 = 0.01$ m, $z_0 = 0.001$ m and $z_0 = 0.0001$ m showed the model ability, in every case, to reproduce the tidal intrusion of spring tides, with decreasing salinities from the mouth (ST1) to upstream (ST3), and with salty water intrusion all over the water column at high tides (Fig. IV.9). However, salinities were overall too high compared to observations, especially in the simulation with $z_0 = 0.0001$ m. This is consistent with the fact that the smaller the roughness coefficient is, the less the bottom interacts with the currents. In addition, the model struggled to reproduce the observed low salinities at low tides, which suggested that either the along estuary tidal dissipation was not efficient enough, either river discharges were not strong enough. Simulation $z_0 = 0.01$ m + 10% showed a better representation of the low salinities at low tides as well as better salinities at ST3.
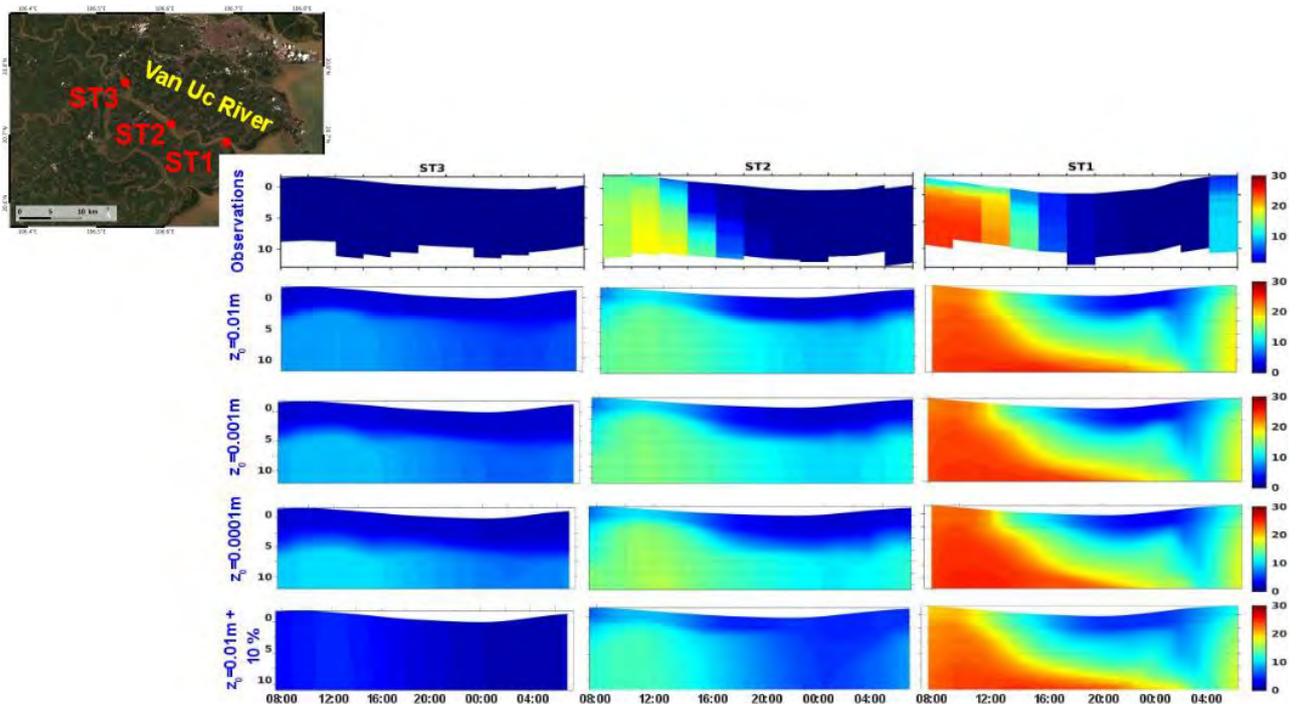
Figure IV.9: Salinity profiles during survey DS (dry season, spring tides) at ST1, ST2 and ST3 (top row) and corresponding salinity profiles from simulation with $z_0 = 0.01$ m (second row), $z_0 = 0.001$ m (third row), $z_0 = 0.0001$ m (fourth row) and $z_0 = 0.01$ m with increased Van Uc discharges by 10% (last row).

Interestingly, in neap tides, all four simulations presented very similar results (Fig. IV.10). The model nicely reproduced the salinity patterns compared with observations, especially in terms of thickness of the salty water layer. In terms of salinity values, simulations slightly underestimated the values of the bottom salty layer at ST1 and overestimated them at ST2. At ST3, the depth of the salinity gradient is well reproduced by the model but the salinity of the bottom layer was overestimated by the simulations. As observations did not show values below 10 m, it is difficult to evaluate the model performance at this station. Here, bottom roughness parameterization and

changes in river discharges did not significantly alter the tide propagation within the estuary. Following the results for neap and spring tides, the choice is made to set the river roughness length in the Van Uc river to 0.01 m and Van Uc river discharges initially given by Vinh et al. (2014) are increased by 10 % .
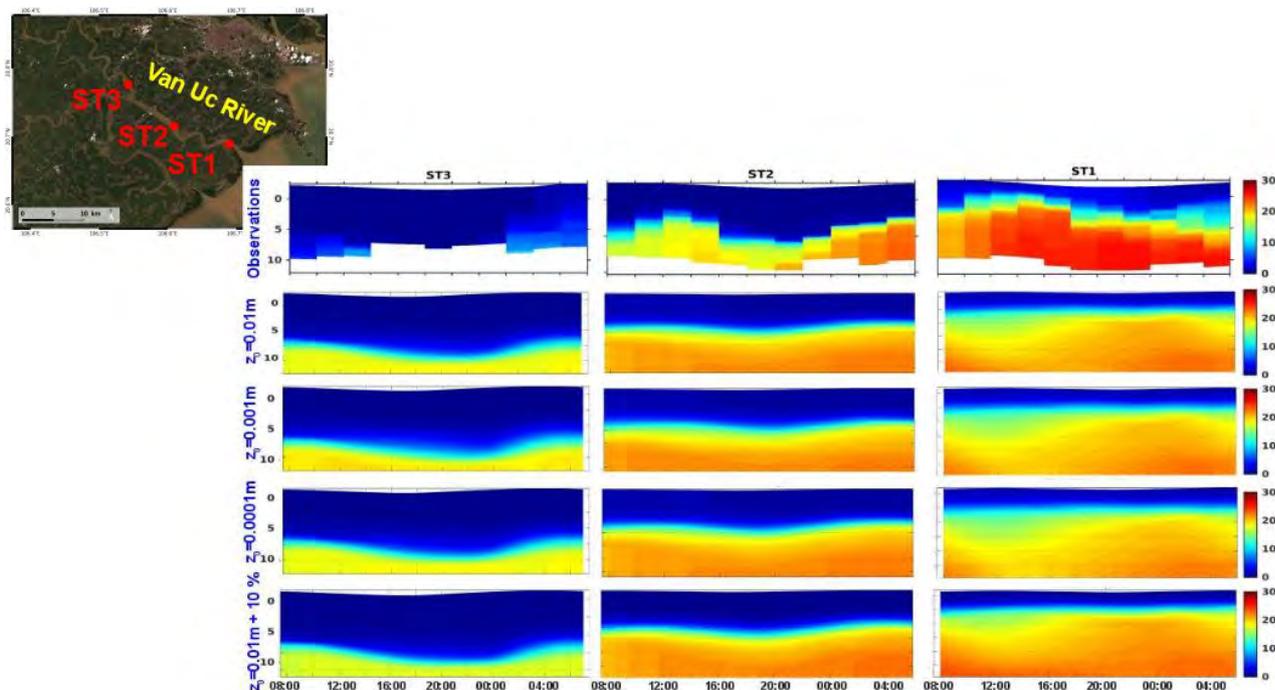
Figure IV.10: Same as Fig. IV.9 but for survey DN (dry season, neap tides).

Lastly, model performances in terms of current velocities within the Van Uc estuary were compared to observations (i.e. ADCP measurement, see Chapter II). Fig. IV.11 a presents the vertical velocity profiles measured in the middle of the Van Uc river, at ST2 during the dry season at neap tides. Measured data showed characteristics velocity profiles of tidal intrusion, especially during floods and high tides, with maximum values between 6 and 8 m depth. These correspond to the tidal currents that propagates along the estuary from flood to high tide during neap tide. Modeled profiles from simulation $z_0 = 0.01$ m + 10 % showed similar results at every tidal stage compared to observations, both in terms of values and patterns (Fig. IV.11 b). Only velocity maxima at flood and high tides were located slightly above the measured maxima (between 5 to 7 m). These small discrepancies suggest a slightly too strong tidal intrusion along the estuary.

Overall, simulation z_0=0.01 m + 10 % showed good agreement with observed water discharges, salinity and currents in the Van Uc estuary. Therefore, the choice was made to use this configuration for the rest of the study.
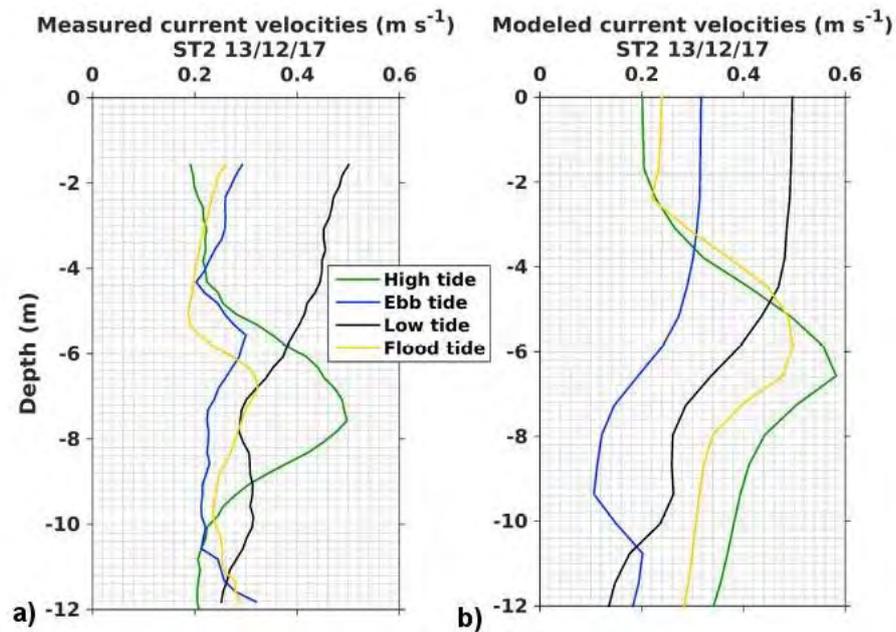
Figure IV.11: Currents velocities (m s^{-1}) measured (a) and modeled (b) at ST2 during survey DN (dry season, neap tide) at high tide (8 am), ebb tide (12 am), low tide (4 pm) and flood tide (2 am).

IV.3.4 Hypothesis frameworks for 2D and 3D approaches

In Chapter III, T-UGO hydrodynamical model was used in its spectral mode (2D) for determining the best grid configuration and bottom parameterization that should be applied to SYMPHONIE. Thanks to its low computational cost, T-UGO 2D proven its efficiency in solving tidal solutions faster than 3D regional models. The main result of this study was the key role played by the bathymetry dataset when modeling shallow-water tides. Indeed, the new bathymetry dataset developed in Chapter III allowed to improve tidal solutions of the four main constituents of the GoT, compared to previous studies using regular GEBCO bathymetry. Besides affecting tidal solutions, bathymetry matters in ocean circulation by influencing the steering and the vertical mixing in the ocean (Gille, 2003; Ledwell et al., 2000; Metzger and Hurlburt, 2001). Therefore, the improvement of the bathymetric dataset is also of particular interest for 3D modeling and is integrated in the SYMPHONIE model configuration used in this chapter.

In addition, the results presented in Chapter III emphasized the role of the bottom friction parameterization when modeling shallow-water tides. Particularly, a spatially regionalized roughness length (z_0) configuration allowed a clear improvement in the tidal solutions compared to previous 3D simulations from the literature and to the tidal atlas FES2014b (without data assimilation) for the semi-diurnal waves. Details of the z_0 regionalization are given in Fig. IV.12.

In this section, this configuration developed with the T-UGO 2D model is tested with the 3D
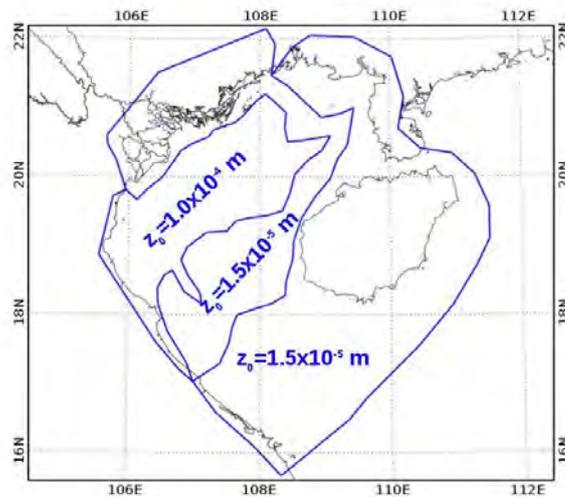
Figure IV.12: Best bottom friction parameterization obtained with T-UGOm in 2D mode.

SYMPHONIE model, and the results are compared with results from SYMPHONIE from a simple bottom-friction parameterization. Two twin simulations (1 year long) forced by FES2014b are performed: one simulation configured with the regionalized bottom friction parameterization developed in Chapter 3 (noted SIMU_varying_z_0), another simulation configured with a uniform bottom friction parameterization for 3D modeling, i.e. with z_0=0.001 m all over the domain (noted SIMU_constant_z_0). Fig. IV.13 presents the differences between the two simulations and FES2014b atlas in terms of tidal amplitudes, for waves O1, K1, M2 and S2.
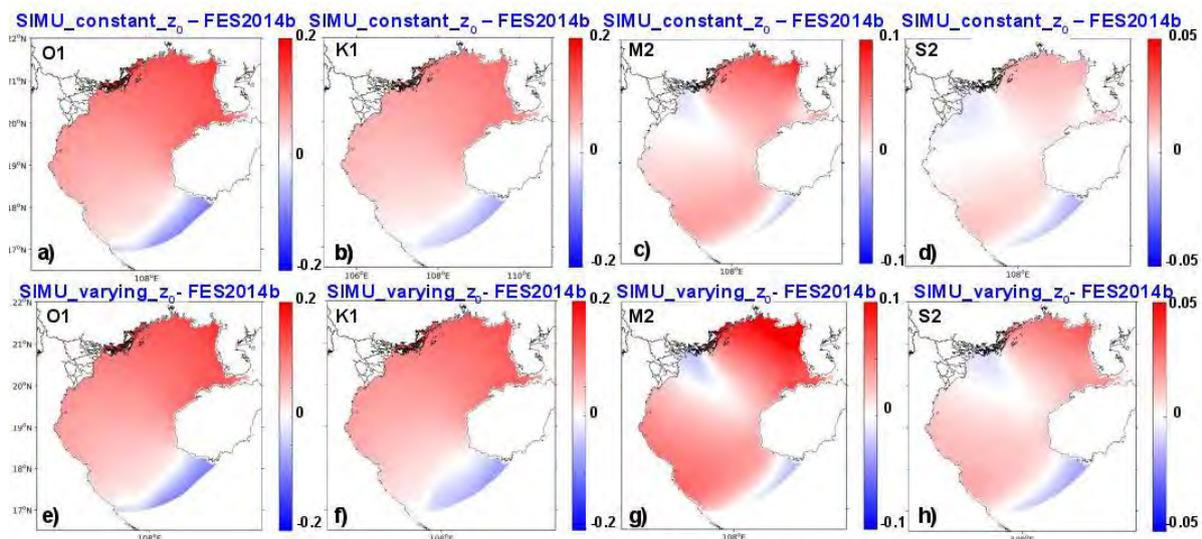
Figure IV.13: Tidal amplitudes differences (in m) between the modeled tidal waves and the forcing tidal waves (FES2014b) for O1 (a,e), K1 (b,f), M2 (c,g) and S2 (d,h), from SIMU_constant_z_0 (top panels) and from SIMU_varying_z_0 (bottom panels).

The patterns of differences of each wave are very similar between the two simulations. Considering the semi-diurnal wave M2, SIMU_constant_z_0 clearly shows smaller differences to FES2014b

(up to 0.06 m) than SIMU_varying_z_0 (up to 0.10 m), especially in the northeastern and south-westen parts of the basin where the wave resonates (Fig. IV.13 c,g). Overall, differences are positive almost all over the domain, meaning that both simulations overestimate M2 amplitude. Similar to M2 case, SIMU_constant_z_0 shows smaller differences (negative and positive) to the tidal atlas for S2 (up to 0.025m) than SIMU_varying_z_0 (up to 0.04 m) (Fig. IV.13 d, h). Again, the largest differences to FES2014b are observed in areas where S2 resonates. The two simulations show approximately the same differences to FES2014b considering the diurnal waves, except for K1 case in the northeastern part of the domain, where slightly higher positive differences appear with SIMU_-varying_z_0 (0.18 m against 0.15 m from SIMU_constant_z_0). Besides showing the sensitivity of SYMPHONIE to the bottom friction parameterization, these results suggest that the bottom friction configuration developed with a 2D model is not appropriate for a 3D modeling.

Therefore, a uniform z_0=0.001 m parameterization over the GoT is chosen for the rest of the study.

IV.4 Evaluation of model results over the Gulf of Tonkin

Using the configuration previously described, a 9 year-long SYMPHONIE simulation was performed over the period 2009-2017. In this section the realism of this simulation, noted SIMU, is evaluated in its representation of seasonal, annual and interannual variability of sea surface temperature (SST), sea surface salinity (SSS), sea level anomaly (SLA) and oceanic circulation. SIMU is compared to the available products and satellite data, to in-situ temperature, salinity and tide gauge data and to surface currents data presented in sections IV.2.1.4 and IV.2.3. If the modeled and observational data have different spatial/temporal resolution, the finer one will be resampled to the same resolution as the coarser one before making comparisons.

IV.4.1 SST

First of all, the realism of the simulation's seasonal SST fields (SIMU) are analysed. Fig. IV.14 shows the seasonally averaged maps of SST in summer (months of June, July, August, noted JJA hereafter) and in winter (months of December, January, February, noted from hereafter DJF), over the GoT for the 2009-2017 period, obtained from OSTIA analysis, SIMU and the forcing field (noted from hereafter GOM, for Global Ocean Model). Compared to OSTIA, the spatial distribution of SST in winter is well reproduced in SIMU, with a spatial correlation (R) of 0.94 (p<0.01), and of 0.95 (p<0.01) in GOM (Fig. IV.14 b, c). In winter, the northeast cold monsoon brings a cold tongue of surface water into the GoT from the SCS (Fig. IV.14 a, b, c). This strongly affects the GoT SST,

causing a clear N-S gradient: SST varies from about 17°C along the Chinese coast to about 25°C in the south of the GoT. In summer, the SST is more homogeneous and warm over the GoT with temperatures varying from ~ 28 to 30 °C (Fig. IV.14 d). Observations also show two small cold water areas of about 28.5 °C: one located near the southernmost Vietnamese coast (between latitudes 17 to 18 ° N) and one along the south-east coast of Hainan Island. Those observed cold patterns are reproduced in SIMU (Fig. IV.14 e) but with even colder temperatures (~ 27.5 °C), while only the cold area along the Vietnamese coast is reproduced in GOM (Fig. IV.14 f). Furthermore, a warm water band along the northern coast of the GoT and of Hainan is observed in SIMU and GOM, which explains the higher mean SST in SIMU (30.07 °C) and GOM (30.24°C) compared to OSTIA (29.87 °C). The spatial correlations over the GoT in summer between OSTIA and SIMU are lower than in winter (R=0.39, p<0.05), but remain higher than between OSTIA and GOM (R=0.25, p=0.12). Some of those weaker correlations in summer than in winter can be explained by the much smaller range of SST spatial variability.
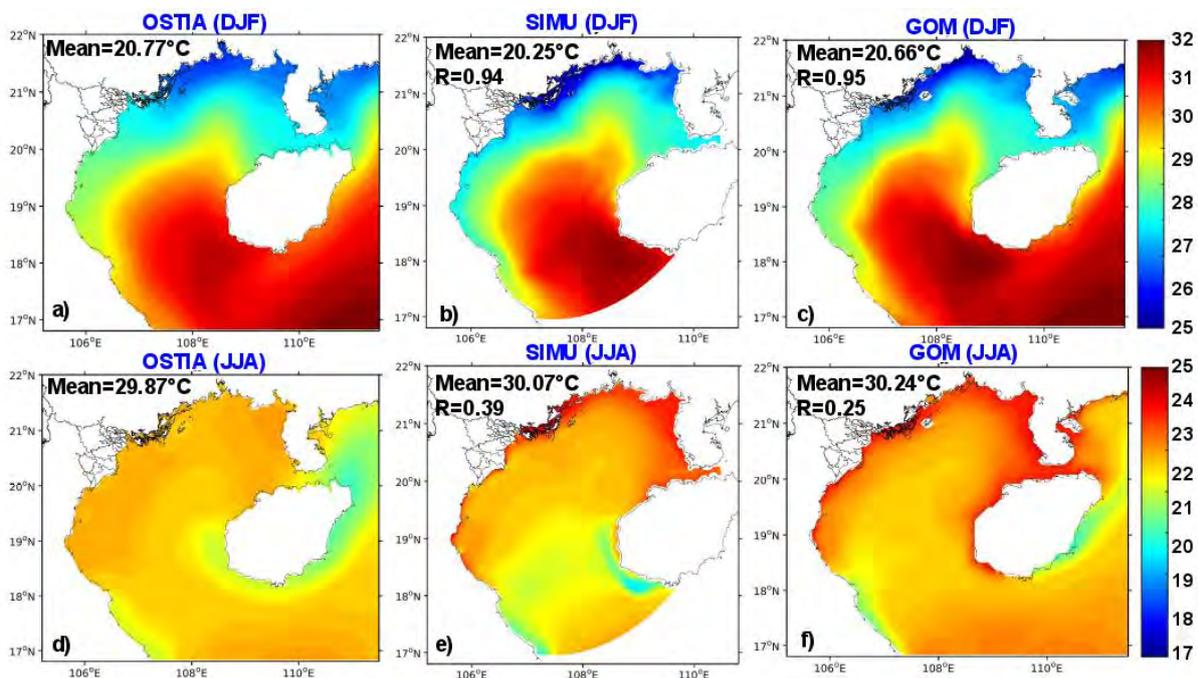
Figure IV.14: Evaluation of SIMU seasonal maps of SST. Climatological comparisons of sea surface temperature (SST, °C) between OSTIA (a, b), SIMU (c, e) and the forcing GOM (c, f) in summer (top panels) and winter (bottom panels)

To further explain these differences in spatial correlation and the inability of GOM to reproduce the cold water area along Hainan Island, a simulation without tide is performed (named SIMU_-No_Tide, Fig. IV.15). The climatological SST patterns for JJA in SIMU_No_Tide are very similar to the ones in GOM. Note that, the forcing model GOM does not integrate any tidal representation in its configuration. SIMU_No_Tide is unable to reproduce the cold water area along Hainan Island

and shows even poorer spatial correlation with OSTIA (R=0.14 (p=0.15)) than the spatial correlation found for SIMU. This suggests that the inability of GOM to represent this cold water area is related to the fact that GOM does not represent the effect of tides, which play a role in SST patterns, particularly in summer, and that implementing them in hydrodynamical simulations is crucial.
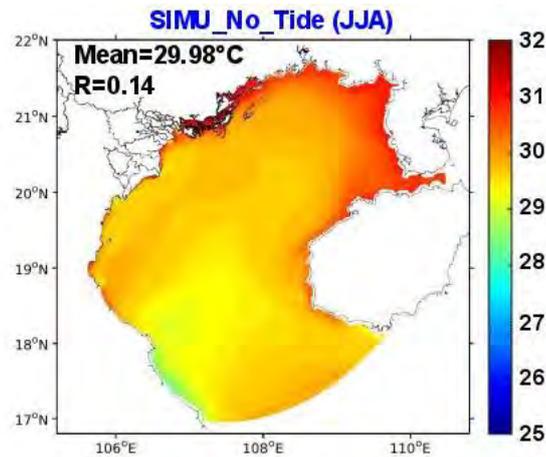
Figure IV.15: Climatological SST of the summer season (JJA) from simulation without tide.

Fig. IV.16 a presents the monthly SST anomaly variability averaged over the GoT for OSTIA, SIMU and GOM. Both models show good correlations with OSTIA. SIMU shows the lowest SST bias (on SST signal, not SST anomaly) to OSTIA (0.24 °C) while GOM shows almost twice bigger bias (0.43 °C). During the winter, SIMU always overestimates the negative SST anomalies compared to OS-TIA, while GOM always underestimates both negative and positive anomalies in winter and summer respectively, compared to OSTIA. SIMU, GOM and OSTIA show good correlation with in-situ datasets, in terms of R and NSE (Fig. IV.16 b, c). In both Bach Long Vi and Hon Dau cases, the highest biases are reached by GOM (0.74 (p<0.01) and 0.84 °C, respectively), while OSTIA is the closest to the in-situ dataset at Bach Long Vi (bias of 0.63 °C) and SIMU the closest to Hon Dau in-situ dataset (bias of 0.43 °C).

Fig. IV.17 presents the annual and interannual cycles of SST averaged over the GoT and at Bach Long Vi and Hon Dau stations. The annual cycle of SST is very well reproduced by both SIMU and GOM, with high correlation values (R and NSE) (Fig. IV.17 a). The model SST follows closely the observed OSTIA values from March to December, while it slightly overestimates the negative SST anomalies in January and February. However, GOM underestimates both negative and positive anomalies in winter and summer respectively, as previously described in Fig. IV.16. The in-situ annual SST cycles are also well reproduced by SIMU at both Bach Long Vi and Hon Dau stations (Fig. IV.17 b, c). Despite the good correlation with the in-situ dataset, all three products (SIMU, OS-
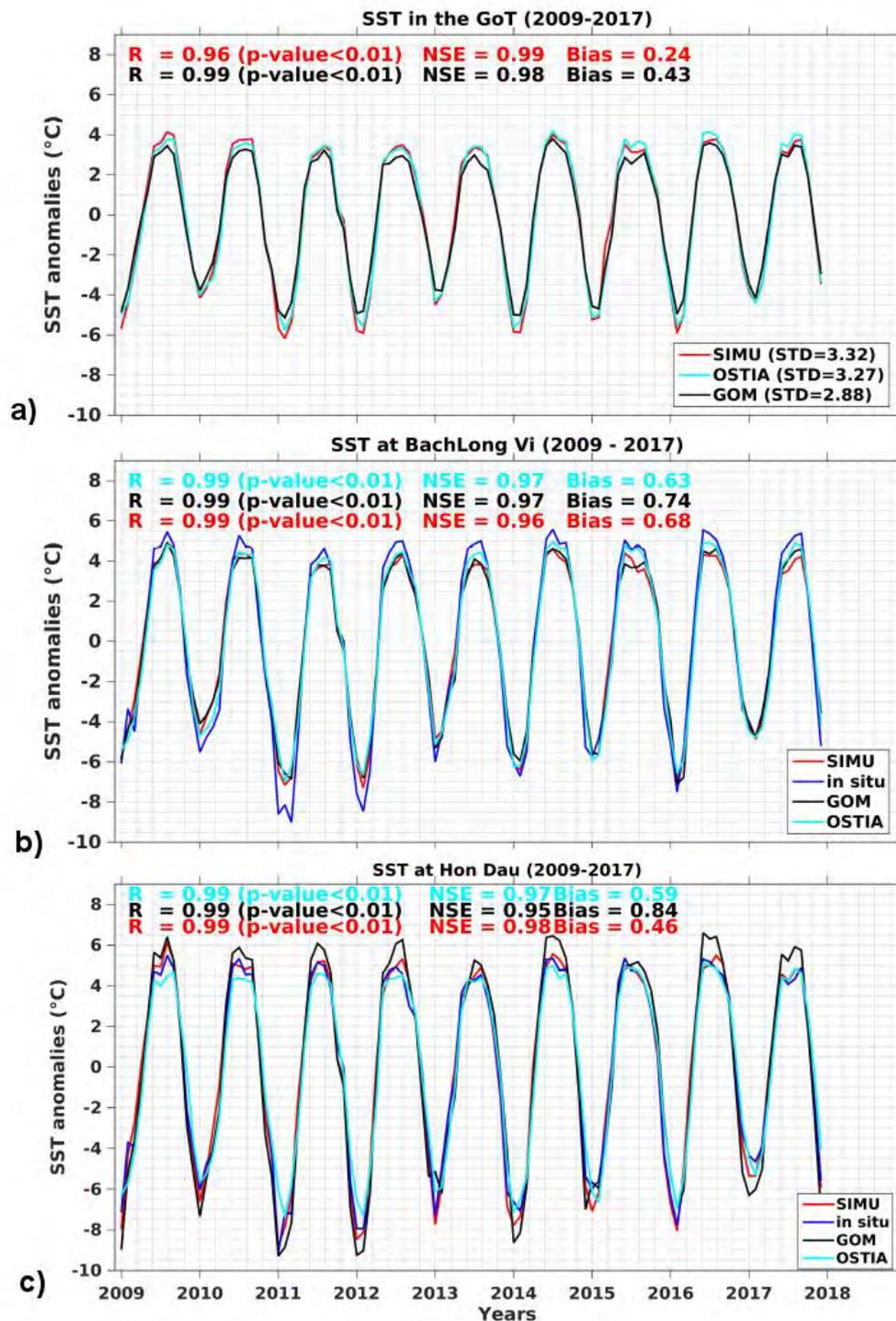
Figure IV.16: Evaluations of the monthly SST anomaly signals over the GoT of SIMU and GOM compared to OSTIA (a); of SIMU, GOM and OSTIA compared to Bach Long Vi hydrological station (b); of SIMU, GOM and OSTIA compared to Hon Dau hydrological station (c). Bias refer to the SST (not anomaly) signal.

TIA and GOM) slightly underestimate the negative and positive anomalies (in winter and summer, respectively) at Bach Long Vi (Fig. IV.17 b) by ~ 0.4 °C.

At interannual time scales, SIMU and OSTIA spatial averaged SST anomaly are also well correlated, with R=0.96 (p<0.01) and NSE = 0.85, which are slightly better correlation values than between

GOM and OSTIA (R=0.88 (p<0.01) and NSE=0.86) (Fig. IV.17 d). At Bach Long Vi and Hon Dau, SIMU shows also better correlation with the in-situ datasets, compared to OSTIA and GOM (Fig. IV.17 e, f).
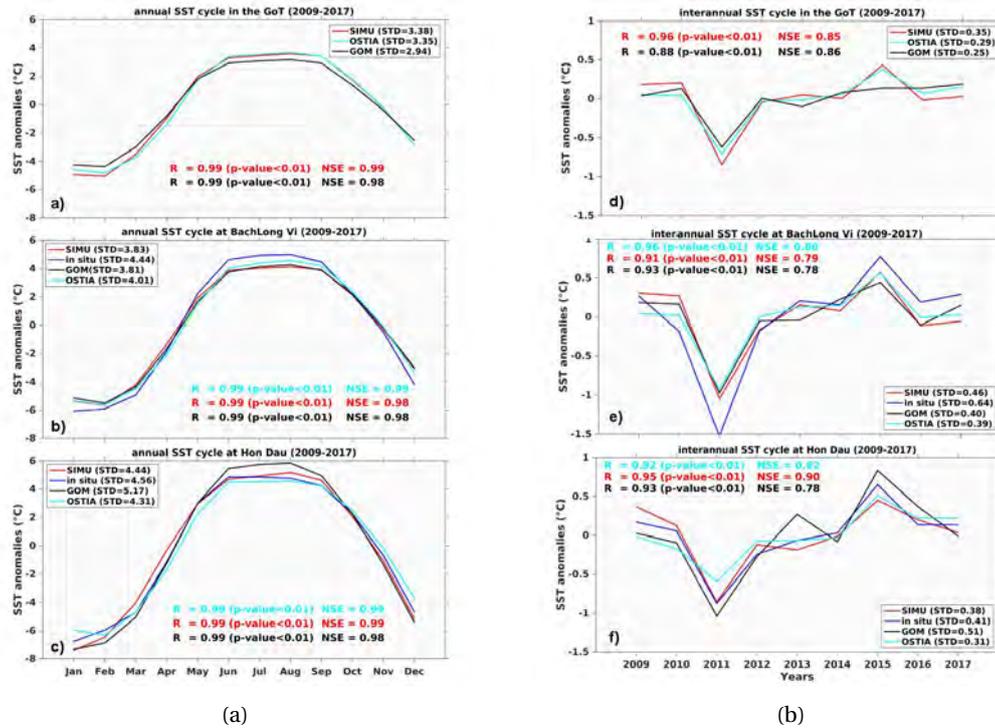
Figure IV.17: Evaluations of the annual (left column) and interannual (right column) SST anomaly signals over the GoT in SIMU and GOM compared to OSTIA (a, d); in SIMU, GOM and OSTIA compared to Bach Long Vi hydrological station (b, e); in SIMU, GOM and OSTIA compared to Hon Dau hydrological station (c, f).

Evaluations of the temporal climatological monthly, annual and interannual evolution of SST, as well as its spatial variability, highlight the very good behaviour of SIMU in terms of SST spatial and temporal representation.

IV.4.2   SSS

Fig. IV.18 shows the mean seasonally averaged SSS comparison between SMOS satellite data, SIMU and GOM. As explained in section 4.2.3, the coverage of SMOS in the GoT is coarse (1/4°) and sparse in the coastal areas. The comparison between model results and those data should therefore be considered with caution. In winter, SSS are rather homogeneous over the GoT (∼ 33 PSU) as rainfalls and associated river discharges are low (Fig. IV.18 a). A lower salinity area (∼ 32 PSU) is in SMOS observed near Hainan Strait and seems to be coming from the strait, possibly pushed along the northern coast by the NE monsoonal winds. SIMU reproduces well those patterns, with a spatial correlation (R) with SMOS of 0.81 (p<0.01), while GOM shows a poorer spatial

correlation (R=0.67 (p<0.01)).
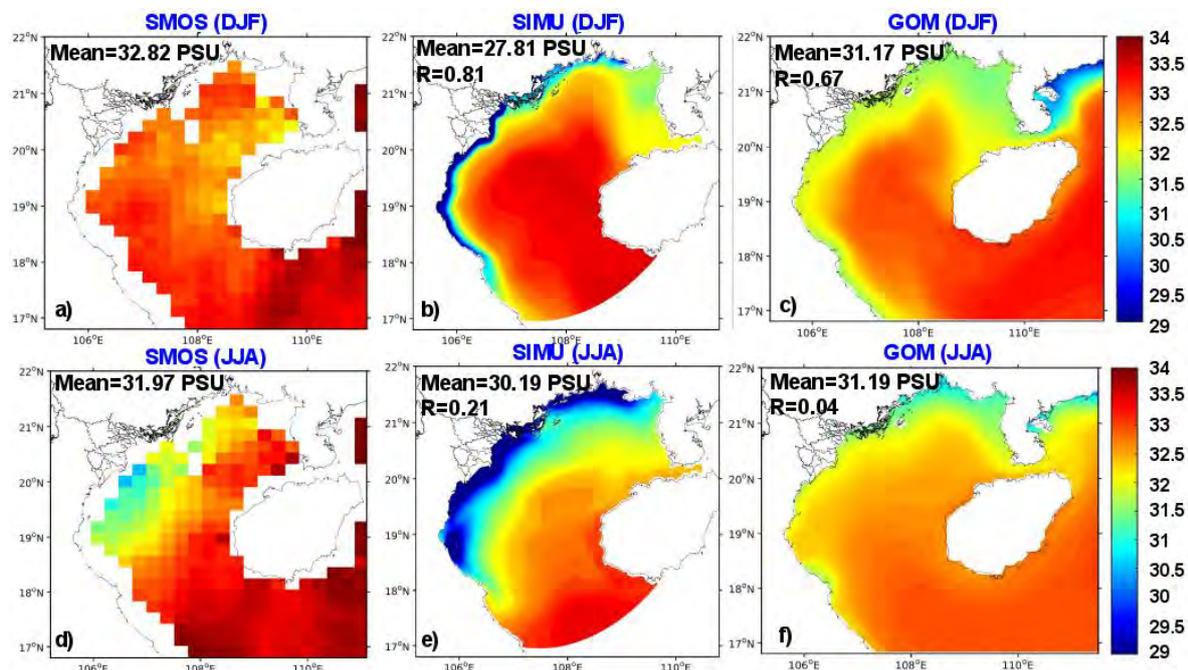
Figure IV.18: Similar to Fig. IV.14 but for sea surface salinity (SSS, PSU) comparison between SMOS, SIMU and GOM.

In summer, the southwest monsoon, associated with heavy rain and strong river discharges, triggers a NW-SE SSS gradient which appears in the observations (from 31 PSU near the coast to 34 PSU in the south of the GoT) (Fig. IV.18 d). The location of this gradient is well reproduced in SIMU and values <29 PSU are observed along the coast (Fig. IV.18 e). However, the poor spatial correlation between SIMU and SMOS (R=0.21 (p=0.12)) is possibly due to the discrepancy in the ranges of SSS values and to the fact that SMOS does not cover the coastal band of very low SSS values. The NW-SE gradient in GOM is weaker than in SMOS and SIMU, with values ranging from 31.5 to 32.5 PSU (Fig. IV.18 f). The rather high SSS values observed along the coast in GOM may result from inaccurate representation of the Red River water discharges in this model (personal comments of Romain Bourdallé-Badie, Mercator). The very poor spatial correlation between GOM and SMOS (R=0.04 (p=0.22)) indicates that water discharges are crucial for SSS patterns in summer in the GoT, and should be carefully represented in ocean circulation models.

Fig. IV.19 shows the monthly SSS variability averaged over the GoT for SMOS, SIMU and GoT. The climatological monthly variations of SIMU are in phase with SMOS variations, despite the inability of SIMU to reproduce the observed SMOS SSS rising trend (Fig. IV.19 a).

Correlation between SMOS and SIMU monthly anomaly values over their common period (R=0.76 (p<0.01), NSE=0.57) are largely better than the correlation with GOM (R=0.25 (p<0.05), NSE=0.01).
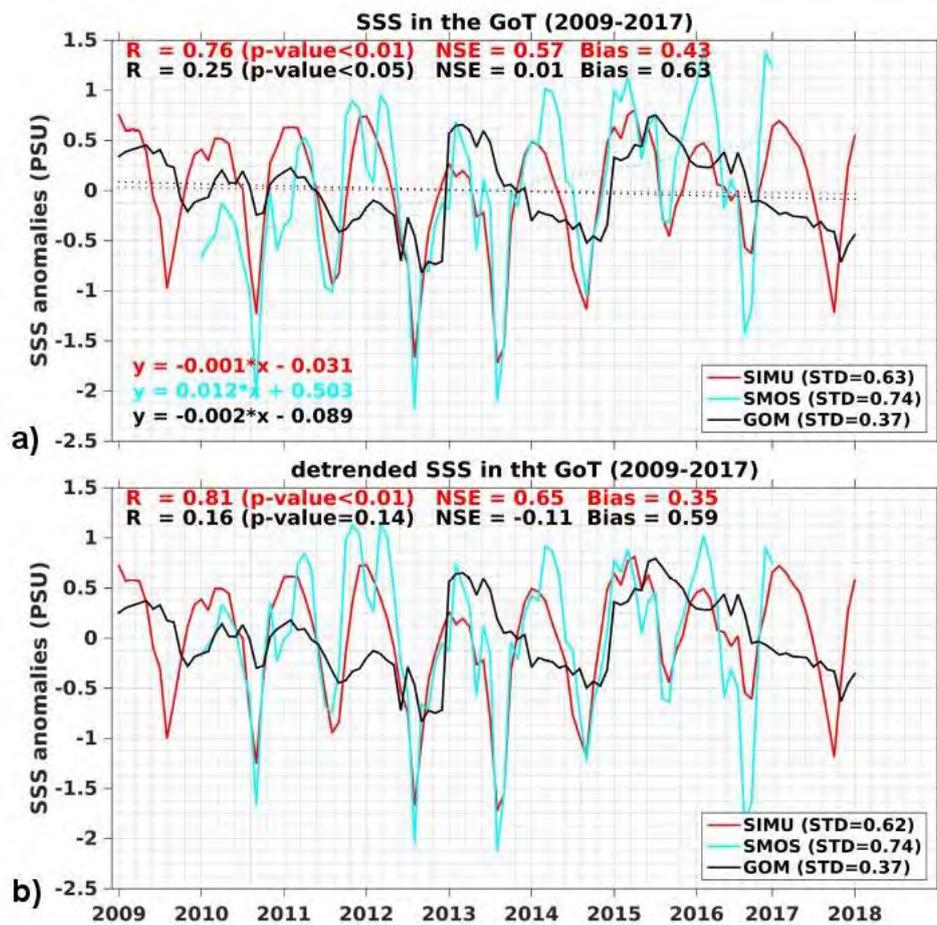
Figure IV.19: Evaluations of the monthly SSS signals over the GoT of SIMU and GOM compared to SMOS (a); same evaluations but with detrended SSS signals (b). Bias refer to the SSS (not anomaly) signal.

Indeed, GOM appears to be limited in reproducing both SSS monthly cycle and trend, the latter appearing even slightly decreasing. The explanation of GOM limitations in reproducing the GoT SSS is beyond the scope of this study, but could be due to the assimilation of in-situ data when estimating the model's initial conditions. The numerical GoT domain used in this study is rather small, which favors a short residence time of the water (∼ 1 y). Therefore, the boundary conditions provided by GOM could largely affect the long term modeled water masses properties variability (i.e. trend), while the shorter time scales (monthly, seasonal) could remained unaffected. The detrended datasets show even better correlation between SMOS and SIMU (R=0.81 (p<0.01), NSE=0.65), while correlation between SMOS and GOM is very low (R=0.16 (p=0.14), NSE=-0.11) (Fig. IV.19 b). Note that the biases between SMOS and SIMU are reduced when using detrended data, compared to trended data.

Furthermore, both GOM annual and interannual SSS cycles show poor correlation with SMOS cycles, with low correlations of respectively 0.37 and 0.13 (Fig. IV.20 a, b). This confirms the inability

of GOM to reproduce the SSS variability over the GoT. On the contrary, SIMU closely follows the annual SSS cycle (R=0.96 (p<0.01), NSE=0.92). The correlation is weaker for the interannual cycle (R=0.70 (p=0.08), NSE=0.37), since SIMU is potentially affected by GOM, however SIMU still performs much better than GOM at the interannual scale.
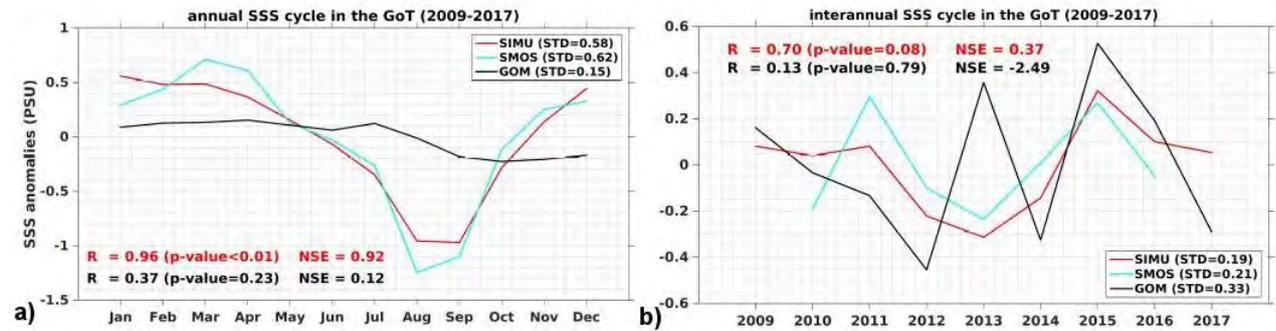
Figure IV.20: Evaluations of the annual (a) and interannual (b) SSS signals over the GoT of SIMU and GOM compared to SMOS.
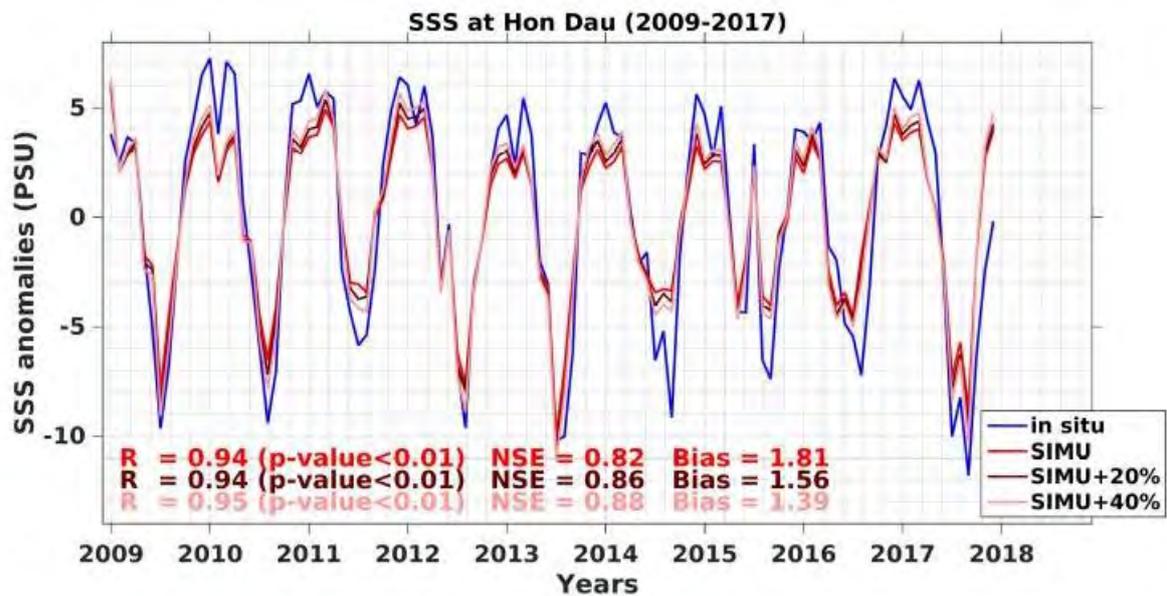
Figure IV.21: Evaluations of the monthly SSS signals at Hon Dau of SIMU, SIMU+20% and SIMU+40% compared to in-situ dataset. Bias refer to the SSS (not anomaly) signal.

SIMU SSS temporal variability evaluation at Bach Long Vi station is not presented as a bias of the in-situ salinity sensor has been depicted from 2014. SIMU SSS temporal variability is however evaluated at Hon Dau station (Fig. IV.21). A comparison with SMOS at Hon Dau station is not possible because it is located outside of the SMOS domain. Hon Dau station is located near the coast in the Red River's plume, a complicated area where the tidal and river discharges signals are strong. GOM temporal variability is not represented here as it shows small non-significant correlation with in-situ measurements (0.32, p=0.12). On the contrary, SIMU reproduces very well the tempo-

ral variability of SSS (R=0.94 (p<0.01), NSE=0.82). However, the positive bias to the observations (not anomaly) of 1.81 PSU suggests that SIMU is limited in reproducing the in-situ seasonal minimum SSS. In river plumes, SSS anomalies are directly driven by river discharges. Therefore, two simulations with increased river discharges (increases of 20% and 40%) are performed and noted SIMU+20% and SIMU+40% . Increasing the discharges tends to increase the correlations with the observations (R= 0.94 and NSE=0.86 for SIMU+20% , R=0.95 and NSE=0.88 for and SIMU+40%) and to decrease the biases (from 1.56 to 1.39 PSU for SIMU+20% and SIMU+40% , respectively) (Fig. IV.21). Among the three simulations, SIMU+40% is the one that best reproduces the observed temporal cycle.

SIMU+40% also best reproduces the annual variability of the observations (R=0.99 (p<0.01), NSE= 0.94 for SIMU+40% , 0.93 for SIMU+20% and 0.88 for SIMU) (Fig. IV.22 a). At the interannual time scale, the simulations are almost similar and all three of them fairly well reproduce the observations, with R between 0.78 and 0.79 and NSE between 0.60 and 0.62 (Fig. IV.22 b).
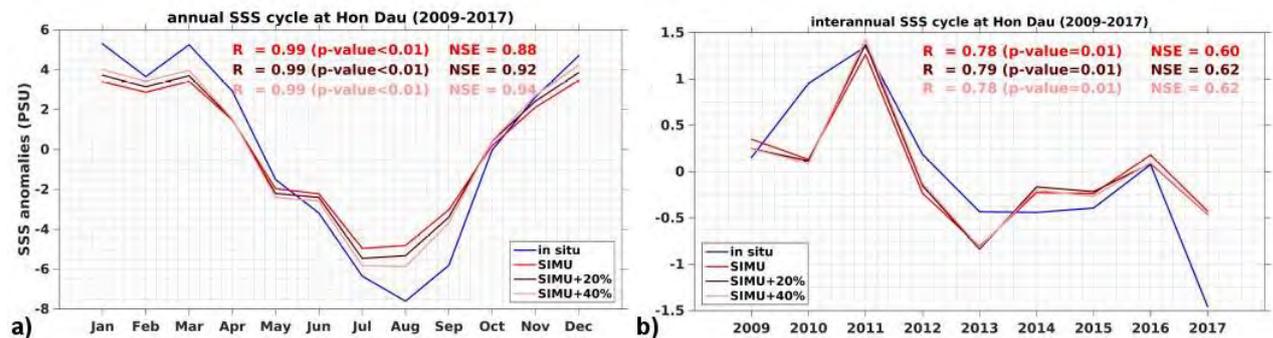
Figure IV.22: Evaluations of the annual (a) and interannual (b) SSS signals at Hon Dau of SIMU, SIMU+20% and SIMU+40% compared to in-situ dataset.

Despite showing the best results in reproducing the observed SSS anomalies at Hon Dau, the river discharges imposed in SIMU+40% (increase of discharges of 40%) are not realistic. Such high river discharge increases could be triggered by short episodic events like typhoons and storms, but in any case could not last for years. Therefore, for the rest of the study, SIMU is kept as reference.

IV.4.3 SLA

Model outputs (SIMU and GOM) and altimetry data (ALTI) are compared over their common period, i.e. 2009-2017. In this section, SLA is therefore calculated both from the models and the data from sea surface height (SSH) fields by removing at each point the mean SSH over the period considered:

$$\mathrm{SLA}\left(i, j, t\right) = \mathrm{SSH}\left(i, j, t\right) - \overline{\mathrm{SSH}}\left(i, j, \overline{2009 - 2017}\right) \tag{IV.36}$$

Fig. IV.23 shows maps of altimetry (ALTI), SIMU and GOM seasonal mean SLA. In winter, a N-S gradient of SLA is observed in the observations with values ranging from 0.02 (in the north) to 0.11 m (in the south) (Fig. IV.23 a). This gradient is possibly enhanced by the NE monsoonal winds blowing over the GoT during this season, which could push the water masses towards the south. SIMU reproduces realistically this spatial variability with R=0.71, and mean values (0.062 m) very close to ALTI mean values (0.061 m) (Fig. IV.23 b). Higher mean value from GOM (0.090) suggests that GOM overestimates the winter positive anomaly of SLA all over the GoT (Fig. IV.23 c).
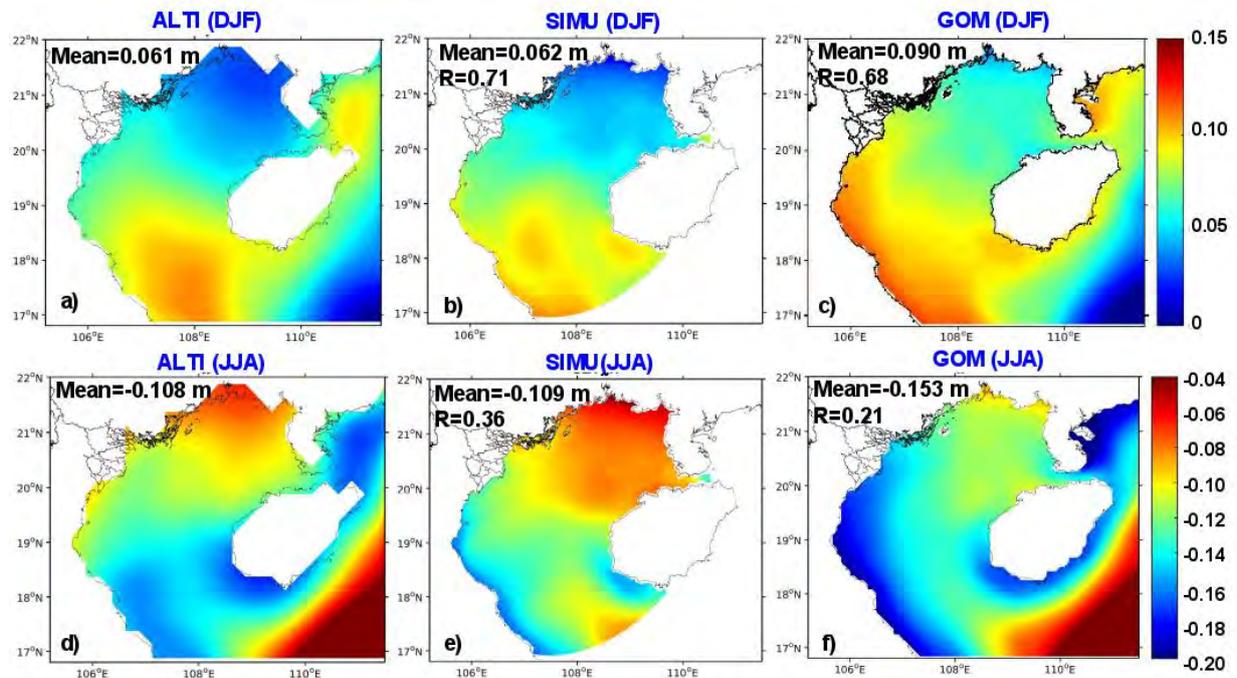
Figure IV.23: Similar to Fig. IV.14 but for sea level anomaly (SLA, m) comparison between ALTI, SIMU and the forcing GOM.

In summer, SLA is negative all over the basin with a mean value of -0.108 m (Fig. IV.23 d). Compared to winter conditions, the N-S gradient is reversed with decreasing SLA values from the north towards the south (lowest values observed in the south as low as -0.18 m). SIMU reproduces well the mean JJA SLA value (-0.109 m) but the gradient is not as strong as in ALTI (Fig. IV.23 c). A patch of SLA ~ -0.10 m is observed at the southern boundary of the domain, which seems enhanced by the forcing GOM (Fig. IV.23 d). GOM does not represent the N-S SLA gradient and generates a band of strong negative values along the Vietnamese coasts, leading to overestimating the mean negative SLA over the GoT (-0.153 m). Despite the rather poor spatial correlations of both models with

ALTI in summer (0.36 and 0.21 for SIMU and GOM, respectively), SIMU overall better reproduces the JJA SLA spatial patterns than GOM. Regarding the monthly temporal series, SIMU better reproduces the ALTI monthly variations of SSS over the GoT (R=0.97 (p<0.01), NSE=0.95) than GOM (R=0.95 (p<0.01), NSE=0.83) (Fig. IV.24 a).
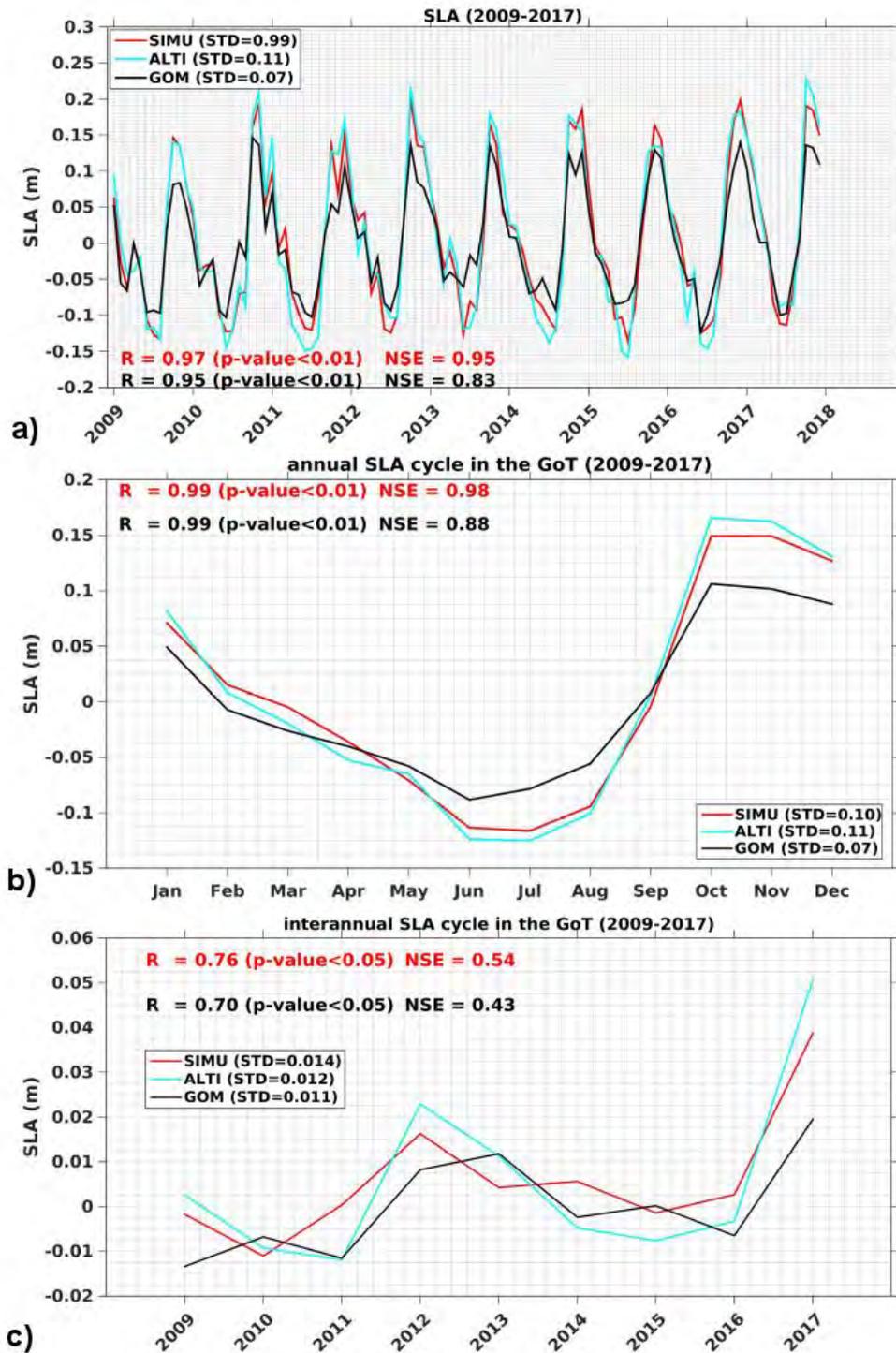
Figure IV.24: Evaluations of the monthly SLA signals over the GoT of SIMU and GOM compared to ALTI (a), at the annual time-scales (b) and at the interannual time-scales (c).

SIMU reproduces well the climatological annual variations of observed SLA (R=0.99 (p<0.01), NSE=

0.98), although the modeled SLA slightly underestimates the negative anomalies in summer and the positive anomalies in winter, compared to ALTI. GOM also well reproduces the SLA annual cycle (R=0.99 (p<0.01), NSE= 0.88) but shows larger underestimations of the minimum and maximum observed in ALTI. At interannual time scales, SIMU spatially averaged SLA shows better correlations with ALTI (R=0.76 (p<0.05), NSE= 0.54) than GOM (R=0.70 (p<0.05), NSE= 0.43).

Evaluations of SIMU, ALTI and GOM compared to in-situ gauges stations are presented in Table IV.2. In both Bach Long Vi and Hon Dau stations cases, SIMU better reproduces the observed SLA monthly, annual and interannual variabilities than ALTI and GOM.

		Bach Long Vi gauge station			Hon Dau gauge station		
	Cycle	**R**	**p-value**	**NSE**	**R**	**p-value**	**NSE**
ALTI	monthly	0.54	<0.01	-0.85	0.71	<0.01	0.05
	annual	0.54	<0.01	-0.41	0.77	<0.01	0.50
	inter.	0.63	0.10	0.34	0.57	0.14	0.23
SIMU	monthly	0.59	<0.01	-0.35	0.76	<0.01	0.50
	annual	0.59	<0.01	-0.61	0.78	<0.01	0.51
	inter.	0.80	<0.01	0.37	0.84	<0.01	0.50
GOM	monthly	0.45	<0.01	-0.60	0.64	<0.01	0.12
	annual	0.52	0.08	-0.87	0.69	<0.05	0.07
	inter.	0.75	<0.05	0.52	0.77	<0.05	0.54

Table IV.2: R, associated significance (p-value), NSE and biases computed for ALTI, SIMU and GOM at the monthly, annual and interannual time-scales compared to Bach Long Vi and Hon Dau gauges stations.

Evaluations of the temporal climatological monthly, annual and interannual evolution of SLA, as well as its spatial variability, highlight the very good behaviour of SIMU in terms of SLA spatial and temporal representation, compared to the forcing model GOM.

IV.4.4   Circulation

In this section, SIMU depth-averaged currents are first compared with currents seasonal maps from the literature (Fig. IV.25), and then, monthly-mean surface circulation are compared with Radar HF data (Fig. IV.26).

Nowadays, uncertainties remain in understanding the GoT circulation, which come from the fact that the GoT has been mostly studied as a by-product of the South China Sea research. In the mid-2000s, longer-term observations and finer-resolution numerical studies enabled the scientific community to fill the gap, but published english-written papers that review the GoT circulation are still a few and the mechanisms behind the seasonal circulation remain controversial, particularly in summer (Gao et al., 2017). As seen in section I.2.2.1 in Chapter I, most studies agree

on a predominance of gulf-scale cyclonic flows during winter but the circulation structure during summer remains uncertain, with either gulf-scale anticyclonic or cyclonic circulation.

In winter, SIMU reproduces the southward current off the Vietnamese coasts that has been emphasized by several authors (Manh and Yanahi, 2000; Ding et al., 2013; Rogowski et al. 2019) (Fig. IV.25 a, b, c). The modeled circulation reveals that this current is strongest in the very near coastal area, with velocities up to 0.25 m s^{-1}. Liu and Yu, 1980 and Yuan and Deng, 1999 suggested that the winter circulation consisted in one cyclonic gyre in the northern GoT and in one anticyclonic gyre in the south (Fig. IV.25 b). SIMU however produces a large cyclonic gyre (Fig. IV.25 a) which is supported by the results of Manh and Yanagi (2000) and Ding et al. (2013) (both based on 3D numerical studies) (Fig. IV.25 c), and a small anticyclonic gyre south of Hainan island. Based on POM model outputs , Sun et al. (2001) verified that the current in the Hainan Strait and off the northwestern coast of Hainan is westward and southwestward respectively, as produced in SIMU (Fig. IV.25 a).
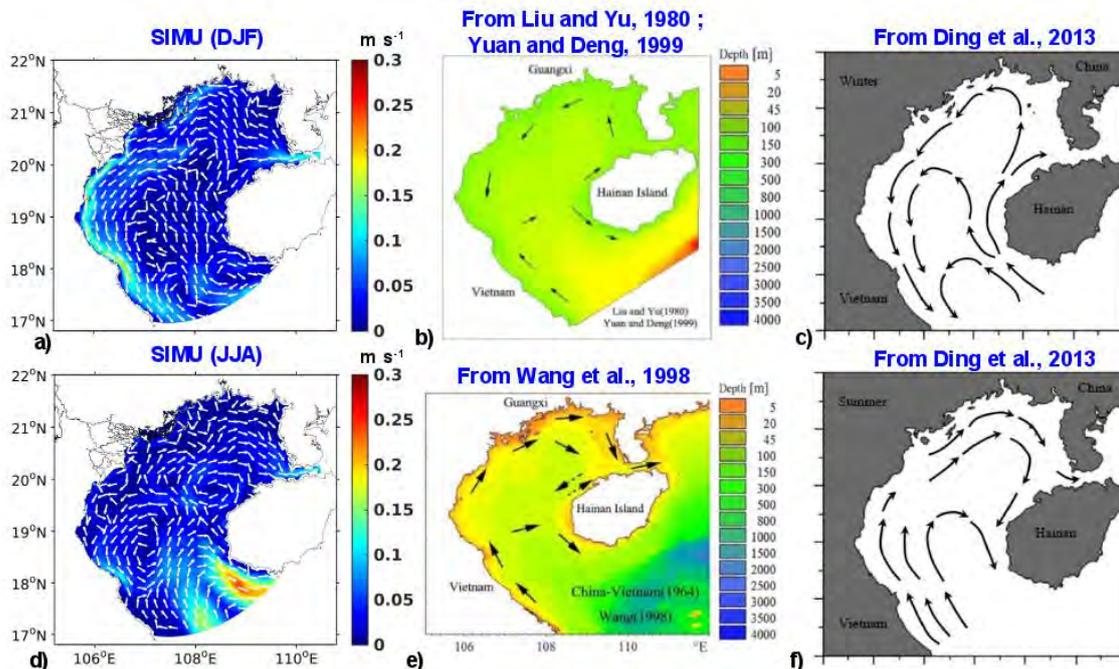
Figure IV.25: Climatological comparisons of SIMU depth-averaged currents (m s^{-1}) (a,b) with schematic circulation patterns found in literature in summer (top panels) and winter (bottom panels).

In summer, SIMU shows a rather complex and mostly-anticyclonic depth-averaged circulation (Fig. IV.25 d) which is supported by Wang et al. (1998) and Ding et al. (2013) (Fig. IV.25 e, f). SIMU shows a large anticyclonic gyre in the southern part of the GoT with an intense southward branch of 0.3 m s^{-1} along the southern coast of Hainan, a cyclonic gyre off the Vietnamese coast at 18-19° N, 106-107.5 ° E and a small anticyclonic eddy appears north west of Hainan island. The Hainan

strait appears dominated by an eastward current which is supported by the results of Gao et al. (2015).

Modeled monthly surface current fields are compared with HF Radar derived surface currents in Fig. IV.26. Despite slightly overestimating the mean velocities of the surface currents (except in April: Fig 4.26. b, g), SIMU reproduces well the current spatial variability compared to observations. Here, for the sake of conciseness and as they represent a good overview of the annual variability, only months of January, April, July, October and December of 2017 are presented, but SIMU reproduces well all months of years 2015, 2016 and 2017. Both SIMU and HF Radar observations exhibit the strong monthly variability of the winter southward coastal current, in terms of speed and direction, which has been previously observed in Fig. IV.25 a. The current is weak and narrow in spring (Fig. IV.25 b, g) with velocities up to 0.2 m s^{-1}, and is confined along the Vietnamese coasts. From summer to fall, the current intensifies (velocities higher than 0.4 m s^{-1}) and becomes larger (up to 75 km width). The mechanisms behind this variability are discussed in section 4.5.
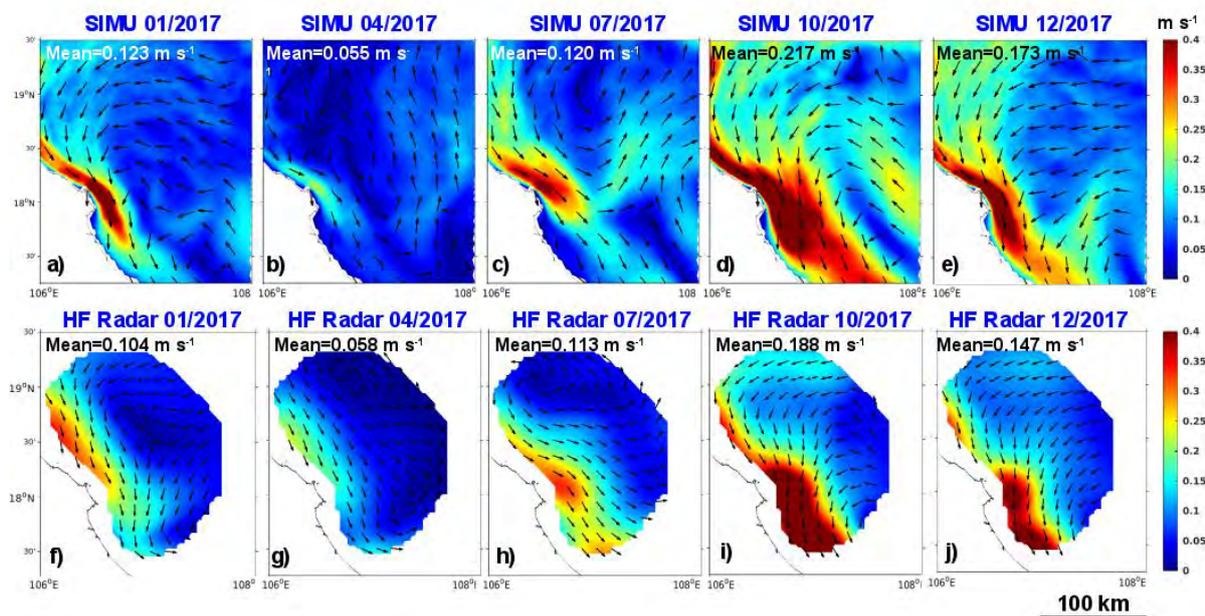
Figure IV.26: Monthly averaged SIMU surface currents intensity fields (in m s^{-1}) overlaid with corresponding current directions (arrows) for January, April, July, October and December of 2017 (panels a,b,c,d,e); monthly averaged HF radar-observed surface current intensities (in m s^{-1}) and corresponding currents directions for January, April, July, October and December of 2017 (panels f,g,h,i,j).

IV.4.5   Vertical structures of temperature and salinity

The ability of SIMU to reproduce the vertical structures of coastal water masses in terms of temperature (Fig. IV.27) and salinity (Fig. IV.28) is evaluated in this section. SIMU is compared to 25

km-long CTD cross-sections collected on the 6th of September 2015, 23rd of December 2015, 26th of May 2016 and on the 25th of July 2016 (see location on Fig. IV.2 a). In almost each case, the observed stratification patterns are well reproduced by SIMU, in terms of position and depth of temperature and salinity gradients (Fig. IV.27 and Fig. IV.28). In terms of intensity, SIMU slightly underestimates the warmer temperatures (by up to 1.5° C) and overestimates the colder temperatures (up to 2° C) (Fig. IV.27 a-i), except in July when SIMU overestimates the entire water column temperature (Fig. IV.27 j-l).
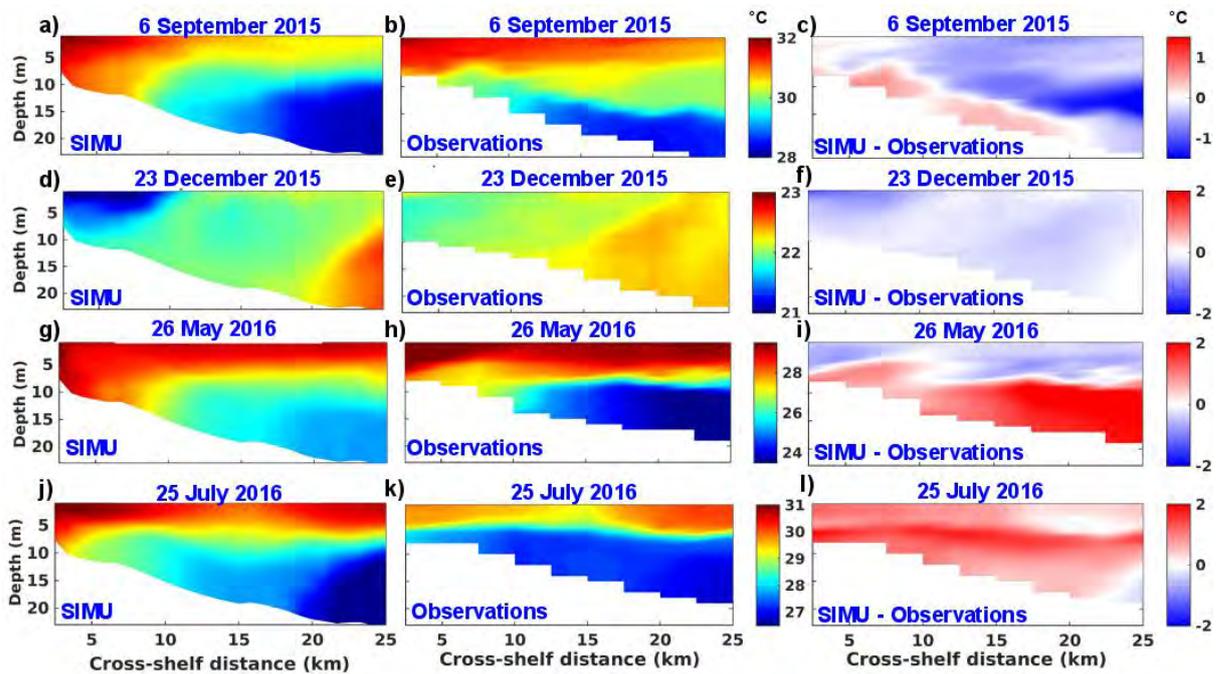
Figure IV.27: Temperature (in ° C) transects along a 25 km across-shore line from SIMU (a,d,g,j), from CTD observations (b,e,h,k) and biases between SIMU and observations (c,f,i,l).

Regarding salinities, SIMU also correctly represents the spatial patterns, but underestimates the minimum values (by up to 4 PSU) and overestimates the maximum values in September, December and May (Fig. IV.28 a-i). Only in July, salinity patterns are not well represented by SIMU, with the low water mass shifted eastwards by ∼ 20 km (Fig. IV.28 j-l).

Despite the complexity of the hydrodynamical dynamics of the coastal ocean, comparisons of vertical profiles of water properties with in-situ observations therefore shows that SIMU provides a realistic representation of the coastal ocean spatial and temporal patterns.
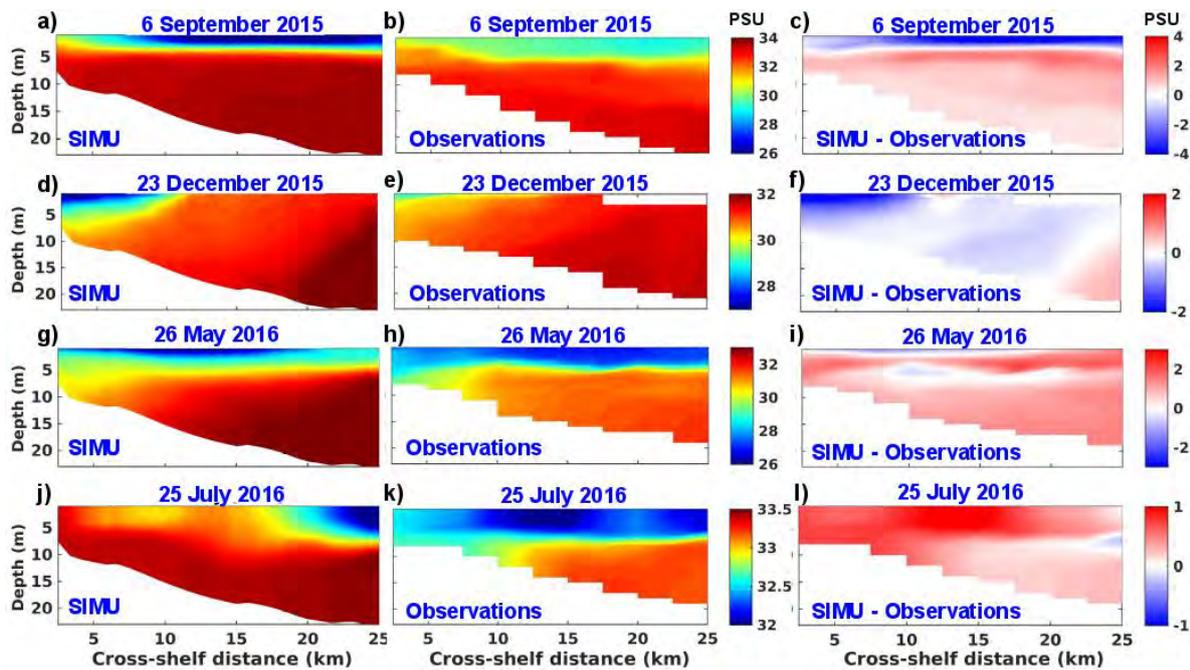
Figure IV.28: Same as Fig. IV.27 but for salinity (in PSU).

IV.5   GoT surface circulation and fluxes

As above mentioned and detailed in Chapter 1 (section I.2.2.1), circulation in the GoT remains uncertain. While most studies agree on a predominance of gulf-scale cyclonic flows during winter, the circulation structure during summer remains a topic of debate. Also, circulation through the Hainan strait is considered as either westwards all year long, or alternating with monsoon winds reversal. In addition, the scientific community disagrees on the mechanisms dominating the surface current variability, whether it is driven by the monsoon wind-induced currents or by the density-gradient currents. In this section, based on results from SIMU, new conclusions on the driving mechanisms of the seasonal and interannual variability of the currents are proposed and estimations of water fluxes at different time-scales are proposed.

IV.5.1   Drivers of the seasonal circulation variability

Section I.2.2.1 in Chapter I highlighted the efforts made by the scientific community to first, document the general circulation of the GoT and second, to understand the mechanisms responsible for the GoT surface current variability. However, conclusions remain controversial on the winter/summer circulation patterns and on whether surface circulation is driven by winds or by density-gradients. To complement the literature and determine the mechanisms dominating the variability of the total surface current (noted U_{total}) and the surface geostrophic currents ($U_{geos.}$) are computed from sea surface height (SSH) fields (from SIMU), and the surface Ekman currents

(U_{Ekman}) are deduced from: $U_{total} = U_{geos.} + U_{Ekman}$. Winter (October, November, December, January) and summer (May, June, July, August) mean fields maps of surface currents U_{total}, U_{Ekman} and U_{geos} are presented in Fig. IV.29. In winter, the total simulated circulation (U_{total}) shows a gulf-scale cyclonic circulation with a strong down-coast current off Vietnam (of ~ 0.4 m s^{-1}), a westward flow through the Hainan strait (of ~ 0.2 m s^{-1}) which joins the coastal current, and a northeastward branch (~ 0.2 m s^{-1}) of an unclosed gyre in the south of the GoT that also joins the coastal current (Fig. IV.29 a). Total surface circulation patterns from SIMU therefore coincides with the fourth option of winter circulation described in section 2.2.2 of Chapter 1. U_{Ekman} circulation patterns are similar to U_{total} patterns over the GoT, with only slightly reduced intensities (Fig. IV.29 b). U_{geos} circulation patterns are similar to U_{total} patterns in the western part of the basin, but shows large discrepancies to U_{total} in the eastern part (Fig. IV.29 c). Furthermore, overall intensities are much smaller in U_{geos} than in U_{total}, except in the boundary current (Fig. IV.29 a, c). Globally, the winter average circulation is therefore mainly driven by wind, except for the boundary current where the density driven and wind driven currents are consistent and both contribute to the total current.
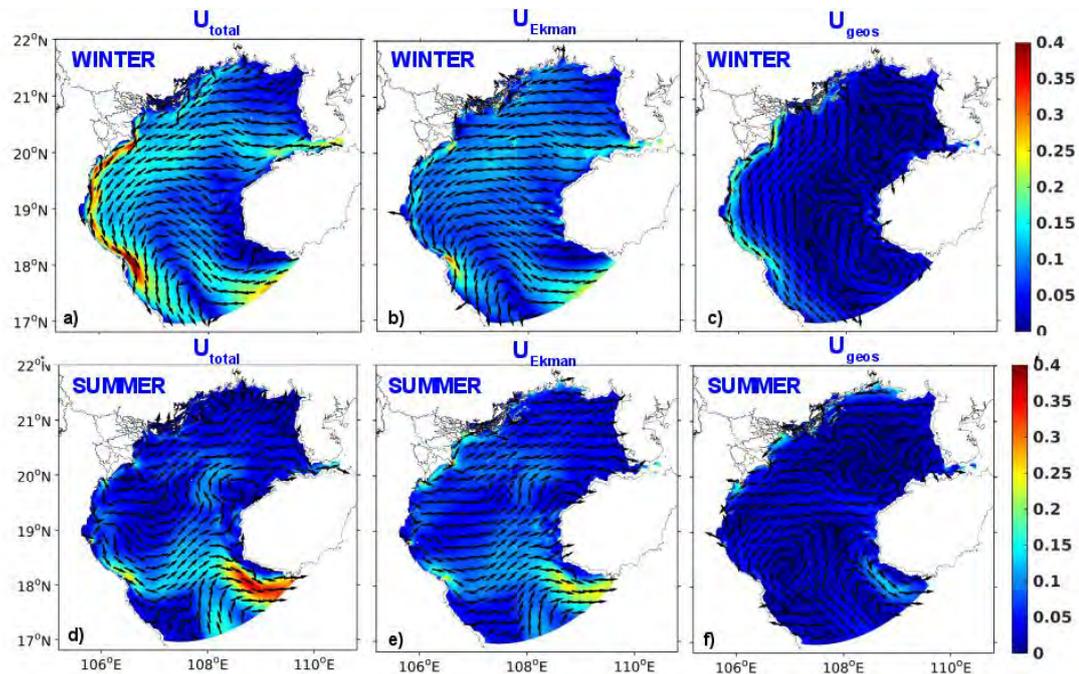
Figure IV.29: Winter (a,b,c) and summer (d,c,f) mean fields of surface U_{total} (a,d), U_{Ekman} (b,e), U_{geos} (c,f) (in m s^{-1}).

In summer, the total simulated circulation (U_{total}) shows a gulf scale anti-cyclonic circulation, with eastward circulation in the Hainan strait (<0.1 m s^{-1}) and strong eastward current south of Hainan flowing outside the GoT (~ 0.4 m s^{-1}), which is fed by eastward current coming from the Viet-namese coast (Fig. IV.29 d). This circulation pattern coincides most to the first pattern described in section I.2.2.1 of Chapter I, despite the fact that Wang (1998) and Sun et al. (2001) did not men-

tion the eastward flow in the Hainan strait. Similar to winter case, U_{Ekman} summer circulation patterns are also very similar to U_{total} but with smaller intensities (Fig. IV.29 e). Besides showing very small current intensities, U_{geos} summer circulation patterns are very different from U_{total} summer patterns, except south of Hainan island (Fig. IV.29 d, f), and are also much weaker. The summer circulation is therefore globally again mainly driven by wind.

These first observations suggest a basin-scale seasonal surface current variability dominated by the Ekman transport rather than by the geostrophic circulation. However, domination of U_{Ekman} circulation over U_{geos} circulation is not evident for smaller scale structures (i.e. boundary current, Hainan strait circulation). Therefore, contributions of U_{Ekman} and U_{geos} to the total circulation, for summer and winter seasons, in terms of relative proportions are detailed in Fig. IV.30. In summer, U_{Ekman} dominates the circulation at ∼ 80% almost all over the GoT and more interestingly, U_{Ekman} is responsible for the strong current flowing south of Hainan island (Fig. IV.30 a, c). This observation is therefore consistent with studies suggesting that the summer circulation is driven by monsoon winds (see section IV.5.1.2; Manh and Yanahi, 2000; Sun et al., 2001). However, summer currents in the northern coastal areas and in Hainan strait appears to be roughly equally controlled by U_{Ekman} and U_{geos} (Fig. IV.30 a, c). Therefore, these results are not sufficient to conclude on the mechanisms behind the Hainan strait circulation as both Ekman and geostrophic circulation contribute to the circulation (as mentioned in section I.2.2.1 of Chapter I).

In winter, U_{Ekman} dominates most of the GoT circulation, especially the Hainan strait westward current and the branch that enters the basin south of Hainan island (Fig. IV.30 b, d). However, U_{geos} dominates the strong boundary coastal current from 60 to more than 80% . This is consistent with the fact that river plumes generate intense density-gradients by inputs of fresher waters, inducing currents to follow these slopes. These results are consistent with the studies suggesting that NW monsoon wind was the primary driving factor of winter surface circulation over the density-gradient term (see section 2.2.1 of Chapter I;Gao et al. 2014b; Manh and Yanahi, 2000; Sun et al. 2001; Xia et al., 2001) but none reported the dominant contribution of the geostrophic currents to the coastal boundary current.

To complement this analysis, Empirical Orthogonal Functions (EOFs) are performed on U_{total}, U_{Ekman}, U_{geos} monthly mean fields from 2009 to 2017, for both zonal (u) and meridional (v) components, to extract the dominant pattern of variability. Only statistically consistent EOFs, based
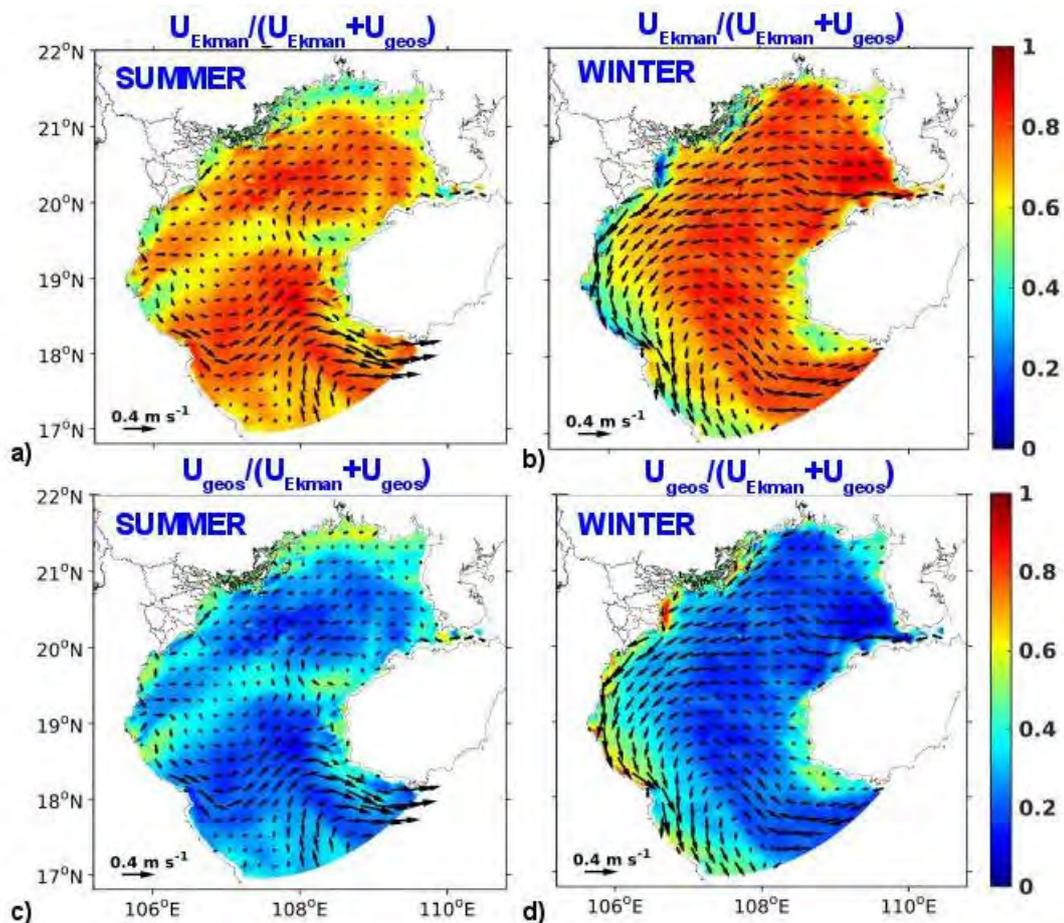
Figure IV.30: Relative proportions of U_{Ekman} (a,b) and U_{geos} (c,d) in summer (a,c) and winter (b,d) superimposed with U_{total} surface currents fields (in m s^{-1}) during corresponding seasons. Note that here, summer corresponds to the months of May, June, July and August, and winter corresponds to the months of October, November, December and January.

on North et al. (1982) are shown here.

The first EOF mode (EOF$_1$) on the zonal component of U_{total} corresponds to 89.9% of the total variance (Fig. IV.31 a). The corresponding spatial pattern shows negative values all over the basin, except along the southern coast of Vietnam, and indicates that the GoT is mostly influenced by this first mode of variability in the Hainan strait, in the region south of Hainan island and along the Red River delta (Fig. IV.31 a). The associated temporal function (PC) denotes a clear seasonal variability (Fig. IV.31 e). In summer, the product of the spatial and temporal functions suggests that this variability is responsible for zonal eastwards currents to flow at ~ 0.15 m s^{-1} over the central part of the GoT and at maximum velocities of 0.40 m s^{-1} in the Hainan Strait, south of Hainan island and along the Red River delta. However, along the southern coast of Vietnam, the EOF$_1$ indicates that the summer total zonal currents are weakened by up to ~ 0.15 m s^{-1}. In winter, zonal circulation reverses with velocities of approximately the same order of magnitude.

The EOF_1 on the zonal component of U_{Ekman} presents similar patterns of spatial variability (except only negative values all over the GoT), with a good spatial correlation of 0.97 (p<0.01) with the spatial patterns of U_{total} (Fig. IV.31 b). The associated temporal function also shows a clear seasonal variability as a first mode of variability (at 67.4%) (Fig. IV.31 e) and is well correlated with the temporal function of EOF_1 on U_{total} (R=0.86 (p<0.01)). In this case, the product of the spatial and temporal functions shows that this mode of variability is responsible for zonal eastward Ekman currents to flow at up to ~ 0.50 m s^{-1} in Hainan strait, south of Hainan island and along the Red River delta during summer.

The EOF_1 on the zonal component of U_{geos} accounts for less than 60 % of the total variance and shows a similar (spatial correlation with U_{total} of 0.87 (p<0.01)) but much weaker spatial influence on the GoT than the EOF_1 on U_{total} and U_{Ekman} (Fig. IV.31 a,b,c). The associated temporal function, which shows poor correlation with U_{total} zonal temporal function (R=0.26 (p<0.01)), suggests that the variability of the zonal geostrophic currents is mostly dominated by an increasing trend rather than by a seasonal variability (Fig. IV.31 e). The product of the temporal and spatial functions gives relatively small current velocities, with a maximum of 2.5x10^{-2} m s^{-1} in winter 2017. However, the second EOF mode (EOF_2) on the zonal component of U_{geos} that accounts for only 29% U_{geos} total variance, reveals a seasonal variability well correlated with the EOF_1 on zonal U_{total} (R=0.78 (p<0.01)) (Fig. IV.31 e). The spatial function (Fig. IV.31 d) varies similarly to EOF_1 on U_{total} (R=0.92 (p<0.01)) but presents more patches of positive values over the basin. During summer, this EOF_2 is responsible for zonal geostrophic currents to flow eastward at ~ 0.10 m s^{-1} in Hainan strait, south of Hainan island and along the Red River delta. In the rest of the basin (areas of positive values on Fig. IV.31 d) geostrophic currents are westward. Similar to EOF_1 on U_{total} and U_{Ekman} cases, geostrophic circulation reverses in winter.

This suggests first that the dominant mode of variability of the current is the seasonal variability. Second that the total seasonal zonal current variability is mainly linked to the seasonal variability of the zonal Ekman transport, and to a lesser extent, to the seasonal variability of the zonal geostrophic current, except for the coastal boundary current. This latter is indeed mostly driven by the seasonal variability of the zonal geostrophic current.

The EOF_1 on the meridional component of U_{total} accounts for the majority of the total variance (85.5%) and also suggests a strong seasonal variability with eastern and western opposite patterns of variability (Fig. IV.32 a, e). Similar patterns of variability appears in the spatial function
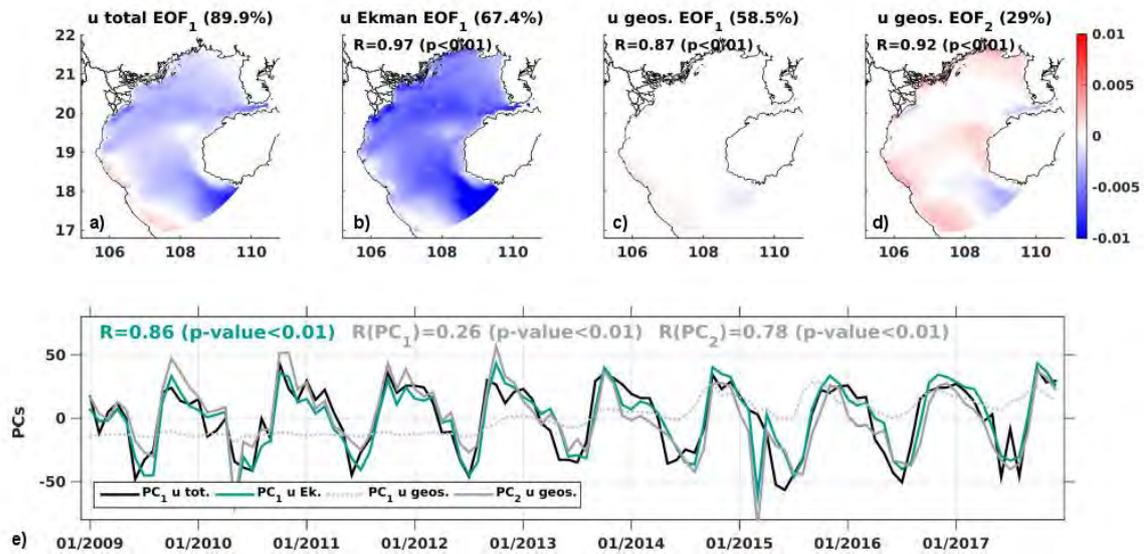
Figure IV.31: Spatial functions (a,b,c,d) and associated principal components (noted PC) of the temporal variability (e) of the first EOF mode on the zonal component of U_{total} (a), on the zonal component of U_{Ekman} (b), on the zonal component of U_{geos} (c), and second EOF mode on the zonal component of U_{geos} (d). The product between the spatial and temporal functions denote the intensity of the considered current. On panels b, c, d, R correspond to the correlations between EOF_1 U_{total} and EOF_1 U_{Ekman}, EOF_1 U_{geos} and EOF_2 U_{geos}, respectively. On panel e, R corresponds the correlation between EOF_1 U_{total} and EOF_1 U_{Ekman}, $R(PC_1)$ corresponds the correlation between EOF_1 U_{total} and EOF_1 U_{geos}, and $R(PC_2)$ to the correlation between EOF_1 U_{total} and EOF_2 U_{geos}.

of the EOF_1 on the meridional component of U_{Ekman} (R=0.90 (p<0.01)). This mode, which also suggests a seasonal variability, is well correlated with the seasonal variability of the EOF_1 of U_{total} (R=0.68 (p<0.01)) but only accounts for 45.5 % of U_{Ekman} total variance (Fig. IV.32 c, e). Similar to the zonal current case, the EOF_1 on the meridional component of U_{geos} depicts that the majority of U_{geos} variability (57.5%) is dominated by an increasing trend with a weaker spatial influence, compared to EOF_1 on U_{total} and U_{Ekman} (Fig. IV.32 a,b,c,e). Only the EOF_2 on the meridional component of U_{geos} shows a temporal function that depicts a seasonal variability well correlated with EOF_1 on U_{total} (R=0.74 (p<0.01)). The associated spatial function presents slightly weaker but similar patterns to EOF_1 on U_{total} (R=0.89 (p<0.01)). Spatial patterns of EOF_1 on meridional U_{Ekman} and EOF_2 on meridional U_{geos} are very similar, even though the range of values is slightly lower for EOF_2 on U_{geos} (from -0.005 to 0.003) than for EOF_1 on U_{Ekman} (from -0.008 to 0.005) (Fig. IV.32 b,d). This suggests that EOF_2 on U_{geos} generates slightly slower current speeds than EOF_1 on U_{Ekman} (as ranges of values on the temporal are roughly the same). Therefore, the meridional component of all three considered currents behave the same, only with different speeds (given by the product of the temporal and spatial functions) (Fig. IV.32 a,b,d). Currents direction is northward in the

western part of the GoT and southward in the eastern part during summer, and reverses during winter.
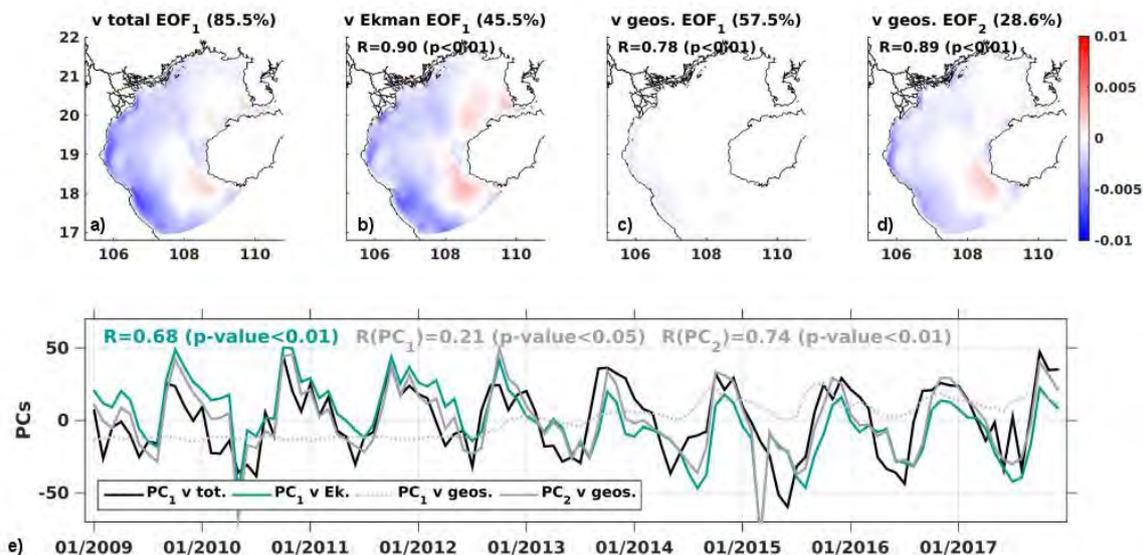
Figure IV.32: Same as for Fig. IV.31 for the meridional component of the currents.

The EOF analysis confirms that the variability of U_{total} is dominated by the seasonal variability, which explains almost 90% of the signal. Seasonal variability also explains the majority of U_{Ekman} signal, while only ~ ¼ of U_{geos} signal variability. U_{Ekman} seasonal cycle generates basin-scale currents intensities stronger than the ones generated by U_{geos} seasonal cycle. Both Ekman and geostrophic seasonal circulations affect the coastal boundary current, the Hainan strait circulation and the southern boundary flow, but in each case, U_{Ekman} trigger stronger current intensities. This confirms that the Ekman transport dominates the total circulation over the geostrophic circulation, and therefore mostly contribute to the seasonal variability of the total current.

IV.5.2   Drivers of the interannual circulation variability

The previous section enhanced the important role of the surface Ekman circulation on the total surface circulation at the seasonal scale. In this section, the dominant patterns of the interannual surface current variability are extracted, with similar EOF analysis performed on detrended and filtered U_{total}, U_{Ekman} and U_{geos} signals (following the TY-H13 method described in section IV.2.4). Contributions of the Ekman transport and geostrophic circulation to the interannual signal of the total currents are assessed, and lastly, potential mechanisms responsible for the observed interannual variability are discussed.

$EOFs_1$ on the interannual signals of zonal U_{total} and U_{Ekman} show similar spatial and temporal functions with correlations of 0.76 (p<0.01) and 0.95 (p<0.01) respectively, and both $EOFs_1$ account for the majority (more than 80%) of the interannual signals (Fig. IV.33 a, b, e). Negative anomalies on PCs_1 are observed in winter 2009/2010 and in summer 2015. These anomalies indicate a strengthening of the eastward total and Ekman currents in the major part of the basin (blue areas), which reach up to 0.1 m s^{-1} in the Hainan strait and along the Red River delta. Along the southern Vietnamese coasts, the $EOFs_1$ indicate a total and Ekman westward circulation of ~ 0.1 m s^{-1}. In contrast, the positive anomalies on PCs_1 of the year 2011, show the $EOFs_1$ were responsible for a westward circulation over the basin and an eastward circulation along the southern vietnamese coast. Besides showing poor correlations with both spatial and temporal functions of $EOFs_1$ on zonal U_{total} (R=0.22 (p<0.01) and R=0.37 (p<0.01), respectively), EOF_1 on zonal U_{geos} reveals that the geostrophic interannual variability generates negligible changes in zonal currents (temporal and spatial functions values are close to 0) compared to changes generated by $EOFs_1$ zonal U_{total} and U_{Ekman} (Fig. IV.33 c, e).
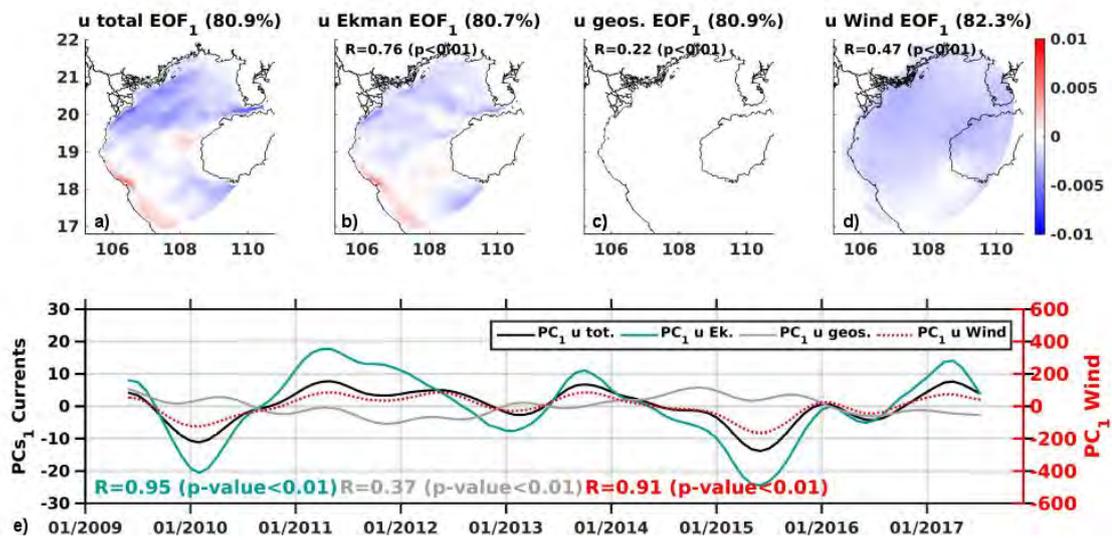
Figure IV.33: Spatial functions (a,b,c,d) and associated principal components of the temporal variability (e) of the first interannual EOF mode of the zonal component of U_{total} (a), of the zonal component of U_{Ekman} (b), of the zonal component of U_{geos} (c), and of the zonal component of the wind (d). The product between the spatial and temporal functions denote the intensity of the considered current. On panels b, c, d, R correspond to the spatial correlations between EOF_1 U_{total} and EOF_1 U_{Ekman}, EOF_1 U_{geos} and EOF_2 U_{geos}, respectively. On panel e, R in blue corresponds to the temporal correlation between EOF_1 U_{total} and EOF_1 U_{Ekman}, R in gray corresponds to the temporal correlation between EOF_1 U_{total} and EOF_1 U_{geos} and R in red corresponds to the temporal correlation between EOF_1 U_{Ekman} and EOF_1 on the zonal wind interannual signal.

These results suggest that the interannual variability of zonal U_{total} is mainly driven by the inter-

annual variability of zonal U_{Ekman}. As the Ekman transport is driven by the winds, EOF analysis are performed on the wind interannual signal (on both zonal and meridional components). The temporal function of EOF_1 on the zonal wind shows a very high correlation of 0.91 (p<0.01) with EOF_1 U_{Ekman} temporal function (Fig. IV.33 e). Therefore, the first mode of variability of the interannual zonal wind dominates the interannual variability of the zonal Ekman transport, which in return is responsible for the majority of the interannual variability of the zonal total current.

Similar to the zonal current case, temporal functions of $EOFs_1$ on meridional U_{total} and U_{Ekman} are well correlated (R=0.93 (p<0.01)) (Fig. IV.34 a, b, e). Despite relatively poor correlation (R=0.31 (p<0.01)), both spatial functions present negative values to the west and positive values to the east. The negative anomalies observed on PCs_1 during winter 2009/2010 and summer 2015 indicate a strengthening of the northward currents in the western GoT (up to 0.15 m s^{-1} for the total current along the vietnamese coast). Additionally, the temporal function of EOF_1 on the meridional wind shows good correlation with $EOFs_1$ on U_{Ekman} temporal function (R=0.87 (p<0.01)). Here again, EOF_1 on meridional U_{geos} generates weak currents (Fig. IV.34 c) and shows poor correlations with EOF_1 on meridional U_{total} (0.03 and 0.33 for spatial and temporal functions, respectively) (Fig. IV.34 e). Therefore, the interannual variability of the meridional wind dominates the interannual variability of the meridional Ekman transport, which in return controls the majority of the interannual variability of the meridional total current.
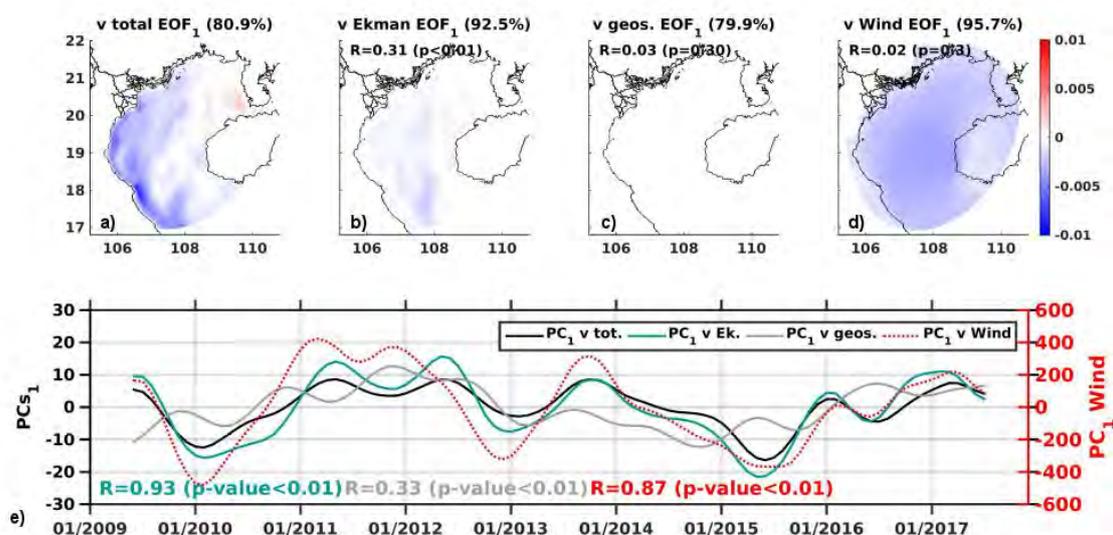
Figure IV.34: Same as Fig. IV.33 but for the meridional component (v) of the currents and the wind.

These results, based on EOF analysis on interannual current and wind signals, show that the inter-

annual variability of the total circulation is mostly driven by the interannual variability of the Ekman transport, which is itself driven by the wind interannual variability, and that the geostrophic component plays a negligible role.

IV.5.3   Hypothesis on drivers of the wind interannual variability

Since wind appears to be the main driver of the surface current interannual variability, the mechanisms behind the wind interannual variability are investigated in this section.

Previous studies related ENSO to the wind interannual variability over the entire South China Sea, using different wind products, time-periods and analysis methods (Wang et al., 2006; Cheng et al., 2016; Piton and Delcroix, 2018). All of these studies suggested lags of 2 to 4 months in the wind response to ENSO events (both La Niña and El Niño events) and attributed these lags to the teleconnection through the Pacific atmospheric bridge (Klein et al., 1999; Wang et al., 2004).

Table IV.3 presents the correlations between the temporal functions of the EOF_1 on zonal and meridional wind components with climate indices which describe Pacific large-scale patterns and which may influence the atmospheric circulation over the GoT (described in section IV.2.3). Note that correlations are computed with detrended and filtered climate indices following the same method (TY-H13) used for currents and winds. Best lagged anti-correlations are found for Niño 4 (ENSO index) (-0.65 and -0.72 for wind u and v respectively, with lags of 3 months) and PDO (Pacific Decadal Oscillation index) indices (-0.78 and -0.67 with lags of 2 and 1 months for wind u and v, respectively) with both wind components (Table IV.3).

	Niño 4	SOI	PDO	DMI	SAM	NP
EOF1 Wind u	-0.65(3)	0.56(4)	-0.78(2)	-0.15(4)	-0.40(0)	-0.15(0)
EOF1 Wind v	-0.72(3)	0.64(3)	-0.67(1)	-0.24(3)	-0.36(0)	-0.20(0)

Table IV.3: Maximum correlation coefficients (at given lags) between EOF_1 principal components of wind u and v and ENSO, PDO, DMI, SAM and NP indices. All values are significant at 99% confidence level.

This suggests that both ENSO and the PDO influence the GoT circulation, with ENSO events leading the wind signals by 3 months and the PDO leading by 1 to 2 months. Even though correlation values indicate good relationships between the wind signal with ENSO and PDO activities, the temporal functions presented on Fig. IV.35 however also suggest that ENSO and PDO activities can not explain the totality of the interannual wind signal. Indeed, depending on the particular period considered, ENSO and PDO indices lead the wind signals or are led by the signals, or seem not related at all.
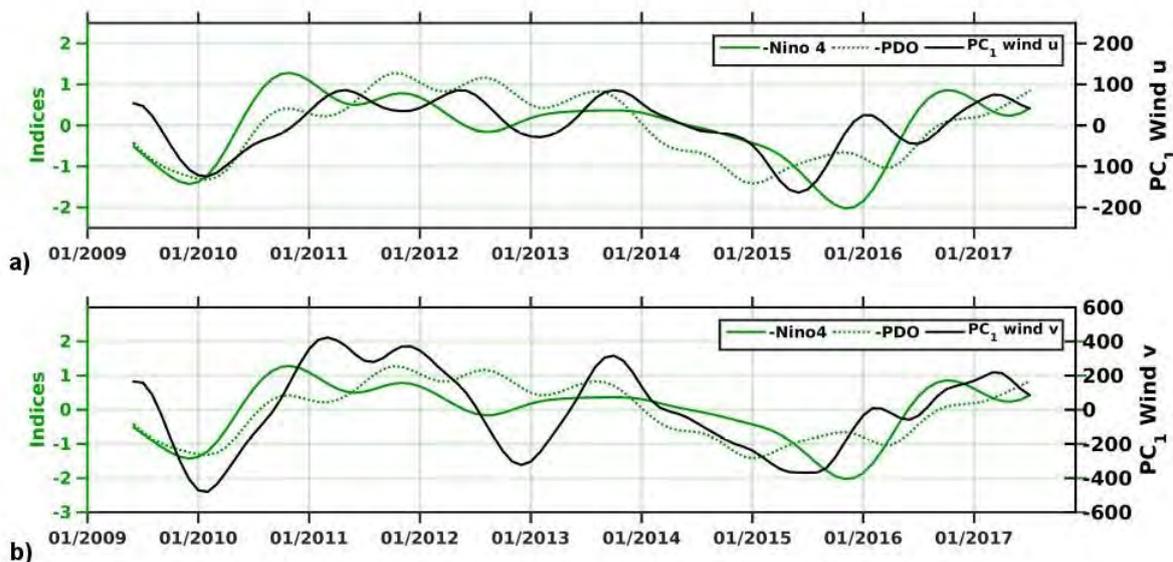
Figure IV.35: Temporal functions (black lines) on the EOF1 on zonal (a) and meridional (b) wind components. Overplotted are Niño 4 (solid green lines) and PDO (dotted green lines) indices detrended and filtered with the TY-H13 method.

Sign of $PC_1(u, v)$ anomaly on Fig. 4.35	Winter wind dir. NE ↙	Summer wind dir. SW ↗
Negative	Weakening of the winds	Strenghtening of the winds
Positive	Strenghtening of the winds	Weakening of the winds

Table IV.4: Wind behaviors in link with signs of PCs_1 on Fig. IV.35 and with the seasonal mean wind.

During periods 2009-2013 and summer 2016 to 2017, the ENSO, PDO and wind signals behave consistently with the above correlation. Details of the wind activity in link with ENSO events are detailed below:

- The strong El Niño event of 2009/10 (represented by a strong negative anomaly of the ENSO index on Fig. IV.35) seems to trigger a negative anomaly on the PC_1 of the wind (both u and v) 2-3 months after the event (Fig. IV.35 a, b). Thus, this event triggered positive wind anomalies (as the products of PC_1 and EOF_1 see Fig. IV.33 d and 4.34 d), of ~ 0.5 m s^{-1} for the zonal wind and of ~ 2.5 m s^{-1} for the meridional wind over the GoT. The mean winter wind being NE, associated with the winter monsoon wind, this anomaly corresponds to a weakening of the winter monsoon winds (see Table IV.4 for wind activity recap according to the sign of the PC1 anomaly and the seasonal mean wind). This is consistent with the

observed 2 to 3 months lagged winter wind weakening in the northern SCS of $\sim$ 3 m s^{-1} observed by Piton and Delcroix (2018). The weakening effect of El Niño events on winter monsoon was also observed by these authors on the 1982-83, 1986-87, 1991-92, and 1997-98 El Niño events.

- The two following La Niña events of 2010/11 and 2012/13, and the La Niña event of 2016/17 (characterized as positive ENSO index anomalies on Fig. IV.35) triggered a lagged response of 5-6 months of the zonal and meridional winds, but with opposite signs to El Niño responses. In these cases, the La Niña events triggered negative zonal and meridional wind anomalies, meaning a strengthening of the NE winter monsoon winds (Table IV.4).

- The long El Niño event that lasted from the end of 2014 through spring 2016, triggered intense negative wind anomalies on PC$_1$, from early spring to summer 2015, that started roughly 4 months after the beginning of the event (Fig. IV.35). This particular event was therefore associated with a weakening of the 2015 NE winter monsoon, similar to the El Niño 2009/10 case, and with a strengthening of the following SW summer monsoon. In winter 2015/16, when the El Niño event reached its maximum intensity, wind anomalies were however close to zero. This will be discussed later on.

In 2013 and in early 2016, relationships between ENSO and wind activity are less clear and factors potentially responsible for the wind interannual variability are proposed here:

- In summer-fall 2013, both EOF$_1$ on zonal and meridional wind show negative wind anomalies over the GoT (positive anomalies of PC$_1$), suggesting a weakening of the summer SW winds (Fig. IV.35; Table IV.4), whereas ENSO and PDO activities were steady. This wind weakening could be explained by the strong typhoon activity observed during June to November 2013 : cyclones travel from the Pacific ocean through the Philippines towards southeast Asia in opposite direction of the summer SW winds and can thus, potentially infer with the summer monsoon winds. Indeed, the 2013 typhoon season was recorded as the most active typhoon season over the Pacific since 2004 and the deadliest since 1975 (Mori et al., 2014). It counted the super Yolanda (Haiyan) typhoon which hit the GoT early November, and was one of the most powerful cyclones in recorded history (Schiermeier 2013; Philippine National Disaster Risk Reduction and Management Council, 2015).

- The strong El Niño event of 2015/16 did not trigger the expected winter wind weakening

like observed for the previous El Niño events (2009/10 and 2014/15). Instead, PCs_1 are close to 0 in winter 2015/16. This could be due to the cold wave that hit East Asia during winter 2015/16, killing more than 100 people and generating temperatures as low as 5 ° C in Hanoi, which were the lowest recorded in the last 20 years. This event was driven by a fast Arctic warming that occured within the troposphere, which forced the Arctic Oscillation to change phase rapidly, facilitating the strengthening of the Siberian high (Wang et al., 2017). Thus, this cold wave triggered by the Arctic Oscillation variability, presumably induced a strengthening in winter NE wind activity that counterbalanced the weakening effect of El Niño.

Results from this section suggest that ENSO interannual variability explain the patterns of wind interannual variability observed over the GoT in general, and particularly for the periods 2009/early-2013, 2014/mid-2015 and mid-2016/2017: El Niño events triggered weaken NE winter winds, whereas La Niña events triggered intensified NE winter winds. Since winds drive the Ekman transport, which is the main driver of the GoT circulation variability, ENSO activity during these periods hence drive the GoT circulation. However, particular events also show that the wind variability could be subjected to other factors such as the typhoon activity, that explains the weakening of the summer SW winds in 2013, and the cold wave of winter 2015/16 that explains the unexpected low wind anomalies after an El Niño event.

IV.5.4   Seasonal circulation and SSS patterns

Now that the GoT surface current variability is clarified, impacts of this variability on water mass distribution are investigated. SSS and surface currents monthly mean fields from SIMU (for March, July, September and December) are presented in Fig. IV.36.

Freshwater discharges and seasonal wind reversals typical of the monsoon climate seem to be the main drivers of the Red River plume. Indeed, the NW-SE SSS gradient previously described in section IV.4.2 shows a strong seasonal extent variability. In winter, due to minimum Red River discharges combined with the strong southward coastal buoyant current (up to 4 m s^{-1}), the extent of the Red River plume (i.e. low salinity waters) is limited to the very near coastal area (Fig. IV.36 a, d), with freshwaters transported as south as 17.2 ° N. In July, in the core of the wet season, due to increasing rainfalls and associated discharges combined with weaker and eastward coastal circulation ($\sim$ 0 to 0.1 m s^{-1}), the freshwater plume extends eastward (approximately $\sim$ 50 km from the coasts) (Fig. IV.36 b), and remains trapped above 18 ° N. In their numerical study using ROMS at 1/15° over the period 2007-2016, Rozowski et al. (2019) simulated a freshwater plume that re-
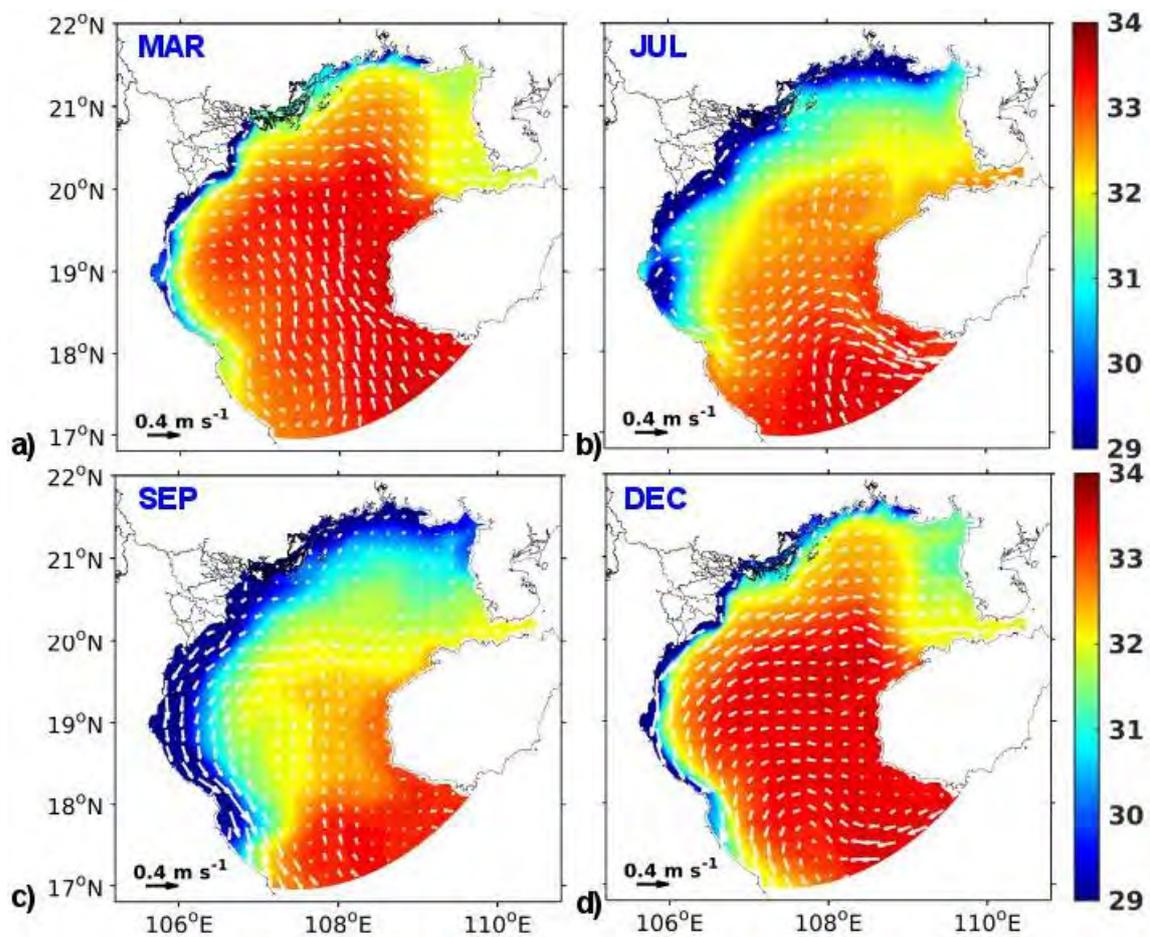
Figure IV.36: March (a), July (b), September (c) and December (d) monthly mean fields of SSS (in PSU) superimposed with surface currents monthly mean fields (in m s^{-1}) from SIMU over the period 2009-2017.

mained trapped right in front of the only Red River distributary represented in their configuration, north of 20° N. This shows the importance of representing in a model configuration each of the seven estuaries of the Red River system, as well as others Vietnamese rivers (such as the Ma, Lac Giang and Lam rivers, Fig. IV.2), as they affect the river plume's representation and associated SSS. In September, the southward coastal current strengthens as northeastern winds pick up, which allows to "release" freshwaters and to export them southward, as low as 17° N (Fig. IV.36 c). As winter progresses (December), river discharges decrease and the southward current intensifies (up to 0.5 m s^{-1}), which diminishes the eastward plume extent, while freshwaters are still transported southward (Fig. IV.36 d). Note that in September and December (Fig. IV.36 c, d), the vanishing of the southward buoyant current south of 17.2 ° N may be caused by GOM lateral boundary conditions, which impose saltier waters at the southern open boundary and therefore limit the freshwaters export outside the domain.

SSS distribution over the GoT, and in particular freshwater distribution, is thus largely depending

on the GoT seasonal surface circulation.

IV.5.5   Water flux variabilities and budgets

In this section, cross-section fluxes are computed over the simulation period 2009-2017 at different time-scales and compared, when possible, with literature.

IV.5.5.1   Seasonal variability

Fig. IV.37 presents the winter and summer water fluxes across five sections, located across the trajectories of the Hainan strait current (section 1), of the current south of Hainan island (section 2), and of the coastal boundary current (sections 3, 4, 5). Atmospheric fluxes are computed over the GoT area encompassed in between sections 1, 2 and 3.
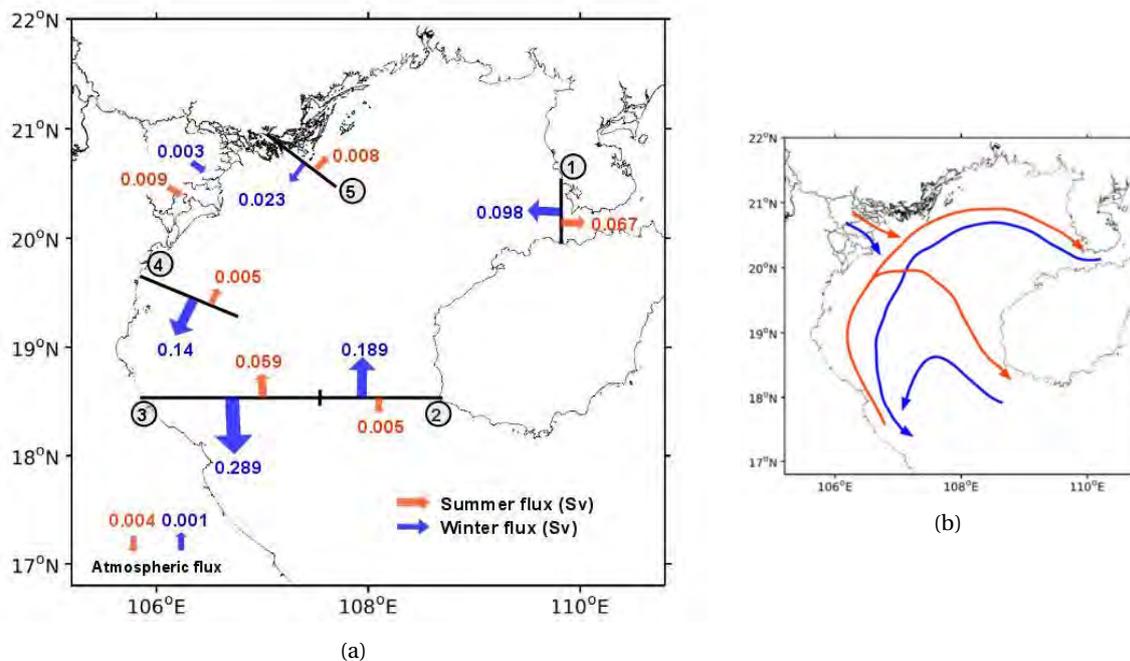
Figure IV.37: Mean summer and winter fluxes (in Sv) through sections 1 to 5 computed from SIMU over the period 2009-2017 (left), schematic representation of flux dispersal (right).

Comparison with existing evaluation

General seasonal water flux values over the GoT computed from SIMU are consistent with the values of Chu et al. (1999) who, in their study over the entire SCS, observed fluxes in the GoT of 0 to 1 Sv in both summer and winter. When considering the flux through Hainan Strait only, flux of -0.067 Sv computed with SIMU falls within the range of the flux observed by Shi et al. (2001) (-0.2 to 0.1 Sv, Table IV.5) but are slightly lower than the ones computed by Gao et al. (2013) from their model (-0.28 to -0.18 Sv).

	Summer	Winter	Method	Period
Shi et al., 2001	-0.2 to 0.1	0.2 to 0.4	in-situ SLA observations	1963-1999
Chen et al., 2009b	0.026	0.116	Numerical model	1-year simulation
Gao et al., 2003	-0.28 to -0.18	0.3 to 0.4	Numerical model	2006-2007
SIMU	-0.067	0.098	Numerical model	2009-2017
SIMU_deeper_Hainan	-0.072	0.102	Numerical model	2009-2017

Table IV.5: Water transport (in Sv) through the Hainan strait from previous studies and from our simulations (negative values indicate an eastward flux).

SIMU flux of 0.098 Sv in the Hainan strait are also slightly weaker than the ones from Shi et al. (2001) and Gao et al. (2013), but are close to the results computed by Chen et al., 2009b (0.116 Sv). Flux discrepancies among the studies may be caused by the different methods and time-periods considered by each author (Table IV.5). Furthermore, flux computations depend on the size of the section and thus on the bathymetry, which could be particularly difficult to represent in straits. In SIMU configuration, the smoothing scheme induced an error of ~ 15% in the Hainan strait bathymetry. In order to evaluate the sensitivity of the water fluxes to changes in bathymetry, a simulation with a bathymetry deepened by 15% (~ 10 m) in the Hainan strait is performed (noted SIMU_deeper_Hainan). Results show that a deeper depth in the strait moderately increases the summer water flux by 7% and the winter water flux by 4% (Table IV.5). These results show the role of bathymetry in the flux computation through the Hainan Strait, but they mitigate its importance.

Seasonal variability of fluxes

Winter fluxes all over the GoT are more intense than summer fluxes: from ~ 1.5 times bigger during winter than during summer across section 1, to 38 times bigger during winter than during summer across section 2 (Fig. IV.37). Furthermore, winter flux along the south of the delta (0.14 Sv, section 4) is larger than along the northern delta (0.023 Sv, section 5), suggesting a 0.114 Sv gain of water from offshore in between these sections (river inputs is only 0.003 Sv). This is confirmed by the winter surface currents (Fig. IV.29 a), which show strong W-SW currents flowing towards the delta. On the contrary, in summer, combined river and section 4 fluxes correspond to 0.014 Sv, whereas flux through section 5 are 0.008 Sv, showing a 0.006 Sv loss of water in between section 4 and 5 associated with a non negligible eastward offshore flux. Summer surface currents (Fig. IV.29 d) indeed indicate a N-NE circulation along the delta, responsible for those eastward offshore fluxes.

Monthly fluxes responsible for input/export of water inside/outside the GoT are presented on Fig 4.38.
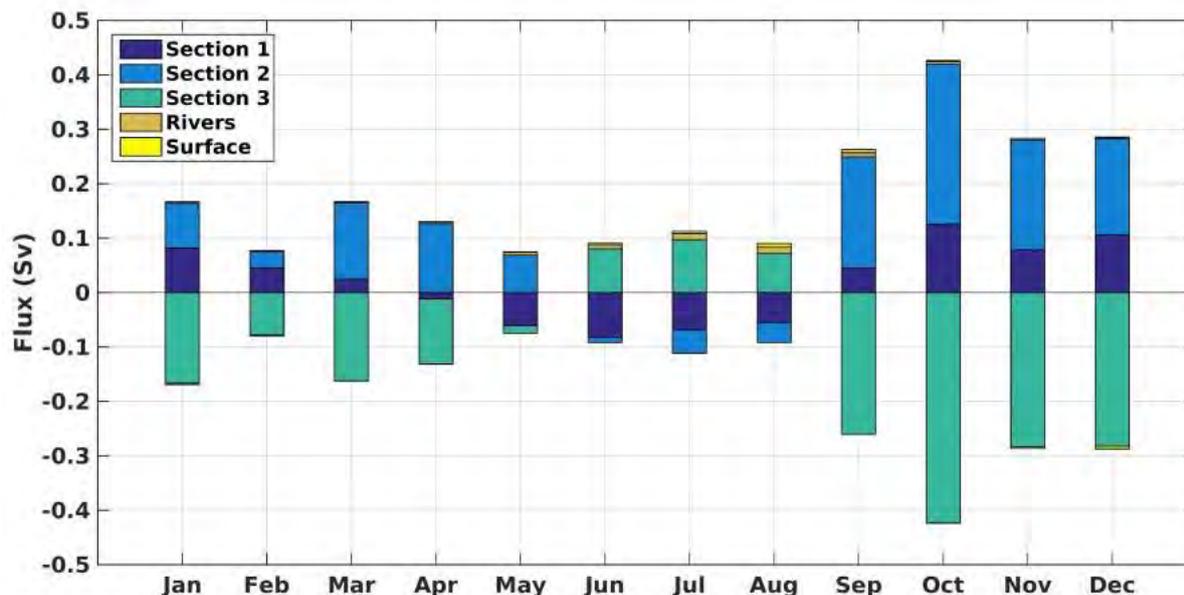
Figure IV.38: Climatological cross-section, rivers and surface fluxes computed for the period 2009-2017. Negative values indicated flux flowing outside the GoT.

During winter, the water input to the GoT mostly occurs through section 2 (from 50 to 90%) and the rest through Hainan Strait (section 1) (Fig. IV.38). This is consistent with results from Shi et al. (2001) who estimated that the flux via the Hainan Strait (section 1) may replenish less than 44% of the GoT water in winter. Contribution of rivers and precipitation to the input of water remain very limited from October to April. Export of water outside the GoT almost only occurs through section 3, i.e., through the coastal boundary current, and less than 0.5 % is exported via the atmospheric flux (i.e. evaporation).

During summer, the GoT waters enter mostly from the SW GoT through section 3, i. e. via the coastal boundary current, and to a much lesser extent ($\sim$ 5%) from rivers and precipitation inputs. Water is mainly exported outside the GoT through Hainan Strait (section 1) (between 60 and 90%) , while the rest is exported through the section south of Hainan (section 2).

These results show that the GoT water renewal mostly occur during winter and that the coastal current plays a key role in exporting waters outside the GoT. Hainan straits fluxes are important for winter water inputs, and crucial in summer for water export outside the GoT. The general circulation drives the flux patterns, leading to offshore flux (eastward) in the delta area in summer, whereas during winter the GoT waters converge towards the western GoT.

IV.5.5.2   Climatological averages

Now that the seasonal fluxes at the GoT boundaries (i.e. the Hainan Strait and the southern open
boundary) are quantified, the annual mean exchanges with the SCS through these passages are
compared with flux estimates in the SCS. Fang et al. (2009) detailed the annual mean water fluxes
through the six main straits of the SCS (Fig. IV.39 and Table IV.5).
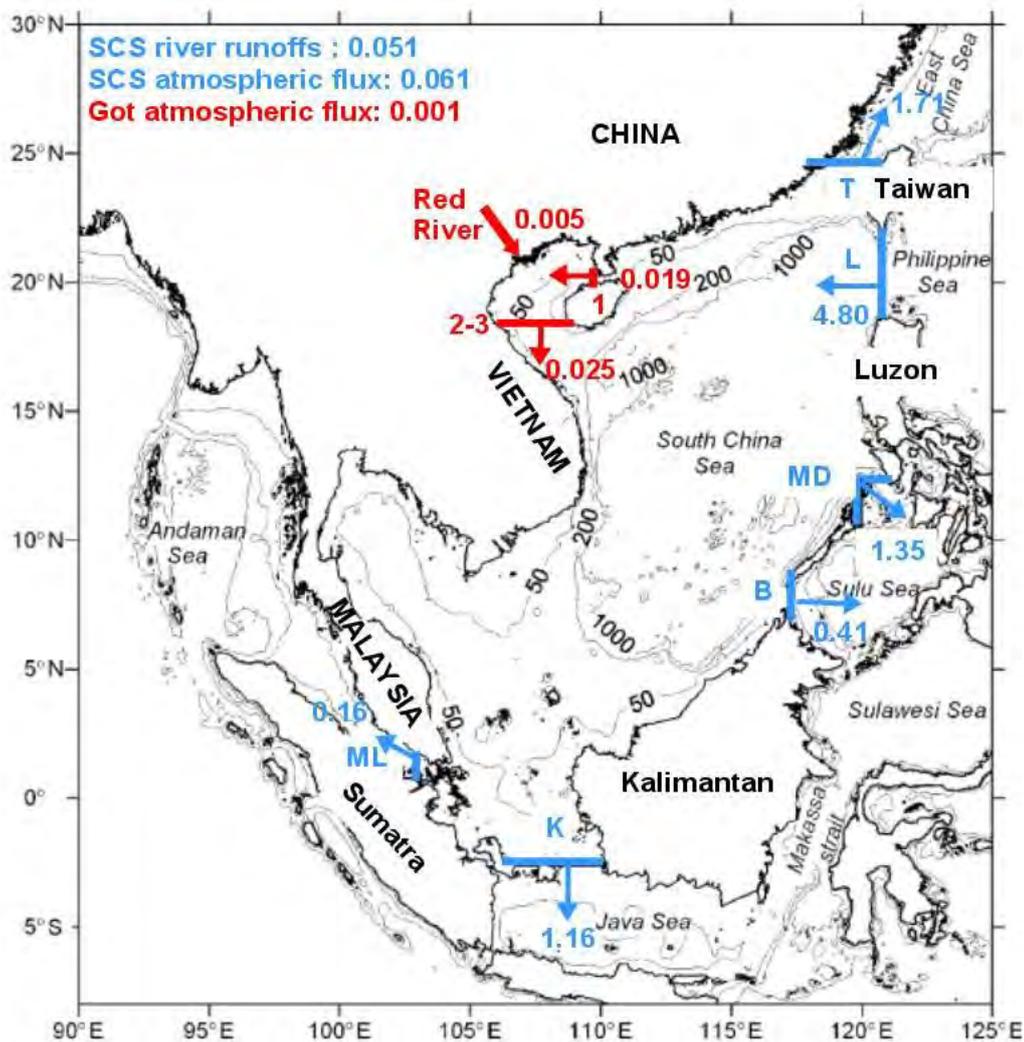
Figure IV.39: Water fluxes (in Sv) in the South China Sea its interocean passages (in blue, adapted from Fang
et al., 2009) and in the GoT (in red, from SIMU). Solid blue lines indicate the cross-sections where fluxes
were computed for the Luzon (L), Taiwan (T), Mindoro (MD), Balabac (B), Karimata (K) and Malacca (ML)
Straits by Fang et al. (2009). Solid red lines indicate the cross-sections for the Hainan strait (1) and for the
total southern boundary of the GoT (2-3), which are computed from SIMU. Arrows denote directions of the
mean water transport. Isobaths are in meters.

In the computation of Fang et al. (2009), western Pacific waters enter the SCS through the Luzon
Strait with an annual mean flux of 4.80 Sv, of which 1.71 Sv returns to the western Pacific (and
East China Sea) through the Taiwan Strait, while 3.09 Sv flow toward the SCS and are exported
to adjacent seas via the different straits. In SIMU, SCS waters entering annually the GoT via the

Hainan Strait correspond to 0.019 Sv, while the GoT exports waters to the SCS via the southern GoT passage at 0.025 Sv. The difference of 0.006 Sv corresponds to the annual Red River fluxes of 0.005 Sv and of the atmospheric flux of 0.001 Sv that feed the GoT with freshwaters. Therefore, the SCS gains annually 0.006 Sv of freshwater from the GoT, that comes from combined inputs of Red River and precipitations. For a superficy of 1.45×10^{11} m², the GoT represents 5% of the SCS superficy ($\sim$ 3.33×10^{12} m²), while it represents 10% of the total SCS river runoffs (0.051 Sv for the whole SCS).

These results highlight the importance of the GoT freshwater fluxes in the total SCS fluxes, and further suggest that all of the Red River runoff that feeds the GoT continental shelf is transported to the SCS. More generally, this suggests that all of the contaminants brought by the Red River to the GoT can be exported to the SCS.

IV.5.5.3   Interannual variability

Previous sections IV.5.2 and IV.5.3 indicated that the interannual variability of the surface circulation in the GoT is mainly driven by the interannual variability of the wind, which is itself mostly controlled by ENSO and also by other factors, such as typhoon activity and Arctic Oscillation variability. In this section the interannual variability of the water fluxes through the GoT boundaries, which interact with the SCS, are investigated. The temporal flux series of sections 1, 2 and 3 are filtered using the TY-H13 method to extract the interannual signals. Good correlations between the filtered signals and the temporal functions of the EOF_1 on the wind interannual variability are found (Table IV.6 and Fig. IV.40).

	$PC_1 wind u$	$PC_1 wind v$
Filtered flux signal - Section 1	0.88 (<0.01)	0.64 (<0.01)
Filtered flux signal - Section 2	0.93 (<0.01)	0.81 (<0.01)
Filtered flux signal - Section 3	-0.93 (<0.01)	-0.74 (<0.01)

Table IV.6: Correlation coefficients (R) values between the interannual water flux signals through sections 1, 2, 3 and the temporal functions of the EOF_1 on zonal and meridional wind.

Such results were expected as surface circulation drives the surface fluxes. Furthermore, as fluxes values correspond to the fluxes integrated over the water column, these results suggest that the wind variability impacts the entire water column. Therefore, as ENSO appears to have a notable impact on the interannual wind variability over the GoT (section IV.5.3), by cascading effect, ENSO also impacts the interannual GoT fluxes variability as follows:

- The El Niño events of 2009/10 and 2014/15, which triggered a weakening of the NE monsoon winds (section IV.5.3) with a potential weakening of the GoT circulation, seems responsible

for decreasing water fluxes through all the GoT boundaries. Indeed, negative flux anomalies through section 2 (meaning a decrease of water input in winter) are observed ~ 3 months after the negative peak on the PC_1 of wind (u), and positive flux anomalies are observed through section 3 (meaning a decrease of water export in winter) with the same lag (Fig. IV.40). Furthermore, this El Niño event seems to also decrease the westward winter flux through Hainan, with negative anomalies observed ~ 3 months after the negative peak of the wind PC_1.

- On the contrary, the La Niña events (2010/11, 2011/12 and 2016/17) which triggered a strengthening of the winter monsoon, potentially intensifying the surface circulation, seemed responsible for fluxes intensification over the GoT. Indeed, positive flux anomalies through sections 1 and 2 (meaning increased water input to the GoT) and negative anomalies through section 3 (meaning increased water export outside the GoT) are observed 3-4 months after the positive peaks on the PC_1 of the wind.

These results, which suggest that El Niño events weaken and La Niña events strengthen the winter GoT fluxes. Qu et al. (2004) also showed an impact of ENSO at the Luzon Strait, based on a numerical modeling study over the period 1982-1998. However they observed an intensification of the water fluxes entering the SCS after El Niño events. They further detailed that El Niño events were responsible for a weakening of the southward Kurushio currents off the Philippines, which provided favorable conditions for the Pacific waters to enter the SCS through Luzon Strait. This suggests that ENSO effects on flux transport through straits depend upon the regional circulation around those straits and on the way it is impacted by ENSO. At least in the SCS, generalizing on the impacts of ENSO on the transports through straits is not possible.

Previous section IV.5.3 shed light on other mechanisms responsible for the wind interannual variability (typhoon activity and Arctic Oscillation variability). Impacts of these mechanisms on the water fluxes are detailed here.

- The catastrophic 2013 typhoon season (summer-fall) that weakened the summer SW monsoon due to strong cyclonic winds, triggered during summer positive flux anomalies through section 1 and 2 (meaning a decrease of summer fluxes entering the GoT) and negative fluxes through section 3 (meaning a decrease of summer fluxes exiting the GoT) (Fig. IV.41).

- Previous section IV.5.3 highlighted the potential role of the cold wave that struck southeast

Asia in early 2016, in counterbalancing the El Niño effects on the wind activity. These effects also appear on the flux variability, since anomalies are close to 0 for the 3 sections considered, whereas negative anomalies for section 1 and 2 and positive anomalies for section 3 could be expected after an El Niño event.
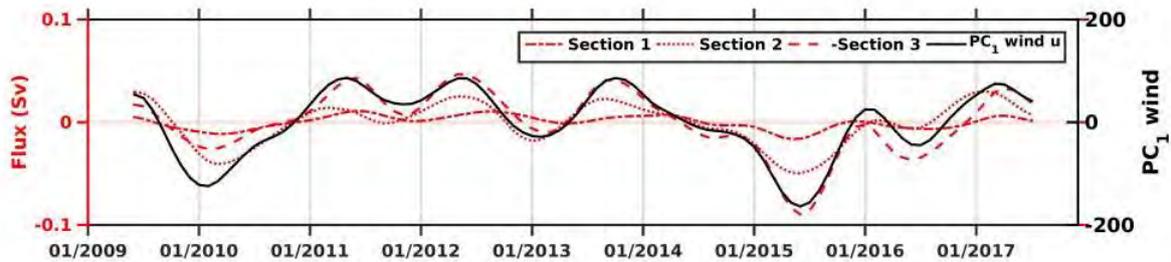
Figure IV.40: Filtered flux signals through sections 1, 2 and 3 (in red) superimposed with EOF1 temporal function of the zonal wind (in black). Positive flux values indicate fluxes entering the GoT, negative values indicate fluxes flowing outside the GoT. Note that Section 3 series is reversed.

These results show that ENSO variability largely influences the GoT fluxes variability, with El Niño events decreasing the winter water fluxes and La Niña intensifying the winter water fluxes. Other factors such as typhoon activity and Arctic Oscillation variability can also influence the flux variability, by weakening the summer water fluxes for the former, and increasing them hence counterbalancing the El Niño influence for the latter.

IV.5.5.4   Typhoon-induced variability

Since the 2013 typhoon activity seems to play a role in the GoT water flux interannual variability, effects of typhoon activity on water fluxes are evaluated in this section. A tropical typhoon (or cyclone) is an intense localized source of surface wind stress that produces a significant response in the ocean environment, especially in the thermal structure, the upper currents and the sea surface height (Chu et al., 2000). Indeed, the most obvious feature of the oceanic responses to typhoon activity is the decrease of SST (Dickey et al., 1998; Walker et al., 2005). Furthermore, due to suction and typhoon entrainment, mixed layer temperature decreases correspondingly with an increase of its thickness (Church et al., 1989; Jacob et al., 2000). This may cause large changes in density structures and current fields of the upper ocean (Dickey et al., 1998; Zelder et al., 2002). Responses to typhoons between coastal regions and open oceans are similar (Chu et al., 2000). In the SCS, Typhoon Ernie (1996) triggered significant SST cooling and sea surface depression in the wake of the storm (Chu et al., 2000). Typhoon Pabuk (2007) largely intensified the near-bottom current along its route (from the Luzon Strait to the Hainan Strait) (Liu et al., 2011). Wang et al.

(2014) also observed a strong deep SCS circulation induced by typhoon activities, which suggests that effects of typhoon can penetrate into the deep ocean.

To our knowledge, no english-written studies have focused on the impacts of typhoons on water fluxes in the SCS nor on the impacts on the GoT circulation.

Among the 18 typhoons passing over the SCS in 2013, four hit the GoT (Joint Typhoon Warning Center). Characteristics of these typhoons and their wind intensities are given on Fig 4.41.
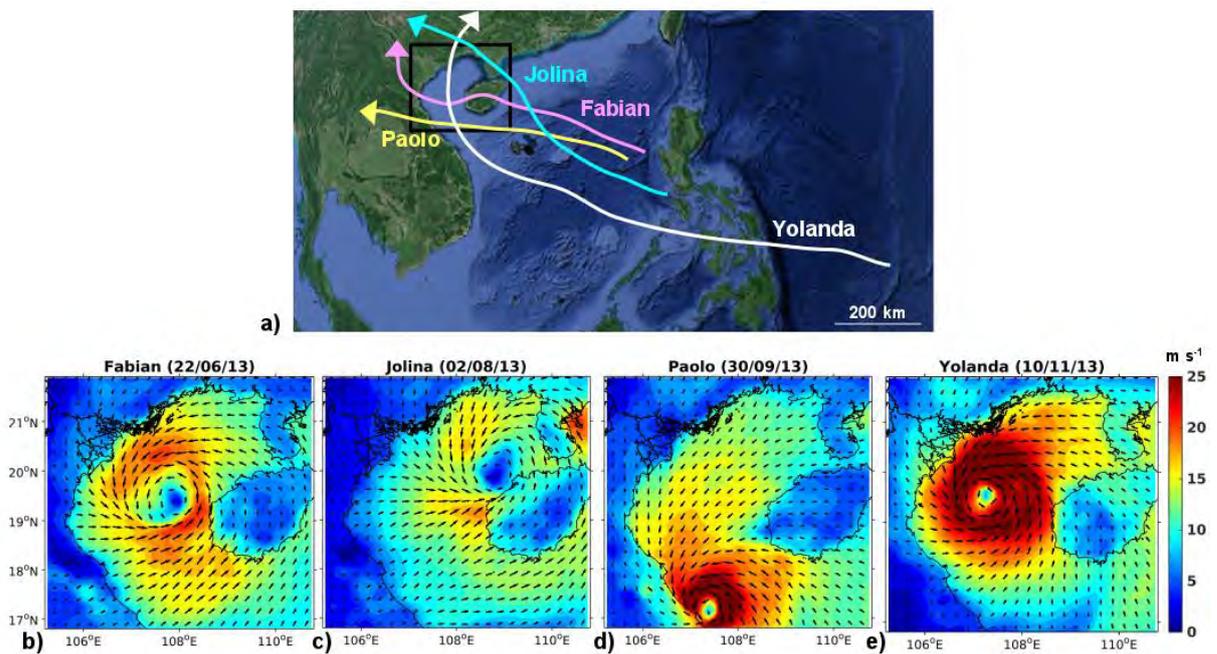
Figure IV.41: Typhoon Fabian, Jolina, Paolo and Yolanda trajectories (a) and associated wind when passing over the GoT (in m s^{-1}) (b, c, d, e).

Daily water budgets are computed for each typhoon on the day it passes over the GoT, and are compared to the total water budget of the corresponding month (Fig. IV.42). Note that these budgets do not correspond to the total budgets generated by the passage of a typhoon, as it has been shown that the strong current induced by a typhoon lasts 3-4 days after its passage over the SCS (Ke et al., 1987).

The following results therefore only represent water budgets during one day, and do not take into account the typhoon inertia effect on water fluxes.

Typhoon impacts on circulation

First, each of the four typhoons generated a westward flux through Hainan Strait (section 1) (Fig. IV.42 a-d). Furthermore, along the RRD (section 4 and 5), all typhoons generated a southward

circulation, which can therefore be determining when studying sediment transport. Typhoons Fabian, Paolo and Yolanda generated cyclonic circulation over the GoT (Fig. IV.42 a, c, d). However, due to its trajectory (passing over the northern part of the GoT), Typhoon Jolina only generated cyclonic circulation through sections 1, 4 and 5 (Fig. IV.42 b).

These results suggest that typhoons generate a cyclonic circulation over the GoT, that enhances the winter circulation, but also occurs when summer anticyclonic surface circulation is dominating (typhoons Fabian and Jolina, Figure IV.42), i. e., typhoons can reverse the circulation.
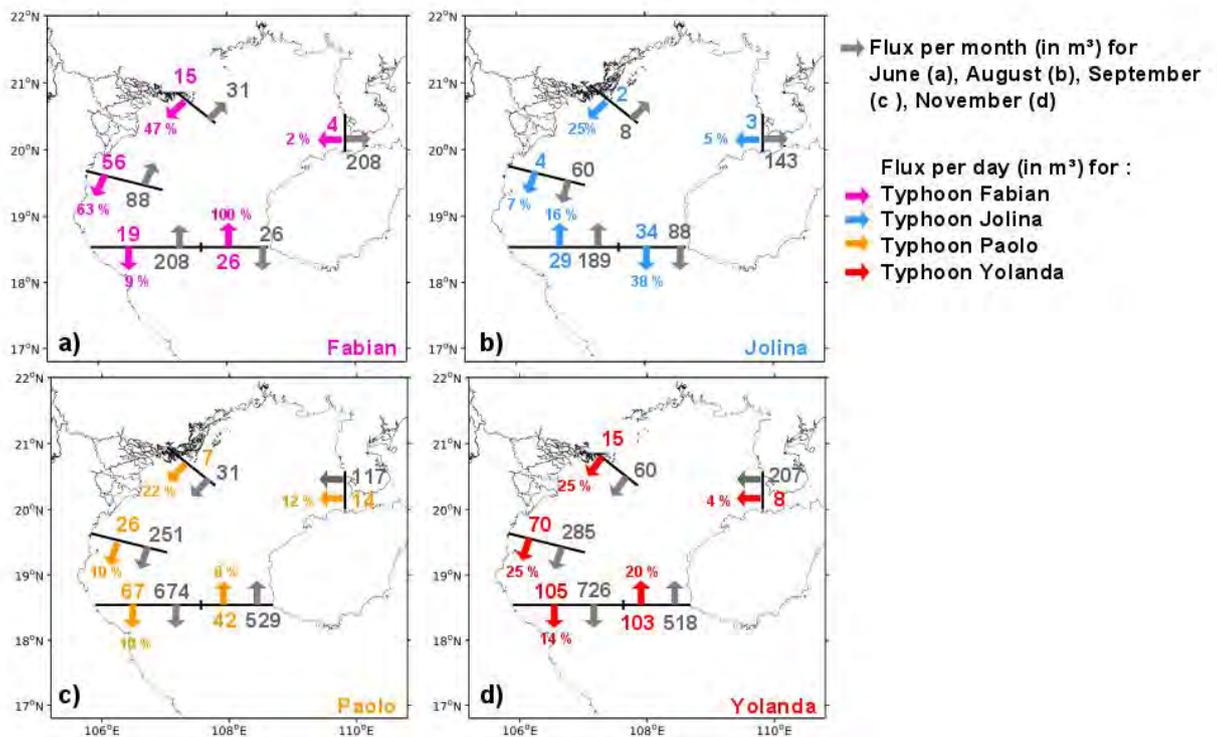
Figure IV.42: Daily-averaged fluxes (in Sv) generated by typhoons (colored arrows) and monthly accumulated daily-averaged fluxes (grey arrows) for (a) typhoon Fabian and month of June, (b) typhoon Jolina and month of August, (c) typhoon Paolo and month of September, and (d) typhoon Yolanda and month November. Percent values correspond to the ratio between typhoon daily fluxes and accumulated fluxes in one month.

Typhoon impacts on flux intensities

The way typhoons impacted the flux intensity varies from a typhoon to another and from a section to another, and are represented on Fig. IV.42. These fluxes, in terms of water budgets are summarized in this section.

First of all, all typhoons generated strong southward fluxes along the RRD (sections 4 and 5), which represented 25 to ~ 50 % of the monthly water flux for typhoon Yolanda and Fabian, respectively

(Fig. IV.42 a, d).

Through the Hainan Strait, the westward daily flux generated by the typhoons represented from 2 (Typhoon Fabian) to 12 % (Typhoon Paolo) of the monthly flux through this section. In terms of water, Typhoon Paolo generated an input of 14000 m^3 of water in one day, i.e. 12% of the total input of 117000 m^3 in November (Fig. IV.42 c).

At the southern GoT boundaries, typhoons Fabian, Paolo and Yolanda generated exports of water through section 3 from 9 to 14 % of the monthly export, and daily inputs of water through section 2 represented from 8 to 100% of the monthly input (Fig. IV.42 a, c, d). Indeed, Typhoon Fabian generated in one day a northward water input of 26000 m^3 through section 2, which corresponds to the total southward export of water through this section in June (Fig. IV.42 a).

These results show that typhoons can significantly modify the circulation and associated water fluxes in the GoT, generating daily fluxes anomalies of the same order as the fluxes accumulated in one month.

Lastly, and as previously mentioned, it has been shown that typhoons can impact circulation days after their passages over the SCS (Ke et al., 1987). Here, typhoons impacted the water fluxes in total during 6 to 8 days (Fig. IV.43). In summer, typhoon Fabian triggered flux decreases and reversals through sections 2 and 3, and Typhoon Jolina through section 1 approximately 4 days before the typhoon's passages. Fluxes reversed back to their initial direction 2 to 3 days later. In winter, typhoon Paolo and Yolanda seemed to generate flux increases through section 2 and 3, approximately 3 days before their passages and their impacts seemed to vanish 2 to 3 days later (Fig. IV.43). This confirms that the typhoon impacts on the circulation last several days before and after the event, and that an estimation of the total water fluxes generated by a typhoon could be obtained by taking into consideration fluxes during 3 days before and after a typhoon's passage.

These results show the strong impacts of typhoons on the GoT water budgets, especially in terms of water input and export, and in the water fluxes along the RRD. Therefore, a good representation of typhoons in regional modeling of the sub-tropical regions is crucial for the study of water budgets and sediment transport.

Relation between typhoon intensities and flux intensities
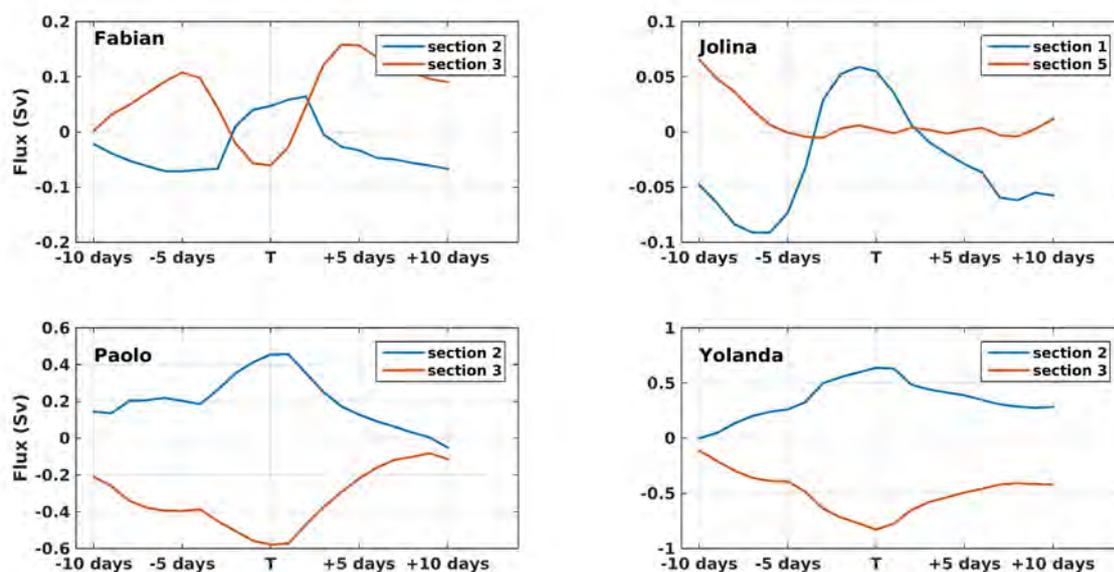
Figure IV.43: Flux temporal series through sections 2 and 3 for typhoon Fabian, Paolo and Yolanda and through section 1 and 5 for Jolina, computed for 10 days before and after the passage of the typhoons over the GoT. The convention is again positive (respectively negative) corresponds to input to (respectively output from) the GoT.

Since typhoons and super typhoons are expected to increase both in number and intensity as a result of global climate change (Bender et al., 2010; Schiermeier, 2010), it is important to understand their impacts on local environments to predict their potential future impacts. Relations between typhoon intensities and induced fluxes are proposed on Fig. IV.44. To improve the robustness of the study, the effects on water fluxes of four more typhoons are assessed: Typhoon Parma which hit the GoT on October 13th 2009, Typhoon Conson on July 17th 2010, Typhoon Nesat on September 29th 2011 and Typhoon Ofel on October 28th 2012. These four typhoons have been chosen according to their routes: only typhoons that perfectly passed over the GoT, potentially affecting all cross-section fluxes, have been selected. Typhoon intensities are characterized as the mean wind intensity on the day the typhoon hits the GoT. Here, only flux through section 3 are considered as they are responsible for most of the GoT water exports. In details, typhoon fluxes through section 3 (Sv) correspond to the daily mean water flux subtracted of the monthly mean flux.

Fig 4.44 shows a good correlation (R=0.87 (p<0.01)) between fluxes and typhoon intensities. Besides, the regression line (with a coefficient of determination of R²=0.79) confirms an increasing regression between these datasets, i.e., the more intense the typhoons is, the more intense the fluxes across section 3 are. For example, Super Typhoon Yolanda, which in terms of intensities is 1.5 times stronger than Typhoon Parma, generated maximum fluxes through section 3 that are 6 times stronger than the maximum fluxes generated by Typhoon Parma. Following this relation,

and if strong typhoons tend to increase in number and intensities in the context of global change , it is expected that GoT water fluxes will be more intensely impacted by cyclones, which will also alter the summer anticyclonic circulation (reversal of the circulation).

Therefore, considering typhoons when studying water fluxes and budgets is crucial, as they trigger cyclonic circulation that can even reverse the mean summer circulation. Furthermore, typhoons enhance water fluxes and water inputs/exports, which seems to intensify along with typhoon intensification. Since water transports suspended particulate matter, typhoons may also play a role in the SPM transport and deposition.
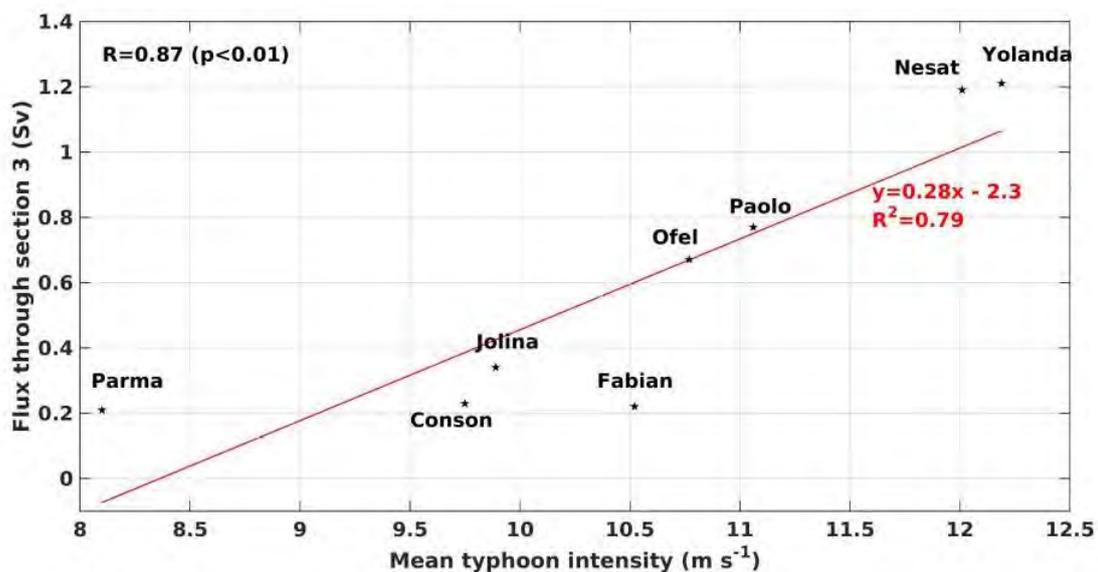
Figure IV.44: Mean wind intensities over the GoT generated by typhoon Parma, Conson, Jolina, Fabian, Ofel, Paolo, Nesat and Yolanda vs. fluxes through section 3 (in Sv) computed for each typhoon event subtracted of the associated monthly mean flux (stars) and Red line linear regression (red line). R is the correlation coefficient between the fluxes and the typhoon intensities and R² is the coefficient of determination of the regression line.

IV.5.6 Complements on Chapter II

One of the conclusions of Chapter II suggested that during the dry season, sampling stations (ST1, ST2 and ST3) were likely located in the saline estuary, while during the wet season stations seemed located in the tidal river as salinity intrusion was pushed seaward. It was further suggested that a numerical study could confirm this hypothesis. Surface and bottom salinity fields from SIMU are plotted for September 4th 2017, corresponding to survey WS (wet season at spring tides) and for December 14 th 2017, corresponding to survey survey DN (dry season at neap tides) (Fig. IV.45).

On September 4th (Fig. IV.45 a, b), both surface and bottom salinity fields emphasize an extent of
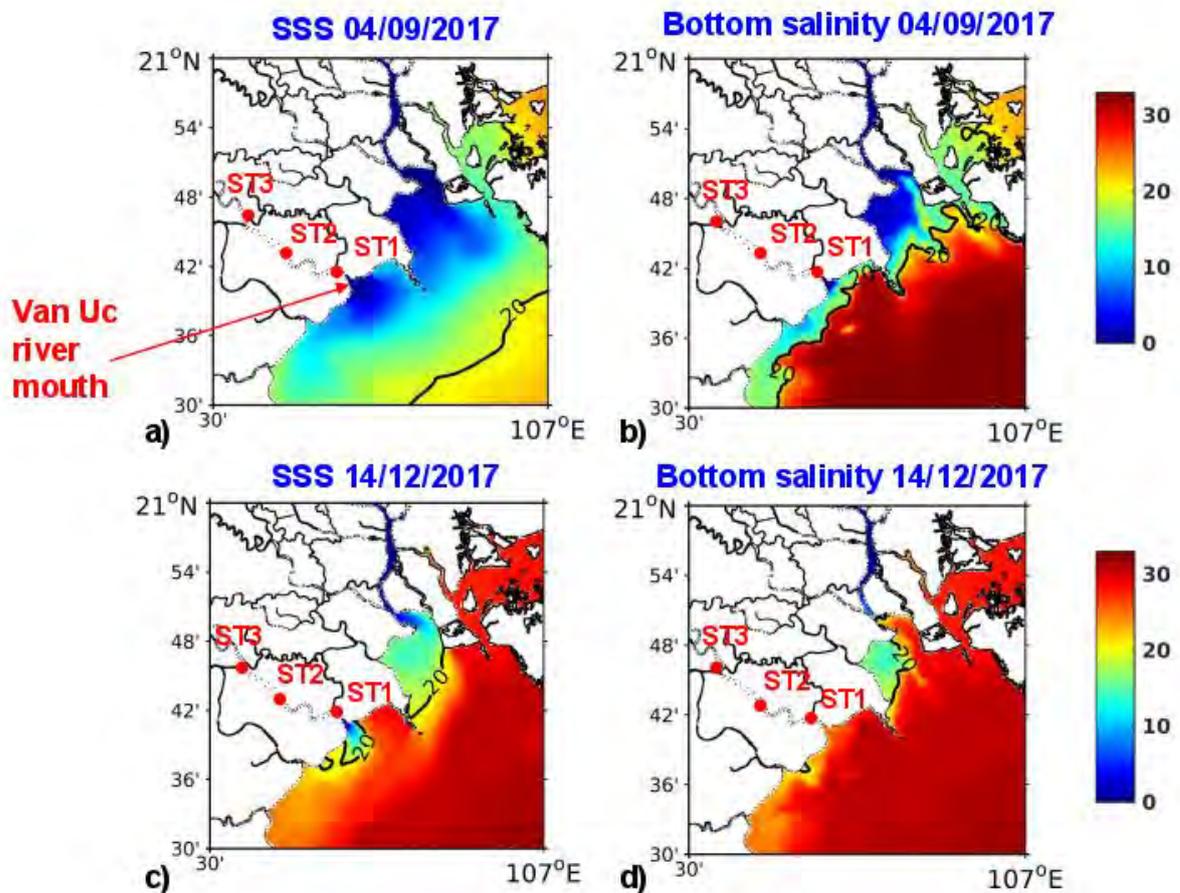
Figure IV.45: Daily mean surface (a, c) and bottom salinity (b, d) (in PSU) from SIMU on September 4th 2017 (a, b) and on December 14th 2017 (c, d). The black solid line represent the isohaline 20 and the locations of sampling stations (ST1, ST2 and ST3) of Chapter II are indicated in red.

the Van Uc river plume, characterized by low salinities, ~ 25 km further seaward than on December 14th (if following isohaline 20) (Fig. IV.45 c, d). This confirms that during the wet season survey, riverine waters were expelled offshore and that the estuary (mixing between riverine and marine waters) developed in the bay and in coastal waters. Sampling stations (ST1, ST2 and ST3) of survey DS were therefore located in the tidal estuary. Salinity fields of December 14th show a reduced freshwater plume at the surface that has disappeared in the bottom layer. These results suggest a strong stratification of the water column during the dry season at neap tides, which has also been observed in the estuary.

IV.6   Conclusion

With the aim of generating a good representation of the GoT hydrodynamics, that will be used for sediment transport modeling, and with the aim of complementing the knowledge on the GoT cir-

culation dynamics and variability, the hydrodynamical model SYMPHONIE was implemented and validated in the Red River estuary and over the GoT. Firstly, the model configuration was optimized in the Van Uc estuary with in-situ data collected in 2017. Then the reference simulation SIMU was compared to available in-situ data, model analysis and satellite observations of basin-scale hydrological characteristics and surface circulation. These comparisons showed that SIMU reproduces correctly the seasonal, annual and interannual cycles and spatial patterns of the surface and upper layer ocean hydrological and dynamical characteristics, whose realism was improved compared to the forcing model (GOM) used at the lateral open boundaries of the configuration. SIMU could therefore be legitimately used to study the surface circulation variability in the GoT.

Previous studies based on observations and numerical models on the GoT surface circulation revealed uncertainties in both circulation patterns and circulation drivers. Some studies suggested a cyclonic summer circulation while others depicted an anticyclonic one. Furthermore, some authors suggested a year-long westward flow through Hainan strait, while others suggested a seasonal reversal of this flow. These studies also raised the questions of drivers of the GoT circulation, with authors suggesting a dominant geostrophic surface circulation and others, a wind-driven circulation. Our high resolution simulation allowed to examine in details these aspects over a rather long 9-year period. Results from SIMU over the period 2009-2017 showed on average a summer anticyclonic surface circulation and a winter cyclonic surface circulation, with a seasonal reversal of the Hainan Strait circulation (eastward in summer and westward in winter). In addition, EOF studies revealed the leading role of the wind-driven currents over the geostrophic currents in controlling the surface GoT circulation and its seasonal and interannual variabilities. Furthermore, we showed that ENSO plays an important role in influencing the wind interannual variability, which is also influenced by other factors such as typhoon activity and Arctic Oscillation variability.

Then, we showed that the seasonal water fluxes follow the seasonal circulation patterns. During winter, water enters the GoT through the Hainan Strait and south of Hainan, flows westward towards the Vietnamese coastline before flowing southward and exiting the GoT through the southwest boundary, i. e., via the coastal boundary current. During summer, water inputs mostly enter through the SW boundary, flows northward following the Vietnamese coastline before separating into two branches near the RRD: one flowing toward the southeast to exit the GoT south of Hainan Island, one following the NE Vietnamese/Chinese coastlines before exiting the GoT through the Hainan Strait. These summer fluxes can however reverse under the action of typhoons, which generate daily water fluxes of the same order as monthly average fluxes. Furthermore, the GoT

contribution to the SCS freshwater fluxes has been estimated to 10% , and could therefore play an important role in terms of sediment inputs and fluxes toward the deeper parts of the open SCS. Lastly, typhoons have been identified as short-term mechanisms responsible for triggering a gulf-scale cyclonic circulation, which can reverse the summer anticyclonic circulation, inducing intense westward fluxes through the Hainan Strait, and southward fluxes along the RRD and at the GoT southern boundary.

In the next chapter, the sediment transport will be studied in link with the circulation variability and typhoon activity.

IV.7 References

- Allan R., Lindsay J., Parker D. (1996), El Niño Southern Oscillation and climate variability. CSIRO Publishing, 150 Oxford St. (PO Box 1139), Collingwood, Victoria 2066, Australia.
- Ashok K., Bahera S. K., Rao S. A., Weng H., Yamagata T. (2007) El Niño Modoki and its possible teleconnection. J. Geophys. Res., 112(C11): 1-27.
- Bao X. W., Hou Y. J., Chen C. S., et al. (2005) Analysis of characteristics and mechanism of current system on the west coast of Guangdong of China in summer. Acta Oceanol. Sin.. 24: 1-9.
- Bender M. A., Knutson T. R., Tuleya R. E., Sirutis J. J., Vecchi G. A., Garner S. T., Held I. M. (2010) Modeled impact of anthropogenic warming on the frequency of intense Atlantic hurricanes, Sciences, 327, 454-458.
- Boutin J., Vergely J.-L., Khvorostyanov D. (2018) SMOS SSS L3 maps generated by CATDS CEC LOCEAN. debias V3.0. SEANOE, http://doi.org/10.17882/52804#57467
- Boutin J., Vergely J.L., Marchand S., D'Amico F., Hasson A., Kolodziejczyk Nicolas, Reul Nicolas, Reverdin G., Vialard J. (2018) New SMOS Sea Surface Salinity with reduced systematic errors and improved variability. Remote Sensing of Environment, 214, 115-134. Publisher's official version : http://doi.org/10.1016/j.rse.2018.05.022 , Open Access version : http://archimer.ifremer.fr/doc/00441/55254/
- Burchard H., Bolding L. (2001) Comparative analysis of four second-moment turbulence closing models for the oceanic mixed layer, J. of Physical Oceanogr.,31 (8), 1943-1968, http://journal.ametsoc.org/doi/abs/10.1175/1520-0485(2001)031%3C1943:CAOFSM%3E2.0.CO%3B2
- Canuto, V., Howard, A., Cheng, Y., Dubovikov, M., 2001. Ocean turbulence.C Part I: One-point closure modelmomentum and heat vertical diffusivities. J. Phys. Oceanogr. 31, 1413–1426.
- Craig P. D., Banner M. L. (1994) Modeling wave-enhanced turbulence in the ocean surface layer. J. of Phys. Oceanogr., 24(12), 2546-2559, doi:10.1175/1520-0485(1994)024<2546:MWETIT>2.0CO;2.
- Chen C. L., Li P. L., Shi M. C., et al. (2009b) Numerical study of the tides and residual currents in the Qiongzhou Strait. Chin. J. Oceanol. Limnol.. 27: 931-942.
- Chen B., Yan J. H., Wang D. R., et al., (2007) The transport volume of water through the Qiongzhou Strait in the winter season. Period. Ocean Univ. China. 37: 357-364 (in Chinese with English abstract).
- Cheng X., Xie S.-P., Du Y., Wang J., Chen X., Wang J. (2016) Interannual-to-decadal variability and trends of sea level in the South China Sea. Clim. Dyn., 46:3113-3126, doi: 10.1007/s00382-015-2756-1.
- Chu P.C., Edmons N. L., Fan C. (1999) Dynamical mechanisms for the South China Sea seasonal circulation and thermohaline variabilities, J. Phys. Oceanogr., 29, 2971-2989.
- Chu P. C., Veneziano J. M., Fan C. W. (2000) Response of the South China Sea to tropical cyclone Ernie 1996, J. Geophys. Res., 105, 13991-14009.
- Church J. A., Foyce T. M., Price J. F. (1989) Current and density observations across the wake of Hurricane Gry, J. Phys. Oceanogr., 19, 259-265.
- Dickey T., Frye D., Mcneil J. (1998) Upper-ocean temperature response to Hurricane Felix as measured by the Bermuda Tested Mooring, Mon. Weather Rev., 126, 1195-1201.
- Ding Y. C. (2014) Observational and model studies of the continental shelf circulation and coastal trapped waves in the northern South China Sea (Doctoral Dissertation). Ocean University of China, Qingdao (in Chinese with English abstract).
- Ding Y. C., Chen C., Beardsley R. C., Bao X., Shi M., Zhang Y., Lai Z., Li R., Lin H., Viet N. T. (2013) Observational and model studies of the circulation in the Beibu Gulf, South China Sea. J. Geophys. Res.. 118: 6495-6510 https://doi.org/10.1002/2013JC009455.

- Doodson A. T. (1927) The analysis of tidal observations. Philosophical Transactions of the Royal Society of London, 227, 223-279.
- Fang G., Wang Y., Wei Z., Fang Y., Qiao F., Hu X. (2009) Interocean circulation and heat and freshwater budgets of the South China Sea based on a numerical model. Dyn. Atm. Oc., 47, 55-72, doi: 10.1016/j.dynatmoce.2008.09.003.
- Gao J. S., Chen B., He X. Y., et al. (2014b) Responses of the circulation and water mass in the Beibu Gulf to the seasonal forcing regime. Acta Oceanol. Sin., 33(7), 1-11.
- Gao J. S., Wu G., Ya H. (2017) Review of the circulation in the Beibu Gulf, South China Sea. Cont. Shelf Res.. 138: 106-119, https://doi.org/10.1016/j.csr.2017.02.009.
- Gaspar P., Gregoris Y., Lefevre J.M. (1990) A simple eddy kinetic energy model for simulations of the oceanic vertical mixing: tests at station Papa and long-term upper ocean study site. J.of Geophys. Res., 95,16179–16193.
- Gao J. S., Xue H. J., Chai F., et al. (2013) Modeling the circulation in the Beibu Gulf, South China Sea. Ocean Dyn.. 63: 979-993.
- Gille S. T. (2003) Float observations of the Southern Ocean: Part 1, Estimating mean fields, bottom velocities, and topography steering. J. Phys. Oceanogr. 33, 1167- 1181, doi: 10.1175/1520-0485(2003)033<1167:FOOTSO>2.0.CO;2 .
- Jacob S. D., Shay L. K., Mariano A. J. (2000) The 3D oceanic mixed-layer response to Hurricane Gilbert, J. Phys. Oceanogr., 4, 454-466.
- Joint Typhoon Warning Center, Annual Tropical Cyclone Report (2013), available at: https://www.metoc.navy.mil/jtwc/products/atcr/2013atcr.pdf (accessed on August 4 2019).
- Kantha L. H., Clayson C. A. (1994) An improved mixed layer model for geophysical applications, J. of Geophys. Res., 99 (C12), 25235-25266 doi: 10.1029/94JC02257.
- Hendershott M. C. (1972) The effects of solid earth deformations on global ocean tides, Geophys. J. Roy. Ast. Soc., 29, 399-402.
- Ke P. H. (1983) A preliminary analysis of currents and water exchanges in the Qiongzhou Strait. J. Trop. Oceanogr.. 2: 42-46 (in Chinese with English abstract)
- Ke P. H., Huang Q. Z., Chen F. P., Huang H. W., Feng S. Y. (1987) Preliminary analysis on the continental shelf current in northern South China Sea driven typhoon. Sci. Atmos. Sin., 11, 441-445.
- Krause P, Boyle D. P., Bäse F. (2005) Comparison of different efficiency criteria for hydrological model assessment, Adv. Geosci., 2, 89-97, doi:10.5194/adgeo-5-89-2005.
- Large W., Yeager S. (2004) Diurnal to decadal global forcing for ocean and sea-ice models: The data sets and flux climatologies, UCAR/NCAR, https://doi.org/10.5065/D6KK98Q6
- Ledwell J. R., Montgomery E. T., Polzin K. L., St. Laurent L.C., Schmitt R. W., Toole J. M. (2000) Evidence of enhanced mixing over rough topography in the abyssal ocean, Nature, 403, 179-182,
- Liu F. S., Yu T. C. (1980) Preliminary study on the oceanic circulation in Beibu Bay. Trans. Oceanol. Limnol.. 1: 9-15 (in Chinese with English abstract)
- Liu J., Cai S., Wang S. (2011) Observations of strong near-bottom current after the passage of Typhoon Pabuk in the South China Sea, J Mar. Sys., 87,102-108, doi: 10.1016/j.jmarsys.2011.02.023
- Liu Z., Yang H., Liu Q. (2001) Regional dynamics of seasonal variability in the South China Sea. J. Phys. Oceanogr.. 31: 272-284.
- Manh D. V., Yanagi T. (2000) A study on the residual flow in the Gulf of Tonkin. J. Oceanogr.. 56: 59-68. https://doi.org/10.1023/A.1011162524466.
- Mantua N. J., Hare S. R. (2002), The Pacific Decadal Oscillation. J. Oceanogr.. 58(1), 35-44.
- Marsaleix P, Auclair F., Estournel C. (2006) Considerations on Open Boundary Conditions for Regional and Coastal Ocean Models, J. Atm. Oc. Tech., 23(11), 1604-1613, doi:10.1175/JTECH1930.1.
- Marsaleix P., Auclair F., Duhaut T., Estournel C., Nguyen C., Ulses C. (2012) Alternatives to

the Robert-Asselin filter. Oc. Modell., 41, 53-66, doi: 10.1016/j.ocemod.2011.11.002.

- Marsaleix P., Auclair F., Estournel C. (2009) Low-order pressure gradient schemes in sigma coordinate models: The seamount test revisited. Oc. Modell., 30 (2-3), 169-177, doi: 10.1016/j.ocemod.2009.06.011.

- Marsaleix P., Auclair F., Floor J. W., Herrmann M. J., Estournel C., Pairaud I., Ulses C. (2008) Energy conservation issues in sigma-coordinate free-surface ocean models, Oc. Modell., 20(1), 61-89, http://dx.doi.org/10.1016/j.ocemod.2007.07.005.

- Marsaleix P., Michaud H., Estournel C. (2019) 3D phase-resolved wave modelling with a non-hydrostatic ocean circulation model. Oc. Modell. 136, 28-50, https://doi.org/10.1016/j.ocemod.2019.02.002.

- Marshall G. J. (2003) Trends in the Southern Annular Mode from observations and reanalyses. J. Clim., 16, 4134-4143.

- Metzger E. J., Hurlburt H. E. (2001) The importance of high horizontal resolution and accurate coastline geometry in modeling South China Sea inflow, Geophys. Res. Lett., 28, 1058-1062, https://doi.org/10.1029/2000GL012396

- Michaud H., Marsaleix P., Leredde Y., Estournel C., Bourrin F., Lyard F., Mayer C., Ardhuin F. (2012) Three-dimensional modelling of wave-induced current from the surf zone to the inner shelf. Oc. Sci., 8 (4), 657-681, doi:10.5194/os-8-657-2012.

- Mori N., Kato M., Kim S., Mase H., Shibutani Y., Takemi T., Tsuboki K., Yasuda T. (2014) Local amplitude of storm surge by Super Typhoon Haiyan in Leyte Gulf, Geophys. Res. Lett., 41,5106-5113, doi:10.1002/2014GL060689.

- Nash J. E., Sutcliffe J. V. (1970) River flow forecasting through conceptual models, Part I - A discussion of principles, J. Hydrol., 10, 282-290.

- North G. R., Bell T. L., Cahalan R. F., Moeng F. J. (1982), Sampling Errors in the Estimation of Empirical Orthogonal Functions. Amer. Meteor. Soc., 110: 699-706, doi: http://dx.doi.org/10.1175/1520-0493(1982)110<0699:SEITEO>1.0.CO;2.

- Piton V., Delcroix T. (2018) Seasonal and interannual (ENSO) climate variabilities and trends in the South China Sea over the last three decades. Ocean Sci. Discuss., https://doi.org/10.5194/os-2017-104.

- Qu T. (2000) Upper-layer circulation in the South China Sea. J. Phys. Oceanogr., 30, 1450-1460, https://doi.org/10.1175/1520-0485(2000)030<1450:ULCITS>2.0.CO;2.

- Qu T., Kim Y. Y., Yaremchuk M., Tozuka T., Ishida A., Yamagata T. (2004) Can Luzon transport play a role in conveying the impact of ENSO to the South China Sea?, Am. Meteorol. Soc., 17, 3644-3657, https://doi.org/10.1175/1520-0442(2004)017<3644:CLSTPA>2.0.CO;2.

- Rayner N. A., Parker D. E., Horton E. B., Folland C. K., Alexander L. V., Rowell D. P., Kent E. C., Kaplan A. (2003), Global analysis of sea surface temperature, sea ice, and night marine air temperature since the late nineteeth century. J. Geophys. Res., 108(D14): 4407, doi: 10.1029/2002JD002670.

- Roarty H., Cook T., Hazard L., George D., Harlan J., Cosoli S., Wyatt L., Alvarez Fanjul E., Terrill E., Otero M., Largier J., Glenn S., Ebuchi N., Whitehouse B., Bartlett K., Mader J., Rubio A., Corgnati L., Mantovani C., Griffa A., Reyes E., Lorente P., Flores-Vidal X., Saavedra-Matta K. J., Rogowski P., Prukpitikul S., Lee S.-H., Lai J.-W., Guerin C.-A., Sanchez J., Hansen B., Grilli S. (2019) The Global High Frequency Radar Network, Front. Mar. Sci., 6:164, doi:10.3389/fmars.2019.00164.

- Rogowski P., Zavala-Garay J., Shearman K., Terrill E., Wilkin J., Lam T. H. (2019) Air-sea-land forcing in the Gulf of Tonkin: Assessing seasonal variability using modern tools. Oceanography. 32(2): 150-161. https://doi.org/10.5670/oceanog.2019.223.

- Saji N.H., Goswami B. N., Vinayachandran P. N., Yamagata T. (1999) A dipole mode in the tropical Indian Ocean. Nature. 401:360-363.

- Schiermeier Q. (2013) Did climate change cause Typhoon Hainan?, Nature, doi: 10.1038/nature.2013.14139.

- Shi M. C., Chen C. S., Xu Q., et al. (2001) The role of Qionqzhou Strait in the seasonal variation of the South China Sea circulation. J. Phys. Oceanogr. 32: 103-121.
- Stark J.D.,Donlon C. J., Martin M. J., McCulloch M. E. (2007) OSTIA : An operational, high resolution, real time, global sea surface temperature analysis system., Oceans 07 IEEE Aberdeen, conference proceedings. Marine challenges: coastline to deep sea. Aberdeen, Scotland.IEEE.
- Sun H., Huang W., Zhao J. S. (2001) Three-dimensional numerical simulation for tide and tidal current in the Beibu Gulf. Acta Oceanologica Sinica. 23(2): 1-8.
- Tan C. H. (1987) Preliminary analysis of hydrologic structure and hydrologic feature in the sera region of the Beibu Gulf, Trans. Oceanol. Limnol., 4, 7-15.
- Trenberth K. E., Stepaniak D. P. (2001) Indices of El Niño Evolution. J. Climate., 14 : 1697-1701., doi: http://dx.doi.org/10.1175/1520-0442(2001)014<1697:LIOENO>2.0.CO;2.
- Phillipine National Disaster Risk Reduction and Management Council (2013) Final Report RE: Effect of Typhoon "Yolanda" (Haiyan). SitRep 60, NDRRMC, Quezon City, Philippines. Retrieved July 30, 2019 from: https://web.archive.org/web/20160630141736/http://ndrrmc.gov.ph/attachments/article/1329/FINAL_REPORT_re_Effects_of_Typhoon_YOLANDA_%28HAIYAN%29_06-09NOV2013.pdf
- UK Met Office. 2005. GHRSST Level 4 OSTIA Global Foundation Sea Surface Temperature Analysis. Ver. 1.0. PO.DAAC, CA, USA. Dataset accessed [2016-10-10] at http://dx.doi.org/10.5067/GHOST-4FK01.
- Vinh V.D., Ouillon S., Tanh T.D., Chu L.V. (2014) Impact of the Hoa Binh dam (Vietnam) on water and sediment budgets in the Red River basin and delta, Hydrol. Earth Syst. Sci., 18, 3987–4005, doi:10.5194/hess-18-3987-2014.
- Walker N. D., Leben R. R., Balasubramanian S. (2005) Hurricane forced upwelling and chlorophyll a enhancement within cold-core cyclones in the Gulf of Mexico, Geophys. Res. Lett., 32, doi: 10.1029/2005GL023716.
- Wang C., Wang W., Wang D., Wang Q. (2006) Interannual variability of the South China Sea associated with El Niño. J. Geophys. Res., 111: C03023, doi: 10.1029/2005JC003333.
- Wang J. F., Wang Y., Sun S. W. (2008) Tidal currents and residual currents in the southeastern Beibu Gulf in spring. The Essay Collection of the Researches on the Ocean Science in the Beibu Gulf- PT II. Ocean Press of China, pp. 47-55 (in Chinese with English abstract).
- Wang S. -Y. S., Lin Y. -H., Lee M.-Y., Yoon J. -H., Meyer J. D. D., Rasch P. J. (2017) Accelerated increase in the Arctic tropospheric warming events surpassing stratospheric warming events during winter, Geophys. Res. Lett., 44, 3806-3815, doi: 10.1002/2017GL073012.
- Wang X., Wang C., Han G., Li W., Wu X. (2014) Effects of tropical cyclones on large-scale circulation and ocean heat transport in the South China Sea, Clim. Dyn., doi: 10.1007/s00382-014-2109-5.
- Wiesner M. G., Stattegger K., Pohlmann T., Chen F., Heddaeus A., Heyckendorf K., Jechlitschek H., Lahajnar N., Liskow I., Li X., Liu Z., Lorenc S., Merfke M., Müller S., Peleo-Alampay A., Schönke M., Schwarzer K., Szczygielski A., Steen E., Unverricht D., Wang X., Welsch A., Wetzel A., Zhao Y. (2017) Cruise report RV Sonne 220 China "Land-Ocean-Atmosphere interactions in the Gulf of Tonkin", doi:10.12140/RG.2.2.12036.22406.
- Xia H. Y., Li S. H., Shi M. C. (2001) Three-D numerical simulation of wind-driven current and density current in the Beibu Gulf. Acta Oceanol. Sin.. 20: 455-472.
- Yu M.G., Liu J. F (1993) South China Sea circulation system and situation. Mar. Forecasts, 10, 13 -17.
- Yang S. Y., Bao X. W., Chen C. S. et al. (2003) Analysis on characteristics and mechanism of current system in west coast of Guangdong Province in the summer. Acta Oceanol. Sin.. 25(6): 1-8 (in Chinese with English abstract).
- Yuan S. Y., Deng J. Z. (1999) Numerical research in the circulation in the Beibu Gulf. Nanhai Yanjiu Yu Kaifa, 2, pp. 41-6 (in Chinese with English abstract).

- Zelder S. E., Dichey T. D., Doney S. C. (2002) Analyses and simulation of the upper ocean's response to Hurricane Felix at the Bermuda Tested Mooring site. J. Geophys. Res., 107, doi: 10.1029/2001JC00969.
- Zu T. T. (2005) Analysis of the current and its mechanism in the Gulf of Beibu (Master dissertation). Ocean University of China, Qingdao, (in Chinese with English abstract).

Chapter V

Conclusion and future work

Contents

Besides playing a key socio-economic role in Vietnam, the RRD constitutes the main input of freshwater and sediments to the GoT and is submitted to a large range of influences of several origins (atmospheric, oceanic, continental and anthropogenic) and scales (from daily scale to climate change). However, the responses of the RRD-GoT system to these different factors of variability are poorly understood, especially in terms of freshwater and sediment fate. In this context, the main objective of this present study was to improve our knowledge on the hydrodynamics variability of the estuary-coastal-open sea continuum and understand the impacts of this variability on the transport and fate of sediment brought by the Red River to the GoT. This objective raised the issue of representing different spatial scales (estuarine, deltaic and regional) and temporal scales (daily, tidal, seasonal, interannual) at once. To fulfill this objective, we collected and used a set of in-situ observations in the frame of this Ph.D., and implemented, calibrated, evaluated and analyzed high-resolution numerical models over our region of interest. Tidal cycle, monsoon induced variability on river discharge and on large scale circulation, long-term ENSO activity and short-term typhoon activity were identified as key mechanisms driving the hydro-sedimentary dynamics in the RRD-GoT system. The variability of this dynamics and its influences on sediment budgets, from the Red River estuary to the GoT, are summarized in the next sections.

V.1   Results summary

V.1.1   Estuarine hydro-sedimentary processes: influence of tidal and seasonal variabilities

We documented the variability of the water and sediment discharges of the third largest estuary of the Red River system, the Van Uc estuary, and the variability of the particles assemblage at seasonal and tidal scales. This work was based on four field campaigns performed in the Van Uc estuary, at the contrasting high flow and low flow seasons, for each neap and spring tides during a full diurnal cycle. Measurements were taken along cross river sections to characterize hydrological parameters and suspended particles properties, using a CTD, a hull-mounted ADCP, a LISST-100X and water samples. Results emphasized a comprehensive regime change in water and sediment discharges between high and low flow seasons (corresponding to respectively wet and dry seasons), between neap and spring tides and between high and low tides. During high-flow season, the intense water discharges induced strictly mixed estuarine conditions with very low salinities (<0.09 PSU). Only spring tides disrupted the seaward river flow by generating a flow reversal around high tides (Fig.V.1 a, b). The tidal distortion (i.e. flood tides are more energetic than ebb tides) led to

a small up-estuary sediment flux at high tide. Otherwise, sediment discharges were driven by the riverine seaward flux component. Mixing between riverine and marine waters likely developed in the bay and in coastal waters (i.e., the estuary developed in the bay). Grain size measurements revealed that riverine sediment loads were composed of primary particles (<3 µm), flocculi (6-10 µm) and microflocs (50-80 µm), which are transported by wash-load and bed-load transport.

During the low-flow season, the reduced water discharges favored a stronger along-estuary tidal intrusion, which induced estuarine conditions to transit from mixed, partly-stratified to very stratified, with salinity from a few PSU to 25 PSU. Spring tides enabled a flow reversal for half the day, while neap tides triggered a gravitational circulation (two-layer circulation) with a flow in both directions (up-estuary for the bottom layer and down-estuary for the top layer) (Fig.V.1 c,d). Saline water appeared to be composed of primary particles, flocculi and microflocs, whereas riverine water were composed of primary particles and flocculi only. Furthermore, high tides induce an up-estuary flux of suspended matter that represent 2/3 of the down-estuary flux. This fine marine sediment import in the estuary is potentially responsible for estuarine siltation.
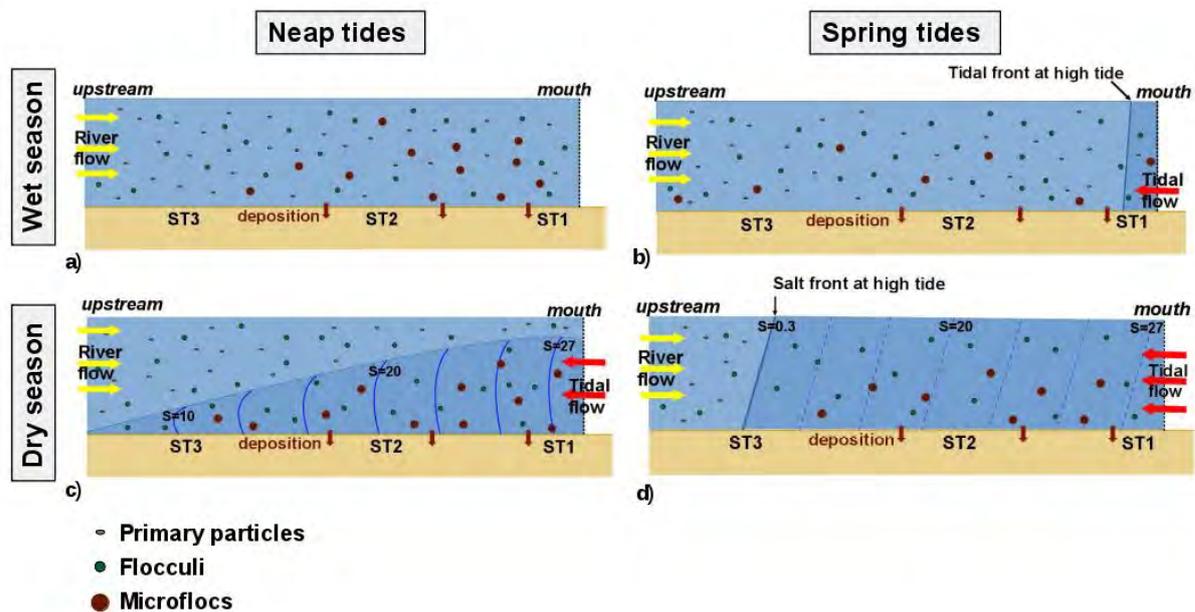
Figure V.1: Schematic representation of the Van Uc estuary during the wet (a, b) and dry season (c, d) at neap tides (a, c) and spring tides (b, d) as observed during surveys WN (a), WS (b), DN (c) and DS (d).

V.1.2 RRD-GoT hydro-sedimentary variability

Numerical modeling was chosen as a tool for addressing the issue of understanding the hydrosedimentary dynamics and variability at the scale of the GoT. The first step of the modeling work consisted in implementing a high-resolution configuration over the RRD-GoT system to satisfy

the prerequisites of modeling fine-scale hydrodynamics and sediment transport. The second step consisted in optimizing the model configuration with first, sensitivity tests of the tidal components to bathymetry and various bottom friction parameterization and second, the construction of realistic Red River distributaries and associated discharges. The third step consisted in performing simulations over the period 2009-2017 using the optimized configuration and evaluating the model performances. The fourth step consisted in investigating the GoT hydrodynamics variability at several time-scales (daily, seasonal and interannual) using the model simulations and to assess the impacts of this variability on suspended matter dynamics.

All of these steps focused on representing the hydrodynamics in the RRD-GoT, which was crucial to first investigate and understand before modeling and studying its impacts on sediment transport and budget. The final step of this work consisted in using a coupled model for sediment transport and transformation, with which preliminary tests were performed.

V.1.2.1   Configuration optimization and model evaluation

The RRD-GoT system was discretized over a bi-polar curvilinear grid which allowed a fine horizontal resolution near the RRD (150 m of resolution) and a larger resolution at the open boundary (5 km), as well as a fine vertical resolution with 20 terrain-following sigma layers. The numerical representation of the complex shorelines and shallow bathymetry of the area was improved using high-resolution shorelines and bathymetric datasets that were built from satellites images, digital elevation models and nautical charts. To satisfy the prerequisites of modelling hydro-sedimentary dynamics in macro-tidal regions, the configuration was further optimized regarding its performances in providing accurate tidal solutions. Sensitivity experiments on the bathymetry and bottom friction parameterization were performed using the frequency-domain solver available in the 2D model T-UGOm that reduced the computational cost and allowed for wider parameter explorations. Our results confirmed the importance of the bathymetry and shoreline dataset and of the choice of bottom friction parameters for the tidal representation over the GoT.

In details, results from the simulations showed that the improved bathymetry dataset allowed to reduce the errors (taking altimetry as a reference) by 40% and 25% for M2 and S2 and by 32% and 6% for O1 and K1, compared to the simulations that used a regular GEBCO dataset. In addition, tests on various parameterizations of the bottom friction (constant C_D, C_D depending on the z_0, uniform or spatially varying z_0) showed the high model sensitivity to this parameter. A regionalized z0 parameterization into three regions displayed the best tidal solutions, even though the

importance of this regionalization was mitigated since tidal solutions obtained with a uniform z_0 of 1.5×10^{-5} m showed very similar results.

Since one of the objectives of this thesis was to understand the hydro-sedimentary dynamics in the Red River estuaries, the last step of the configuration optimization consisted in constructing the rivers of the Red River system and associated discharges. The tuning of the river channels and the performances of the configuration were tested with the SYMPHONIE 3D model using several simulations performed for the year 2017, to coincide with the observations available in the Van Uc river. The model showed good efficiency in reproducing tidal dissipation along the Red River channels, and in reproducing observed water flux, temperature and salinities in the Van Uc river. After this optimization of the configuration, in terms of bathymetry, coastlines and rivers representation, we performed a SYMPHONIE simulation (SIMU) for the period 2009-2017 where the model was forced at its open boundaries by interannually varying daily atmospheric and monthly oceanic fields, and by daily river discharges. Model outputs were compared with available in-situ and satellite observations and analysis of water masses hydrological characteristics and surface circulation. These comparisons showed that SIMU reproduced correctly the seasonal, annual and interannual cycles and spatial patterns of the surface and upper layer ocean hydrological and dynamical characteristics, whose realism was improved compared to the forcing model (GOM) used at the lateral open boundaries of the configuration. SIMU could therefore be legitimately used to study the hydrodynamics variability and to be coupled with a sediment transport module (MUSTANG).

V.1.2.2   Dynamics

Results from SIMU over a 9-years period allowed to first, document the variability of the GoT surface circulation and second, determine the mechanisms behind this variability, which both remain a topic of debate in the scientific community.

Seasonal

We highlighted a summer anticyclonic surface circulation and a winter cyclonic surface circulation, with a seasonal reversal of the Hainan Strait circulation (eastward in summer and westward in winter). EOF studies revealed the leading role of the wind-driven currents over the geostrophic currents in controlling these seasonal circulation. We showed that the seasonal water fluxes followed these seasonal circulation patterns. During winter, water enters the GoT through the Hainan

Strait and south of Hainan, flows westward towards the Vietnamese coastline before flowing southward and exiting the GoT through the southwest boundary, i.e., via the coastal boundary current. During summer, water inputs mostly enter through the SW boundary, flows northward following the Vietnamese coastline before separating into two branches near the RRD: one flowing toward the southeast to exit the GoT south of Hainan Island, one following the NE Vietnamese/Chinese coastlines before exiting the GoT through the Hainan Strait. We further estimated that the GoT contributed annually to 10% of the SCS freshwater fluxes, even though its superficy represents only 5% of the total SCS superficy.

Interannual

EOF studies further revealed the leading role of the wind-driven currents over the geostrophic currents in controlling the interannual variability of the GoT surface circulation. We also showed the important role played by ENSO in influencing the interannual variability of wind, hence of the circulation. Indeed, El Niño events weakened the winter monsoon winds, potentially weakening the winter surface circulation, while they strengthened the summer monsoon winds, potentially resulting in an intensified summer surface circulation (Fig.V.2 b,e). Typhoon activity and the Arctic Oscillation variability have also been emphasized as factors driving the wind variability over the GoT, and therefore, potentially impacting the surface circulation.

Impacts of extreme events

We highlighted the importance of typhoon events on the GoT circulation and associated fluxes. Indeed, typhoons have been identified as short-term mechanisms responsible for triggering a gulf-scale cyclonic circulation, which can reverse the summer anticyclonic circulation, inducing intense westward fluxes through the Hainan Strait, and southward fluxes along the RRD and at the GoT southern boundary (Fig.V.2 c,f). Conversely during winter, typhoons are able to intensify the cyclonic circulation and generate intense water fluxes. We quantified the water fluxes generated by several typhoons and showed that they could induce daily fluxes of the same order of magnitude as monthly fluxes.
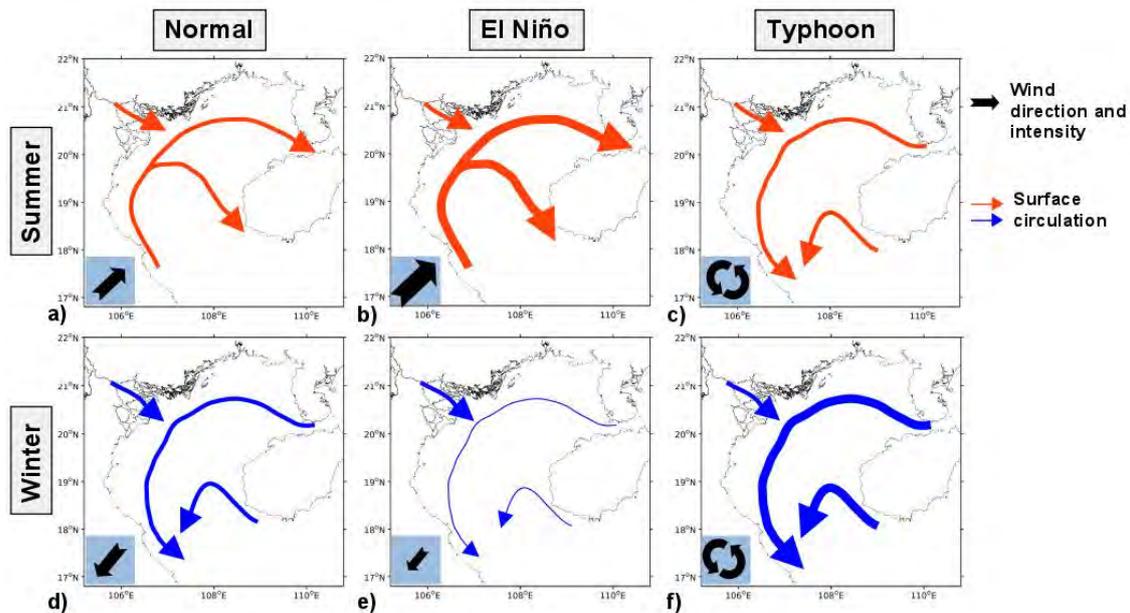
Figure V.2: Schematic patterns of the GoT seasonal circulation under normal (a, d), El Niño (b, e) and typhoon (c, d) conditions.

V.2 Perspectives

Despite improving the general knowledge of the hydro-sedimentary dynamics in the RRD-GoT system, this work showed some limitations, associated with the methodological choices we made and the data and tools that were available. Further work and studies are still necessary to better understand the functioning and variability of the hydro-sedimentary processes along the river-estuary-coastal ocean continuum in the region.

V.2.1 Suggestions for future observations

One of the biggest limitations of this Ph.D. work was the scarcity of available in-situ data, not only for understanding hydro-sedimentary processes but also for calibration and evaluation of models. A non-exhaustive list of future in-situ observations is suggested next to fulfill this gap.

ETM

The formation of a double core ETM in the Cam estuary has been identified as the principal factor responsible for the Haiphong harbor siltation (Vinh et al., 2018). Therefore, understanding the siltation processes in the Van Uc river could be of great interest for boat traffic and dredging activities. In Chapter II, we emphasized a potential ETM formation 15 km upstream from the Van Uc river mouth during the dry season. The ETM characteristics (mechanisms of formation, location and variability) of the Van Uc estuary could be studied with along river transects measurements of

salinity, SPM concentration and PSD, collected during the dry season at high tides.

Disaggregation

In link with ETM observations and in order to assess the importance of aggregation processes in the ETM formation, the absolute particle size distribution (APSD) could be measured. This would allow to obtain the fraction of flocs present in the water column and to understand their compositions. Opposite to the effective particle size distribution (EPSD) measurements that have to be performed in-situ (with laser based technology devices), the APSD, which consists in the disaggregation of flocs into individual particles, is performed in the laboratory using solutions of sodium pyrophosphate and laser sizer technology (Mikkelsen and Perjup, 2000).

Organic matter content

The estimations of organic matter content of SPM measurements by filtration on GF/F filters have failed during the Van Uc river campaigns (Chapter II) due to a dysfunction of the laboratory oven. However, information on the content of organic matter in the Van Uc estuary, and in the other estuaries of the Red River, would help quantify the importance of organic matter, SPM concentration or salinity gradient on flocculation processes in the estuaries. This measurement should therefore be considered in future field campaigns.

Plume dynamics

Future observations should focus on the RRD plume area since its variability in terms of extent and sediment processes is poorly documented in both dry and wet season and since results from Van Uc campaigns suggested that the mixing between riverine and marine waters are likely to happen in the plume area during the wet season. The Van Uc river plume dynamics and variability could be studied with hydrodynamics and particle properties measurements along a cross shelf section from the river mouth to offshore, completed with two transverse sections parallel to the shore as suggested in Fig.V.3. Campaigns should be carried out at different seasons and at different tidal regimes. As the area is subjected to waves, these campaigns require the use of a hull boat rather than the flat-bottom boat (which was used for the surveys in Chapter II).

Seabed composition

One of the biggest challenges and limitations for sediment modeling studies in the RRD-GoT system is the lack of data of the seabed composition for both model initialization and evaluation. In-
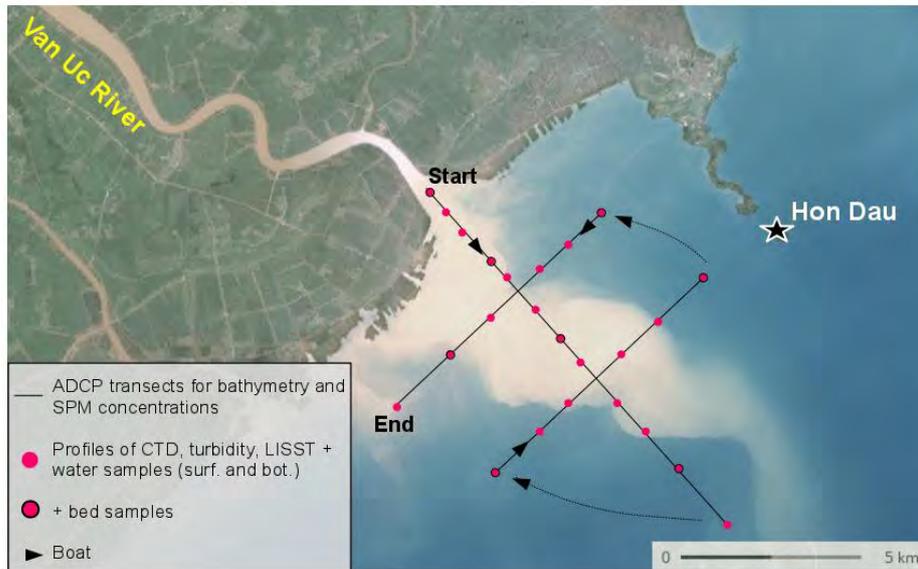
Figure V.3: Boat trajectories and sampling stations of potential future field campaigns in the Van Uc river's plume.

deed, for modeling sediment dynamics, knowledge of the bottom composition is crucial as rates of erosion and consolidation highly depends on the bed composition. This gap needs to be filled in order to improve the initial conditions prescribed to sediment models and to evaluate the model outputs. For that, dedicated campaigns should be considered both in the estuary and plume area as well as all over the basin. For example, samples of the surficial bed could be collected during the above mentioned campaigns in the Van Uc estuary and along the plume (see Fig.V.3 for potential bed sampling stations). At the scale of the basin, dedicated campaigns should be considered in order to confirm the seabed map proposed by the Atlas of Natural Conditions and Environments of Vietnam Sea and Adjacent Area (published in Vietnamese in 2007).

Bathymetry

A general effort in collecting and distributing bathymetric data should be made all over the RRD-GoT system. Due to the difficulty of bathymetric measurements in areas of intense boat traffic and dredging activities and due to the restricted access to existing data, bathymetric data are particularly lacking in the estuaries of the Red River, in Ha Long Bay and in the very near coastal regions. These shallow regions are however key regions for hydro-sedimentary processes where bathymetric uncertainties can largely impact the representation of currents and associated shear stress.

For hydrodynamics evaluation

In Chapter IV, a SMOS product was used to evaluate SYMPHONIE's ability to reproduce the observed seasonal, annual and interannual SSS cycles and spatial fields. The relevance of this product in representing accurate SSS patterns at scales of interest can be discussed as its resolution of about 45 km can only depict large changes across the GoT basin. As a consequence of its resolution, SMOS SSS between the coastline and 45 km offshore are blanked out by its land-sea mask, limiting the observation of the Red River plume. Future products using a combination of SMOS (2010-) with Aquarius (2011-2015) and SMAP (2015-) L-band radiometers provided by the ESA (European Space Agency) SSS CCI (Climate Change Initiative) should provide better quality SSS fields over the GoT but will not increase its resolution. However, the SMOS HR (High-Resolution) project (in its CNES phase 0) would maintain the continuity of L-band measurements while increasing the spatial resolution to 15 km and thus provide data closer to the coast. Therefore, considering these products for future model evaluation should help evaluate the model's performance in terms of SSS. In addition, SYMPHONIE model evaluation in reproducing accurate vertical structures of temperature and salinity was very limited due to the lack of available data for comparisons. In the region, deployments of autonomous profilers (gliders, Argo floats) for collecting such data is not considered, due to intense fisheries activities and boat traffic that could intercept the profiler trajectory, and due to local authorities permissions. Therefore, dedicated cruise campaigns should be considered.

V.2.2   Suggestions for future modeling work

V.2.2.1   Configuration improvements

Despite showing good results in terms of representation of hydrodynamical processes compared to observations, further developments in our SYMPHONIE configuration could be made to improve the realism of its outputs.

First of all, bathymetry remains a crucial parameter for hydrodynamical modeling. In our SYMPHONIE configuration, more detailed representation of the channel bathymetric profiles should be considered for future studies. Indeed, six out of the seven distributaries of the Red River system were constructed as simple channels as their respective bathymetric profiles were unknown (see Chapter IV). Adjusting the bathymetry of these channels, at least in the estuarine parts, could improve the realism of the currents within the channel and therefore of estuarine dynamics. Such improvements would allow to study the variability of estuarine dynamics among the different distributaries of the Red River.

Second, the representation of the Van Uc estuary could also be improved. In Chapter II we have seen that the Luoc river, which flows into the Van Uc river at 20 km upstream of the river mouth, is potentially responsible for the water discharge increases observed between ST3 and ST2. Adding the Luoc river to the configuration could help verify this hypothesis and allow a better representation of the Van Uc river discharges.

Third, the water discharges prescribed to the rivers that are not part of the Red River system (i.e. rivers represented as single grid point) should be prescribed more accurately. In Chapter IV, we emphasized the importance of prescribing accurate daily river discharges to the SSS representation in the RRD coastal area. Even though the Red River system is the main source of freshwater to the GoT, the impacts of prescribing accurate daily water discharges (rather than climatological discharges) to the seven other rivers that feed the GoT should be studied in terms of SSS and vertical mixing.

Lastly, taking waves into account in an ocean circulation model allows a better representation of currents during storm events in nearshelf zones (Michaud et al., 2012 & 2013). Therefore, considering the coupling of SYMPHONIE with the WWIII wave generation and propagation model (Tolman, 2009) could improve the simulated circulation. Such coupling has already been done for a SYMPHONIE configuration over the Gulf of Lions (Mikolajczak, 2019). Results of Mikolajczak (2019) indicated that the waves impacted mostly the very near coastal areas and that the presence of waves allowed a better vertical representation of the currents, compared to a simulation without waves. Therefore, a SYMPHONIE configuration including waves representation could also impact the shallow nearshore transport of sediments along the RRD.

V.2.2.2   Preliminary tests with the coupled model SYMPHONIE-MUSTANG and suggestions of future work

Due to lack of time, only preliminary tests were performed on the sensitivity of the module MUS-TANG to the erosion parameterization, to the settling velocities of particles and to the seabed composition. The module description and the choice of parameterization and initialization for these tests are presented in Appendix A. The impacts of the parameterization of the critical shear stress for erosion (τ_{cr}) on surface SPM concentrations along the RRD in a "mud only" environment were first assessed. 6 simulations (simulation #1 to #6, see Table A.4 in Appendix A) of 5-months (April-August 2009) using different set of particles (set-1: fast settling velocities; set-2: slow settling velocities) and different values of τ_{cr} (0.2, 0.35 and 0.5 N m^{-2}) are compared to satellite observations

and are presented in Fig.V.4. Results of these simulations first indicate that the module is both sensitive to crvalues and to the settling velocities of particles. Indeed, increasing values of τ_{cr} induced decreases of SPM surface concentrations along the RRD in all simulations, due to an increase of erosion limitation with increasing τ_{cr} values (Fig.V.4 b-g). Simulations performed with particles of set-2 (i.e. slow settling velocities) (Fig.V.4 c,e,g) showed patterns of SPM of higher values and further westward extends than the SPM patterns obtained with the simulations performed set-1(Fig.V.4 b,d,f). This indicates that the water column is preferentially composed of microflocs and flocculi that settle fast (0.24 and 0.052 mm s^{-1}, respectively) rather than microflocs and flocculi with slower settling velocities (0.13 and 0.023 mm s^{-1}, respectively).

Second, results from simu #3 showed the closest SPM concentrations and patterns to the observation, even though some discrepancies remained. The simulation overestimates the SPM concentrations of the Ba Lat river plume and along Hai Hau beach, but slightly underestimates the concentrations in front of the Van Uc river.

Based on these results, we wanted to assess the impact of sand on erosion and resuspension episodes. Taking the parameterization of simu #3, we performed 2 other simulations with modified seabed composition by adding 20% of sand (seabed-2) and 50% of sand (seabed-3) (Table A.3 in Appendix A) (Fig.V.5).

Results from simu #7 and simu #8 emphasized the sensitivity of the model to the seabed composition and suggest that resuspension of particles is limited with increasing sand content. These results show however large discrepancies with the observations (Fig.V.4 a). The simulations underestimate the SPM concentrations in the plume areas and largely overestimate the concentration in the bay, south of Hai Hau beach. In the light of these results, many more tests on the model parameterization and improvements of the configuration are to be considered for numerically studying the sediment in the RRD-GoT system. This could constitute the work of a future Ph.D and a list of research suggestions is proposed next.

Seabed and water column initialization

Even though we dispose of very few sediment bottom data, it is likely to expect that the bottom substrate is composed not only of mud, but of sand and coarser particles, since sandy beaches are observed along the RRD. Therefore, future simulations should include realistic initial sediment bottom conditions, at least in the coastal area where sandy beaches are known to exist. This sand
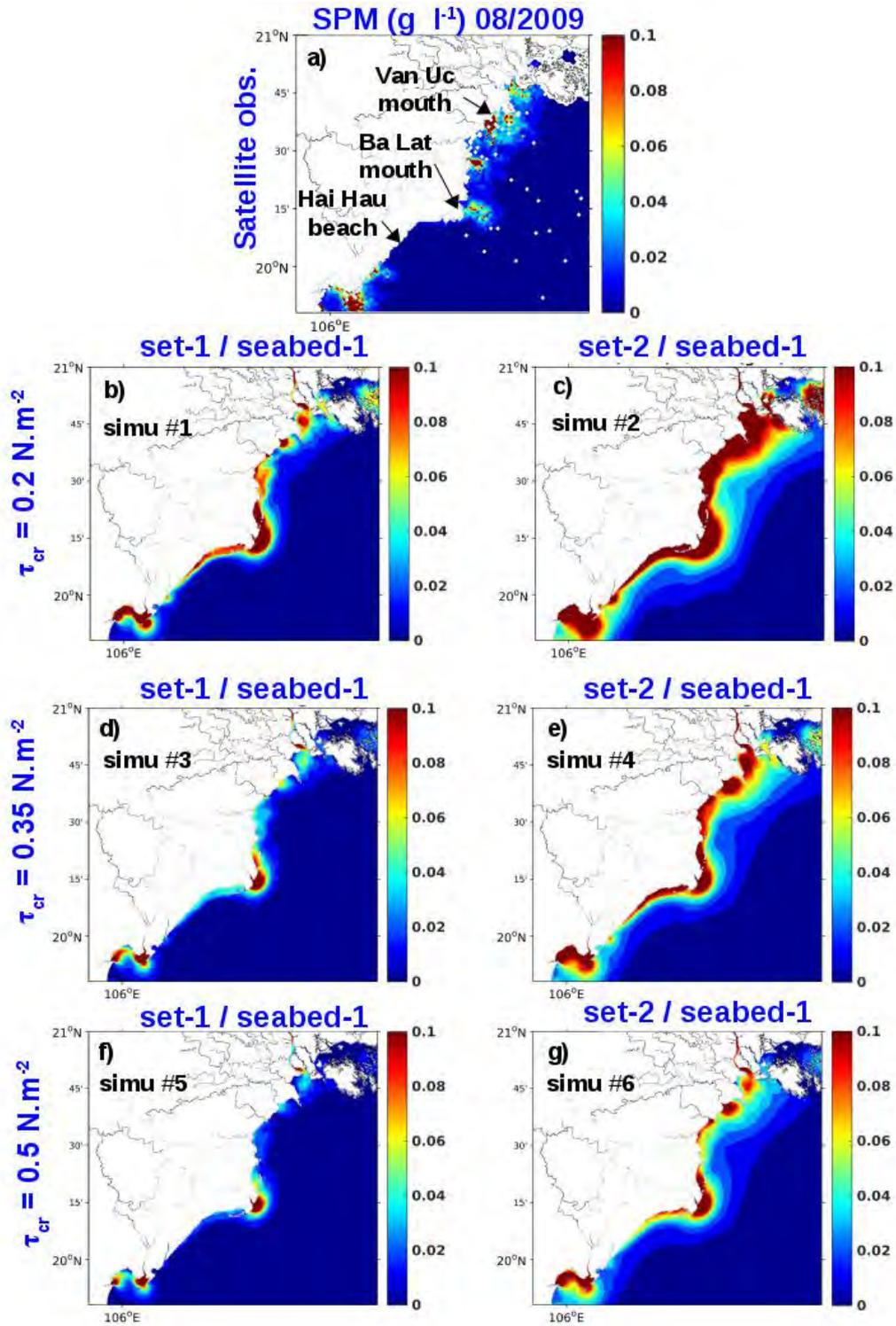
Figure V.4: Monthly mean surface SPM concentrations (g l^{-1}) of August 2009 from satellite observations (a) and from simulation #1 to #6 (b-g).
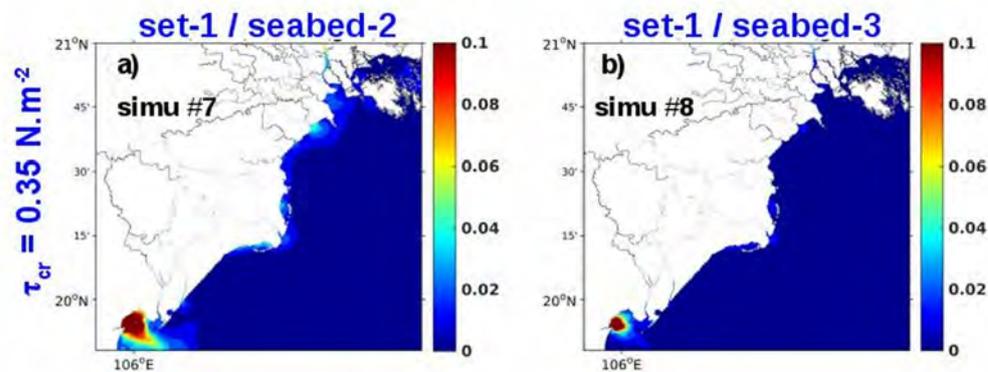
Figure V.5: Monthly mean surface SPM concentrations (g l^{-1}) of August 2009 from simu #7 (a) to #8 (b).

input could be crucial on erosion/accumulation patterns since previous experiments have shown that the resistance to erosion increases when sand is added to mud (Partheniades 1965; McCave 1984; Ockenden and Delo 1988; Mitchener and Torf 1996; Ahmad et al. 2011). Furthermore, patterns of erosion and deposition also largely depend on the sediment in the water column and of its associated settling velocities. Therefore, the composition of the water column prescribed to the module should be improved with in-situ observations.

Flocculation

Flocculations processes are crucial in fine sediment cycle within estuaries and plumes and can explain most of the sedimentation of fine sediments (Gibbs, 1985; Van Leussen, 1994; Dyer and Manning, 1999). In MUSTANG, this process is usually taken into account through an empirical relationship between the settling velocity of mud and the suspended concentration of mud, multiplied by a function of turbulence (Le Hir et al., 2011). In this study however, the flocculation process was not activated. In future studies, taking this process into account should be considered and impacts on deposition of particles should be assessed

Parameterization

In this preliminary study with the coupled SYMPHONIE-MUSTANG model, only few parameterizations were tested. More tests should be performed to determine the best parameterization in terms of erosion, resuspension and deposition. For example, the sensitivity of the model to the erodibility parameter E_0 (for sand and mud), to the different formulations of the erosion transition trends between sand and mud (linear or exponential) and to the critical shear stress for depo-

sition (τ_d) should be tested. Furthermore, the sediment discharge inputs were prescribed at the first grid point of each river channel. This therefore enabled the particles to deposit all along the channel which potentially decreased the SPM concentrations before the riverine water reached the river mouth. Limiting the particles deposition along the river channels could influence the plume patterns and should be considered in future studies.

Online retroactions

In this study, MUSTANG was considered as a module integrated to SYMPHONIE, which can be, or not, activated. In details, SYMPHONIE provided the hydrodynamical conditions necessary to MUSTANG at each time step. This methodology however excludes the possibility of retroactions of the sediment module outputs on the hydrodynamical model, i.e. SYMPHONIE does not take into account any changes in morphology or water column composition that could be induced by the sediment model. However, bathymetric changes in the RRD shallow area induced by erosion/deposition could influence current intensities and shear stress. In addition, large sediment concentrations in the water column induced by resuspension or river inputs could influence the water mass density. For more realistic simulation, future studies should therefore integrate retroactions of the sediment module on the hydrodynamics.

Suggestions for future modeling studies

Finally, the SYMPHONIE model configuration implemented in this Ph.D. study can also be used to study other processes in the GoT. For example, the Ph.D. of D.T. Nguyen that started in October 2018, aims at analyzing the sensitivity of the freshwater plume to small perturbations of the forcing fields by running ensemble simulations. Once improved and evaluated, the coupled configuration SYMPHONIE-MUSTANG could be used to study:

- the variability of the coastal boundary current and its role in sediment transport;

- the role of extreme events, like storms and typhoons, on erosion and sediment transport;

- the spread of the Red River plume into the GoT in terms of suspended matter and assess the seasonal and interannual variability of the matter fluxes in link with the water fluxes observed in Chapter IV;

- the influence of different wave regimes in the coastal resuspension and morphological changes;

- the role of tides in the vertical mixing of sediments south-west off Hainan island;

- the sediment model outputs could be used to improve the accuracy of the suspended matter inputs of the currently on-going coupled physical-biogeochemisty studies in the SCS (with SYMPHONIE-Eco3m-s) (Ph.D. of Trinh Bich Ngoc and Ph.D. of To Duy Thai).

These suggestions for future research lie at the core of the LOTUS (Land-Ocean-aTmosphere regional coUpled System) mixed international laboratory based at the University of Science and Technology of Hanoi which federates IRD (Institut de Recherche pour le Développement) researchers from Vietnamese and French institutes. The modeling work and in-situ campaigns suggested in this Chapter could be carried out under this frame.

V.2.3 References

- Ahmad M.F., Dong P., Mamat M., et al. (2011) The critical shear stresses for sand and mud mixture, Appl. Math. Sci., 5, 53-71,
- McCave I.N. (1984) Erosion, transport and deposition of fine-grained marine sediments. Geolological Society, London, Special Publications, 15, 35-69.
- Michaud H., Leredde Y., Estournel C., Berthebaud E., Marsaleix P. (2013) Modeling and in-situ measurements of intense currents during a winter storm in the Gulf of Aigues-Mortes (NW Mediterranean Sea), Comptes Rendus Geosciences, 345 (9-10), 361-372, doi: 10.1016/j.crte.2013.07.001.
- Michaud H., Marsaleix P., Leredde Y., Estournel C., Bourrin F., Lyard F., Mayet C., Ardhuin F. (2012) Three-dimensional modelling of wave-induced current from the surf zone to the inner shelf, Ocean Sci., 8(4), 657-681, doi: 10.5194/os-8-657-2012.
- Mikkelsen O.A., Pejrup M. (2000) In situ particle size spectra and density of particle aggregates in a dredging plume, Mar. Geol., 170, 443-459, https://doi.org/10.1016/S0025-3227(00)00105-5
- Mikolajczak G. (2019) Dynamique de l'eau et des apports particulaires originaires du Rhône sur la marge continentale du Golfe du Lion, Ph.D. Thesis, University of Toulouse 3 Paul Sabatier.
- Mitchener H., Torfs H. (1996) Erosion of mud/sand mixtures. Coast. Engineer., 29, 1-25, https://doi.org/10.1016/S0378-3839(96)00002-6.
- Ockenden M. C., Delo E. (1988) Consolidation and erosion of estuarine mud and sand mixtures - an experimental study, HR Wallingford Report No. SR 149.
- Partheniades E. (1965) Erosion and deposition of cohesive soils. J. Hydraul. Div. 91, 105-139.
- Tolman H. L. et al. (2009) User manual and system documentation of WAVEWATCHIII ™ version 3.14, Technical note, MMAB Contribution, 276, https://nopp.ncep.noaa.gov/mmab/papers/tn276/MMAB_276.pdf
- Vinh, V.D., Ouillon S., Uu D.V. (2018) Estuarine Turbidity Maxima and Variations of Aggregate Parameters in the Cam-Nam Trieu Estuary, North Vietnam, in Early Wet Season, Water, 68, 1-33, doi: 10.3390/w10010068.

Conclusion générale

Objectifs

Le Delta du Fleuve Rouge (DFR) joue un rôle socio-économique clé pour le Vietnam et représente le principal apport d'eau douce et de sédiments au GdT et est soumis à un large éventail d'influences de plusieurs origines (atmosphérique, océanique, continentale et anthropogénique) à différentes échelles de temps (de l'échelle journalière à celle du changement climatique). Les réponses du système DFR-GdT à ces différents facteurs de variabilité sont cependant mal comprises, en particulier concernant le devenir de l'eau douce et des sédiments apportés par le Fleuve Rouge.

Dans ce contexte, l'objectif principal de cette thèse a été d'améliorer les connaissances sur la variabilité hydrodynamique du continuum estuaire-océan côtier et de comprendre les influences de cette variabilité sur le transport et sur le devenir des sédiments apportés par le Fleuve Rouge vers le GdT. Cet objectif a soulevé la question de la représentation, à la fois, des différentes échelles spatiales (estuarienne, deltaïque et du golfe) et des différentes échelles temporelles (journalière, cycle de marée, saisonnière, interannuelle). Pour atteindre cet objectif, nous avons utilisé des observations *in-situ* collectées pendant ce doctorat ainsi que des sorties de modèle numérique à haute résolution (modèle qui a préalablement été implémenté, calibré et validé pour la zone d'étude).

Les cycles de marée, la variabilité induite par la mousson sur le débit fluvial et sur la circulation à grande échelle, la variabilité interannuelle d'ENSO et les événements courts et extrêmes comme les typhons ont été identifiés comme des mécanismes clés dans le contrôle de la dynamique et du transport sédimentaire du système DFR-GdT. La variabilité de ces mécanismes et leurs influences sur la dynamique hydro-sédimentaire, de l'estuaire du Fleuve Rouge au GdT, sont résumées dans les sections suivantes.

Influences de la marée et de la variabilité saisonnière sur la dynamique hydro-sédimentaire de

l'estuaire

Nous nous sommes tout d'abord intéressés à documenter la variabilité de la dynamique estuari-
enne et son influence sur le transport et sur les processus sédimentaires à l'échelle des cycles de
marée et des cycles saisonniers. La variabilité des débits d'eau et de sédiments du troisième plus
grand estuaire du Fleuve Rouge et la variabilité de son assemblage particulaire ont en particulier
été étudiées. Ce travail s'est basé sur quatre campagnes de terrain réalisées dans l'estuaire de la riv-
ière Van Uc, au cours des saisons contrastées de crues et d'étiage, pour chaque marée de mortes-
eaux et de vives-eaux, pendant un cycle diurne complet. Les mesures ont été réalisées le long
de sections transverses au cours de la rivière, pour caractériser les paramètres hydrologiques et les
propriétés des particules en suspension, à l'aide d'une CTD, d'un ADCP de coque, d'un LISST-100X
et d'échantillons d'eau.

Les résultats de ces mesures ont mis en évidence de fortes variations dans le régime de débits
d'eau et de sédiments entre les saisons de crues et d'étiage (respectivement, la saison des pluies
et la saison sèche), ainsi qu'entre les marées de vives-eaux et mortes-eaux et entre marée haute et
marée basse.

Pendant la saison des crues, les forts débits ont favorisé un estuaire strictement mélangé, avec des
salinités très faibles (<0,09 PSU). Seules les marées de vives-eaux sont parvenues à perturber le
débit fluvial en générant une inversion du courant à marée haute (voir Fig. VI.1 a, b). L'asymétrie
de la marée (c.-à-d. le flot est plus énergétique que le jusant) a entraîné, à marée haute, un flux de
sédiments vers l'amont de l'estuaire. Le reste du temps„ les débits sédimentaires ont été dominés
par la composante fluviale, c.-à-d., un flux allant de l'estuaire vers l'océan. Le mélange entre les
eaux douces de rivière et les eaux salées océaniques a alors probablement eu lieu dans la baie (c.-
à-d. à l'extérieur de l'estuaire). Les mesures de la taille des particules en suspension ont révélées
que l'assemblage des sédiments fluviaux était principalement composé de particules primaires
(<3 μm), de flocculi (6-10 μm) et de microflocs (50-80 μm), qui ont été transportés par lessivage et
charriage.

Pendant la saison d'étiage, l'affaiblissement des débits fluviaux a permis des intrusions d'eaux
salées par la marée, tout le long de l'estuaire, générant des conditions estuariennes variant de
mélangées à partiellement stratifiées et à très stratifiées, avec des salinités allant de quelques PSU
à ~ 25 PSU. Les marées de vives-eaux ont permis d'inverser le sens d'écoulement fluvial de l'eau
et des sédiments (pendant la moitié de la journée, aux alentours de marée haute), tandis que

les marées de mortes-eaux ont déclenché une circulation gravitationnelle (circulation bi-couche) avec un écoulement dans les deux directions (vers l'amont pour la couche inférieure et vers l'aval pour la couche supérieure) (voir Fig. VI.1 c, d). L'assemblage particulaire de ces eaux salées était constitué de particules primaires, de flocculi et de microflocs, tandis que celui des eaux fluviales était seulement constitué de particules primaires et de flocculi. Nous avons également montré que les marées hautes ont pu générer des flux de matière en suspension (MES) vers l'amont de l'estuaire, représentant jusqu'à 2/3 du flux vers l'aval de l'estuaire. Cette importation de sédiments fins d'origine marine dans l'estuaire a été identifiée comme potentiellement responsable de l'envasement de celui-ci.

Variabilité hydro-sédimentaire à l'échelle du DFR-GdT

Dans un second temps, la modélisation numérique a été choisie comme outil pour aborder la question de la compréhension de la dynamique et de la variabilité hydro-sédimentaire à l'échelle du GdT. La première étape de ce travail de modélisation a consisté à implémenter une configuration à haute résolution dans le système DFR-GdT afin de satisfaire aux pré-requis de la modélisation à fine échelle du transport sédimentaire. La deuxième étape a consisté à optimiser la configuration du modèle avec, d'une part, des tests de sensibilité réalisés sur les composantes de la marée par rapport à la bathymétrie et à diverses paramétrisations du frottement de fond et, d'autre part, à la construction des différentes rivières du Fleuve Rouge avec des débits associés réalistes. La troisième étape du travail de modélisation a consisté à réaliser des simulations sur la période 2009-2017 en utilisant la configuration optimisée et à évaluer les performances du modèle. La quatrième étape a consisté à étudier la variabilité hydrodynamique du GdT à plusieurs échelles temporelles (journalière, saisonnière et interannuelle) à l'aide des sorties du modèle et à évaluer l'influence de cette variabilité sur la dynamique des MES.

Toutes ces étapes ont donc été dédiées à l'hydrodynamique dans le DFR-GdT, qu'il était crucial de représenter et de comprendre avant de pouvoir modéliser et étudier son influence sur les transports et les bilans sédimentaires. La dernière étape de ce travail a consisté à utiliser un modèle couplé dédié au transport et à la transformation des sédiments, avec lequel des essais préliminaires ont été réalisés.

A) **Optimisation de la configuration**

Le système DFR-GdT a été discrétisé sur une grille curviligne bipolaire permettant une ré-

solution horizontale fine près du DFR (~ 150 m de résolution) et plus large aux frontières ouvertes (~ 5 km), ainsi qu'une résolution verticale fine avec 20 couches sigma. La représentation de la complexité de la topographie des côtes et de la bathymétrie peu profonde de la région a été améliorée grâce à une nouvelle base de données haute-résolution construite à base d'images satellites, de modèles numériques de terrain et de cartes marines à haute résolution.

Pour satisfaire aux conditions préalables pour la modélisation de la dynamique hydro-sédimentaire dans les régions macro-tidales, la configuration a été optimisée en terme de performances à fournir des solutions de marée précises. Des tests de sensibilité sur la bathymétrie et sur la paramétrisation du frottement du fond ont été effectués à l'aide du modèle 2D T-UGOm qui, avec des coûts de calcul réduits, permet d'explorer un large éventail de paramétrisations. Nos résultats ont confirmé l'importance d'une bathymétrie réaliste et de la paramétrisation du frottement de fond pour la représentation de la marée dans le GdT.

En détail, les résultats des simulations ont montré que notre base de données bathymétrique "améliorée" a permis de réduire les erreurs (en prenant l'altimétrie comme référence) de 40% et 25% pour M2 et S2 et de 32% et 6% pour O1 et K1, par rapport aux simulations utilisant une bathymétrie GEBCO. De plus, des tests avec différentes paramétrisations du frottement de fond (C_D constant, C_D fonction du z_0, z_0 uniforme ou variant dans l'espace) ont montré la forte sensibilité du modèle à ce paramètre. Une paramétrisation avec un z_0 régionalisé sur trois régions a montré de meilleures solutions de marée, même si l'importance de cette régionalisation a été nuancée par le fait que les solutions de marée obtenues avec un z_0 uniforme de $1,5 \times 10^{-5}$ m ont donné des résultats très semblables.

Puisque l'un des objectifs de cette thèse était de comprendre la dynamique hydro-sédimentaire des estuaires du Fleuve Rouge, la dernière étape dans l'optimisation de la configuration a consisté à construire les différentes rivières du réseau et à déterminer leurs débits associés. L'optimisation des canaux et les performances de la configuration ont été testés avec plusieurs simulations du modèle 3D SYMPHONIE réalisées pour l'année 2017, afin de comparer nos résultats avec les observations disponibles dans la rivière Van Uc. Le modèle a prouvé sa capacité à reproduire la dissipation de la marée le long des canaux du Fleuve Rouge ainsi qu'à reproduire le réalisme des débits d'eau, des températures et des

salinités mesurés dans la rivière Van Uc.

Suite à l'optimisation de la configuration, nous avons réalisé une simulation SYMPHONIE (appelée SIMU) pour la période 2009-2017 pendant laquelle le modèle a été forcé à ses frontières ouvertes par des champs atmosphériques et océaniques et par des débits de rivières journaliers. Cette simulation a été comparée à des observations *in-situ*, à des images satellites et à des analyses représentant les caractéristiques hydrologiques des masses d'eau et de la circulation en surface. Ces comparaisons ont montré que SIMU reproduisait correctement les cycles saisonniers, annuels et interannuels et les caractéristiques spatiales des masses d'eau et de la circulation de surface. SIMU était, en outre, plus réaliste que le modèle forçant (GOM) utilisé aux frontières latérales ouvertes de la configuration. SIMU a donc été légitimement utilisée pour étudier la variabilité hydrodynamique du GdT et le couplage à un module de transport de sédiments (MUSTANG) a pu être considéré.

B) **Dynamique**

SIMU a permis, d'une part, de documenter la variabilité de la circulation de surface du GdT et, d'autre part, de déterminer les mécanismes à l'origine de cette variabilité, qui sont actuellement des sujets de débats au sein de la communauté scientifique.

Concernant la circulation saisonnière, nous avons mis en évidence une circulation de surface anticyclonique en été et une circulation de surface cyclonique en hiver, avec un renversement saisonnier de la circulation dans le détroit de Hainan (vers l'Est en été et vers l'Ouest en hiver). Des analyses en EOF ont révélé le rôle dominant des courants d'Ekman, comparés aux courants géostrophiques, dans le contrôle de cette circulation saisonnière. Nous avons montré que les flux saisonniers d'eau suivaient les structures de circulations saisonnières. En hiver, l'eau entre dans le GdT par le détroit de Hainan et par le Sud de l'île d'Hainan, puis s'écoule vers l'Ouest en direction de la côte Vietnamienne avant de s'écouler vers le Sud et de quitter le GdT par la frontière Sud-Ouest du bassin, c'est-à-dire par le courant de bord Ouest. En été, les apports d'eau se font principalement par la frontière Sud-Ouest du bassin, puis l'eau s'écoule vers le Nord le long de la côte Vietnamienne avant de se séparer en deux branches près de DFR: une branche s'écoulant vers le Sud-Est pour sortir du GdT au sud de l'île d'Hainan, l'autre suivant les côtes Nord-Vietnamiennes et Chinoises avant de quitter le GdT par le détroit d'Hainan.

Nous avons de plus estimé que le GdT contribue annuellement à environ 10 % des flux d'eau douce

de la MCM, même si la superficie de celui-ci ne représente qu'environ 5 % de la superficie totale de la MCM.

Concernant la variabilité interannuelle, des analyses en EOF ont également révélé le rôle dominant du transport d'Ekman, comparés aux courants géostrophiques, dans le contrôle de la variabilité interannuelle de la circulation de surface du GdT. Nous avons aussi montré le rôle important joué par ENSO dans l'influence de la variabilité interannuelle du vent, et donc de la circulation de surface. En effet, nous avons vu que les événements El Niño pouvaient affaiblir les vents de mousson d'hiver et donc potentiellement la circulation de surface en hiver, tandis qu'ils pouvaient renforcer les vents de mousson d'été, entraînant potentiellement une intensification de la circulation de surface en été (Fig. V.2 b, e). Une forte saison de typhons ainsi que la variabilité de l'Oscillation Arctique ont également été mis en évidence comme mécanismes pouvant contrôler la variabilité du vent dans la région du GdT et, par conséquent, pouvant influencer la circulation de surface.

Finalement, concernant la variabilité journalière, nous avons souligné l'importance des événements extrêmes, comme les typhons, sur la circulation du GdT et sur les flux d'eau associés. En effet, les typhons ont été identifiés comme des mécanismes à court terme responsables du déclenchement d'une circulation cyclonique à l'échelle du Golfe, pouvant inverser la circulation anticyclonique établie en été, induisant des flux intenses vers l'Ouest à travers le détroit d'Hainan, et des flux vers le Sud s'écoulant le long du DFR (figure V.2 c, f). Inversement, en hiver, nous avons montré que les typhons sont capables d'intensifier la circulation cyclonique et de générer d'intenses flux d'eau. Nous avons également quantifié les flux d'eau générés par plusieurs typhons et montré qu'ils pouvaient induire des flux journaliers du même ordre de grandeur que des flux mensuels.

Dans la section suivante, des perspectives de recherche pour la modélisation couplée hydro-sédimentaire sont proposées, basées sur des expériences préliminaires réalisées avec le module sédimentaire MUSTANG. Il est à noter que ces résultats sont présentés dans le Chapitre V et en Appendix A, et que des perspectives de travail portant sur des observations de terrain et sur l'amélioration de la configuration SYMPHONIE sont également proposées dans le Chapitre V.

Perspectives pour la modélisation du transport sédimentaire

Faute de temps, seuls des tests préliminaires ont été réalisés sur la sensibilité du module MUS-

TANG à la paramétrisation de l'érosion, aux vitesses de chute des particules et à la composition du fond marin. La description du module ainsi que les choix de paramétrisation et d'initialisation faits pour ces tests sont présentés en annexe A.

Ces premiers tests ont montré que la colonne d'eau dans la région du DFR serait principalement composée de flocculi et de microflocs, ayant des vitesses de chutes de 0.24 et 0.052 mm s^{-1} respectivement, et qu' une valeur de 0.35 N m^{-2} attribuée à τ_{cr} permettrait une meilleure représentation des processus d'érosion et de remise en suspension. La composition du sédiment de fond semble aussi être importante dans la représentation de la MES le long du DFR, puisque l'ajout de sable (en différentes proportions), a changé les structures de MES de surface.

Ces résultats préliminaires suggèrent que de nombreux autres tests sur le paramétrisation du module et sur l'amélioration de la configuration sont à envisager pour la modélisation du transport sédimentaire dans le système DFR-GdT. Cela pourrait constituer le travail d'un futur doctorat et des suggestions d'amélioration et des pistes de recherche sont proposées ci-après:

- **Initialisation de la colonne d'eau et du sédiment de fond**.

Même si très peu de données sont disponibles sur la composition du sédiment de fond dans la zone, il est probable que le substrat du fond soit composé, en plus de vase, de sable et de particules plus grossières, puisque des plages de sable existent le long du DFR ainsi que dans la baie d'Ha Long. De ce fait, les futures simulations devraient inclure des conditions initiales réalistes du sédiment de fond, au moins dans les zones côtières où ces plages existent. Cet ajout de sable pourrait être crucial pour les structures d'érosion/accumulation, puisque de précédentes études ont montré que la résistance à l'érosion augmente lorsque du sable est ajouté à la vase (Partheniades 1965; McCave 1984; Ockenden et Delo 1988; Mitchener et Torf 1996; Ahmad et al. 2011).

De plus, les modes d'érosion et de dépôt dépendent aussi largement des particules présentes dans la colonne d'eau et de leurs vitesses de chute associées. Par conséquent, la composition particulaire de la colonne d'eau, qui est prescrite au module sédimentaire, devrait être également améliorée et basée sur observations *in-situ*.

- **Floculation**

Dans les estuaires et les zones de panache des rivières, le processus de floculation est crucial et peut expliquer la majeur partie de la sédimentation des sédiments fins (Gibbs, 1985 ; Van Leussen,

1994 ; Dyer et Manning, 1999). Dans le module MUSTANG, ce processus est généralement pris en compte à travers une relation empirique entre la vitesse de chute des vases et leurs concentrations en suspension, multipliée par une fonction de turbulence (Le Hir et al., 2011). Dans notre étude cependant, le processus de floculation n'a pas été activé. Il conviendrait d'envisager la prise en compte de ce processus dans les futures études, et d'évaluer son influence sur les dépôts des particules.

- **Paramétrisation du module**

Dans cette étude préliminaire réalisée avec le modèle couplé SYMPHONIE-MUSTANG, seuls quelques paramétrisations ont été testées. D'autres tests devraient être effectués afin de déterminer la meilleure paramétrisation des termes d'érosion, de remise en suspension et de dépôt. Par exemple, la sensibilité du modèle au paramètre d'érodabilité E_0 (pour le sable et la vase) et à la tension critique de dépôt (τ_d) ainsi qu'aux différentes formulations (linéaire ou exponentielle) pour la transition du régime d'érosion entre le sable et la vase dans le cas d'un sédiment mixte pourraient être testées.

De plus, les concentrations en MES pour les rivières ont été prescrites au premier point de grille de chaque cours d'eau. Cela permet donc aux particules de se déposer tout le long de la rivière, ce qui peut potentiellement diminuer les concentrations de MES dans la colonne d'eau, avant que l'eau fluviale n'atteigne l'embouchure de la rivière. De futures simulations pourraient inclure une limitation du dépôt de particules le long des rivières, et l'influence de cette limitation sur la composition particulaire du panache et sur les structures d'érosion et de dépôt pourrait être évaluée.

- **Rétroactions "on-line"**

Dans l'étude préliminaire réalisée avec le modèle couplé, MUSTANG a été considéré comme un module intégré à SYMPHONIE, qui peut être activé ou non. En détail, SYMPHONIE fourni les conditions hydrodynamiques nécessaires à MUSTANG à chaque pas de temps. Cette méthode exclut cependant la possibilité de rétroactions du module sédimentaire sur le modèle hydrodynamique, c'est-à-dire que SYMPHONIE ne tient pas compte des changements morphologiques ou de composition de la colonne d'eau qui pourraient être générés par le module sédimentaire. Cependant, dans les zones peu profondes comme celles du DFR, des variations de bathymétrie générées par de l'érosion et/ou du dépôt pourraient influencer les champs de courants et les con-

traintes de cisaillement. De plus, de fortes concentrations de MES dans la colonne d'eau, induites par de la remise en suspension ou par des apports fluviaux, pourraient modifier la densité des masses d'eau. En vue de simulations plus réalistes, les futures études devraient donc intégrer les rétroactions du module sédimentaire sur le modèle hydrodynamique.

Suggestions pour de futures études couplées

Une fois améliorée et évaluée, la configuration couplée SYMPHONIE-MUSTANG pourrait être utilisée pour étudier :

- la variabilité du courant de bord Ouest et son rôle dans le transport des sédiments;

- le rôle des événements extrêmes, comme les tempêtes et les typhons, sur l'érosion et le transport des sédiments;

- la propagation du panache du Fleuve Rouge dans le GdT en terme de MES et l'étude de la variabilité des flux de MES en lien avec l'étude des flux d'eau présentée dans le Chapitre IV;

- l'influence des différents régimes de vagues sur la remise en suspension le long des côtes et sur les changements morphologiques;

- le rôle de la marée dans le mélange vertical des sédiments au Sud-Ouest de l'île d'Hainan ;

- les résultats du modèle sédimentaire pourraient être utilisés pour améliorer la précision des apports de MES par les fleuves dans des études couplées hydro-biogéochimiques (avec SYMPHONIE-Eco3m-s) qui sont actuellement en cours dans le MCM (doctorats de Trinh Bich Ngoc et de To Duy Thai).

Ces pistes de recherche sont au cœur des objectifs du Laboratoire Mixte International LOTUS (Land-Ocean-aTmosphere regional coUpled System) basé à l'Université des Sciences et Technologies de Hanoi, qui fédère des chercheurs de l'IRD (Institut de Recherche pour le Développement) au sein d'instituts Vietnamiens et Français. Dans ce contexte là, les travaux de modélisation et les campagnes d'observations *in-situ* proposés dans ce chapitre devraient y être soutenus et réalisés.

Appendix A

Description of the SYMPHONIE-MUSTANG coupled model and of the modeling strategy for preliminary sensitivity tests

Contents

This appendix presents the sediment transport module MUSTANG, which was coupled with SYM-PHONIE model, and describes the first choices made for the module parameterization and initialization. The results of this preliminary study are presented in Chapter V (section V.2.2.2).

A.1   MUSTANG module description

The module MUSTANG aims at simulating the transport and evolution of all kinds of sediment mixtures under the effect of hydrodynamic forcings (waves and currents). The module handles the sediment transport in the water column, the exchanges with the bed by erosion (E) and deposition (D) and the consolidation processes in the bed. As a result, MUSTANG simulates sediment concentrations (C) and related fluxes, as well as the morphological changes that are likely to occur in sediment nature, by mixing or sorting (Le Hir et al., 2011). Hence, the formulation of the module can be written as follows:

$$\frac{\delta C}{\delta t} = -\frac{\delta C u_i}{\delta x_i} + \frac{\delta C W_i}{\delta z} + \frac{\delta}{\delta z}(K_z \frac{\delta C}{\delta z}) + E - D \tag{A.1}$$

with $\frac{\delta C u_i}{\delta x_i}$ the transport by currents (u), $\frac{\delta C W_i}{\delta z}$ the sediment settling with W_s the settling velocity, $\frac{\delta}{\delta z}(K_z \frac{\delta C}{\delta z})$ the vertical molecular and turbulent mixing, E the erosion process and D the deposition process. The following sections detail the processes behind the source and sink terms E,Wsand D for cohesive and non-cohesive sediments. Note that the present study does not consider the consolidation process, since it is not represented in our version of MUSTANG. The modeling strategy is presented in section A.2 and the forcings data are presented in section A.3.

A.1.1   Erosion

Erosion flux E depends on the bottom stress linked to currents and waves (τ_{bot}) and on the choice of the erosion law.

A.1.1.1   Bottom shear stress

The bottom stress linked to waves τ_w is defined by Jonsson (1967) as:

$$\tau_w = \frac{1}{2} f_w |u_{orb}|_2 \tag{A.2}$$

where the wave friction factor is given by Myrhaug et al. (2001) as:

$$f_w = 1.39(\frac{|u_{orb}|\text{T}}{2\pi z_0})\text{-0.52} \tag{A.3}$$

where T is the wave period, z_0 the roughness length and u_{orb} is the bottom wave orbital velocity. This latter can be written as:

$$|u_{orb}| = \frac{\sigma \text{H}_s}{\sqrt{8}\sinh(k\text{D})} \tag{A.4}$$

with H_s the wave height, k the wave number, σ the relative frequency and D the water depth.

The bottom stress due to the current only is expressed as follows:

$$\tau_c = \rho_w u_{2*} \tag{A.5}$$

with ρ_w the density of water and u_* the friction velocity (or shear velocity). Since both waves and currents enhance the shear stress at the bottom, a mean stress τ_m that combines the two stresses is given by Soulsby (1997) and expressed as:

$$\tau_m = \tau_c[1 + 1.2(\frac{\tau_w}{\tau_c + \tau_w})\text{3.2}] \tag{A.6}$$

Finally, the bottom stress τ_{bot} linked to waves and currents can be expressed as a vectorial sum of τ_m and τ_w as:

$$\tau_{bot} = [(\tau_m + \tau_w|\cos\phi|)_2) + (\tau_w\sin\phi)_2]_{0.5} \tag{A.7}$$

where ϕ is the angle between current direction and wave propagation.

Here, H_S, k, σ and T are provided by a wave hindcast database built with the WAVEWATCH III wave model, hereafter WW3 (Tolman (2008, 2009); Ardhuin et al. (2010)). For this thesis work, WW3 simulations were performed over the period 2009-2017 by the Laboratoire d'Aérologie (Toulouse,

France) on the grid used in Chapter III and Chapter IV, horizontally degraded every second point and extended of 5 points at the open lateral boundary. These simulations on a bigger grid thus provide the wave conditions at the open lateral boundary of the grid used for hydrodynamics.

A.1.1.2 Erosion law

The mud erosion rate is expressed as a function of the excess shear stress to a power, which depends on the particle diameter (higher power for smaller particles). For cohesive and non-cohesive sediments, the Partheniades-Ariathurai (1962, 1974) erosion law is prescribed as:

$$
\begin{cases}
E = E_0 (\dfrac{\tau_{bot}}{\tau_{cr}} - 1)_n, & if\, \tau_{bot} \geqslant \tau_{cr} \\
E = 0, & if\, \tau_{bot} < \tau_{cr}
\end{cases}
\tag{A.8}
$$

As often most in literature, n is equal to 1 (Ferré et al., 2008; Mengual et al., 2017; Gangloff, 2017; Mikolajczak, 2019), while E_0 the erodibility parameter and τ_{cr}, the critical shear stress for erosion are to be determined for each sediment class i. The erosion flux can therefore be expressed by particle class according to their respective proportion in the sediment (p_i) as:

$$
\begin{cases}
E_i = p_i E_{0,i} (\dfrac{\tau_{bot}}{\tau_{cr,i}} - 1)_{ni}, if\, \tau_{bot} \geqslant \tau_{cr,i} \\
E_i = 0, if\, \tau_{bot} < \tau_{cr,i}
\end{cases}
\tag{A.9}
$$

Three types of erosion are considered depending on the sediment composition: erosion of mud only (cohesive), erosion of sand only (non-cohesive) or erosion of a mixture of mud and sand. The different cases are determined by the mud fraction (f_m) of the sediment, which is compared to two critical mud fractions: *mudfr1* and *mudfr2*. The critical value of *mudfr1* is formulated according to the diameter of sand (d_s) following the recommendations of Panagiotopoulos et al. (1997) and Le Hir et al. (2011) as:

$$
mudfr1 = \alpha_0 d_S
\tag{A.10}
$$

where d_s is the diameter of the sand fraction and α_0 is set to 10_3 m$_{-1}$. The value of *mudfr2* is fixed to 70% following the recommendations of Le Hir et al. (2011). For each sediment mode to be eroded (described next), each class of sediments are eroded following Eq. A.9.

1/ If f_m > *mudfr2*(i.e. cohesive sediment) In this case, the sediment is eroded with an erodibility parameter $E_{0,mud}$ fixed at $2 \times 10_{-5}$ kg m$_2$ s$_{-1}$ following the work of Vinh (2018) in the RRD area, and different values of $\tau_{cr,mud}$ are tested in this study (from 0.2, 0.35 and 0.5 N. m$_{-2}$), following the choices made by Mikolajczak (2019), Dufois (2008) and Gangloff (2017).

2/ If f_m < *mudfr1*(i.e. non-cohesive sediment) In this case, the erodibility parameter E$_0$,sandis fixed at $1 \times 10_{-4}$ kg m$_{-2}$ s $_{-1}$ following Vinh (2018), while τ_{cr},sand is in this case expressed as follows:

$$\tau_{cr,sand} = \max(\frac{\sum_{j=1}^{2} (p_{sand(j)} \tau_{cr,sand(j)})}{\sum_{j=1}^{2} (p_{sand(j)})}, \tau_{cr,sand2}) \tag{A.11}$$

with $\tau_{cr,sand1}$ and $\tau_{cr,sand2}$ expressed following the formulation of Soulsby (1997):

$$\tau_{cr,sand j} = \theta_{cr,sand(j)} (\rho_{sand(j)} - \rho w) g d_{s(j)} \tag{A.12}$$

where g=9.81 m s$_{-1}$ is the gravitational acceleration constant, $\rho_{sand(j)}$ is the density of each sand class j, ρ_w=1025kg m$_{-3}$ is the density of water and $\theta_{cr,sand(j)}$ is the Shields threshold for each sand class, defined as:

$$\theta_{cr,sand(j)} = \frac{0.3}{(1 + 1.2 d_{*,sand(j)})} + 0.055(1 - e_{-0.02d*,sand(j)}) \tag{A.13}$$

with

$$d_{*,sand(j)} = d_{s(j)} [\frac{(\frac{\rho_{sand(j)}}{\rho_w} - 1)g}{\nu_2}]_{1/3} \tag{A.14}$$

where ν is the kinematic water viscosity (1.14 10$_{-6}$ m$_2$ s$_{-1}$).

3/ If *mudfr1*<f_m<*mudfr2* (i.e. sand/mud mixture) In this case, the erosion parameters (τ_{cr}, E$_0$, n) are interpolated from the respective sand and mud parameters with an exponential transition trend, following the recommendations of Mengual et al. (2017).

A.1.1.3 Sediment layers erosion

In MUSTANG, the bed is composed of superimposed sediments layers that can be eroded one after another. This is the concept of active layer which allows erosion of underlying layers to start if the

upper layer have been eroded within the time step dt. Erosion lasts until the time step is over or if the active layer if fully eroded.

A.1.2   Settling velocities

Settling velocities of particles vary with particles properties (size, effective density) and fluid characteristics (viscosity, turbulence). SSC also contribute to particle settling, with high SSC (>1 g l$_{-1}$) limiting the particle settling by space limitation (Le Hir, 1999). In addition, aggregation processes by collision, salt flocculation (Thill et al., 2001), or by electro chemical action of the organic matter (Naudin et al., 1997) are also phenomena responsible for modification of settling velocities. However, these latter processes are not taken into consideration in this present study. In MUSTANG, settling velocities for cohesive sediments and flocs can be directly prescribed by the user. Settling velocities for cohesive particles of each class i can be estimated following the Stokes formulation:

$$W_{s,i} = \frac{(s_l - 1)g d_{2i}}{18\nu} \tag{A.15}$$

where s_l represents the relative grain density as $s_l = \frac{\rho_{s,i}}{\rho_w}$, with ρs the grain density and ρ_w the water density and d represents the median diameter of each sediment (i.e. D$_{50}$).

For flocs, settling velocities can be estimated with the Agrawal and Pottsmith (2000) formulation for an estuary:

$$W_{s,i} = 0.45 x 10_{-3} (\frac{d_i}{2})_{1.17} \tag{A.16}$$

where W_s is expressed in cm s$_{-1}$ and d in μm.

Lastly, settling velocities for sands are computed by MUSTANG, following the Soulsby law:

$$W_{s,j} = \frac{\nu}{d_{sj}} [(10.36_2 + 1.049 d_{3*,sand(j)})_{0.5} - 10.36] \tag{A.17}$$

Characteristics of modeled particles and associated settling velocities for our present case study are described in section A.2.1.

n	1
$\tau_{cr,mud}$	0.2;0.35;0.5 N m$_{-2}$
$E_{0,mud}$	2 10$_{-5}$ kg m$_2$ s$_{-1}$
$E_{0,sand}$	1 10$_{-4}$ kg m$_2$ s$_{-1}$
α_0	1000 m$_{-1}$
$mudfr2$	70%
τ_d	1000 N m$_{-2}$
dz_{sedmax}	0.5 m
N_{max}	10

Table A.1: Erosion, deposition and configuration parameters values used in this study.

A.1.3   Sediment deposition

The deposition flux of each cohesive sediment class i follows the Krone law:

$$\begin{cases} D_i = W_{s,i}C_i(1 - \dfrac{\tau_{bot}}{\tau_{d,i}}), & if\,\tau_{bot} \geqslant \tau_{d,i} \\[2mm] D_i = 0, & if\,\tau_{bot} < \tau_{d,i} \end{cases} \qquad (A.18)$$

where $W_{s,i}$ is the settling velocity, C_i is the suspended sediment concentration in the closest mesh to the bed and $\tau_{d,i}$ is the critical shear stress for deposition. This latter represents a threshold above which deposition does not occur. In this study and following Mengual (2017) and Vinh (2018), τ_d=1000 Pa for each sediment class in order to allow depositing material to leave the water column whatever the turbulence level near the bottom.

Once deposition begins, sediments start filling the bed layer. If the thickness of the deposited sediments exceeds the maximum layer thickness (dz_{sedmax}), a new layer is generated. If the maximum number of layers created is reached (N_{max}), the two most underlying layers can merge into one, and a new layer can be generated on the top (Le Hir et al., 2011). Here, dz_{sedmax}=0.5 m and N_{max} = 10. The values of all erosion and deposition parameters above-mentioned and used in this study are summarized in Table A.1.

A.2   Modeling strategy

The aim of this preliminary study is to test the model sensitivity, in terms of sediment transport, to different model parameterizations, seabed compositions and types of particles in the water column, with the longer term objective of using the model to study sediment transport in our region of interest. The different tests and model set ups are made accordingly and are described

in the next sections.

A.2.1 Choice of class of particles in the water column

To assess the model sensitivity to the types of particles in the water column, different particles and associated properties are tested. Based on field measurements, the results from Chapter II emphasized the presence of 3 types of sediments in the Van Uc estuary water column (see Fig. II.7 a): primary particles (<3 μm), flocculi (6-10 μm) and microflocs (50-80 μm). This study further emphasized that the concentrations of the finest fraction of particles (primary particles) drastically decreased during the low-flow season and with the intrusion of salty seawater along the estuary. It was suggested that this decrease could be due to the transfer of primary particles into larger flocs by flocculation and/or aggregation. Indeed, the combined effects of the along-estuary salinity gradient at high tide and the decrease of turbulence at low-flow could have favored particles aggregation, and thus a decrease in primary particles concentration. As the aim of this study is to simulate the sediment transport in the ocean, the choice is made to only consider the coarser fraction of particles (flocculi and microflocs) since concentrations of primary particles were low in the presence of sea water. Diameters of 8 and 60 μm are chosen for flocculi and microflocs, respectively. In addition, results from Chapter II showed that primary particles, flocculi and microflocs occupied respectively 25%, 50% and 25% of the total volume of particles. As we do not represent the primary particles in this study, it is thus considered that flocculi and microflocs represent 60% and 40% of the total SSC from the rivers, respectively. Lastly, we test the model sensitivity to the choice of settling velocities for both flocculi and microflocs. Two sets of particles are tested, one set (set-1) with faster settling velocities than the second one (set-2). W_s for the microflocs and flocculi of set-1 are computed following Eq. A.16 (i.e. W_s for flocs) and Eq. A.15 (i.e. W_s for unique cohesive particles), respectively (Table A.2). For set-2, W_s of microflocs is obtained from Vinh (2018) in the Cam - Bach Dang estuary and W_s of flocculi is computed following the formulation of W_s for flocs (Eq. A.16) (Table A.2).

	Sediment type	D (μm)	ρ_s (kg m$_{-3}$)	$W_s(mms_{-1})$	Sources	Proportion (%) in the water column
set-1	Microflocs	60	-	0.24	Eq. A.16	40
	Flocculi	8	2650	0.052	Eq. A.15	60
set-2	Microflocs	60	-	0.13	Vinh (2008)	40
	Flocculi	8	-	0.023	Eq. A.16	60

Table A.2: Water column particles characteristics for set-1 and set-2.

A.2.2 Choice of seabed composition

In sediment transport models, the bed layer is usually initialized with an approach based on core samples and/or on sea bed composition measures (Bever and Mac Williams, 2013). However, in the present study, we do not dispose of enough seabed measurements to produce sufficiently accurate spatial coverage. Therefore, we test 3 different seabeds (seabed-1, seabed-2, seabed-3) with various compositions (Table A.3). First, seabed-1 is chosen to be composed of only flocculi (60%) and microflocs (40%) following the proportions of particles chosen for the water column in section A.2.1. Second, grain size distributions of seabed samples collected in the Cam and Bach Dang estuary revealed high contents of particles 8 µm, of particles 60 µm and of coarser particles 100-200 µm (Lefebvre et al., 2012). Following these observations, two seabeds with various sand contents are tested: seabed-2 with 20% of sand, 35% of microflocs and 45% of flocculi, and seabed-3, with 50% of sand, 20% of microflocs and 30% of flocculi (Table A.3).

	seabed-1	seabed-2	seabed-3
Flocculi	60%	45%	30%
Microflocs	40%	35%	20%
Sand	0%	20%	50%

Table A.3: Proportions (%) of particles in the bottom sediment for different seabed configurations.

A.2.3 Strategy of sensitivity simulations

Various water column composition, seabed composition and τ_{cr} values are tested through sensitivity simulations summarized in Table A.4. In order to perform fast tests, the simulations are only performed over 5 months from April to August 2009. This allows 4 months of model spin-up as only the month of August will be studied.

simulation	set-1	set-2	seabed-1	seabed-2	seabed-3	τ_{cr} N m$_{-2}$	period
# 1	x		x			0.2	04-08/2019
# 2		x	x			0.2	04-08/2019
# 3	x		x			0.35	04-08/2019
# 4		x	x			0.35	04-08/2019
# 5	x		x			0.5	04-08/2019
# 6		x	x			0.5	04-08/2019
# 7	x			x		0.35	04-08/2019
# 8	x				x	0.35	04-08/2019

Table A.4: Summary of sensitivity simulations.

A.3   Data for model forcing and model evaluation

A.3.1   Suspended sediment concentration in rivers

The suspended sediment concentrations (SSC) at the upstream limit of the 7 rivers of the Red River system modeled in this study are derived from SSC in-situ data that were collected by the National Hydro-Meteorological Service (NHMS) of Vietnam at the hydrographic station of Son Tay (see Fig. IV.2 b in Chapter IV for location). Following Vinh et al. (2014), who estimated the contribution of each distributary to the total Red River sediment discharges using the MIKE11 model, a percentage of the total Son Tay's daily sediment discharges was attributed accordingly to each distributary: 6.9% of the total discharge was attributed to the Bach Dang River, 13.9% to the Cam River, 14.4% to the Van Uc River, 6.4% to the Thai Binh River, 30% to the Ba Lat River, 5.6% to the Ninh Co River and 22.8% to the Day River. The forcing variable is imposed at the most upstream channel grid point. As explained in section IV.3.1 of Chapter IV, Son Tay hydrological station is located further upstream of each first grid point of each river, therefore, a delay t is applied for each SSC time series of each river (see Table IV.1 in Chapter IV for t values). In other rivers of the GoT (i.e. these represented by green dots on Fig. IV.2 a), SSC are set to 0 g l_{-1} as we do not have access to any sediment discharges data in these rivers.

A.3.2   Observations

Model outputs are compared to monthly mean of SPM derived from remote sensing ocean color data collected by the MEdium Resolution Imaging Spectrometer (MERIS) at full spatial resolution (300 x 300 m_2), here for August 2009. SPM are computed using Han (2016) algorithm and are available at `ftp://ftp.ifremer.fr/ifremer/sextant_data/GLOBCOAST/SPM` (Loisel and Dessailly, 2016).

The results of the modeling strategy and of the simulations presented in this appendix are shown and discussed in section V.2.2.2 of Chapter V.

A.4   References

- Agrawal Y. C., Pottsmith H. C. (2000) Instruments for particle size and settling velocity observations in sediment transport, MG, 168, 89-114.
- Ardhuin F., Rogers E., Babanin A. V., Filipot J., Magne R., Roland A., van der Westhuysen A., Queffeulou P., Lefevre J., Aouf J., Collard F. (2010) Semiempirical dissipation source functions

for ocean waves. Part I: Definition, Calibration, and Validation, J. Phys. Oceanogr., 40, 1917-1941, doi:10.1175/2010JPO4324.1.

- Ariathurai C. R. (1974) A finite element model of cohesive sediment transportation. Ph.D. thesis, University of California, Davis, USA.

- Dufois F. (2008) Modélisation du transport particulaire dans le Golfe du Lion en vue d'une application au devenir des traceurs radioactifs issus du Rhône, Ph.D. thesis, Université du Sud Toulon Var, Toulon, France.

- Ferré B., Durrieu de Madron X., Estournel C., Ulses C., Le Corre G. (2008) Impact of natural (waves and currents) and anthropogenic (trawl) resuspension on the export of particulate matter to the open ocean, Cont. Shelf. Res., 28, 2071-2091, doi: 10.1016/j.csr.2008.02.002.

- Gangloff A. (2017) Fate of Rhône River sediment inputs to the Gulf of Lions: study of the Rhône River turbid plume dynamics in response to hydro meteorological forcings, Ph.D. thesis, Université de Bretagne Occidentale (Brest, France), https://tel.archives-ouvertes.fr/tel-01797368.

- Han B., Loisel H., Vantrepotte V., Mériaux X., Bryère P., Ouillon S., Dessailly D., Xing Q., Zhu J. (2016) Development of a Semi-Analytical Algorithm for the Retrieval of Suspended Particulate Matter rom Remote Sensing over Clear to Very Turbid Waters, Remote Sens., 8, 211, doi:10.3390/rs8030211 2016.

- Jonsson I. G. (1997) Wave boundary layers and friction factors, Coastal Engineering 1966, pp 127-148.

- Le Hir P., Cayocca F., Waeles B. (2011) Dynamics of sand and mud mixtures: a multiprocess-based modelling strategy, Cont. Shelf. Res., 31(10); S135-S149; doi: 10.1016/j.csr.2010.12.009. Lefebvre, J. P., S. Ouillon, V. D. Vinh, R. Arfi, J. Y. Panché, X. Mari, C. V. Thuoc and J. P. Torréton. (2012) Seasonal variability of cohesive sediment aggregation in the Bach Dang-Cam Estuary, Haiphong (Vietnam), Geo.-Mar. Lett., 32, 103-121, doi: 10.1007/s00367-011-0273-8.

- Loisel H., Dessailly D. (2016) GlobCoast Moyenne mensuelle des Matières En Suspension (MES). Université du Littoral Côte d'Opale. https://doi.org/10.12770/543e3c3f-3842-4c1d-b192-afe2f3f4271b

- Mengual B., Le Hir P., Cayocca F., Garlan T. (2017) Modelling fine sediment dynamics: towards a common erosion law for fine sand, mud and mixtures, Water 9, 564, https://doi.org/10.3390/w9080564

- Mikolajczak G. (2019) Dynamique de l'eau et des apports particulaires originaires du Rhône sur la marge continentale du Golfe du Lion, Ph.D. thesis, University of Toulouse (France).

- Naudin J. J., Cauwet G., Chétiennot-Dinet M. J., Deniaux B., Devenon J. L., Pauc H. (1997) River discharge and wind influence upon particulate transport at the land-ocean interaction: case study of the Rhone River Plume, Estuar. Coast. Shelf Sci., 45(3), 303-16, doi:10.1006/ecss.1996.0190.

- Panagiotopoulos I., Voulgaris G., Collins M. B. (1997) The influence of clay on the threshold of movement of fine sandy beds, Coastal Engineer., 32, 19-43, https://doi.org/10.1016/S0378-3839(97)00013-6.

- Partheniades E. (1962) Erosion and deposition of cohesive soils. Journal of the Hydraulics Division, 91, 105-139.

- Soulsby R. (1997) Dynamics of marine sands: a manual for practical applications. Thomas Telford.

- Thill A., Moustier S., Garnier J. M., Estournel C., Naudin J. J., Bottero J. Y. (2001) Evolution of particle size and concentration in the Rhone river mixing zone: influence of salt flocculation, Cont. Shelf Res., 21(18), 2127-40, https://doi.org/10.1016/S0278-4343(01)00047-4

- Tolman H. (2008) A mosaic approach to wind wave modelling, Ocean Modell., 25, 35-47, doi:10.1016/j.ocemod.2008.06.005.

- Tolman H. (2009) User Manual and system documentation of WAVEWATCH-III version 3.14. Technical Report, Tech. Rep. 276, NOAA/NWS/NCEP/MMAB/ Vinh V. D. (2018) Suspended

sediment dynamics in Red River distributaries and along the Red River delta: Focus on estuarine processes and recent balances, University of Sciences and Technology of Hanoi, Hanoi, Vietnam.

- Vinh V.D., Ouillon S., Tanh T.D., Chu L.V. (2014) Impact of the Hoa Binh dam (Vietnam) on water and sediment budgets in the Red River basin and delta, Hydrol. Earth Syst. Sci., 18, 3987–4005, doi:10.5194/hess-18-3987-2014.

Abstract

Deltas and coastal regions deliver the largest inputs of freshwater and sediments to the shelf and open ocean, understanding water and sediment dynamics and variability in those regions is therefore crucial. The spatio-temporal variability of estuarine and ocean dynamics under the influence of natural forcings and their impact on sediment transport and fate was assessed along the Red River estuary - coastal ocean - Gulf of Tonkin continuum. First, in-situ estuarine observations evidenced the seasonal and tidal variabilities of flow and suspended matter, and showed in particular the role of tidal pumping in the estuary siltation. Second, a 3D realistic hydrodynamic model was set up and calibrated with various observations and satellite data. Beforehand, a high-resolution model configuration was implemented and optimized with sensitivity tests of the Gulf of Tonkin's tidal components to bathymetry and various bottom friction parameterizations. Third, the resulting optimized configuration was used to study the large scale Gulf of Tonkin circulation at daily, seasonal and interannual scales, and to identify the drivers of their variabilities. Ekman transport variability due to monsoon winds reversal drives the seasonal circulation, which can be reversed in summer by episodic typhoon events and intensified in winter. ENSO, strong typhoon activity and Arctic Oscillation have been identified as drivers of the interannual circulation variability. Lastly, preliminary tests with a sediment transport module coupled with the hydrodynamics model revealed the importance of the seabed composition and of the parameterization of the erosion coefficients.

Keywords : estuarine to regional circulation, sediment transport, variability, in-situ observations, regional ocean modelling, estuary-coastal ocean continuum, Red River, Gulf of Tonkin

---

Résumé

Les deltas et les régions côtières constituent les sources les plus importantes d'eau douce et de matière en suspension vers le plateau continental puis le large, la compréhension de leur dynamique et de leur variabilité est donc cruciale. Cette thèse vise à mieux comprendre la variabilité spatio-temporelle de la dynamique estuarienne et océanique sous l'influence de forçages naturels et l'influence de cette variabilité sur le transport et devenir des sédiments le long du continuum estuaire - océan côtier du Fleuve Rouge au Golfe du Tonkin. Des observations in-situ collectées dans l'estuaire ont d'abord mis en évidence l'influence de la variabilité saisonnière et de la variabilité due à la marée sur le débit et sur le devenir des matières en suspension, en particulier le rôle du pompage tidal dans l'envasement de l'estuaire. Deuxièmement, un modèle hydrodynamique 3D réaliste, basé sur une configuration haute-résolution et un paramétrage optimisés et validés à partir de plusieurs jeux d'observations in-situ et de données satellitaires, a été utilisé pour l'étude de la circulation à l'échelle du Golfe du Tonkin. Cette configuration a préalablement été optimisée à l'aide de tests de sensibilité des solutions de marée à la bathymétrie et à la paramétrisation du frottement de fond. Les facteurs de la variabilité de cette circulation aux échelles journalière, saisonnière à interannuelle ont été identifiés. La variabilité du transport d'Ekman due à l'inversion saisonnière des vents de mousson a été identifiée comme le principal moteur de la circulation saisonnière, cette dernière pouvant être inversée (intensifiée) en été (hiver) par le passage de typhons. ENSO, l'Oscillation Arctique ou encore une forte activité cyclonique ont été identifiés comme les facteurs de la variabilité interannuelle. Des tests préliminaires avec un module de transport sédimentaire couplé au modèle hydrodynamique ont révélé l'importance, pour la représentation réaliste du transport de matière en suspension, de la composition du sédiment de fond et du paramétrage des coefficients d'érosion.

Mots clés : circulation estuarienne à régionale, transport sédimentaire, variabilité, observations in-situ, modélisation océanique régionale, continuum estuaire-océan côtier, Fleuve Rouge, Golfe du Tonkin